VOLUME V

BOOK 6

SUBSYSTEM AND TECHNICAL ANALYSES

MECHANICAL SUBSYSTEMS

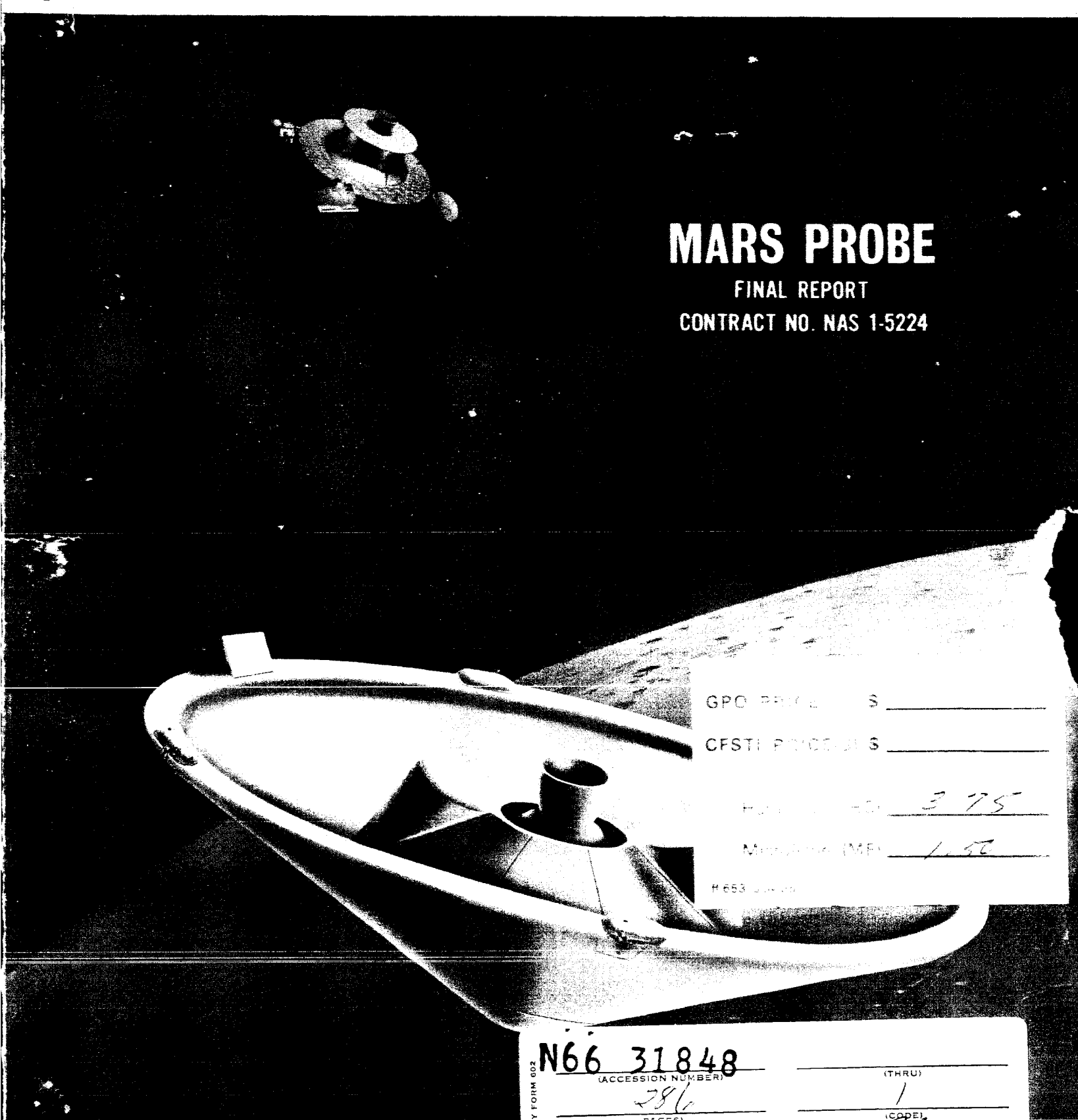

MARS PROBE

FINAL REPORT

CONTRACT NO. NAS 1-5224

AVCO CORPORATION

BOOK INDEX

VOLUME	I	SUMMARY
VOLUME	II	PROBE/LANDER, ENTRY FROM THE APPROACH TRAJECTORY
Book	1	System Design
Book	2	Mission and System Specifications
VOLUME	III	PROBE, ENTRY FROM ORBIT
Book	1	System Design
Book	2	Mission, System and Component Specifications
Book	3	Development Test Programs
VOLUME	IV	STERILIZATION
VOLUME	V	SUBSYSTEM AND TECHNICAL ANALYSES
Book	1	Trajectory Analysis
Book	2	Aeromechanics and Thermal Control
Book	3	Telecommunications, Radar Systems and Power
Book	4	Instrumentation
Book	5	Attitude Control and Propulsion
Book	6	Mechanical Subsystems

COMPARATIVE STUDIES OF CONCEPTUAL DESIGN AND QUALIFICATION PROCEDURES FOR A MARS PROBE/LANDER

FINAL REPORT

VOLUME V - SUBSYSTEM AND TECHNICAL ANALYSES

Book 6 - MECHANICAL SUBSYSTEMS

Prepared by

SPACE SYSTEMS DIVISION
AVCO CORPORATION
Lowell, Massachusetts

AVSSD-0006-66-RR
Contract NAS 1-5224

11 May 1966

Prepared for

NATIONAL AERONAUTICS AND SPACE ADMINISTRATION
LANGLEY RESEARCH CENTER
LANGLEY STATION
Hampton, Virginia 23365

PREFACE

The results of Mars Probe/Lander studies, conducted over a 10-month period for Langley Research Center, NASA, are presented in detail in this report. Under the original contract work statement, studies were directed toward a direct entry mission concept, consistent with the use of the Saturn IB-Centaur Launch Vehicle, wherein the landing capsule is separated from the spacecraft on the interplanetary approach trajectory, some 10 to 12 days before planet encounter. The primary objectives of this mission were atmospheric sampling by the probe/lander during entry and terrain and atmosphere physical composition measurement for a period of about 1 day after landing.

Studies for this mission were predicated on the assumption that the atmosphere of Mars could be described as being within the range specified by, NASA Mars Model Atmospheres 1, 2, 3 and a Terminal Descent Atmosphere of the document NASA TM-D2525. These models describe the surface pressure as being between 10 and 40 mb. For this surface pressure range a payload of moderate size can be landed on the planet's surface if the entry angle is restricted to be less than about 45 degrees.

Midway during the course of the study, it was discovered by Mariner IV that the pressure at the surface of the planet is in the 4 to 10 mb range, a range much lower than previously thought to be the case. The results of the study were re-examined at this point. It was found that retention of the direct entry mission mode would require much shallower entry angles to achieve the same payloads previously attained at the higher entry angles of the higher surface pressure model atmospheres. The achievement of shallow entry angles (on the order of 20 degrees), in turn, required sophisticated capsule terminal guidance, and a sizeable capsule propulsion system to apply a velocity correction close to the planet, after the final terminal navigation measurements.

Faced with these facts, NASA/LRC decided that the direct entry from the approach trajectory mission mode should be compared with the entry from orbit mode under the assumption that the Saturn 5 Launch Vehicle would be available. Entry of the flight capsule from orbit allows the shallow angle entry (together with low entry velocity) necessary to permit higher values of M/C_DA, and hence entry weight in the attenuated atmosphere.

It was also decided by LRC to eliminate the landing portion of the mission in favor of a descent payload having greater data-gathering capacity, including television and penetrometers. In both the direct entry and the entry from orbit cases, ballistic atmospheric retardation was the only retardation means considered as apecifically required by the contract work statement.

Four months had elapsed at the time the study ground rules were changed. After this point the study continued for an additional five months, during which

period a new design for the substantially changed conditions was evolved. For this design, qualification test programs for selected subsystems were studied. Sterilization studies were included in the program from the start and, based on the development of a fundamental approach to the sterilization problem, these efforts were expanded in the second half of the study.

The organization of this report reflects the circumstance that two essentially different mission modes were studied -- the first being the entry from the approach trajectory mission mode and the other being the entry from orbit mission mode -- from which two designs were evolved. The report organization is as follows:

Volume I, Summary, summarizes the entire study for both mission modes.

Volume II reports on the results of the first part of the study. This volume is titled Probe/Lander, Entry from the Approach Trajectory. It is divided into two books, Book 1 and Book 2. Book 1 is titled System Design and presents a discursive summary of the entry from the approach trajectory system as it had evolved up to the point where the mission mode was changed. Book 2, titled Mission and System Specifications, presents, in formal fashion, specifications for the system. It should be understood, however, that the study for this mission mode was not carried through to completion and many of the design selections are subject to further tradeoff analysis.

Volume III is composed of three books which summarize the results of the entry from orbit studies. Books 1 and 2 are organized in the same fashion as the books of Volume II, except that Book 2 of Volume III presents component specifications as well. Book 3 is titled Development Test Programs and presents, for selected subsystems, a discussion of technology status, test requirements and plans. This Book is intended to satisfy the study and reporting requirements concerning qualification studies, but the selected title is believed to describe more accurately the study emphasis desired by LRC.

Volume IV presents Sterilization results. This information is presented separately because of its potential utilization as a more fundamental reference document.

Volume V presents, in six separate books, Subsystem and Technical Analyses. In order (from Book 1 to Book 6) they are:

Trajectory Analysis
Aeromechanics and Thermal Control
Telecommunications, Radar Systems and Power
Instrumentation
Attitude Control and Propulsion
Mechanical Subsystems

Most of the books of Volume V are divided into separate discussions of the two mission modes. Table of Contents for each book clearly shows its organization.

CONTENTS

1.0 Separation Subsystems 1

1.1 Summary 1
1.2 Required Conditions and Constraints 2

1.2.1 Launch Vehicle 2
1.2.2 Environmental 2
1.2.3 Functional 2
1.2.4 Sterilization 4

1.3 General Methods 4

1.3.1 Actuation Methods 4
1.3.2 Retaining Methods 5
1.3.3 Impulse Methods 5

1.4 Selected Subsystems -- Entry from the Approach Trajectory Design 6

1.4.1 Sterilization Canister-Lid Deployment 6
1.4.2 Entry-Vehicle Separation 6
1.4.3 ΔV Propulsion and ACS Electronics Separation ... 9
1.4.4 Parachute Deployment 10
1.4.5 Entry Shell Separation 10
1.4.6 Landed Capsule Release 10
1.4.7 Tether Release 12
1.4.8 Impact Attentuator Jettison 12
1.4.9 Payload Erection (Flotation Sphere Only) 15
1.4.10 Instrument Deployment 15

1.5 Selected Subsystems -- Entry from Orbit Design 15

1.5.1 Sterilization Canister-Lid Deployment 18
1.5.2 Entry-Vehicle Separation 22
1.5.3 Parachute Deployment 22
1.5.4 Entry-Shell Separation 22
1.5.5 Nose-Cap Separation 25
1.5.6 Penetrometer Separation 27

1.6 Problem Areas 27

1.6.1 Entry-Shell Separation Signal Timing 27
1.6.2 Nose-Cap Separation Characteristics 31

CONTENTS (Cont'd)

2.0 Parachute Subsystem 32

2.1 General Summary 32
2.2 Parachute Materials 36

2.2.1 Selection Criteria 38
2.2.2 Weight and Air Permeability 38
2.2.3 Riser and Shroud Lines 39
2.2.4 Test Data 40
2.2.5 Temperature Effects (Sterilization) 40
2.2.6 Chemical Sterilization Effects 46
2.2.7 Problem Areas 47

2.3 Parachute Configurations 48

2.3.1 Performance Characteristics 49
2.3.2 Reliability 49
2.3.3 Weight Penalty 49
2.3.4 Development Risk 50
2.3.5 Main Parachute 50
2.3.6 Drogue Parachute 54
2.3.7 Pilot Parachute 56

2.4 Entry from Approach Trajectory Design 57

2.4.1 Summary 57
2.4.2 Main Parachute Analysis 58
2.4.3 Drogue Parachute Analysis 77
2.4.4 Selected Design 96
2.4.5 Actuation System 96
2.4.6 Dynamic Analysis 101

2.5 Entry from Orbit Design 107

2.5.1 Summary 107
2.5.2 Main Parachute Analysis 108
2.5.3 Actuation System 118
2.5.4 Dynamic Analysis 132
2.5.5 System Analyses 141

2.6 Significant Problem Areas 156

2.6.1 Supersonic Deployment 156
2.6.2 Low Inflation Pressures 157

CONTENTS (Concl'd)

2.6.3 Wind Gust Oscillations 157
2.6.4 Blunt Body Effects 157
2.6.5 Parachute Materials 157

2.7 Future Concepts 158

3.0 Impact Attenuation Subsystem for Landed Capsule (Entry from Approach Trajectory 159

3.1 Summary 159
3.2 Analysis Methods and Results 160

3.2.1 Introduction 160
3.2.2 Survey of Crushable Materials 160
3.2.3 Foam-Filled Fiberglass Honeycomb 163
3.2.4 Balsa Wood 190
3.2.5 Air Bags 198
3.2.6 Terrain Feature Management 204

3.3 Significant Problem Areas 208

3.4 Future Concepts 211

4.0 Sterilization Canister Pressurization Subsystem 212

4.1 Summary 212
4.2 Requirements 212
4.3 Major Tradeoffs 213
4.4 Methods and Results 213

4.4.1 Leakage Rate 213
4.4.2 Resupply Method 214
4.4.3 Venting and Relief Approach 217

4.5 Problem Areas 222

Appendixes

A. Impact Dynamics Analysis -- Prolate and Oblate Spheroid Landers A-1
B. Sterilization Canister Leakage Rate B-1

ILLUSTRATIONS

Figure 1 Flight Operational Sequence 7

2 Blunt Cone--Oblate Spheroid Launch Configuration 8

3 Blunt Cone--Oblate Spheroid Entry Configuration 11

4 Oblate Spheroid Landed Capsule 13

5 Flotation Sphere Landed Capsule 14

6 De-orbit Sequence 16

7 Terminal Descent Sequence 17

8 Sterilization Cansiter Separation Subsystem 19

9 FLSC-Separation Joint Test Apparatus 20

10 Actuation of FLSC Separation Joint 21

11 Entry-Vehicle Separation Subsystem 23

12 Parachute Deployment Sequence 24

13 Entry-Shell Separation Subsystem 26

14 Nose-Cap Separation Subsystem 28

15 Penetrometer Separation Subsystem 29

16 Entry-Shell Separation Logic 30

17 Percent Strength Retention versus Temperature for Candidate Canopy Materials 45

18 Single Parachute System -- Impact Velocity versus Main Parachute Area/Suspended Weight 60

19 Single Parachute System -- Main Parachute Weight versus Impact Velocity 62

20 Single Parachute System -- Main Parachute Nominal Diameter versus Impact Velocity 63

ILLUSTRATIONS (Cont'd)

Figure 21 Percent Main Parachute Weight versus Impact Velocity 64

22 Single Parachute System -- Main Parachute Weight versus Suspended Weight..... 65

23 Single Parachute System -- Main Parachute Weight versus Suspended Weight 66

24 Single Parachute System -- Suspended Weight versus Main Parachute Diameter 67

25 Suspended Weight versus Main Parachute Weight -- Three Parachute Cluster 69

26 Main Parachute Weight and Diameter versus Suspended Weight for Three and Five Parachute Clusters .. 70

27 Opening Shock Load versus Reefed Parachute Area/Full Open Area 72

28 Descent Time versus A_{mc}/W_{susp} 73

29 Full-Open Altitude versus Descent Time 75

30 Main Parachute Weight versus Dynamic Pressure 76

31 Fabric Mach No. Limit versus Altitude (Nomex Fabric) 78

32 Fabric Mach No. Limit versus Altitude (Nylon Fabric) 79

33 Fabric Temperature Limited Mach No. versus Altitude ... 80

34 M/C_DA versus Deployment Altitude (Mach 3.5 Deployment)..... 82

35 M/C_DA versus Deployment Altitude (Mach 2.75 Deployment) 83

36 Dynamic Pressure versus Deployment Altitude 84

37 Altitude at Main Parachute Depolyment versus A_D/A_V (Drogue Deployment at Mach 3.5 in the Model 3 Atmosphere) 85

ILLUSTRATIONS (Cont'd)

Figure 38 Altitude at Main Parachute Deployment versus A_D/A_V (Drogue Deployment at Mach 2.75 in the Model 3 Atmosphere) 86

39 Hyperflo and Ring-Sail Drag Coefficients versus Mach Number 88

40 Entry Weight Less Droge Parachute Weight versus M/C_DA 89

41 Drogue Diameter/Vehicle Diameter versus M/C_DA 90

42 Drogue Diameter versus M/C_DA 91

43 Altitude at Main Parachute Deployment versus A_D/A_V (Drogue Deployment at Mach 3.5 in the Model 2 Atmosphere) 92

44 Altitude at Main Parachute Deployment versus A_D/A_V (Drogue Deployment at Mach 2.75 in the Model 2 Atmosphere) 93

45 Entry Weight Less Drogue Weight versus M/C_DA 94

46 Drogue Diameter/Vehicle Diameter versus M/C_DA 95

47 Time from Peak Acceleration to Mach 1.3 versus Peak-g 99

48 Sensing System Schematic 100

49 Parachute/Capsule Dynamic Geometry and Nomenclature 103

50 Dynamic Response of Mars Lander Main Parachute Subjected to Wind Gusts of 50 ft/sec for 10 seconds 104

51 Dynamic Response of Mars Lander Capsule Subjected to Wind Gusts of 50 ft/sec for 10 seconds 105

52 Relative Horizontal Velocity of Capsule with Respect to Mars Surface During Wind Gusts of 50 ft/sec for 10 seconds 106

ILLUSTRATIONS (Cont'd)

Figure 53 Single Parachute System-Impact Velocity versus Main Parachute Area/Suspended Weight 111

54 Nominal Parachute Diameter versus Suspended Weight 112

55 Opening Shock Load versus Dynamic Pressure 113

56 Parachute Descent Time versus Full-Open Altitude in the VM-3 Atmosphere 114

57 Parachute Descent Time versus Full-Open Altitude in the VM-4 Atmosphere 115

58 Parachute Descent Time versus Full-Open Altitude in the VM-7 Atmosphere 116

59 Parachute Descent Time versus Full-Open Altitude in the VM-8 Atmosphere 117

60 Peak Acceleration versus Time from G_{max} to Mach 1.2 (V_e = 12000 ft/sec) 119

61 Peak Acceleration versus Time from G_{max} to Mach 1.2 (V_e = 13000 ft/sec) 120

62 Peak Acceleration versus Time from G_{max} to Mach 1.2 (V_e = 14000 ft/sec) 121

63 Peak Acceleration versus Time for G_{max} to Mach 1.2 (V_e = 15000 ft/sec) 122

64 Sumary Initiation Data -- Peak Acceleration versus Time for G_{max} to Mach 1.2 123

65 Deployment Schematic 125

66 Mach Number Initiation Backup -- Peak Acceleration versus Time from G_{max} to Mach 0.85 (nominally) 126

67 Parachute Dynamics Pictorial 133

68 Parachute Dynamics -- Angle Definitions 134

ILLUSTRATIONS (Cont'd)

Figure 69 Parachute Swing Angle versus Time (effect of gust magnitude) 135

70 Capsule Swing Angle versus Time (effect of gust magnitude) 136

71 Capsule Swing Rate versus Time (effect of gust magnitude) .. 137

72 Parachute Swing Angle versus Time (effect of A/W ratio) .. 138

73 Capsule Swing Angle versus Time (effect of A/W ratio) 139

74 Capsule Swing Rate versus Time (effect of A/W ratio) 140

75 Parachute Attachment Concepts 142

76 Parachute Descent Time versus Full-Open Altitude in the VM-8 Atmosphere 144

77 Parachute Descent Time versus Full-Open Altitude ($A/W = 5.0\ ft^2/lb$) 146

78 Main Parachute Assembly (ring-sail) 152

79 Parachute Canister Installation 155

80 Properties of Crushable Material 161

81 Anisotrophy of Crushable Materials 162

82 High Strain Rate Tester (showing temperature chamber in position) 164

83 Ultrahigh Strain Rate Loading Device 166

84 Fiberglass Phenolic Honeycomb 1/8-inch cell-- Polyurethane Foam Filled 167

85 Film Sequence of Impact in Ultrahigh Strain Rate Loading Device 168

86 Schematic of Ultrahigh Strain Rate Loading Device 170

ILLUSTRATIONS (Cont'd)

Figure 87 Static Load Deflection Curve--Fiberglass Phenolic 171

88 Fiberglass Phenolic Honeycomb--3/8 inch Cell 172

89 Impact Test on Resin-Dipped Polyurethane Foamed--3/8-inch Cell Honeycomb 173

90 Nylon Phenolic Honeycomb--3/16-inch Cell 174

91 Effect of Density and Angle of Impact on Dynamic Response of Polyurethane Foam-Filled Honeycomb 176

92 Lander Geometrics 177

93 Curve Fit to Anisotropic Material Properties 179

94 Total Weight versus Radius-Isotropic Sphere Lander 180

95 Total Weight versus Semi-Minor Axis-Isotropic Prolate Spheroid Lander 181

96 Total Weight versus Semi-Minor Axis Isotropic Oblate Spheroid Lander 182

97 Total Weight versus Radius-Anisotropic Sphere Lander..... 183

98 Total Weight versus Radius--30-Degree Lenticular Lander.... 184

99 Total Weight versus Radius--45-Degree Lenticular Lander.... 185

100 Total Weight versus Radius--60-Degree Lenticular Lander.... 186

101 Payload Weight Fraction versus Impact Velocity--Anisotropic Sphere Lander 188

102 Lander Geometrics Fit Into Entry Vehicles 189

103 Balsa Wood--Crushing Stress versus Density Literature Search 191

104 Balsa Wood--Crushing Stress versus Density--Test..... 192

105 Balsa Wood--Anisotropy--Test 193

ILLUSTRATIONS (Concl'd)

Figure 106 Impact Tests on Balsa Wood 194

107 Anisotropic Cosine Functions 195

108 Payload Weight Fraction versus n--Balsa Wood 196

109 Peak Deceleration versus n--Balsa Wood 197

110 Five-Sphere Toroidal Air-Bag Design 200

111 Spherical Air-Bag Design 201

112 Air-Bag Parameters 203

113 Lander Hitting Hemispherical Hump 207

114 Oblate Spheroid Lander on Slope 209

115 Lander Angle versus a/b Ratio 210

116 Sterilization Canister Gas Temperature--Pressure Variation 216

117 Cycle Length Effect on Sterilization Canister Pressure Differential 218

118 Saturn V Launch/Altitude History 220

119 Saturn V Launch Ambient Pressure History 221

A-1 Prolate Spheroid Geometry A-3

B-1 Cycle Length Effect on Sterilization Canister Pressure Differential B-5

TABLES

Table	I	Parachute Configuration Evaluation Matrix for Main Parachute Canopies	34
	II	Parachute/Spacecraft Advanced Mission Evaluation Matrix	35
	III	Reefed Main Parachute Actuation Performance	98
	IV	Summary of Model Atmosphere Parameters for Mars (Models VM-3, -4, -7 and -8)	109
	V	Trajectory Results and Deployment Conditions in the VM-3 Atmosphere	127
	VI	Trajectory Results and Deployment Conditions in the VM-4 Atmosphere	128
	VII	Trajectory Results and Deployment Conditions in the VM-7 Atmosphere	129
	VIII	Trajectory Results and Deployment Conditions in the VM-8 Atmosphere	130
	IX	Backup Mode Deployment Summary	131
	X	Main Parachute Descent Time Summary -- Primary and Backup Modes	147

ACKNOWLEDGMENT

The conduct of the study and technical preparation of this report involved the participation and close coordination of many people, all of whose contributions were important to the end results.

It is impractical to single out each individual, but the major contributors to the study, reflected in the material presented in this Book, are as follows:

Responsible Manager

T. R. Ellis

Major Contributors

Name	Section
Coderre, W.	Appendix B
Cloutier, G. J.	3, Appendix A
DiCarlo, P.C.	2
Herrick, R. N.	1, 4
(Northrop Corporation, Ventura Division)	2

Approved by

Signature	Title
Max. D. Russell	Chief, Systems Design
T. R. Ellis	Manager, Systems Engineering

INTRODUCTION

Included in this book are the mechanical subsystem analysis and resulting designs that are incorporated in the flight capsule designs for the entry from approach trajectory and entry from orbit studies. The mechanical subsystems discussed herein are: 1) separation subsystem, 2) parachute subsystem, 3) impact attenuation subsystem, and 4) sterilization canister pressurization subsystem. Each of the subsystem analyses are discussed in terms of both studies when applicable, with summary results of the design concept for each study.

Impact attenuation is utilized for the landed capsule, hence, the analyses and discussion presented only apply to the entry from approach trajectory study where a landed capsule was employed. The entry from orbit study did not use a landed capsule because of weight restrictions and revised-study ground rules.

The sterilization-canister pressurization subsystem analysis is only presented for the entry from orbit since both studies employed similar subsystems and environments. However, the resulting design approach is applicable to both studies.

Flight-capsule terminology, system and subsystem characteristics, and environmental conditions for each study are presented in Volume II, Book 1, and Volume III, Books 1 and 2 of the final report. When applicable, these data are employed in the analyses and discussion of the respective subsystems presented herein.

1.0 SEPARATION SUBSYSTEMS

1.1 SUMMARY

This section defines the requirement for the separation subsystems,the conditions under which it operates,the constraints that restrict the design,the general methods for attaining the actuation,and the selected subsystems for the reference design. The selected subsystems are divided into entry from an approach trajectory and an entry from orbit designs.

In both design concepts the separation subsystems are similar except for particular aspects inherent to each concept. Common to both design concepts: 1) sterilization canister-lid separation, 2) entry-vehicle separation from the flight spacecraft, 3) parachute deployment (only difference being in the reefed chute utilized in the entry from approach trajectory) and 4) entry shell jettison. In most of the separation subsystems for these two concepts the functional sequence (i.e., time and place) are similar but the operational aspects (i.e., type of separation mechanism) are completely different. The change in mechanisms is the result of further understanding of the design and the easing of weight restrictions. This allowed the use of more reliable mechanisms and the addition of more redundant actuation methods.

In addition to the four separation subsystems stated above, the entry from approach trajectory mode includes five more. Prior to entry, the expended ΔV rocket motor, along with the ACS electronics, are jettisoned to reduce the entry weight. Additional separation subsystems are associated with survivable landing: 1) landed capsule separation on a tether line, 2) release of the tether at impact, 3) jettisoning of the impact attenuation, and 4) deployment of the instrumentation for surface operations. An alternate landed-capsule design utilizing a flotation sphere was also considered. In this design, an added separation subsystem is used to uncage the payload sphere to allow vertical erection.

Since the weight of the entry from orbit design was not critical it was possible to minimize the number of separation functions; some separations are necessary to reduce entry weight (i.e., the expended ΔV rocket motor, in the entry during approach mode). Two other separation subsystem were included in the entry from orbit design in addition to the four stated earlier. These included the nose cap separation and the instrumentation (penetrometer) deployment. The nose cap separation is a back-up system for a failure mode, which permits television pictures to be taken prior to impact in case the entry shell fails to separate.

The subsystems (of standard design) are used in many previous applications and only modified to account for particular characteristics of the flight capsule design and the mission environments.

1.2 REQUIRED CONDITIONS AND CONSTRAINTS

1.2.1 Launch Vehicle

The launch vehicle employed for the entry from approach trajectory design is the Saturn 1B/Centaur. The Saturn V launch vehicle was used for the entry from orbit design. Neither of these vehicles impose particular conditions or constraints on the flight-capsule separation-mechanism design except for the environmental conditions defined in the following section. However, due to the overall size constraints imposed on the flight capsule by these vehicles, the separation mechanisms can be indirectly affected.

1.2.2 Environmental

The flight capsule must withstand many environments from manufacturing to final impact. These are listed in Volume II, Book 2 for the entry from approach trajectory and in Volume III, Book 2 for the entry from orbit trajectory; however, the methods of handling and protecting the flight capsule from recontamination reduces the critical environments to the shock and vibration loads of ground handling and launch, the high sterilization temperature, high vacuum conditions of outer space, and cold soak during planetary transfer. The launch-vehicle vibrational conditions are unknown at this time but could be critical at lift off and during the ascent sonic-velocity regime.

Since the sterilization canister is to be vented during the launch phase to keep the internal pressure from exceeding 1.0 $lb/in.^2$ over ambient, and totally vented during the Earth parking orbit, the high vacuum of outer space will be experienced during the entire cruise phase. Cold soak during the cruise phase will reach a minimum temperature at the outer rim of the canister of about -100°F.

1.2.3 Functional

Separation systems can be categorized as either functional separations or discard separations and can effectively be used to reduce the complexity and power requirement of a flight system. Functional separations, such as the ejection of a parachute, contribute to the proper operation of a component, while discard separations, such as the ejection of the expended rocket motor, are performed to reduce the maneuverable weight of the remaining system, or to provide clearance for subsequent operations of the system. A detailed description of the operation of the flight-capsule separation systems for entry from the approach trajectory and for entry

from orbit designs are given in paragraphs 1.4 and 1.5, respectively. The functional requirements, conditions, and constraints are similar for all separation subsystems and are discussed in the following paragraphs.

1.2.3.1 Debris

The separation must be accomplished cleanly without allowing the discard of debris that might degrade the performance of the planetary-vehicle, flight-spacecraft, and flight-capsule missions. This debris includes parts or particles that could impact with other equipment and cause physical damage or, by deposition, cause the operation of the equipment to be degraded. Specifically, all major parts shall be attached to the equipment being discarded, if possible, and in a manner that will eliminate interference with the separating systems. Explosive residue shall be contained unless purely gaseous products are given off.

1.2.3.2 Interference

It is essential that all subsystems separate without causing interference with other assemblies. The interferences are of three types: 1) hangups, where adjacent assemblies interlock and fail to separate, 2) bump, where the assemblies impact and may or may not continue to separate, and 3) slide, where adjacent surfaces slide along each other and slow the separation velocity with possible degradation of the mission.

The design concepts must minimize tip off rates and the protrusions of one system into another to reduce these interferences. Adjacent parts that might slide against each other during an unusual perturbation in the separation sequence should be designed to slide without danger of small protrusions locking together. Tip off of the spring-ejected systems can be minimized by selecting matched springs. In the case of entry-vehicle separation, selection of springs with compression load matched within 1.0 percent will limit the maximum possible tip-off rates caused by spring mismatch to approximately 0.3 deg/sec.

1.2.3.3 Power Requirement

The selected subsystem should utilize as little power as possible for actuation to eliminate requirements for additional batteries or flight-spacecraft power.

1.2.3.4 Redundancy

It is imperative that the probability of actuation remain high, thus redundant initiating components should be used wherever possible.

1.2.4 Sterilization

The total mission probability of contaminating Mars with a viable microorganism from Earth is required to be less than 10^{-4}. This requirement establishes the need for a biological barrier around the entry vehicle and imposes an additional environmental condition for the flight capsule. The biological barrier must prevent recontamination of the entry vehicle after terminal sterilization. In order to accomplish these requirements, the flight capsule must be completely encapsulated in a metal canister. This effectively adds another separation subsystem since removal of a portion of the canister will be required to facilitate egress of the entry vehicle.

The environmental condition imposed by terminal sterilization is a dry heat cycle of 125°C for 24 hours for flight qualification (JPL Specification VOL-50503-ETS). In addition to the terminal sterilization, each component must be qualified to an ethylene oxide bath and three dry-heat cycles at 135°C.

1.3 GENERAL METHODS

1.3.1 Actuation Methods

All of the actuation systems in the reference designs utilize explosives. Explosive actuation methods have been selected because of low power requirements to ignite the explosive and the high power available from the explosive to actuate subsystems. This low power requirement for ignition means that the actuation will not be a large drain on the flight-capsule batteries or flight-spacecraft power supply. The high power available from the explosive assures that minor binding of the actuation mechanisms can be overcome by the force available.

The actuation system debris is retained by applying the explosive force in a chamber against a piston that in turn releases the mating mechanism by shearing pins, or equivalent retainers, and forces the mechanism to separate by means of the piston stroke. The piston then bottoms and seals the chamber to retain the remaining gasses. The ejected portion of the mechanism is retained on its respective assembly. In the case of the V-type clamp-rings, the clamp-rings are attached to one of the major assemblies by springs to assure pulling the ring clear of the separation joint, thus preventing interference with the separation and later operations of the entry vehicle or flight spacecraft.

Redundancy is achieved by using two igniter circuits, either one of which can initiate the explosive cartridges or detonators; redundancy is also provided by using where possible, two or more actuators, any one of which will release the entire separation subsystems. All explosive cartridges, detonators, and detonating fuses used in the separation mechanism

are required to conform to the environmental, sterilization, and safety condition specifications of Volume II, Book 2 and Volume III, Book 2 (entry from approach and orbit, respectively).

1.3.2 Retaining Methods

In the flight-capsule design for the entry from the approach trajectory mode, multi-point tie down separation subsystems were used because of weight considerations. In the entry from orbit mode, weight was less critical permitting the substitution of V-type clamp rings for the multi-point subsystems. Due to the large size of the flight-capsule structure and its light weight, the load distribution characteristics of the V-type clamp rings provide more secure, vibration-resistant connections between the assemblies. Also, because of the size and weight of the structure, cables holding multi-point clamps were not selected because of stress concentrations at the clamps. Multi-point tie down is still used on the nose cap (see paragraph 1.5.5) to accommodate high velocity ejection requirements and design limitations. The canister lid is retained by the continuity of the canister shell and the separation system is attached to the shell. This is required to eliminate all possible leaks through the canister. Straps are used to retain the landed capsule for the entry from approach trajectory design and the penetrometers on the entry from orbit design to simplify the separation release mechanism.

1.3.3 Impulse Methods

There are two types of components used to provide separation impulse. These are explosive charges and springs. Explosive charges are used where the force and/or stroke requirements exceed spring capabilities. Explosive impulse is also used where it is required for unlocking and the excess energy is available and convenient to use for the separation force (such as the sterilization canister lid).

Springs are used to increase the reliability of achieving minimum tip off rates. The spring forces can be matched prior to installation to provide matched-force outputs during the separation process.

Some of the subsystems utilize inertia and gravity forces for the separation impulse. The entry shell, landed capsule, and penetrometers are released during descent on the parachute. The entry shell utilizes both inertia and the gravity forces acting in opposition to the parachute drag to accomplish the separation. The landed capsule and the penetrometers use the gravity forces for separation. A spring has been added to the penetrometer separation subsystem and entry shell but only to assure that the ejection is positive and frictional forces or other minor surface binding forces do not abort the separation.

1.4 SELECTED SUBSYSTEMS--ENTRY FROM THE APPROACH TRAJECTORY DESIGN

There are ten primary separation subsystems in the entry-from-approach trajectory design. The operational flight sequence for this design is presented in Figure 1. In the following subsections, each of the separation mechanisms is discussed in detail.

1.4.1 Sterilization Canister-Lid Deployment

This discard separation event is necessary to allow subsequent separation of the entry vehicle from the flight spacecraft.

Since the sterilization canister is effectively a continuous shell of 0.030 aluminum, the separation system must cut the lid free and develop an impulse to drive the lid away at 1.5 ft/sec. For clearance purposes, the maximum tip off rate allowable is 7 deg/sec. A 5-grain/ft, flexible linear-shaped charge (FLSC) retained in a plastic ring will be used to sever the sterilization canister lid. The FLSC will be made up of four continuous lengths with butt joints since available FLSC lengths are limited to 12 feet. The FLSC will be ignited at two points for redundancy by electric detonators. A method of attachment is shown in detail A of Figure 2. The plastic ring is clamped against the canister skin by an extruded angle that is bolted to a ring which is welded to the canister.

Previous testing has shown that the FLSC can provide the necessary impulse by careful design of the separation subsystem. Special attention must be given to the stiffness of the structure in the immediate vicinity of the FLSC and the shell deformation after cutting to allow residual gas pressure to aid in the separation.

1.4.2 Entry-Vehicle Separation

This section describes the functional separation of the entry vehicle from the flight spacecraft prior to entry into Mars atmosphere. A backup separation joint outside the sterilization canister between the flight capsule and the flight spacecraft is used to discard the entire flight-capsule system if this separation or the canister lid separation fails.

The entry vehicle separation system is required to release the entry vehicle with an impulse of 163.0 lb-sec to provide an ejection velocity of 3 ft/sec. This velocity will expedite flight-capsule displacement to ranges adequate for minimizing ΔV rocket plume impingement on the flight spacecraft. At this velocity, the maximum allowable tip-off rate (for clearance) is 20 deg/sec. The method of separation, as shown in Figure 2, detail C, consists of four pressure-actuated ball-lock release mechanisms mounted equally spaced around the circumference of the flight-spacecraft forward adapter. Each ball lock latches to sockets mounted

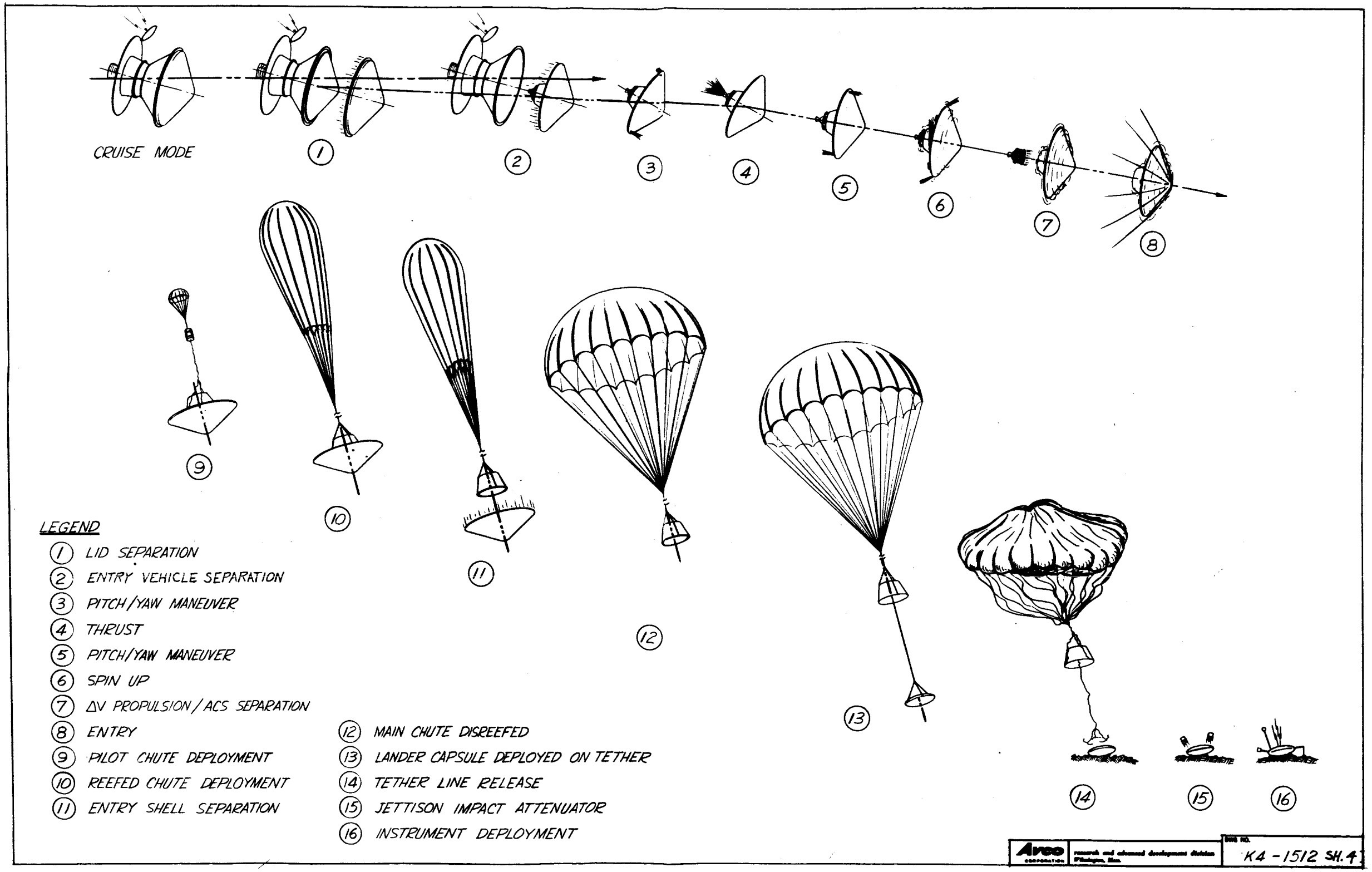

Figure 1 FLIGHT OPERATIONAL SEQUENCE

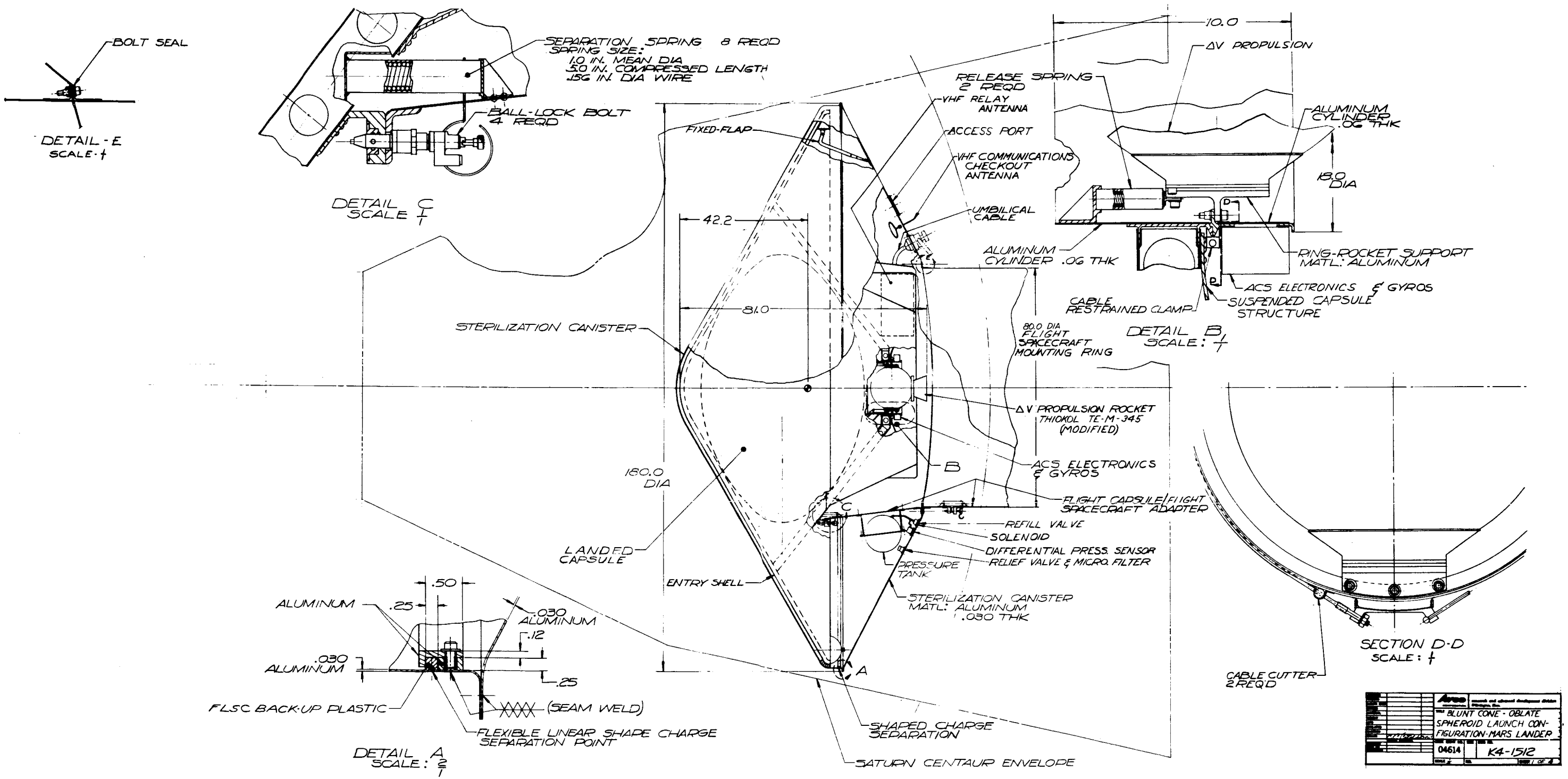

Figure 2 BLUNT CONE--OBLATE SPHEROID LAUNCH CONFIGURATION

8-1

on the suspended capsule structure mating ring. An explosive, dual-gas-generator manifold system is utilized to ensure that each ball lock is released at exactly the same time.

The separating force is provided by eight coil springs mounted in pairs, one on either side of each ball-lock release mechanism. Eight springs were used, although four would have been adequate for tip-off rate considerations, to reduce the size of each individual spring. The backup separation system is the same, except that it is mounted outside of the sterilization canister between the aft adapter and the intermediate adapter.

The electrical separation of the flight capsule from the flight spacecraft is provided by an explosive umbilical mounted at the mechanical separation joint.

1.4.3 ΔV Propulsion and ACS Electronics Separation

Separation of the expended ΔV rocket motor and ACS electronics is a discard function to reduce the entry weight. The alignment through the separation joint is critical and must be held such that the rocket thrust vector is within 0.042 inch and 0.167 degree of the entry vehicle center of gravity. The separation joint therefore, must be close fitting with a possibility of high friction. The separating velocity of 1.0 ft/sec is provided by separation springs with a spring force sufficiently high to alleviate the effects of friction. The configuration of the separating parts is such that high tip off rates are acceptable.

The separation subsystem is shown in Figure 2. Four segments of tapered flanges typical of V-type clamp rings are located around the interface diameter of the ΔV rocket and the suspended-capsule structure. Each of these extends through an arc of 20 degrees and is clamped together by a V-clamp with sides that are tapered to match the flanges. These channels are held against the flanges by a stranded steel cable. The ends of the cable terminate in swaged-on threaded fittings at one of the clamp segments to allow proper tension adjustment of the cable. A stranded cable is used to allow flexibility so that when the cable is cut, it will not restrict the radial movement of the clamps.

Two explosively-actuated shearing cable cutters, mounted on the adapter, cut the cable at two points for redundancy. The clamp segments are forced out by the tapered flange surfaces. Four coil springs provide the required separation impulse.

Electrical separation is provided by severing the interface cables with an electrically ignited cable cutter mounted inside the suspended-capsule structure.

1.4.4 Parachute Deployment

Parachute deployment is the functional separation which includes pilot-chute ejection, main parachute-container lid removal, and main parachute deployment.

The parachute container will be internally pressurized during the space flight, and therefore a pressure retaining lid must be ejected. This is accomplished by the pilot-chute deployment. An ejection velocity of 100 ft/sec is required to deploy the pilot parachute into the aerodynamic flow field. A mortar (gas generator) is used for pilot-chute ejection. As a failure mode requirement, this ejection system must be capable of functioning after the effects of a partial rearward entry and wake heating. The main chute is first deployed in an 18 percent reefed condition which is later disreefed prior to entry shell deployment. Details of the pilot parachute, main parachute, and associated hardware are discussed in Section 2.0.

1.4.5 Entry-Shell Separation

The entry shell is separated at the beginning of parachute descent to expose the engineering instrumentation and also to reduce the suspended weight on the parachute.

This separation subsystem has no impulse mechanisms and only unlatches the entry shell. The separating force is provided by inertia and gravity forces.

The subsystem uses four pressure-actuated, ball-lock release mechanisms mounted equally spaced around the forward circumference of the external payload support structure as shown in Figure 3. The mating sockets are mounted on a circumferential ring that is part of the entry-shell structure. An explosive, dual-gas-generator manifold system is mounted on the inside of the suspended-capsule structure. Ball-lock release mechanisms were chosen over a modified Marman clamp arrangement because the large tensile loading at the separation joint due to parachute deceleration will significantly increase the Marman clamp size and weight.

A cable cutter is used to sever the electrical cables to the entry shell.

1.4.6 Landed-Capsule Release

The landed capsule is lowered from the suspended capsule on a tether prior to impact to reduce the impact weight and to enhance adequate clearance between the landed capsule and the parachute and suspended-capsule structure after impact.

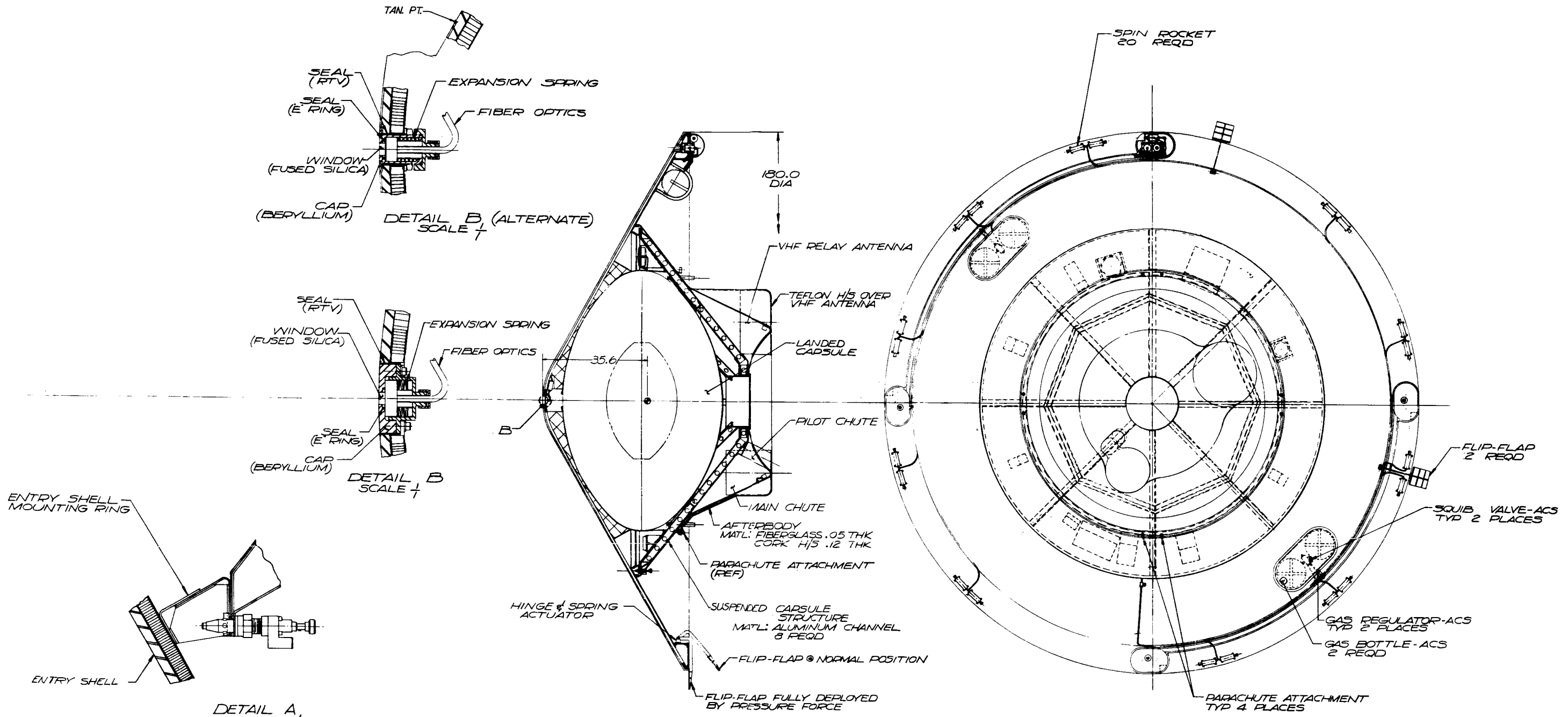

Figure 3 BLUNT CONE--OBLATE SPHEROID ENTRY CONFIGURATION

Until the separation of the entry shell, the landed capsule is supported by the foam bearing pad on the entry shell. However, when the entry shell is dropped, the load of the landed capsule is transferred to sling-type straps attached to the suspended-capsule structure. On the under side of the landed capsule the straps are restrained by a flexible steel cable. The cable is cut by an explosively-actuated cable cutter (similar to a Holex Model 2800), releasing the straps and dropping the landed capsule on the 20-foot tether.

The electrical umbilical is cut by an explosively-actuated cable cutter (similar to a Gould Laboratories (GLCC-250-1), mounted in the cavity formed by the landed-capsule and suspended-capsule structure.

1.4.7 Tether Release

Tether release at impact is required to allow the suspended-capsule structure to be carried clear of the landed capsule by the parachute.

The tether is attached to the landed capsule by a two-legged bridle. The bridle legs attach to the landed-capsule structure through an explosive bolt-release mechanism, which when initiated at the instant of impact, drives the bridle ends up through the clearance holes in the impact attenuator, freeing the landed capsule from the tether.

1.4.8 Impact Attenuator Jettison

The impact-attenuator discard separation facilitates the deployment of the scientific instruments.

The impact-attenuator ejection system must function after entry deceleratio of 200 g, entry heating conditions, and the impact deceleration of 500 g. The attenuator material must be ejected to a minimum of 5 feet from the landed capsule to prevent interference with the instrument deployment. The two landed-capsule shapes which were considered have the following unique requirements:

1. Oblate Spheroid (reference design)-- The 17-inch thick attenuator material, consisting of four segments of 1-inch thick balsa wood and triple layers of honeycomb and polyurethane foam must be cut and ejected. As shown in Figure 4 a cylinder of fabric explosive is imbedded in the impact attenuator to explosively cut the clearance holes for the instrument deployment.

2. Flotation Sphere (alternate design)--A similar attenuator (14 inches thick) must be cut and ejected. The attenuator must be completely ejected. The method, as illustrated in Figure 5 uses a flexible linear-shaped charge mounted against the flotation sphere to cut a hemi-

Until the separation of the entry shell, the landed capsule is supported by :he foam bearing pad on the entry shell. However, when the entry shell is dropped, the load of the landed capsule is transferred to sling-type straps attached to the suspended-capsule structure. On the under side of the .anded capsule the straps are restrained by a flexible steel cable. The :able is cut by an explosively-actuated cable cutter (similar to a Holex Model 2800), releasing the straps and dropping the landed capsule on the 20-foot tether.

The electrical umbilical is cut by an explosively-actuated cable cutter similar to a Gould Laboratories (GLCC-250-1), mounted in the cavity ormed by the landed-capsule and suspended-capsule structure.

.4.7 Tether Release

Tether release at impact is required to allow the suspended-capsule tructure to be carried clear of the landed capsule by the parachute.

The tether is attached to the landed capsule by a two-legged bridle. The ridle legs attach to the landed-capsule structure through an explosive olt-release mechanism, which when initiated at the instant of impact, rives the bridle ends up through the clearance holes in the impact ttenuator, freeing the landed capsule from the tether.

.4.8 Impact Attenuator Jettison

The impact-attenuator discard separation facilitates the deployment of the cientific instruments.

The impact-attenuator ejection system must function after entry deceleratio f 200 g, entry heating conditions, and the impact deceleration of 500 g. he attenuator material must be ejected to a minimum of 5 feet from the anded capsule to prevent interference with the instrument deployment. he two landed-capsule shapes which were considered have the following nique requirements:

1. Oblate Spheroid (reference design)-- The 17-inch thick attenuator material, consisting of four segments of 1-inch thick balsa wood and triple layers of honeycomb and polyurethane foam must be cut and ejected. As shown in Figure 4 a cylinder of fabric explosive is imbedded in the impact attenuator to explosively cut the clearance holes for the instrument deployment.

2. Flotation Sphere (alternate design)--A similar attenuator (14 inches thick) must be cut and ejected. The attenuator must be completely ejected. The method, as illustrated in Figure 5 uses a flexible linear-shaped charge mounted against the flotation sphere to cut a hemi-

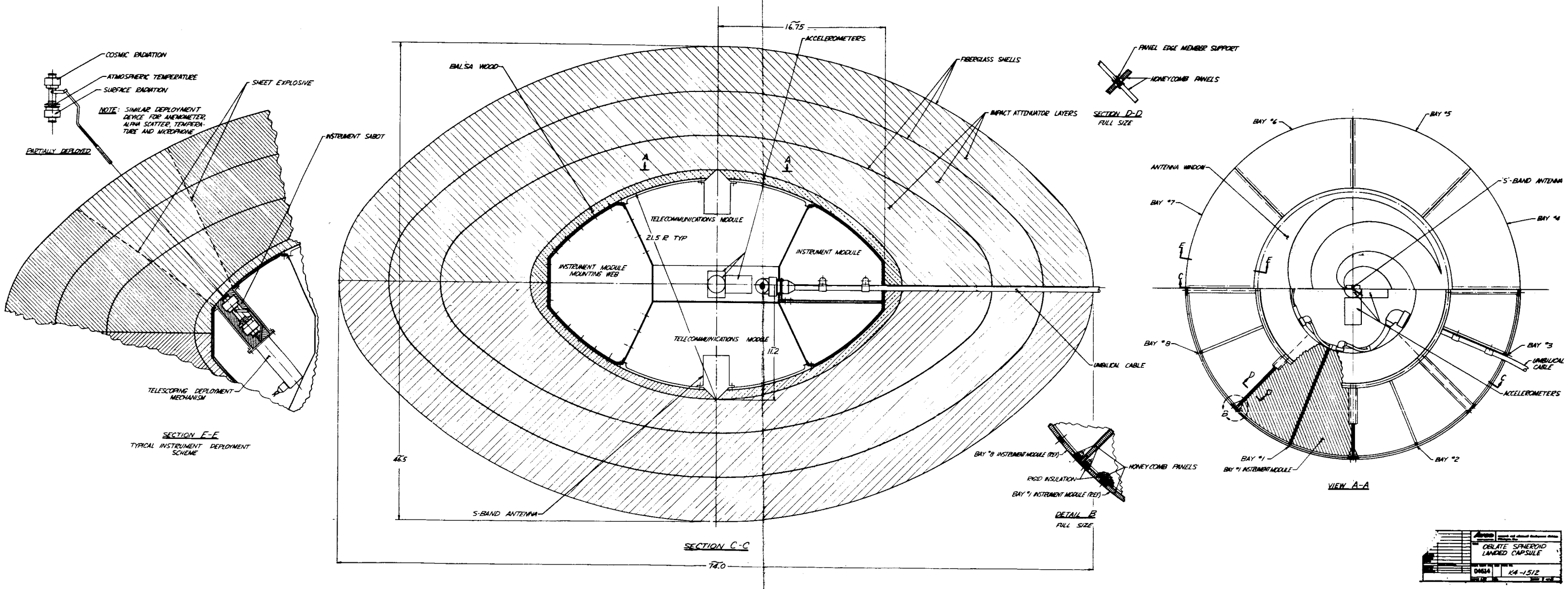

Figure 4 OBLATE SPHEROID LANDED CAPSULE

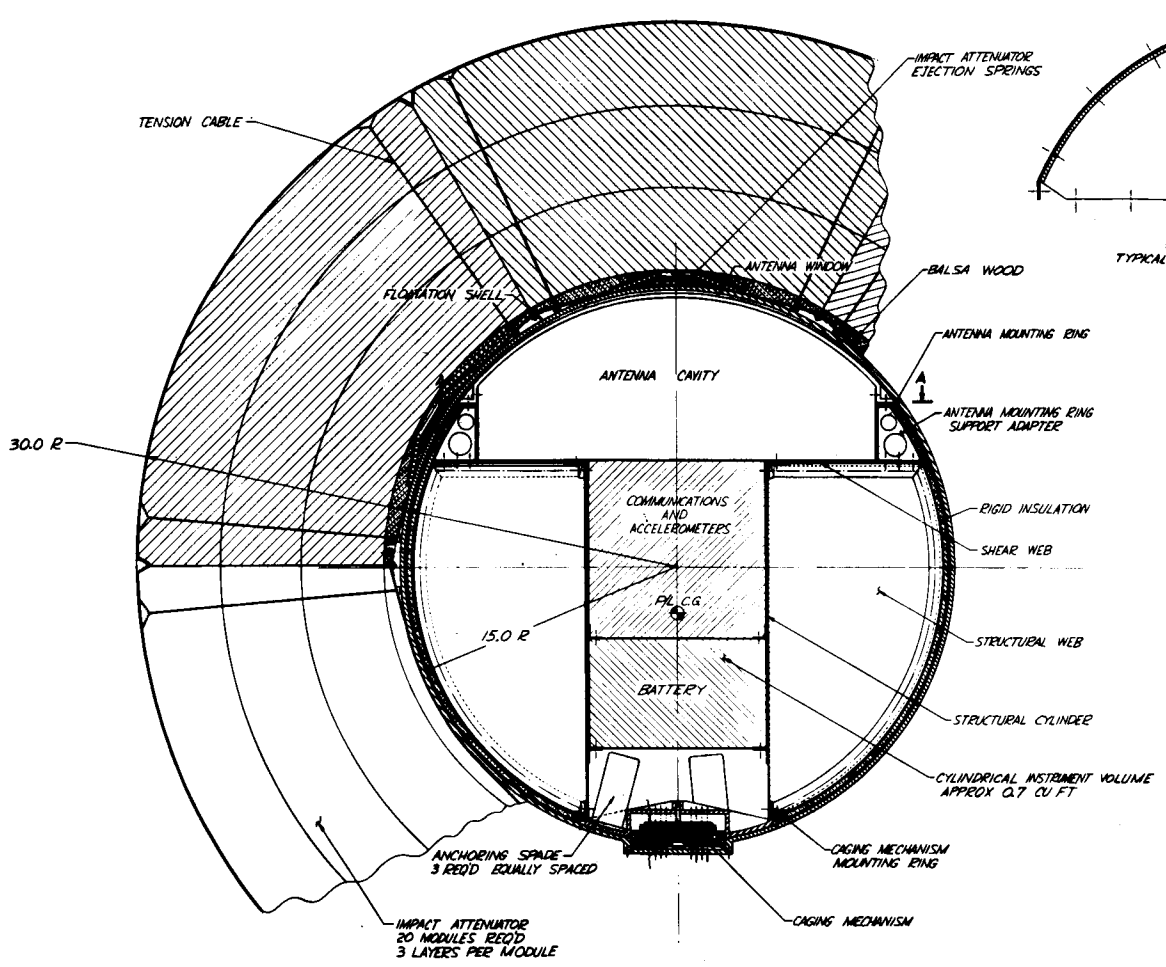

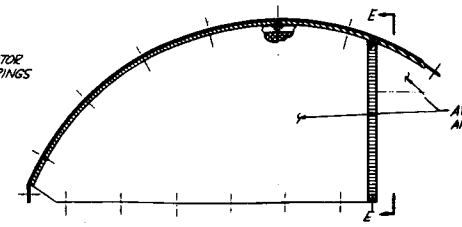

SECTION D-D
TYPICAL INSTRUMENT MODULE STRUCTURE

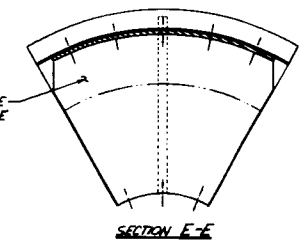

SECTION E-E

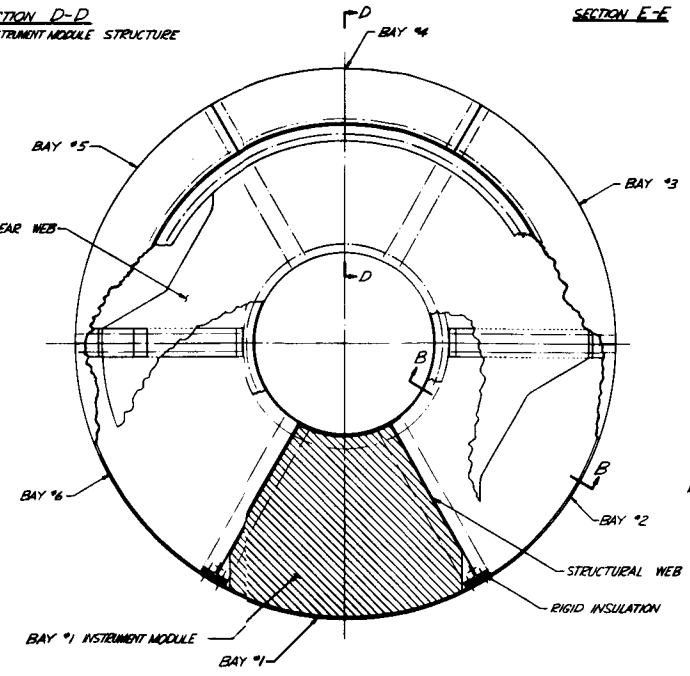

VIEW A-A
PLAN VIEW WITH ANTENNA REMOVED

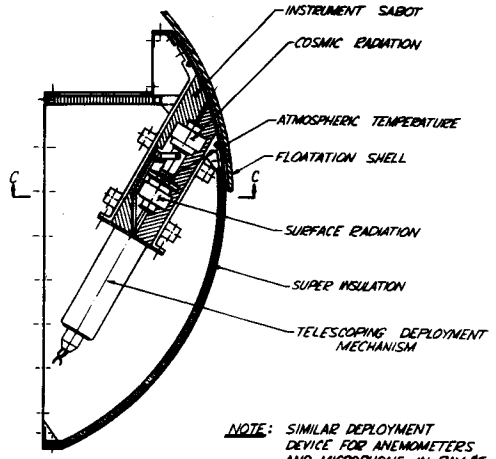

SECTION B-B
PACKAGED

NOTE: SIMILAR DEPLOYMENT DEVICE FOR ANEMOMETERS AND MICROPHONE IN BAY #5

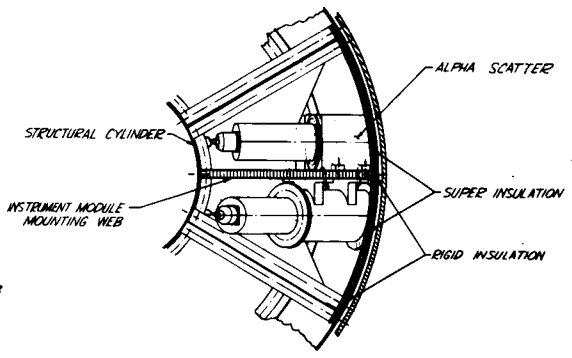

SECTION C-C

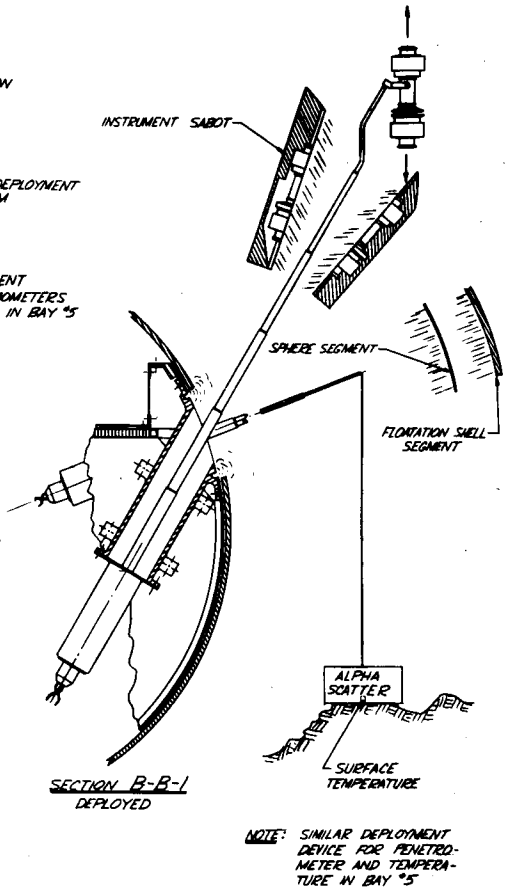

SECTION B-B-1
DEPLOYED

NOTE: SIMILAR DEPLOYMENT DEVICE FOR PENETROMETER AND TEMPERATURE IN BAY #5

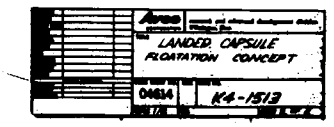

Figure 5 FLOTATION SPHERE LANDED CAPSULE

14-1

spherical shell to which the preformed attenuator segments are bonded. A conical coil spring is recessed into the hemispherical shell under each segment of the attenuator to increase the separation velocity.

1.4.9 Payload Erection (Flotation Sphere Only)

An additional separation function is necessary for the spherical lander to uncage the internal payload sphere from the flotation sphere. The payload caging mechanism must function after the 500 g impact. Two rotary caterpillar motors (sealed bellows-gas generator operated) actuate the caging mechanism. When the bellows are expanded by the gas the extension provides rotation to unlatch the caging mechanism.

The payload sphere is balanced with a slightly lower center of gravity then the center of buoyancy. Since the layer between the two spheres (flotation sphere and payload sphere) is filled with a flotation fluid, the payload sphere will seek the vertical.

1.4.10 Instrument Deployment

This is a functional deployment, which provides instrument access for atmosphere and surface sampling after impact. Hence, the deployment subsystems must function after experiencing the 500 g impact.

The deployable instruments are mounted on the ends of pressure-actuated telescoping booms which are mounted in the landed-capsule structure. Two explosive gas generators feeding into a manifold and piping system provide the deployment pressure. Precut holes are provided in the oblate spheroid landed capsule skin for the deployment of the instruments. It is necessary, however, to cut holes in the flotation sphere of the spherical landed capsule. This is accomplished by flexible linear-shaped charges, initiated simultaneously with the deployment gas generator to provide ports for instrument deployment.

1.5 SELECTED SUBSYSTEMS--ENTRY FROM ORBIT DESIGN

There are six primary separation subsystems in this design. These are illustrated in Figures 6 and 7 for the deorbit sequence and terminal descent sequence, respectively. The first four separation subsystems (canister lid, entry vehicle, parachute, and entry shell) are similar to the subsystems in the entry from approach trajectory design. The remaining two (nose-cap jettison and penetrometer release) are unique to the entry from orbit design. Each of the separation subsystems are discussed in terms of the pertinent characteristics in the following sections.

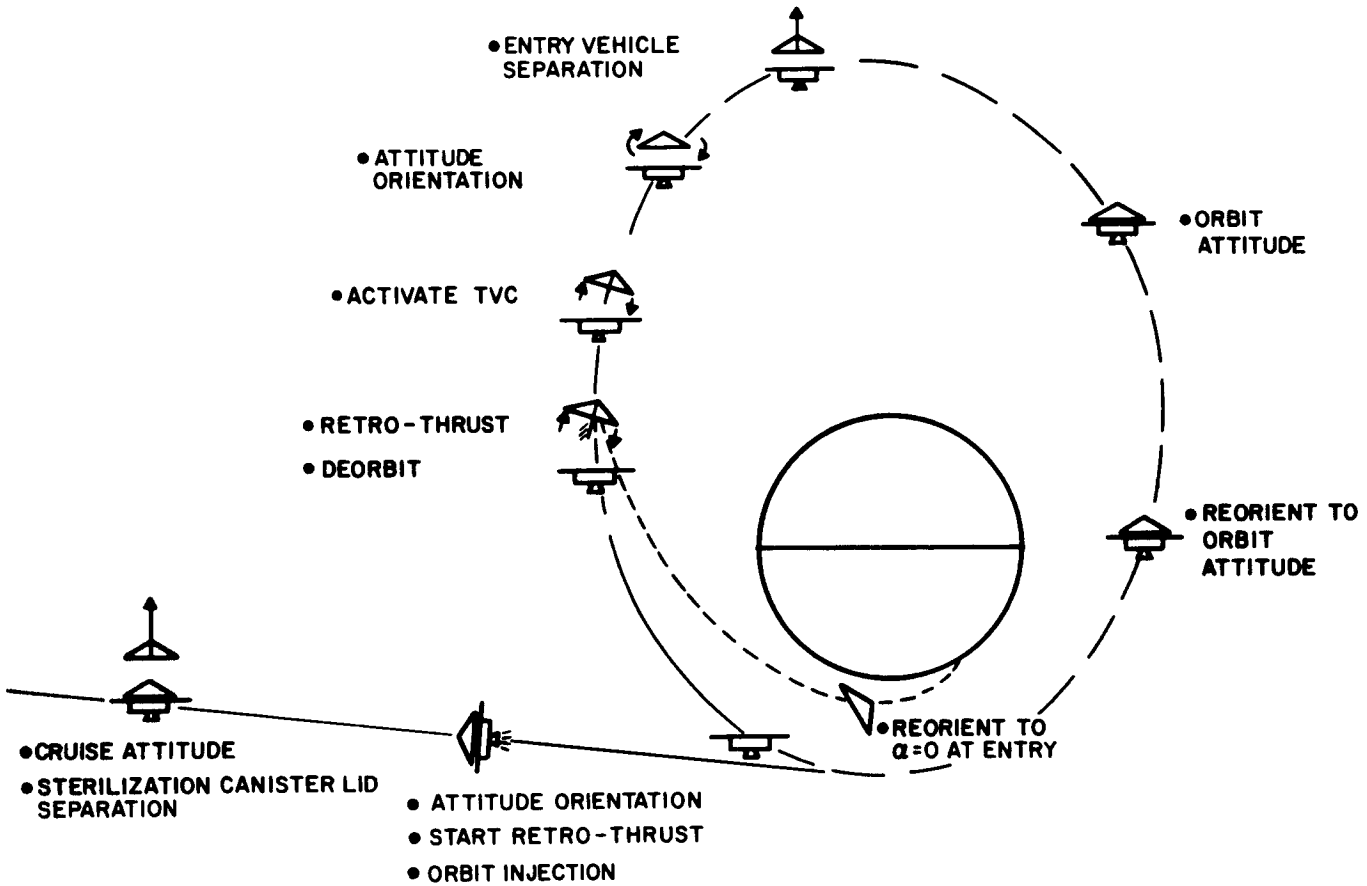

25-0997

Figure 6 DE-ORBIT SEQUENCE

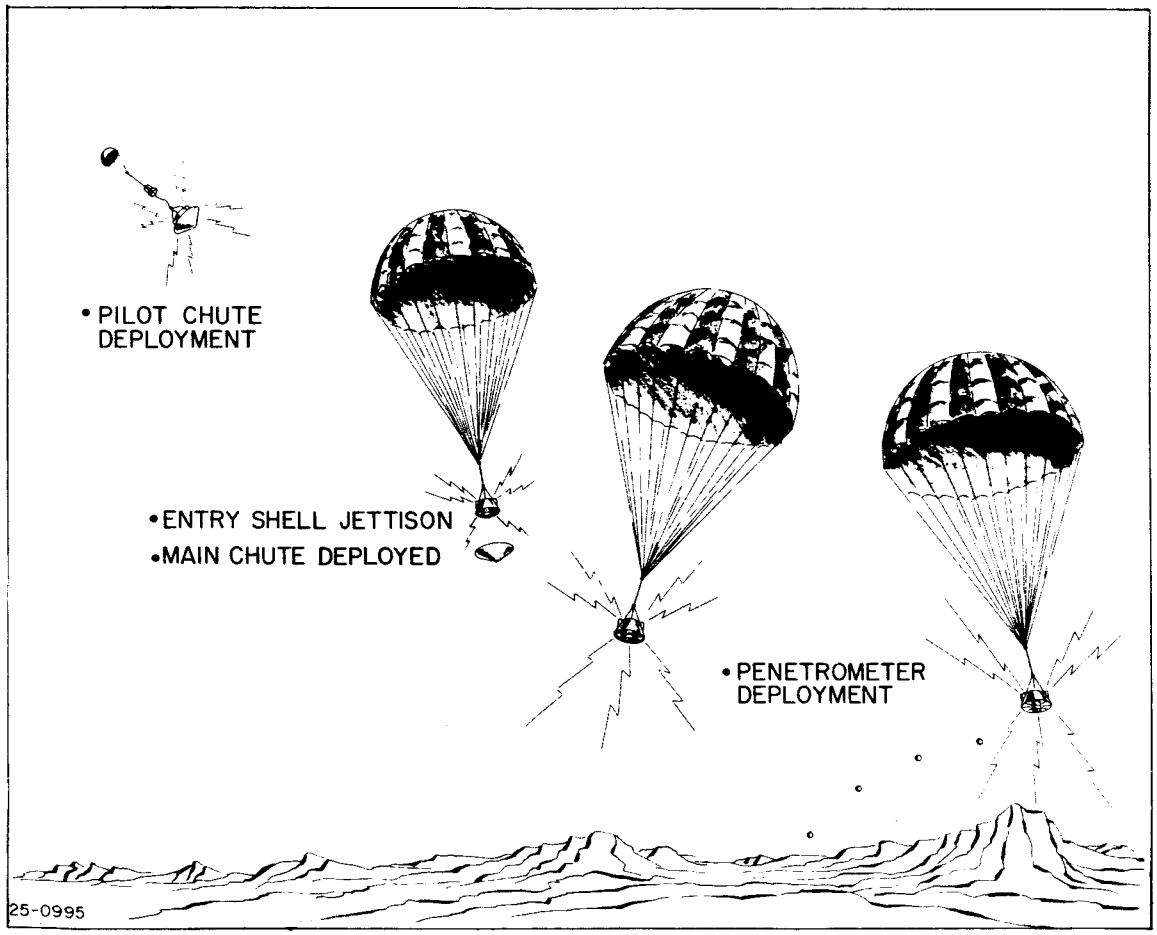

Figure 7 TERMINAL DESCENT SEQUENCE

Detail sketches of each separation subsystem, which were extracted from the flight-capsule design inboard-profile layout presented in Volume III, Book 1, paragraph 3.5, are illustrated. Design integration of the complete flight-capsule system is also discussed in Volume III, Book 1, Section 3.0.

1.5.1 Sterilization Canister-Lid Deployment

The requirements of the sterilization canister-lid deployment are to separate cleanly with a minimum velocity of 1.5 ft/sec and to maintain the sterile condition of the entry vehicle. To accomplish this, the reference design, as shown in Figure 8 uses an elastomer-encased mild detonating fuse (MDF) and a shear ring on the canister shell. Ignition of the MDF generates gas pressure in the elastomer tube which expands and shears the canister shell at the shear ring. After shearing the shell, the remaining expansion of the tube is used to impart a velocity to the canister lid.

A nominal velocity of 1.5 ft/sec is required for the canister lid to provide adequate clearance between the lid and planetary vehicle. Since the lid weighs 120 pounds, the minimum impulse required is 5.59 lb-sec. The requirement for redundancy is satisfied in the ignition and detonating components. The MDF is one piece which encircles the canister at the lid-base junction and has the free ends butted together. For ignition of the MDF, two detonators are located 180 degrees apart. Each detonator has a dual igniter circuit and the ignition of the MDF in either direction by either detonator will separate the canister lid.

Possible recontamination of the sterile entry vehicle at the canister-lid separation is prevented by the elastomer tube which retains the explosive residue and isolates the canister shell from the entry vehicle during the canister shearing action and as the lid moves away from the base. Detail development tests are required to establish the design characteristics and to ensure the shearing action.

Tests have been performed on the alternate design using flexible linear shaped charge (FLSC) to separate the canister lid. It has been shown that an FLSC type separation joint can be designed to give the necessary impulse, however, these tests were simple element tests to check the type of gross contamination problems that are inherent in an FLSC separation subsystem. Figure 9a shows a separation joint using FLSC and including a plastic foam fragmentation absorber held by an aluminum shield. A similar unit was constructed without the shield to obtain information for comparing the gas flow in the two subsystems. Figure 9b shows the shielded subsystem after actuation and shows that most of the debris was captured by the foam. High speed pictures were taken of the two units during actuation and are shown in Figure 10a and 10b. Future tests should have blast plates located to determine if the gas escaping from the shield contains particles that would prove deleterious to the planetary vehicle. The gas plume cannot be contained except by the encased MDF concept used in the reference design.

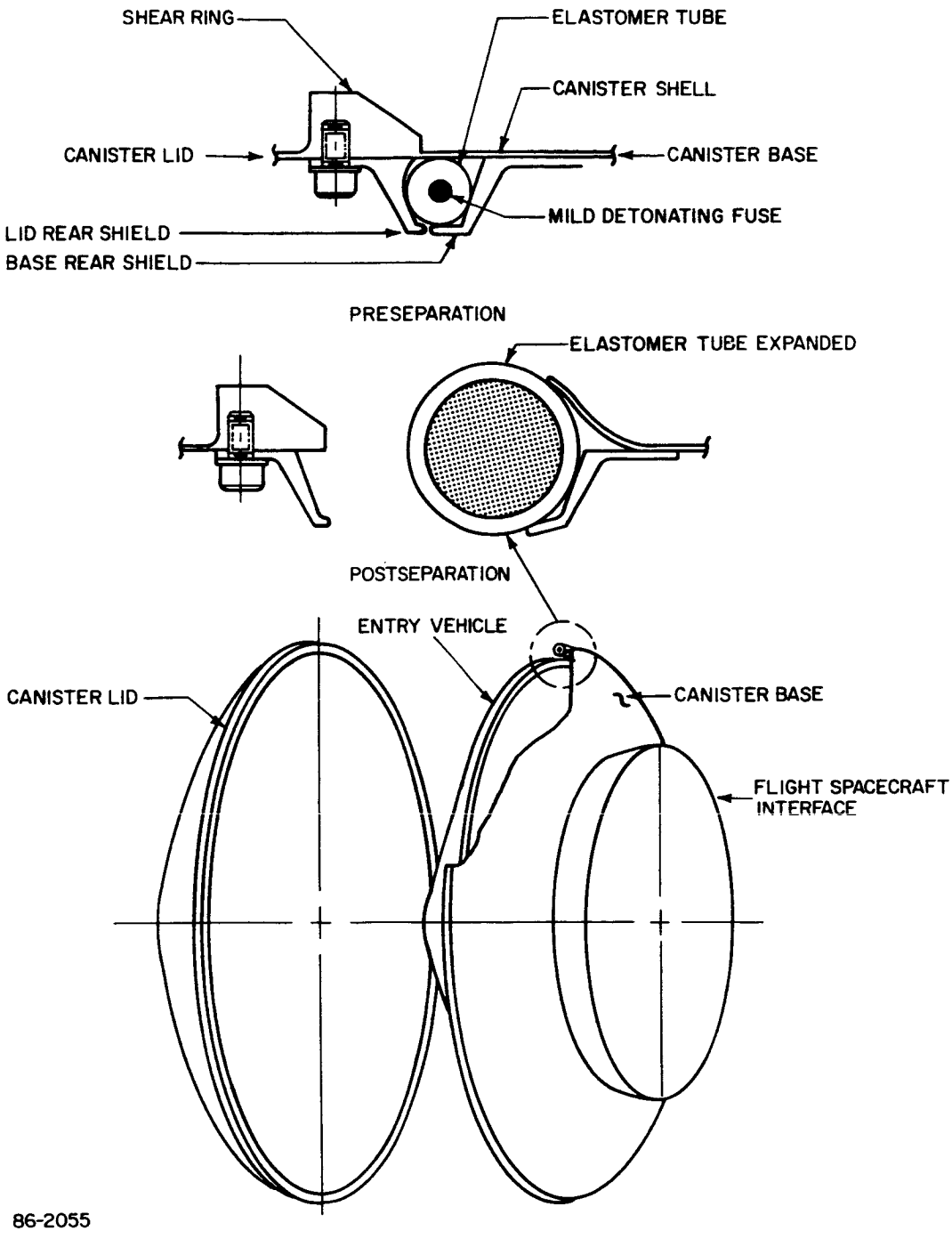

Figure 8 STERILIZATION CANISTER SEPARATION SUBSYSTEM

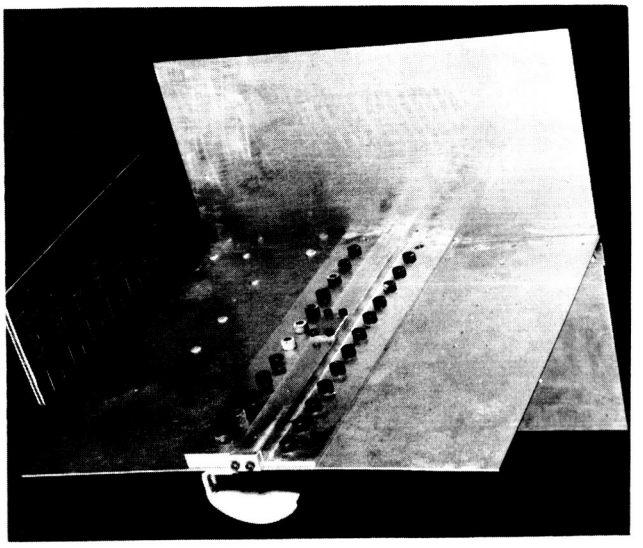

a. BEFORE ACTUATION

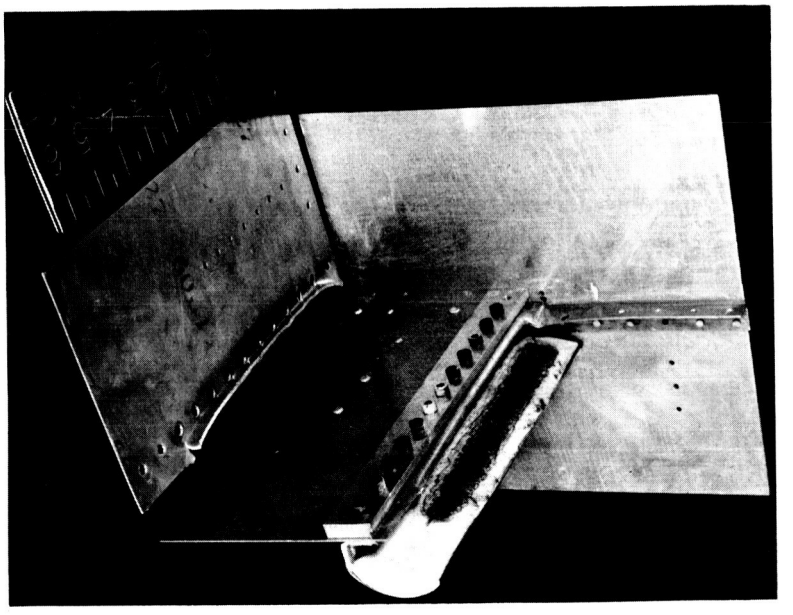

b. AFTER ACTUATION

Figure 9 FLSC-SEPARATION JOINT TEST APPARATUS

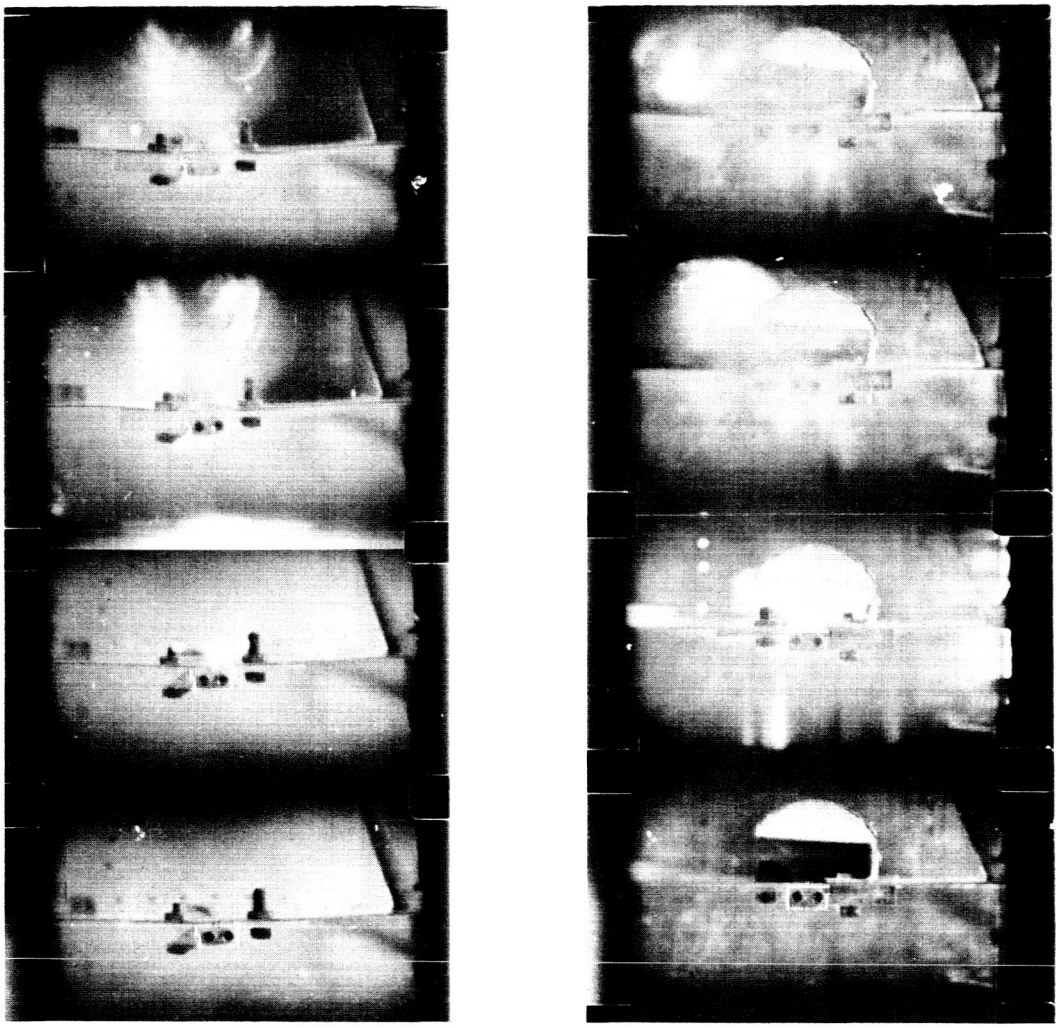

a. UNSHIELDED

b. SHIELDED

Figure 10 ACTUATION OF FLSC SEPARATION JOINT

1.5.2 Entry-Vehicle Separation

The entry vehicle/flight spacecraft separation subsystem is shown in Figure 11. The subsystem must provide a separation velocity of 1.5 ft/sec with tip off rates less than 9 deg/sec, assuming the spacecraft as a solid base, to avoid bumping during separation. Assuming the spacecraft has the same moment of inertia around the tip off axis as the entry vehicle and the flight spacecraft center of gravity at 104 inches from the interface, the relative rate must be reduced to approximately 3 deg/sec maximum.

This system consists of a V-clamp ring segment with four clamp separators. Commercial separators are available but allow the explosive residue to escape with the separating bolt (or stud). The residue can be retained with slight modification. Dual initiating circuits ignite dual gas generators for each separator to release the clamp-ring. The clamp-ring separates into four sections and is spring loaded to pull clear of the interface flanges. The springs retain all parts to the adapter section. Eight of ten springs provide the separating impulse while two springs are used to overcome electrical connector friction. The entry vehicle at separation (called the separated vehicle in weight breakdowns) weighs 2459 pounds and requires an impulse of 115 lb-sec to attain the 1.5 ft/sec velocity relative to the spacecraft.

Disconnection of the electrical umbilicals is accomplished mechanically as the two vehicles separate.

1.5.3 Parachute Deployment

The parachute deployment characteristics are essentially the same as that for the entry-from-approach design in that the cover of the main parachute canister is pulled off by the pilot parachute and in turn pulls out the main parachute pack. The parachute deployment sequence (Figure 12) consists of the pilot chute ejection, the canister cover ejection, the main parachute pack extraction, main parachute inflation and finally entry shell jettison. Detail discussion of the parachute subsystem is presented in Section 2.0.

1.5.4 Entry-Shell Separation

The entry shell is jettisoned to lighten the suspended capsule and uncover the television cameras so pictures can be taken of the planet surface during descent. The separation subsystem differs from that of the entry-from-approach design in that a V-clamp ring in used (which is identical to the entry-vehicle separation mechanism) for locking the entry shell to the suspended capsule. Separation force is supplied by the parachute drag on the suspended capsule opposing the inertial and gravity forces on the entry shell.

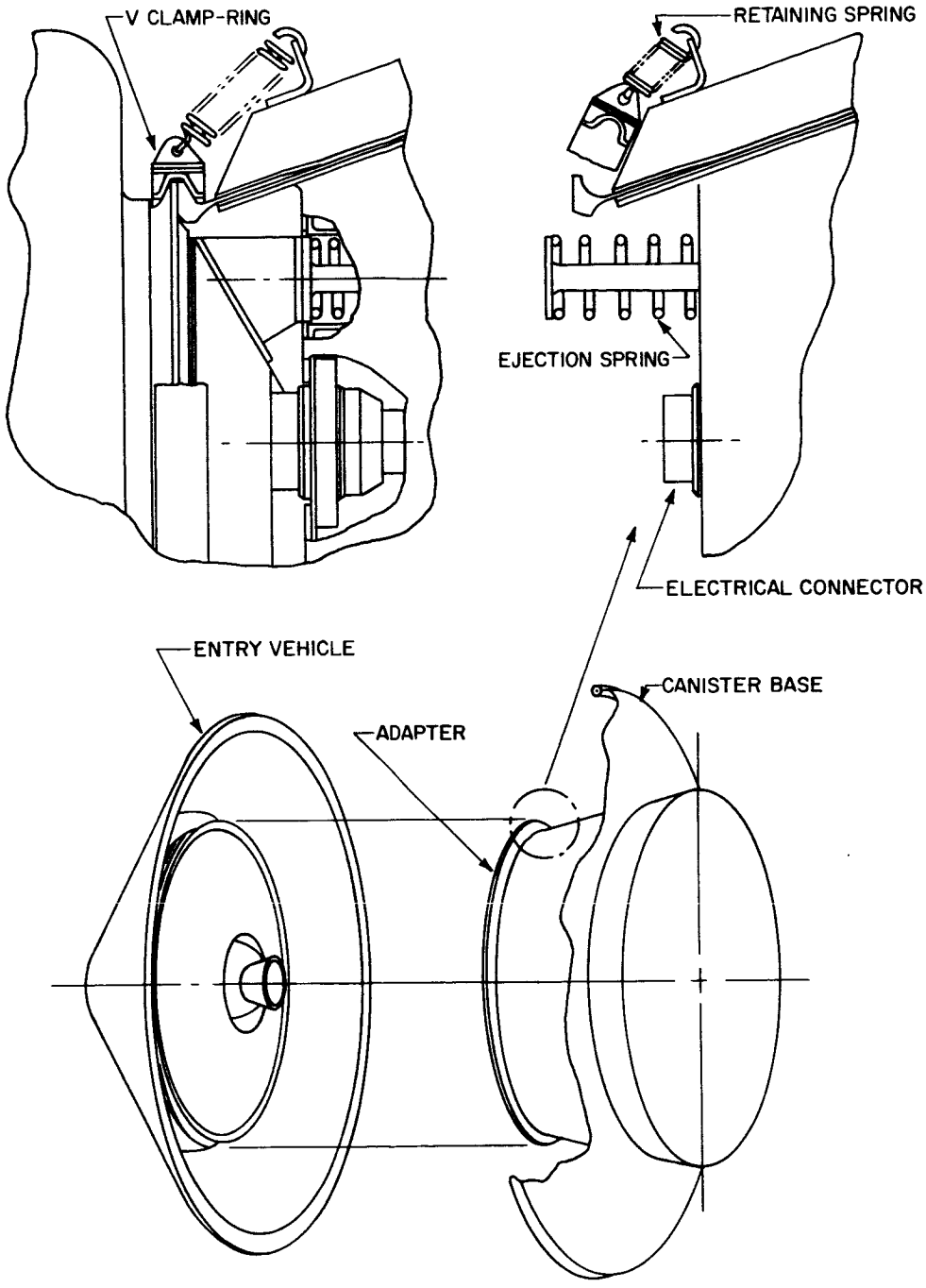

Figure 11 ENTRY VEHICLE SEPARATION SUBSYSTEM

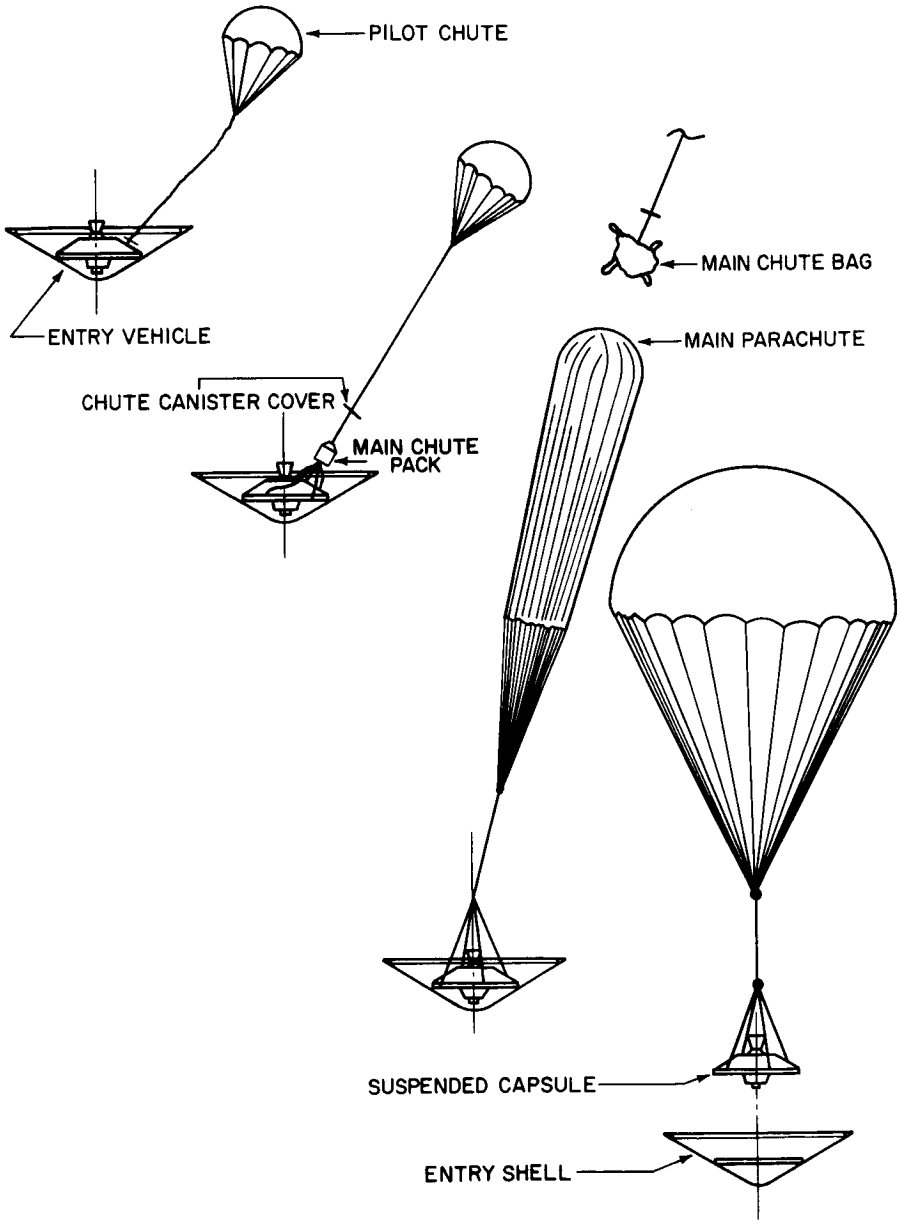

Figure 12 PARACHUTE DEPLOYMENT SEQUENCE

The initiation technique requires additional study to determine the best means of timing the release signal (see paragraph 1.6). The initiation signal could originate from a load cell on the parachute riser line or the accelerometers in the instrumentation package. The present design calls for initiation just after peak deceleration during parachute opening. Release of the entry shell is delayed until after the transient dynamics of parachute deployment have damped out to reduce the danger of bumping of the suspended capsule at release.

The V-clamp ring is released by a clamp separator identical to those of the entry-vehicle separation system of paragraph 1.5.2 (illustrated in Figure 11). Figure 13 shows the separation joint location and a view of the V-clamp ring in the locked and in the unlocked position. The springs shown, act both to pull the V-clamp ring clear of the separating flanges and to retain it with the entry shell.

1.5.5 Nose-Cap Separation

Nose-cap separation clears the field of view of the television cameras as a failure mode in case the entry shell fails to separate. Failure of the entry shell to jettison could result from two possible sources. If a failure occurs in the parachute deployment sequence, the entry shell will not separate since its deployment is initiated by the loads induced in the parachute riser line. In this case, no signal will reach the entry shell but the nose-cap separation will be initiated.

If the parachute subsystem operates normally, the entry shell separation signal will also be sent through a 2-second delay switch to the nose-cap separation mechanism. The nose-cap separation mechanism will receive the initiation current only if the entry shell fails to separate and the electrical umbilical is still attached to the suspended capsule.

The nose-cap separation system must meet two requirements. The first is to clear the field of view of the television cameras, particularly the high resolution camera which has the narrowest field of view. The nose cap is ejected at a minimum angle of 5 degrees from the entry vehicle roll axis. At this angle, the nose cap will be out of the television camera field of view, when it reaches about 42 feet ahead of the vehicle.

The second requirement is to clear the path of the entry vehicle and eliminate any chance of bumping (this case is pertinent only if parachute deployment fails). To properly design for this case, detailed aerodynamic studies are required (see paragraph 1.6). The M/C_DA of the nose-cap at zero angles of attack was made the same as that of the entry vehicle. The weight of the nose-cap then becomes 33.4 pounds. To obtain this weight, a 0.6-inch thick aluminum nose-cap structure was employed.

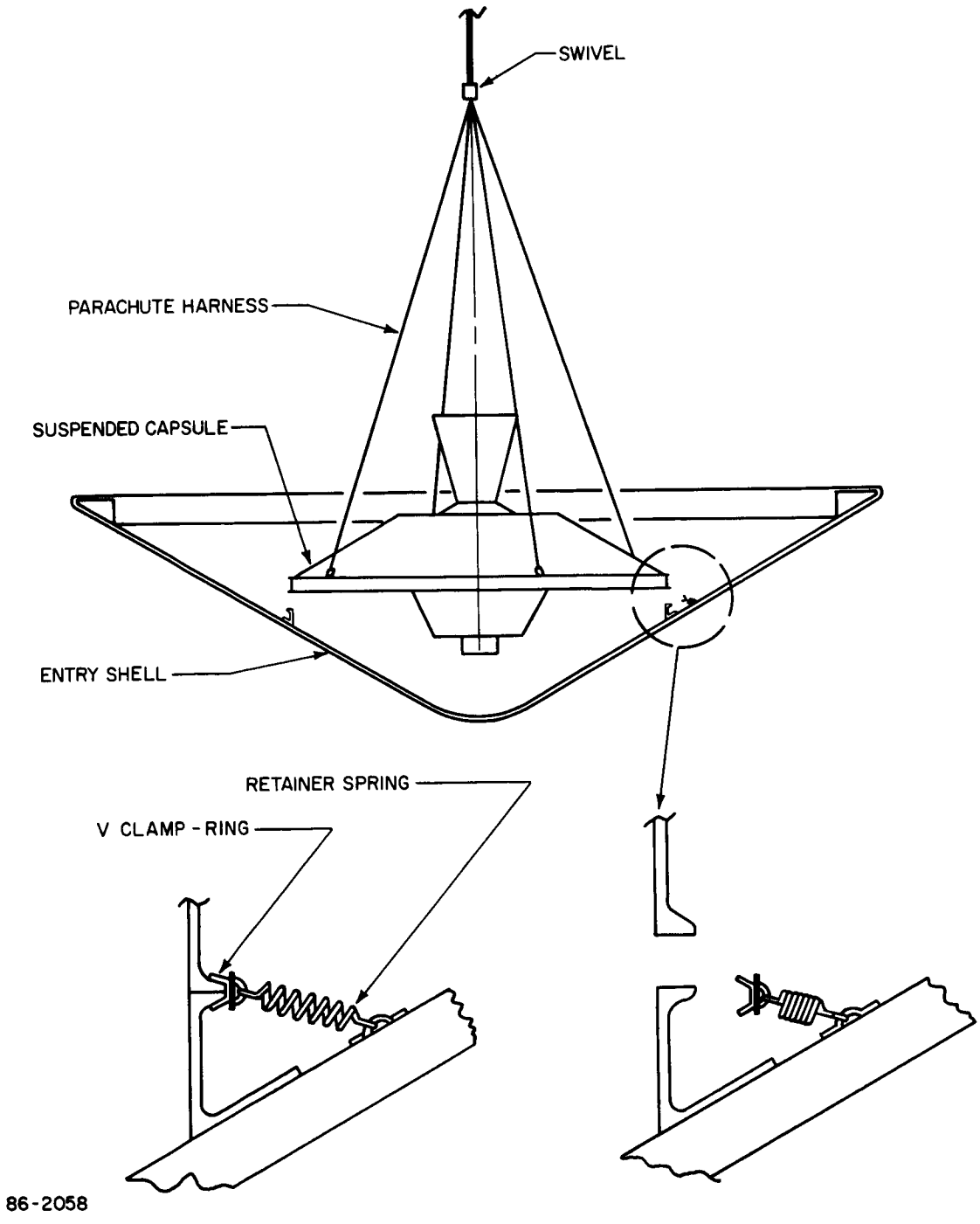

Figure 13 ENTRY SHELL SEPARATION SUBSYSTEM

An ejection velocity of 50 ft/sec was necessary to clear the television field of view in one second and appears to be sufficient for clearance of the entry vehicle (see paragraph 1.6). To achieve this ejection velocity, four explosive thruster bolts are used. Each bolt produces 900 pounds of thrust. All gaseous products are contained within the thruster-bolt housing. Details on the separation are shown in Figure 14.

1.5.6 Penetrometer Separation

The penetrometers must be released, prior to impact of the suspended capsule, to record bearing strength of the surface of the planet. The penetrometers are held by three straps joined at a center ring. One strap incorporates an adjustment mechanism and is fastened to the structure, while two are held by the explosively-actuated pin pullers. Figure 15 shows the penetrometer support and the action of the pin-puller release. Each penetrometer is released by a separate signal at 5 second intervals starting at 3500 feet. The signal utilizes dual igniter circuits to initiate explosive cartridges which in turn pull the pins to release the penetrometers (either one of the two pin pullers will release a penetrometer). To ensure clean separation, penetrometers are ejected by springs at a maximum velocity of 5 ft/sec.

1.6 PROBLEM AREAS

Several problem areas have been discussed in the preceding sections. Two of the more pertinent areas are the timing of the entry shell separation signal and the aerodynamic characteristics of the nose-cap separation. These are discussed in the following sections.

1.6.1 Entry-Shell Separation Signal Timing

Figure 16 shows the load history experienced by entry vehicle during the parachute deployment sequence. The initial reaction is the mortar ejection of the pilot parachute. The pilot parachute snatch load includes deployment of the main parachute canister cover. The next pulse is the main parachute snatch load, followed by the drag force as the main parachute inflates. Four ways to time the entry-shell release signal are indicated on the figure. The selected release technique must provide shell release at a time when the entry vehicle has stabilized after the inflation transients. The first technique actuates the release at a prescribed time after parachute deployment initiation. Selection of the time interval is fairly critical. Too short a time period might allow the signal to occur before peak opening loads. The entry vehicle dynamics at this time could be excessive, which, in turn might cause the entry shell to bump the suspended capsule. Too long a time period will allow the entry vehicle to maintain a high descent velocity to a lower altitude, and decrease the time for taking pictures.

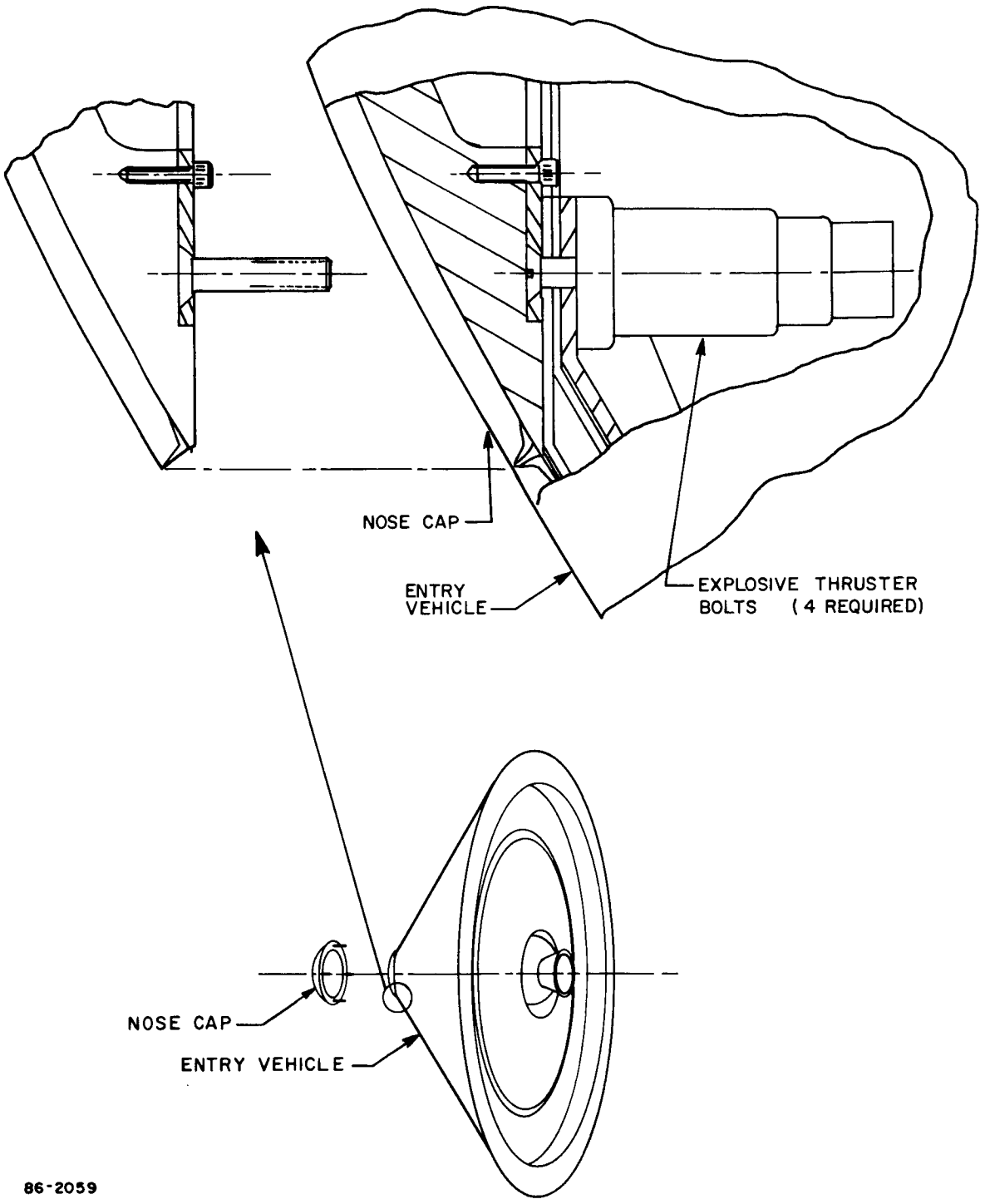

Figure 14 NOSE CAP SEPARATION SUBSYSTEM

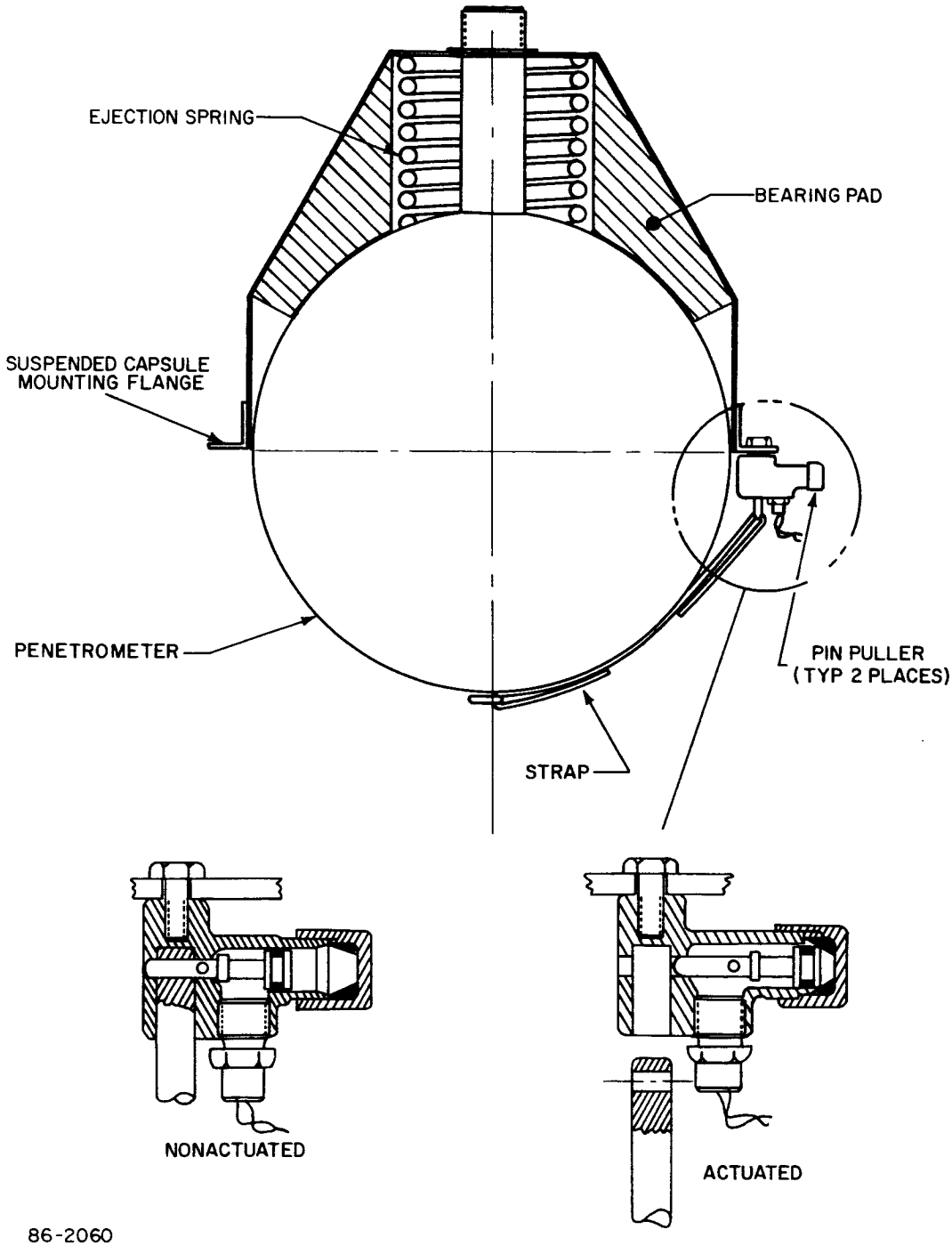

Figure 15 PENETROMETER SEPARATION SUBSYSTEM

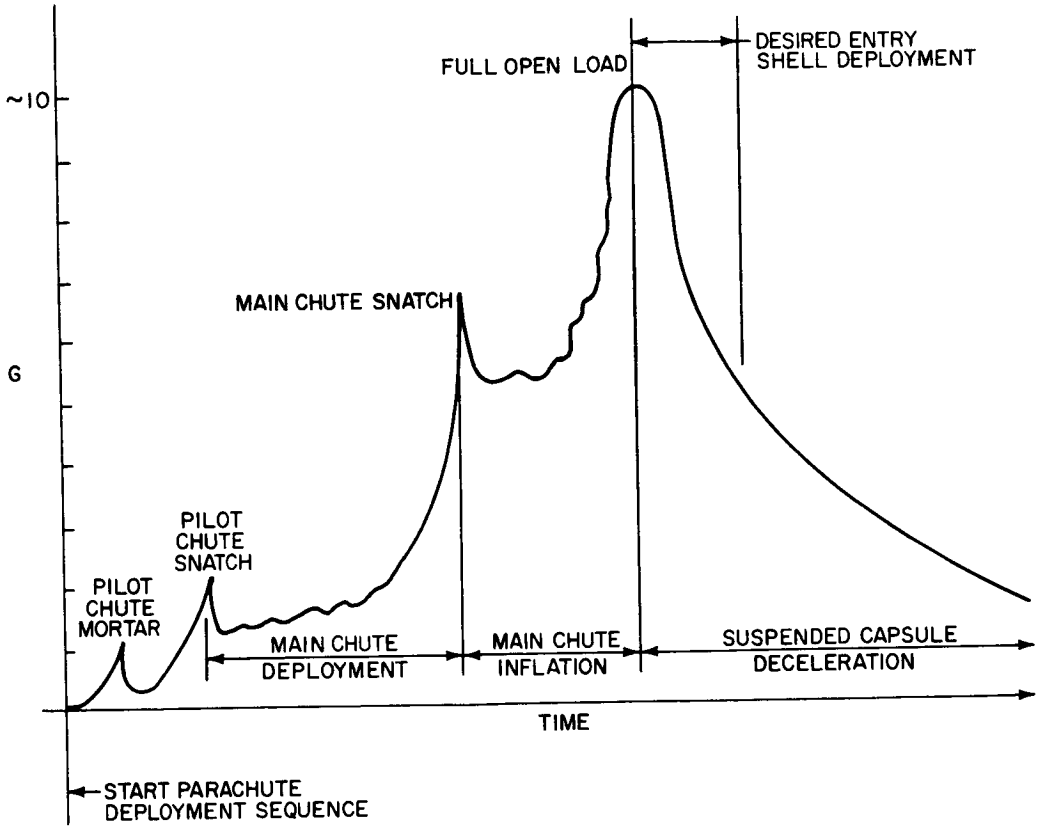

ENTRY SHELL INITIATION METHODS

- PARACHUTE DEPLOYMENT INITIATION
- FIXED PEAK G-SWITCH
- PROGRAMED ACCELEROMETER
- PROGRAMED LOAD CELL

86-2061

Figure 16 ENTRY SHELL SEPARATION LOGIC

The second method of initiation is to deploy the entry shell at a preselected g-loading. This technique presupposes that the peak loading is well known and that no other peak loading will approach this value. Even then, a short delay will be required if it is desired to initiate on the decreasing side of the parachute peak load.

The third and fourth methods require programming to deploy the entry shell at a prescribed time after peak load has been detected. As can be seen from Figure 16 the load peaks, prior to the open parachute drag load, are sharp peaks with steep slopes. The main parachute drag pulse is the obvious choice for programming. Two signal sources are considered for obtaining the peak opening load, the accelerometers in the instrumentation package or a load cell to read the parachute input loads directly. It was decided to use the load cell on the reference design because the accelerometers are located where parachute loading inputs cannot be isolated sufficiently to assure the correct input while the load cell will read only these inputs directly. The final selection of entry shell separation technique will require development flight tests in order to predict the initiation timing accurately.

1.6.2 Nose-Cap Separation Characteristics

The nose-cap separation requires more detail aerodynamic studies and tests to assure that the nose cap will clear the path of the entry vehicle. The cap is ejected while the entry vehicle is at supersonic velocity and the aerodynamic interaction between the objects may make the selected ejection velocity insufficient. The cap is designed to have the same M/C_DA as the entry vehicle but may require a flap to turn it on edge, thereby reducing its drag and allowing it to travel away from the entry vehicle flight path.

2.0 PARACHUTE SUBSYSTEM

2.1 GENERAL SUMMARY

The selection of a retardation and landing system for a vehicle entering the atmosphere of Mars should be based first on reliability, second on weight penalty, and then on performance and development risk in that order of importance. The reliability inherent in a particular system concept may be gauged by the number of sequential events that occur in completing the system's functions. For example, a passive system has good reliability because no active events are required. To achieve a passive retardation and landing on Mars, the entry vehicle would have to posses sufficient drag and stability during entry into the atmosphere to decelerate to a low enough terminal velocity at impact. A low impact is required so as not to exceed the shock resistance capability of the surviving experimental package. It is estimated that such a vehicle would require a ballistic coefficient on the order of 0.03 slug/ft^2, whereas high-drag configurations with a ballistic coefficient less than 0.15 slug/ft^2 are difficult to achieve with sufficient weight reserved for the payload after meeting the structural and thermal protection requirements. Therefore, a passive retardation and landing concept is not feasible.

The next best approach is a one-function system, one which employs a large lightweight drag device (parachute) to provide a low terminal descent velocity. The entry vehicle must have sufficient drag to assure satisfactory conditions at deployment. A parachute system normally involves canister cover removal before parachute deployment, hence, an additional function must occur before the drag device can function. Thus, two events are necessary and inherent reliability drops in value. Several methods of parachute deployment are possible: ejection by mortar and extraction by pilot parachute are considered the most favored approaches. The large size of the main parachute precludes ejection by mortar except as a failure mode. Removal of the canister cover can be accomplished by a pilot parachute, which subsequently extracts the main parachute.

Weight penalty may be reduced and/or experimental objectives may be enhanced by reaching deployment conditions at an early point in the vehicle entry trajectory. Augmenting the vehicle drag with a drogue parachute capable of being deployed at supersonic speed permits either a higher vehicle ballistic coefficient (lower specific drag) or main parachute deployment at a higher altitude above the surface of Mars. The drogue parachute can be deployed by mortar and perform the main parachute canister-cover removal and deployment functions in lieu of the pilot parachute. The advantages of a two-parachute system (drogue and main) are reflected in payload gain for a given launch weight constraint with a probable penalty in development and overall program cost. In a two-parachute

system, drogue operation becomes the third function (pilot and main parachute deployment being the others) that must occur in the successful retardation and landing sequence of a Mars experimental vehicle. The inherent reliability of the three-function system is lower than a two or one-function system.

The specific main parachute configurations investigated were the ribbon, ring-slot, ring-sail, extended skirt, and annular canopies. In selecting the candidate canopy type for a given recovery task, four basic selection factors are considered. These are: 1) performance characteristics, 2) reliability, 3) weight (volume) penalty, and 4) development. Selection of the optimum parachute configuration for a given application requires simultaneous evaluation of the preceding interrelated factors, coupled with an appraisal of parachute configuration on payload characteristics and payload subsystem requirements. Using the above mentioned considerations as tradeoff rationale, an investigation of candidate parachute configurations for the descent system was conducted. With the present available data, it was found that the ring-sail canopy satisfied the above requirement best, hence, it was utilized as the selected configuration (see Tables I and II).

The goal in the selection of parachute material is to maximize reliability and efficiency while minimizing weight. This requires a careful determination of the strength of each candidate material at its temperature and pressure environments during prelaunch, launch, interplanetary flight, entry, deployment, and descent. A number of organic textile materials are available for the construction of parachute systems. These include Nylon, Dacron, and Nomex. Three additional textile materials have been developed to a point where it is reasonable to anticipate their availability as parachute materials by 1967. These are duPont PRD-14 (a polyamide), Chemstrand X-101 (a polyamide) and PBI (polybenzimidazole).

In view of the favorable properties of the new organic fibers being developed, there apprears to be no need to seriously consider some of the more exotic textile materials (glass, quartz and metal) which are also being developed for parachute use. However, some other materials which are not usually employed in parachute design, such as thin reinforced polymer films (Mylar), may be worthy of evaluation. For a main parachute canopy, the zero porosity of a polymer film may be an advantage unless it adversely affects the stability characteristics of the particular parachute-canopy configuration. The reliability of available fabrication techniques must also be considered. In order to obtain reliability equivalent to that of a textile material, it would undoubtedly be necessary to overdesign parts which utilize the polymer film, hence inducing a consequent weight penalty. Finally, since there is little background of experience with films as parachute materials, development costs would be a definite disadvantage.

In conclusion, a parachute canopy and line material cannot be conclusively selected for a mission without further development tests of the candidate materials under the expected loading, heating (sterilization), vacuum and radiation conditions.

TABLE I

PARACHUTE CONFIGURATION EVALUATION MATRIX FOR MAIN PARACHUTE CANOPIES

Evaluation Factor	Descent Weighting Factor (1-10)	Parachute Configuration (Projected 1967 Data)									
		Ribbon		Ringslot		Ring Sail		Annular		Ext. Skirt	
		Factor	Score	Factor	Score	Factor	Score	Factor	Score	Factor	Score
I. Performance											
1.1 Opening Shock	8	10	80	9	72	8	64	8	64	8	64
1.2 Descent Stability	5	8	40	8	40	6	30	9	45	7	35
1.3 Mach Sens.	5	10	50	8	40	5	25	4	20	5	25
1.4 Drag	10	5	50	6	60	9	90	10	100	9	90
			220		212		209		229		214
II. Reliability											
2.1 Inflation	7	8	56	8	56	10	70	9	56	9	63
2.2 Damage Tol.	4	8	32	8	32	10	40	4	16	5	20
2.3 Fab. Tol.	2	8	16	8	16	8	16	6	12	7	14
2.4 Packing Tol.	3	8	24	9	27	9	27	7	21	9	27
			128		131		153		105		124
III. Weight Penalty											
3.1 Specific Drag	9	3	27	4	36	6	54	8	72	6	54
3.2 Inflation Penalty	6	9	54	9	54	8	48	7	42	8	48
3.3 Environment	1	8	8	8	8	7	7	7	7	7	7
			89		98		109		121		109
IV. Development Risk											
4.1 High Speed	3	10	30	8	24	6	18	1	3	7	21
4.2 Low Density	3	8	24	2	6	1	3	0	0	2	6
4.3 Low Canopy Load	3	1	3	1	3	1	3	1	3	2	6
4.4 Configuration	6	9	54	8	54	8	48	3	18	8	48
			111		87		72		24		81

TABLE II

PARACHUTE/SPACECRAFT ADVANCED MISSION EVALUATION MATRIX

PARACHUTE CONFIGURATION

Evaluation Factor	Mission Weighting Factor (1-10)	Ribbon		Ringslot		Ring Sail		Annular		Ext. Skirt	
		Merit Score	Mission Score	Merit Score	Mission Score	Merit Score	Mission Score	Merit Score	Mission Score	Merit Score	Mission Score
I. Performance	7	220	1540	212	1484	209	1463	229	1603	214	1498
II. Reliability	10	128	1280	131	1310	153	1530	112	1120	124	1240
III. Weight Penalty	10	89	890	98	980	109	1090	121	1210	109	1090
IV. Development Risk	2	111	222	87	174	72	144	24	48	81	162
TOTAL MISSION SCORE			3982		3948		4227		3981		3990
RELATIVE MISSION RATING			0.930		0.934		1.000		0.942		0.994

Nylon fabric would be a good main parachute canopy because it has good strength to weight properties under dynamic loading conditions. It is lightweight and there is a great deal of experience in its fabrication. The question of whether or not Nylon can withstand the high temperature, sterilization criterion must be determined by tests. A specially treated, heat resistant Nylon (type 330, for example) may survive this test and warrants further investigation at this time.

The material presented in this section has been contributed in part by Northrop Corporation, Ventura Division, particularly in the areas of parachute dynamics, materials selection, and parachute configuration.

2.2 PARACHUTE MATERIALS

A number of organic textile materials are available for the construction or parachute systems. These include Nylon, Dacron and Nomex. Three additional textile materials have been developed to a point where it is reasonable to anticipate their availability as parachute materials by 1967. These are duPont PRD-14 (a polyamide), Chemstrand X-101 (a polyamide) and PBI (polybenzimidazole).

Suitable textiles must posses the necessary strength, energy absorption ability, and porosity characteristics with the minimum possible weight. In addition, the textiles must be capable of withstanding sterilization environment and still maintain the required properties. At the time of deployment, a drogue parachute must be able to withstand a high temperature of short duration. The main parachute, on the other hand, will not be subjected to high deployment temperatures. Here, strength with minimum weight and low fabric porosity are important.

For most landing system applications the current textile of choice is high tenacity Nylon. The high strength to weight ratio, the availability of fine denier fabrics, and the variety of textile forms which can be produced, are all desirable characteristics which Nylon possesses. However, Nylon has definite limitations in respect to its maximum operating temperature and resistance to extended periods at elevated temperatures. Although not ordinarily specified for parachute systems heat resistant types of Nylon are available. These are much less susceptible to heat damage than the ordinary types of Nylon as shown by the data (from duPont) in the following table.

Dacron is preferable for some parachute applications because of its small percent elongation under a given load. The use of Dacron involves a 10 to 15 percent weight penalty compared to Nylon and has a lower energy absorption capability for a given weight of material. Fabrication experience is somewhat limited for Dacron.

BREAKING STRENGTH OF NYLON AT ROOM TEMPERATURE
AFTER EXPOSURE TO 350°F IN DRY AIR

Exposure Time (hours)	Percent of Original Strength	
	Not Heat Resistant (type 300)	Heat Resistant (type 700)
1	48	98
10	28	77
100	12	24
180	8	13
320	8	9

Nomex offers the advantage of far greater resistance to heating than Nylon or Dacron and is useful for long periods of time up to temperatures between 600 to 700°F. However, when compared with Nylon, it has a lower strength to weight ratio and the finer denier fabrics are not presently available. The new textile materials (PRD-14, X-101 and PBI) appear to have characteristics at elevated temperatures approximately equal to or superior to Nomex (PBI has useful properties at temperatures in excess of 1000°F). In addition, it is expected that these new materials may easily be produced as finer denier yarns than is presently practical for Nomex.

Some room-temperature characteristics of currently available and future textile materials are listed in the following table.

ROOM TEMPERATURE CHARACTERISTICS OF TEXTILE YARNS

	Tenacity (grams/denier)	Elongation at Break (percent)	Specific Gravity
Nylon, Type 700*	8.8	16.5	1.14
Dacron, Type 52*	8.3	12.0	1.38
Nomex*	5.5	17.0	1.38
PRD-14**	7.2	13.0	--
X-101**	4.2	20.5	--
PBI Fiber**	3.2	28.0	--

*DuPont data
**AFML-TR-65-29 (May 1965)

In view of the properties of the new organic fibers under development, there appears to be no need to seriously consider some of the more exotic textile materials (glass, quartz and metal) which are also being developed for parachute use. However, some other materials which are not usually employed in parachute design such as thin reinforced polymer films (Mylar) may be worthy of evaluation. For a main parachute canopy, the zero porosity of a polymer film may be an advantage unless it adversely affects the stability characteristics of the parachute. Fabrication techniques must also be considered. In order to obtain reliability equivalent to that of a textile material, it would undoubtedly be necessary to overdesign parts which utilize the polymer film, hence a consequent weight penalty results. Finally, since there is little background of experience with films as parachute materials, development costs would enter as a definite factor.

2.2.1 Selection Criteria

The goal in the selection of parachute materials is to obtain a maximum in reliability and efficiency with a minimum weight. This requires a careful determination of the strength of each candidate material at the temperature and pressure conditions the material will experience during prelaunch, launch, interplanetary flight, entry, deployment and descent environments. The strength of the material will be related not only to the conditions experienced at deployment but also on the past history of the material, i.e. the amount and type of degradation experienced by pressure packing, sterilization, and the effects of the ambient conditions experienced between Earth and Mars. After having determined the strength available and the requirements of a material, a selection can be made to give the desired performance with the minimum weight. Other criterion which must also be considered are the uniformity of available supplies, fabrication problems such as difficulties in reliable joining, and dimensional distortion during sterilization. For a new material, development costs would also be part of the selection criteria.

2.2.2 Weight and Air Permeability

A drogue parachute will require a fabric material with high air permeability* (or porosity); the main parachute canopy on the other hand should have a low air permeability. The permeability of a parachute fabric is related to a number of factors such as the twist of the yarn, the weave style, the tightness of the weave and the calendering of the woven fabric. Low permeability and minimum fabric weight is provided by fine yarn denier. The finer the denier, the thinner (hence, lighter) the construction of the fabric.

* The air permeability of canopy fabric is commonly expressed as the volume of air flowing through a unit area in a unit time ($ft^3/min/ft^2$) at a constant specified pressure-differential.

The lightest weight, low permeability Nylon practicable at the present time is in the range of about 3 ft^3 of air/min/ft^2 of fabric (air pressure differential of 0.5 inch of water). Low weight, low-porosity Dacron fabrics would be comparable.

Existing low permeability Nomex fabric is considerably heavier than Nylon or Dacron with comparable permeability. The lowest practicable weight for a low porosity Nomex fabric is around 2 ounces per square yard. Fabric of this weight can be obtained with a permeability around 29 cfm. Additional calendering could reduce the porosity to a point where it approaches 10 cfm. However, the permanence of this lower permeability has yet to be determined. One of the reasons why Nomex fabric is heavier than Nylon fabric of comparable permeability is because the finest Nomex yarn in production is 100 denier. Although not commercially available, it is understood that the production of 30 denier yarn is technically feasible. If 30 denier Nomex yarn were produced, it is reasonable to assume that a fabric could be made with weight and permeability characteristics which approach those of Nylon (0.6 to 1.0 oz/yd^2).

Representative weight and permeability characteristics of Nylon and Nomex fabrics are listed below.

REPRESENTATIVE VALUES FOR LIGHT-WEIGHT LOW PERMEABILITY FABRICS

Type of Fabric	Weight (oz/yd^2)	Permeability (cfm)
Nylon	4.8	0.6
Nylon	3.9	2.2
Nylon	2.0	2.9
Nylon	0.6-1.0	3.0-4.0
Nomex	5.0	8.6
Nomex	3.7	15.3
Nomex	2.0	29.0

2.2.3 Riser and Shroud Lines

In general the problems discussed for canopy materials are applicable to riser and suspension-line materials. Differences in application requirements, however, alleviate some of the problems. Low elongation (under tensile stress) is desirable for parachute riser and shroud lines since it minimizes oscillatory motions which adversely affect parachute stability.

As the parachute size increases, it becomes more important that elongation be minimal since oscillatory problems increase with the size of the parachute. For this reason, Dacron would be better than Nylon for the main parachute riser and suspension lines.

For drogue parachutes it is possible that protective coverings may be necessary on the risers to alleviate the possibility of damage due to contact with the ablating forebody.

2.2.4 Test Data

There is a considerable amount of test data available on effects of temperature, radiation and vacuum exposure on Nylon, and to a somewhat lesser extent on Dacron and Nomex. Similar data for PBI, X-101 and PRD-14 are beginning to appear.

Test data, together with theoretical considerations, make it possible to estimate the suitability of textile materials to withstand postulated conditions. There exists however, major discrepancies and gaps in test results. While these discrepancies may be explained by variation in basic materials, more accurate and detailed information than is now available must be obtained before a Mars descent system can be optimized. One primary reason for the discrepancy and difficulty in correlating prior tests results is the lack of proper definition of the test sample materials and environments. In addition, most data on the relationships between strength, temperature and time at a given temperature were obtained in air under ordinary atmospheric conditions. Heating in a dry nitrogen atmosphere (required for sterilization) and also in a partial vacuum will in general cause less degradation than an equivalent amount of heating in the presence of oxygen. There is very little data available to indicate improved performance under these conditions. The amount of degradation of Nylon during sterilization is crucial in deciding whether or not Nylon is suitable for parachute canopy use.

Northrop (Ventura Division) is presently conducting a preliminary in-house program to determine the variations in textile strength, elongation, and dimensions due to prolonged heating in a nitrogen atmosphere. It is essential that a more detailed and controlled testing program be established at the earliest possible date to assess all of the candidate materials under all of the possible environments.

2.2.5 Temperature Effects (Sterilization)

1. Nylon

The strength of Nylon (Type 300) decreases as the temperature of the fibers is increased with 50 percent of the room temperature strength

being retained at about 360°F. If the exposure is not extended to the point where heat deterioration is produced, the original room-temperature strength is observed upon return and conditioning at room temperature. Zero strength temperature for Nylon is about 473°F and melts at 482°F. When heated at temperatures of 300°F or higher, particularly while under pressure, there is a tendency for the fibers to stick together and when cooled they stiffen and set.

If heated to a temperature higher than that employed in the calendering* and heat-setting processes, Nylon will shrink. This is a permanent change. Heating Nylon at a given temperature for a sufficiently long period of time will produce permanent changes in strength. The extent of the permanent deterioration produced by elevated temperatures is a relatively complex question and depends on a number of factors which include the following:

a. Temperature

b. Duration of exposure

c. Type of atmosphere (primarily whether or not oxygen is present)

d. Type of Nylon (heat resistant or non-heat resistant)

e. Textileprocessing procedures (whether scoured or unscoured, etc)

There is a marked difference in resistance to damage between ordinary Nylon and that Nylon which has been specifically treated to provide heat resistance. Unfortunately, literature reports generally do not indicate what kind of Nylon has been tested beyond a Mil-Spec description which ordinarily does not specify the degree of heat resistance required. Usually, very little is known about the type of Nylon that went into the textile or the processing the Nylon was subjected to during textile fabrication. This is undoubtedly a major contributing factor to the considerable variation in reported values for the heat deterioration of Nylon textiles. A good example of the difference between heat resistant and non-heat resistant Nylons is given in a recent report on sterilization effects (see Reference 1). After being subjected to 145°C (293°F) for a total of 108 hours in nitrogen, type 300 Nylon cord and type 380 Nylon-fabric specimens retained an average of about 20 percent of their original strength after return to room conditions. Neither type 300 nor type 380 is heat resistant Nylon. Type 330 Nylon is a heat resistant type.

* Pressing the material between rollers to make it smooth.

There was a considerable range in individual values for the type 330 Nylon ribbon. This may be attributed to the fact that the Nylon samples had been scoured. According to duPont test data, un-scoured heat-resistant Nylon is more stable at elevated temperatures than scoured Nylon. It is probable that the wide range of values may be partially due to an uneven degree of scouring.

The effect of the flight qualification sterilization requirement of 275°F (135°C) for 24 hours, can be demonstrated in the following table, where test data of several textile specimens are listed. Each textile specimen has been heated in air then tested after the specimens were returned to room conditions.

STRENGTH RETENTION OF NYLON TEXTILES AFTER HEATING IN AIR AND RETURNED TO ROOM CONDITIONS FOR TESTING

Type of Textile	Type of Nylon	Temp (°F)	Time (hours)	Strength Retention (percent)	Source
Average of 3 kinds of fabrics 2 kinds of webbing 1 kind of cord	(1)	250 300	24 24	86 47	(2) (2)
1.1 ounce (fabric)	(1)	225 275 275	96 16 64	97 89 42	(3) (3) (3)

(1) Type not specified, but assumed to be non-heat resistant
(2) WADC-TR-54-117
(3) Northrop/Ventura test data

Assuming linear interpolation, the averaged WADC data would suggest 66 percent strength retention for Nylon (non-heat resistant) after 24 hours at 275°F in air and the Northrop Ventura data would suggest strength retention of 81 percent. The Northrop Ventura data indicates a strength retention of a little above 50 percent after three 24-hour cycles at 275°F.

In a similar manner, the corresponding qualification test conditions (293°F dry heat for 36 hours, three cycles) can be listed with predicted yarn-strength retention after being heated in air and then returned to room conditions for testing.

PREDICTED NYLON YARN STRENGTH RETENTION AFTER HEATING IN AIR AND RETURN TO ROOM CONDITIONS FOR TESTING

Temperature		Time for Three Cycles (hours)	Type 300 (Non-Heat Resistant) Strength Retention (percent)	Type 700 (Heat Resistant) Strength Retention (percent)
°F	°C			
293	145	108	40	85
284	140	151.2		
275	135	205.2		
266	130	388		
257	125	594		
248	120	945		
239	115	1512		

The above predicted strength retention can be compared with the values reported in Reference 1, which indicates 20 percent strength retention for textiles made of type 300 and 380 Nylon and 70 percent for scoured heat resistant Nylon (type 300 heated a total of 108 hours in nitrogen).

It can be concluded from the above discussion that presently available data do not present a clear picture of what can be expected of Nylon textiles after being subjected to sterilization conditions. It would appear that heat-resistant Nylon will withstand three cycles under the sterilization conditions (and in an inert atmosphere even type 300 may demonstrate favorable strength retention).

Under the sterilization qualification conditions, significant strength changes must be anticipated particularly with type 300 Nylon. Note that a drastic reduction in Nylon strength can be tolerated if this is taken into consideration in the design of the parachute system if a small weight penalty is acceptable. Nylon, especially of the heat resistant type, should be retained as a candidate material. Further tests of various types of Nylon and textile geometrics (in an inert atmosphere under sterilization qualification conditions) are clearly required before a realistic selection can be made.

2. Dacron

Dacron has a zero strength point at 473°F (245°C) and melts at 482°F (250°C). At 400°F its strength is 50 percent of the room temperature strength. The duPont test data on deterioration dur to heating in air indicates a negligible amount of textile degradation from sterilization flight

qualification conditions and better than 80 percent strength retention after being subjected to subsystem qualification conditions. This is in reasonable agreement with other test results. At a given temperature, Dacron retains a larger percentage of its original strength than Nylon and degrades less when exposed to elevated temperatures. As with Nylon, strength degradation from heating in air can be expected to be more severe than heating in an inert atmosphere.

3. Nomex

Nomex does not melt although it does deteriorate rapidly at temperatures above 700°F (371°C). At the melting point of Nylon (482°F), Nomex fibers still retain 60 percent of their room-temperature strength. Strength retention of Nomex textiles when tested at 600°F is around 25 percent, and at 650°F it is approximately 15 percent. Nomex fabric elongation has been found to remain generally constant up to 600°F and in the range of 20 to 25 percent. This is in contrast with Nylon which becomes rather plastic at 300°F with an attendant elongation of almost 35 percent. Exposure to a temperature of 293°F for 108 hours (subsystem sterilization qualification) can be expected to have a negligible effect on Nomex textiles, particularly in an inert atmosphere.

4. New High Temperature Textiles

The development of three new textile fibers for elevated temperature applications has progressed to the point where it is reasonable to predict that they will be available for use as parachute canopy textiles by 1967. These are a polyimide fiber designated PRD-14, a new polyamide fiber (X-101) and a polybenzimidazole fiber (PBI). It is expected that these new textiles will offer some advantages as parachute materials over Nomex in availability of finer denier and lower porosity fabrics. It is anticpated that the thermal stability of PRD-14 and X-101 will be approximately equal to that of Nomex or possibly a little better. PBI appears to be substantially more heat stable with some strength remaining at temperatures in excess of 1000°F. The following table presents the strength retention of these materials at temperatures of 293 and 650°F. Note that heat resistant Nylon has a 70 to 80 percent strength retention after 108 hours at 293°F and Nomex has a 99 percent retention for the same conditions.

Figure 17 (see Reference 2) further illustrates the relationship between temperature and strength, giving a comparison of the strength retention of Nylon, Nomex and PBI fibers at various temperatures.

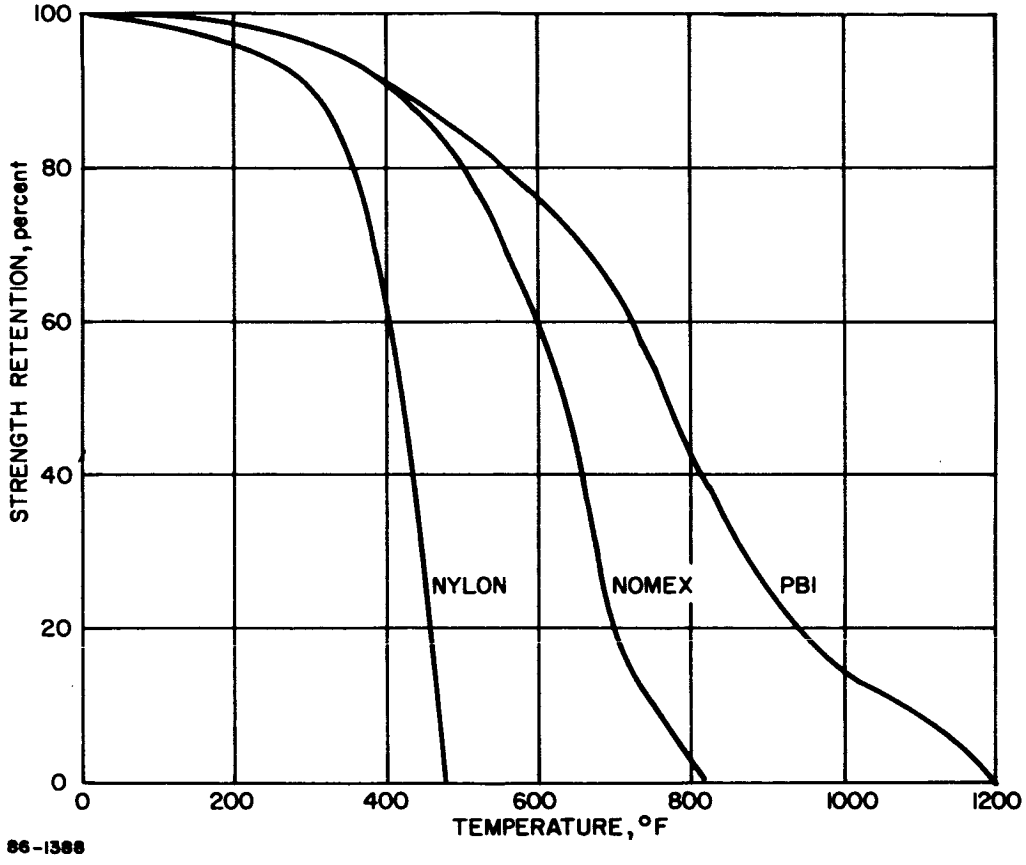

Figure 17 PERCENT STRENGTH RETENTION VERSUS TEMPERATURE FOR CANDIDATE CANOPY MATERIALS

TEXTILE PROPERTIES AT ELEVATED TEMPERATURES

	Estimated Room Temp. Strength Remaining After 108 Hours at 293°F (percent)	Estimated Residual Strength When Tested at 65°F (percent)
Nylon (not heat resistant)	20 to 40	0
Nylon (heat resistant)	70 to 80	0
Dacron	80	0
Nomex Fibers	99	40
Nomex Textiles	99	15
PBI Fibers	99	70

2.2.6 Chemical Sterilization Effects

The effects of a chemical sterilization (in addition to dry-heat sterilization) on organic textiles must also be considered. At present, it is assumed that chemical sterilization will involve subjecting the textile materials to a gaseous mixture of 12 percent ethylene oxide and 88 percent Freon-12. Sufficient water will be added to produce a relative humidity of 40 to 50 percent with temperatures up to 40°C (104°F) for a duration of from one to several days.

Under these conditions, one would anticipate no significant effect on the basic strength of any of the textile materials which have been discussed (Nylon, Dacron, Nomex, PRD-14, X-101 and PBI).

Ethylene oxide-Freon mixtures have been found to be particularly useful in sterilizing articles which are sensitive to heat or moisture. It is frequently utilized in sterilizing products made of wood, paper, leather, plastics, elastomers, and textiles, as well as delicate instruments.

Ethylene oxide* is chemically quite reactive to certain materials and the use at temperatures much higher than 40°C (104°F) should be approached with caution. A chemical sterilization temperature of 100°C (212°F) or higher would become quite questionable, as would also the addition of any ingredient which would produce a basic (alkaline) condition.

* If the ethylene ozide procedure is found to be critically damaging to the parachute materials, then the parachute subsystem will be packed in a sealed pressurized container.

The sterilization mixture can be expected to be soluble in the ordinary types of silicone textile lubricants. It is also anticipated there would be some sterilization chemicals dissolved in the lubricant during sterilization. The dissolved chemicals should dissipate subsequent to the chemical sterilization with no significant effects anticipated.

2.2.7 Problem Areas

The selection of the most suitable materials and components is dependent upon a tradeoff of the characteristics and properties of the various candidates. This assumes the availability of reliable test data and information. However, the descent system will be subjected to conditions for which data in many cases are either limited or do not exist.

Problem areas can be related to the following:

1. sterilization
2. prolonged storage in an interplanetary environment
3. hypersonic deployment in the Mars atmosphere

Heat sterilization requirements represent a severe environment for most organic materials, pyrotechnics, and electronic components. In the case of organic materials, heat sterilization in an inert atmosphere reduces the amount of degradation which may be experienced. However, the temperatures and time durations still represent a severe environment. Among the organic materials, the principle problem areas are in the selection of parachute (canopy) materials. There are a number of advantages in utilizing Nylon as the main parachute. However, more information is required to define the effects of heat sterilization on Nylon and particularly on heat-resistant Nylon.

In the case of other candidate textile materials (Dacron, Nomex, PRD-14, X-101, PBI) it is felt that there is no particular problem of strength loss due to heat sterilization but this should be verified. The effect of heat sterilization on dimensional stability, porosity and elongation should be determined. No particular problems are anticipated in the selection of non-textile organic components or in electronic components. However, the functional suitability after sterilization of specific preliminary selections should be investigated by suitable test procedures. In the case of pyrotechnics, sterilization will require considerable change in existing components. Although it is felt that suitable substitute pyrotechnic materials are available, their stability and functional characteristics after sterilization will require careful assessment.

In summary, the components and materials for which heat sterilization presents selection problems are:

1. Organic materials, including textiles
2. Electronic components
3. Pyrotechnics

Chemical sterilization at ambient or slightly above ambient temperatures is expected to present no particular problems. However, the compatibility of preliminary material selections with chemical sterilization should be surveyed.

Prolonged storage of the sterilized descent subsystem in interplanetary space involves exposure to a combined cold-soak and space-vacuum environment which has not been duplicated in laboratory tests. Analyses and tests on Apollo components and materials have indicated no difficulties for lunar orbital missions up to 34 days. The major areas of concern are related to the high vacuum in interplanetary space. These areas are of particular concern because of the limited background of information on the behavior of materials in a space environment. Testing to simulate the long duration of a mission will be required in the course of development and qualification of a descent subsystem. Potential problem areas are listed below:

1. Effect on pressure packed textiles stored in a space-vacuum environment for a prolonged period of time.

2. Effect of exposure of other organic components to space vacuum for a prolonged period of time.

3. The possible occurence of cold welding.

4. Adequacy of pyrotechnic seals.

Hypersonic drogue-parachute deployment in the Mars atmosphere introduces the problems of aerodynamic heating and the possibility of chemical interaction between the atmosphere and the parachute materials. Hypersonic deployment (Mach 3.0 to 4.0) will limit parachute materials to Nomex and the newer high temperature textiles (Nylon could be used up to Mach. 2.75). Determination of strength characteristics under deployment conditions (after sterilization and space storage) will be required during the process of development and qualification.

2.3 PARACHUTE CONFIGURATIONS

Four basic factors were considered in selecting candidate parachute configurations: 1) performance characteristics, 2) reliability, 3) weight penalty, and 4) development risk.

2.3.1 Performance Characteristics

Consideration of performance characteristics of the candidate parachutes has been made in terms of presently available data on:

1. Opening shock characteristics -- Low opening forces of symmetrically inflating parachutes result in a lighter parachute.

2. Stability of descent -- High stability parachutes are desirable from the standpoint of minimizing vertical descent rate.

3. Sensitivity to Mach number -- Certain parachutes are acknowledged to perform satisfactorily under supersonic conditions. Sonic inlet flow problems on some decelerators preclude their use above sonic velocity.

4. Drag characteristics -- The inherent capability of a given configuration to produce sufficient drag force to satisfy a given descent rate limit at ambient density values is of significant importance. The parachute cloth area and/or weight is effected.

2.3.2 Reliability

The preliminary reliability assessment, emphasized the effects of known uncontrollable variables on parachute performance along with performance deviation probability. The following reliability areas were evaluated:

1. Positive Inflation Tendency -- Certain canopies consistently inflate uniformly and usually remain inflated in a stable condition.

2. Tolerance for Damage -- The effects which localized damage may have on performance and confidence that local damage will not propagate is a strong factor in the selection process.

3. Manufacturing Tolerance Sensitivity -- Certain configurations are very sensitive to uncontrollable manufacturing variations. This effect is amplified by the size of parachute under consideration.

4. Susceptibility to Backing Deviation -- Some parachute types must be deployed in a precise manner in order to ensure satisfactory performance. Candidate configurations were appraised in terms of present manrated system packing/inspection procedures.

2.3.3 Weight Penalty

A comparative analysis was conducted to evaluate the weight penalty of each configuration studied. In each instance, materials improvement anticipated within 1967 technology was considered for the particular configuration. The following considerations were included as tradeoff rationale:

1. Specific drag -- Potential levels for the drag area obtainable per pound of parachute.

2. Nonuniform inflation penalty -- Certain parachutes typically inflate assymetrically requiring appropriate adjustment of design factors.

3. Sensitivity to storage/sterilization environment -- The weight effects of various preoperational environments were appraised for each parachute configuration considering fibrous material variations in strength, tear resistance, elongation, flexibility, and elastic recovery.

2.3.4 Development Risk

A large gap exists between theoretical performance for the condidate parachutes and their practical application to a particular descent system. A development risk assignment has therefore been made for the concepts considered in terms of the extent of available data. The development considerations are as follows:

1. Extent of high speed data -- Effects of operation near or above Mach 1 on deployment and inflation characteristics must be established.

2. Extent of low-density data -- Performance data under the condition of large parachute cloth surface area coupled to low payload weights is essential.

3. Scope of configuration data -- History of a particular concept, independent of the deployment conditions and performance requirements, provides technical information around which theoretical performance extensions may be made.

Using the preceding considerations as the tradeoff rationale, a preliminary investigation of candidate parachute configurations for the descent system was conducted. Parachutes included were the ribbon, ringslot, ringsail, extended skirt, and annular canopies. Viewed from the standpoint of parachute descent only, Table I shows the ribbon parachute to be best slightly better than the ringsail.

The overall descent merit score was then coupled with overall mission penalty factors as adapted to the parachute variables. Preliminary consideration of parachute configuration versus the flight capsule mission are presented in Table II. As typical of most manrated spacecraft recovery systems currently developed or being qualified, the ring-sail canopy was found to provide the highest total mission score. Continuous updating of the weighting factors must be conducted as further data becomes available.

2.3.5 Main Parachute

This section describes candidate descent parachute types, design characteristics, and general range of performance. Operational aspects under normal deployment and descent conditions are listed.

Current or likely concept extension studies are discussed in terms of scope and objectives for each configuration.

1. Ribbon Parachute

This canopy concept involves the formation of drag producing surface predominantly by means of circumferential and radial tapes intersecting each other to form a geometrically porous grid. Basic variations in the cross section and planform define classification of ribbon decelerators as follows:

Type	Cross Section	Planform
Fist	Flat	Polygon
Conical	Conical	Polygon
Hemisflo	Hemispherical	Circle
Hyperflo	Flat Crown-Solid Conical Extended Skirt	Polygon

This configuration has been primarily utilized in high speed decelerator systems where deployment Mach numbers of 1.2 have been experienced. Sizes have been small with diameters of approximately 6.0 feet. Of particular interest to this program is the Hyperflo concept which is currently under development as a high supersonic decelerator (see paragraph 6). Listed below are some design characteristics of the Hyperflo parachute. Note its well behaved stability.

Diameter Ratios		Drag Coefficient (Based on D_p)	Opening Shock Factor	Lateral Stability (degrees)
D_p/D_c	D_o/D_c			
0.67	1.00	0.45 to 0.55	1.05	± 3 to 5
(0.90)	(0.693)	(0.42 to 0.10 super-sonic)		

where:

D_o = nominal diameter

D_p = projected diameter

D_c = constructed diameter

The ribbon parachute concept (Hyperflo configuration) is presently being examined for Mach 3 to 4 recovery applications. Sufficient wind tunnel and free flight data have been obtained through Mach 4.5 to warrant pursuit of such a design in a current development program, while concurrent research programs are providing additional performance information.

2. Ring-slot Parachute

The ring-slot canopy design follows a concept of concentric rings of reinforced cloth with intervening air slot spaces to establish geometric porosity or openings. In many high speed applications, the ring-slot has proven more efficient than the ribbon parachute, particularly when staging limits demand a combination recovery/deceleration canopy.

Limited variation of cross section and planform have been pursued. These include flat, conical, biconical, and triconical cross sections combined with a polygon planform.

This configuration has been used primarily for deceleration applications in sizes up to 40 feet in diameter with deployment Mach numbers up to 0.9. Smaller sizes are being explored for use as an air pickup parachute for air retrieval systems. Listed below are some design characteristics of the ring slot parachute.

Diameter Ratios		Drag Coefficient (Based on D_p)	Opening Shock Factor	Lateral Stability (degrees)
D_p/D_c	D_o/D_c			
0.70	1.00	0.50 to 0.65	1.10	± 5 to 7

Much intermediate altitude data have been gathered on the ring-slot canopy as a combination recovery/air pickup parachute or air pickup/deceleration parachute. However, the scope of the data is limited to moderate canopy sizes. Future development activity will likely be limited to pursuit of the ring-slot as an air pickup parachute in aerial retrieval systems and as an aircraft deceleration parachute.

3. Ring-sail Parachute

This canopy consists of a series of concentric rings (similar to the ring-slot) developed on a quarter spherical surface coupled with unique fullness distribution in the lower gore and geometric porosity in the crown area. Moderate geometric porosity is distributed by radial

spaces over approximately 40 percent of the gore height measured from the vent. Leading edge fullness, ranging from 2 to 15 percent and increasing toward the skirt, is introduced over the remaining 60 percent of the gore height to create crescent shaped slots conducive to positive inflation and high drag.

This configuration has been used primarily for recovery of the manned space vehicles (Mercury, Gemini, Apollo) as well as drone and escape capsule recovery. Sizes have ranged up to 88 feet in diameter with development Mach numbers of 0.5. During one test, this parachute was deployed at a Mach number of 1.2. Larger diameter parachutes up to 127 feet have been constructed and tested. Listed below are some design characteristics of the ring-sail parachute. Note the fairly high-drag coefficient.

Diameter Ratios		Drag Coefficient (Based on D_p)	Opening Shock Factor	Lateral Stability (degrees)
D_p/D_c	D_o/D_c			
0.70	1.16	0.70 to 0.90	1.05 to 1.20	± 10 to 15

Present ring-sail development programs being conducted are providing data on this canopy concept in both single canopy and cluster configurations. As a recovery parachute, the ring sail offers the greatest reservoir of advanced performance data upon which theoretical performance extension may be founded. Feasibility studies involving ring-sail canopies of up to 187 feet nominal diameter are also underway.

4. Annular Parachute

The annular parachute configuration is formed of a solid cloth surface developed from a 45-degree truncated cone. The upper plane defines a vent diameter which typically ranges from 50 to 80 percent of the projected diameter of the canopy. Listed below are some design characteristics of the annular parachute. Note the extremely high drag coefficient.

Diameter Ratios		Drag Coefficient (Based on D_p)	Opening Shock Factor	Lateral Stability (degrees)
D_p/D_c	D_o/D_c			
0.50 to 0.80	0.76 to 1.05	0.85 to 1.10	1.10	± 3 to 5

Considerable development activity is in process to establish the annular parachute as part of a high efficiency aerial recovery concept. Results to date have proven favorable. Fabrication and testing of configurations up to 69 feet in diameter have been accomplished with deployment altitudes up to 45,000 feet (Earth) at Mach numbers of approximately 0.4. Further development for Mach 1.0 deployment is presently being investigated.

5. Extended Skirt Parachute

The extended skirt canopy design is characterized by a flat circular center with an added skirt extension in the form of an inverted truncated cone. This configuration has been utilized for aerospace recovery, aerial drop, and personnel applications. Sizes up to 100 feet in diameter have been fabricated. Deployment Mach numbers of 0.8 have been achieved. This configuration produces low opening shock forces coupled with relatively high oscillations during descent. Listed below are some design characteristics of the extended skirt parachute.

Diameter Ratios		Drag Coefficient (Based on D_p)	Opening Shock Factor	Lateral Stability (degrees)
D_p/D_c	D_o/D_c			
0.76	1.24	0.65 to 0.85	1.20	± 10 to 20

Extensive performance data for large sizes and high subsonic deployment is available for this configuration.

2.3.6 Drogue Parachute

The development of supersonic parachutes suitable for high Mach number application was started in 1948 and has resulted in the following designs:

1. Conical ribbon parachutes: these parachutes are suitable for applications up to Mach 1.5.

2. Hemisflo ribbon parachutes: suitable for application up to Mach 2.5.

3. Hyperflo parachutes: these have been tested in wind tunnels up to Mach 6.0 and in free-flight tests up to approximately Mach 4.5.

The goal of obtaining a successful supersonic parachute involves two major problems:

1. To obtain proper inflation and inflation stability (breathing).

2. To maintain sufficient transverse and longitudinal stability for the particular application required.

It was found that the following factors primarily contribute to successful supersonic parachute operation:

1. Stabilization of the shock waves formed by the canopy and the suspension line confluence points in front of the canopy.

2. Proper consideration of forebody wake and wake interaction with the parachute.

3. Establishment of proper pressure distribution in the canopy behind the shock wave for proper inflation and inflation stability.

Tests have shown that conical ribbon parachutes can be used successfully up to Mach 1.5 without undue canopy oscillation or canopy deflation provided a proper canopy inlet to outlet area ratio is maintained. This can be accomplished by fixed reefing and by a certain amount of canopy shaping.

Standard solid flat or conical ribbon parachutes form gore pockets that support proper inflation at subsonic velocities. However, it was observed in supersonic application that these pockets have a tendency to flutter in and out, thereby causing heavy canopy breathing (inflation instabilities) and canopy deflation. Control of this canopy breathing made it possible to use conical ribbon parachutes up to Mach 1.5. At higher Mach numbers, the shock wave in front of the canopy is swallowed, resulting in deflation of the canopy leading edge, extreme canopy vibration, and ultimate destruction of the canopy due to overstress.

The hemisflo parachute was the next development step. This is still a ribbon parachute with the shape being a perfect hemisphere with a (10-percent of the projected diameter) attached to the leading edge of the hemisphere. This configuration avoids canopy breathing by eliminating excess material and by stabilizing the shock wave in front of the canopy. Several hemisflo parachutes have been used for system applications up to Mach 2.5 to 3.0. An advantage of the hemisflo parachute is its high drag coefficient in the Mach 0.5 to 2.5 range.

The extensive research conducted by the USAF Systems Command led to the development of the hyperflo parachute. This parachute combines effects of the slotted ribbon parachute with the stabilized leading edge effect of the guide surface parachute. It was pointed out previously that stabilization of the shock wave in front of the canopy and operating the canopy in subsonic

flow behind the shock was a prime contributing factor for proper operation. This was successfully obtained with the hyperflo parachute in wind tunnels up to Mach 6.0 and in free flight application up to Mach 4.5. However, many variables in canopy and system design have to be considered such as:

1. effect of suspended capsule
2. effect of shock wave generated by the suspension line confluence point
3. stabilization of the canopy shock wave in front of the canopy
4. distance of canopy leading edge to maximum forebody diameter
5. canopy leading edge cone inlet angle
6. canopy inlet area to outlet area ratio
7. canopy roof porosity and porosity distribution
8. canopy suspension line length.

Considerable insight has been gained in the interelationship of these parameters. However, the present understanding of hyperflo parachute operation has not progressed to a point where a design can evolve without further wind-tunnel testing and confirming free-flight tests. This is especially important if very large blunt suspended capsules are used and if the development is extended beyond the known range of design data.

Hyperflo parachutes have presently been tested with 6.5 foot nominal diameters, velocities up to Mach 4.5 in free flight, 120,000 feet altitude, and dynamic pressures in excess of 5000 lb/ft.^{2}. Reference 3 presents considerable performance data for hyperflo parachutes showing the effects of various design parameters.

2.3.7 Pilot Parachute

The principle function of a pilot chute is to provide deployment of a large parachute. A pilot chute is frequently employed with an extra large main parachute to aid uniform inflation and to stretch out the canopy so that the initial mass of entering air will reach the vent at the apex rather than be trapped in a pocket of side panels. Stretch out of the canopy is achieved by permanently attaching the pilot chute to the apex of the main parachute.

In the deployment of the main parachute at subsonic speeds, the pilot parachute may serve the function of removing the cover of the recovery compartment from the vehicle, followed in tandem by the main parachute pack.

In this operational concept the pilot parachute is not attached to the apex of the main parachute but merely removes the deployment bag from the main canopy after the suspension lines have been pulled out. The pilot parachute then serves to carry the cover away and lower it at a slow rate to avoid interference by collision with the inflating main parachute system.

In the event that a drogue parachute is used for supersonic deceleration and is too large for direct mortar deployment, a pilot parachute ejected by mortar is a recommended deployment means for the drogue parachute.

Ribbon and ring-slot canopies are most suitable for pilot chute applications. The selection factors discussed in paragraph 2.3.5 for these configurations also apply to pilot parachute utilization. The conical or hemisflo ribbon configurations are recommended for a single parachute system where pilot deployment will be in the low supersonic to mid-subsonic speed range. For deployment of a drogue parachute, the hyperflo ribbon configuration is recommended.

Size of a pilot chute is determined by the drag needed to extract the main or drogue parachute from its compartment with a positive 3 to 5g force. The riser length must position the pilot canopy at least 7 vehicle body diameters behind the suspended capsule. The pilot parachute size should take into account the effect of supersonic wake, and the materials of construction should be capable of sustaining low aerodynamic heating.

2.4 ENTRY FROM APPROACH TRAJECTORY DESIGN

2.4.1 Summary

The primay objective of the parachute descent system is to decelerate the landed capsule to a reasonably low vertical impact velocity (hard impact, survivable lander) while rendering adequate communications time during the terminal phase of the flight. The type parachute system and allowable attendant deployment conditions dictate to a large degree the maximum M/C_DA that can be achieved for a vehicle entering a given atmosphere with particular entry conditions. The final selection of the parachute descent system should be based first on reliability, second on weight, and then on performance and developmental risk in that order of importance.

The selected descent system must contain a terminal descent parachute which is fully inflated and subsonic at a minimum altitude of 15,000 feet. The system must also ensure a vertical impact velocity of no greater than 80 feet per second (study ground rule) for the worst case (terminal descent atmosphere).

The model atmospheres used in the entry from approach trajectory design were the models 1, 2, and 3 combined with a terminal descent atmosphere (Reference 4). A study ground rule stated that the descent system must be designed to sustain the atmospheric environments of models 1, 2, and 3 and that at commencement of descent retardation the model be switched to the terminal descent atmosphere. Switching to the terminal descent atmosphere at parachute deployment had the effect of changing the Mach number while maintaining the same flight velocity. It was concluded that model 3 atmosphere dictated the allowable M/C_DA based on the design deployment conditions of the descent system and that the terminal descent atmosphere governed the parachute size necessary to satisfy descent time and impact velocity criterion.

The selected retardation system concept utilizes a single main parachute which is pulled out of its canister by a pilot parachute. The main parachute is deployed in a reefed condition at Mach 1.3 and is disreefed at 16,000 feet by a signal from the radar altimeter. Selection of the canopy configuration for this mission was based on four factors, namely: 1) performance characteristics, 2) reliability, 3) weight penalty, and 4) development. An optimum parachute configuration requires simultaneous evaluation of the above mentioned factors coupled with an appraisal of the effect of parachute configuration on mission requirements. Utilizing all of these considerations as tradeoff rationale, it was found that the ring-sail canopy satisfied the design requirement best and hence was chosen as the selected configuration.

The use of a two parachute (drogue-main) retardation system was investigated and found that it could be incorporated to serve one of two alternatives, namely: 1) increase the M/C_DA and realize an increase in the scientific mission 2) increase the main parachute deployment altitude by maintaining the same M/C_DA as would be used in the single parachute design. It was concluded that for the scientific mission being considered an increased M/C_DA was not necessary and that the single parachute system would yield adequate deployment altitude and/or descent time for the mission.

2.4.2 Main Parachute Analysis

The parametric analyses shown in this section are based on the ring-sail configuration utilizing a drag coefficient of 0.7 based on nominal chute diameter. Parachute weights and dimensions can be easily scaled for other configuration with different drag coefficients.

The most severe design condition for parachute descent is to utilize the model 3 atmosphere until deployment initiation and then descend in the terminal descent atmosphere. (Labeling on the curves model 3 - terminal descent atmosphere refers to the above mentioned composite atmosphere model.)

The main chute weights and dimensions are based on terminal descent velocity using the equation,

$$A_{mc} = \frac{2 W_{susp}\ g_{\sigma}}{\rho\, C_D\, V_v^2\, g_{\oplus}}$$

where,

A_{mc} = main parachute canopy area based on nominal diameter, ft^2

W_{susp} = suspended weight on the parachute plus the parachute system weight, pounds

g = gravitational acceleration, ft/sec^2

ρ = sea level surface density, $slugs/ft^3$

C_D = drag coefficient based on nominal diameter

V_v = vertical impact velocity at sea level, ft/sec

2.4.2.1 Parametric Results

The effective drag area of the suspended capsule is neglected since it is small compared with the drag area of the parachute system. Figure 18 shows the required main parachute canopy area (based on nominal diameter) per pound of suspended capsule weight (A_{mc}/W_{susp}) for each of the atmospheres under consideration. The ratio of A_{mc}/W_{susp} allows a quick parametric evaluation of parachute system size for a given suspended weight. The results shown are plotted as a function of vertical impact velocity and indicate that for a vertical sea level descent velocity of 80 ft/sec (study ground rule) the ratio of A_{mc}/W_{susp} is approximately 6.1 ft^2/Earth pound in the terminal descent atmosphere. If the vertical impact velocity requirement were to be decreased to say 50 ft/sec, the A/W ratio increases to 16.1 reflecting approximately a 160 percent increase in descent system weight. If the parachute system were designed to descend to sea level in the model 3 atmosphere (10 mb) and impact at 80 ft/sec, the A/W ratio would decrease to 4.0. This results in approximately a 35 percent decrease in system weight compared to the terminal descent atmosphere case.

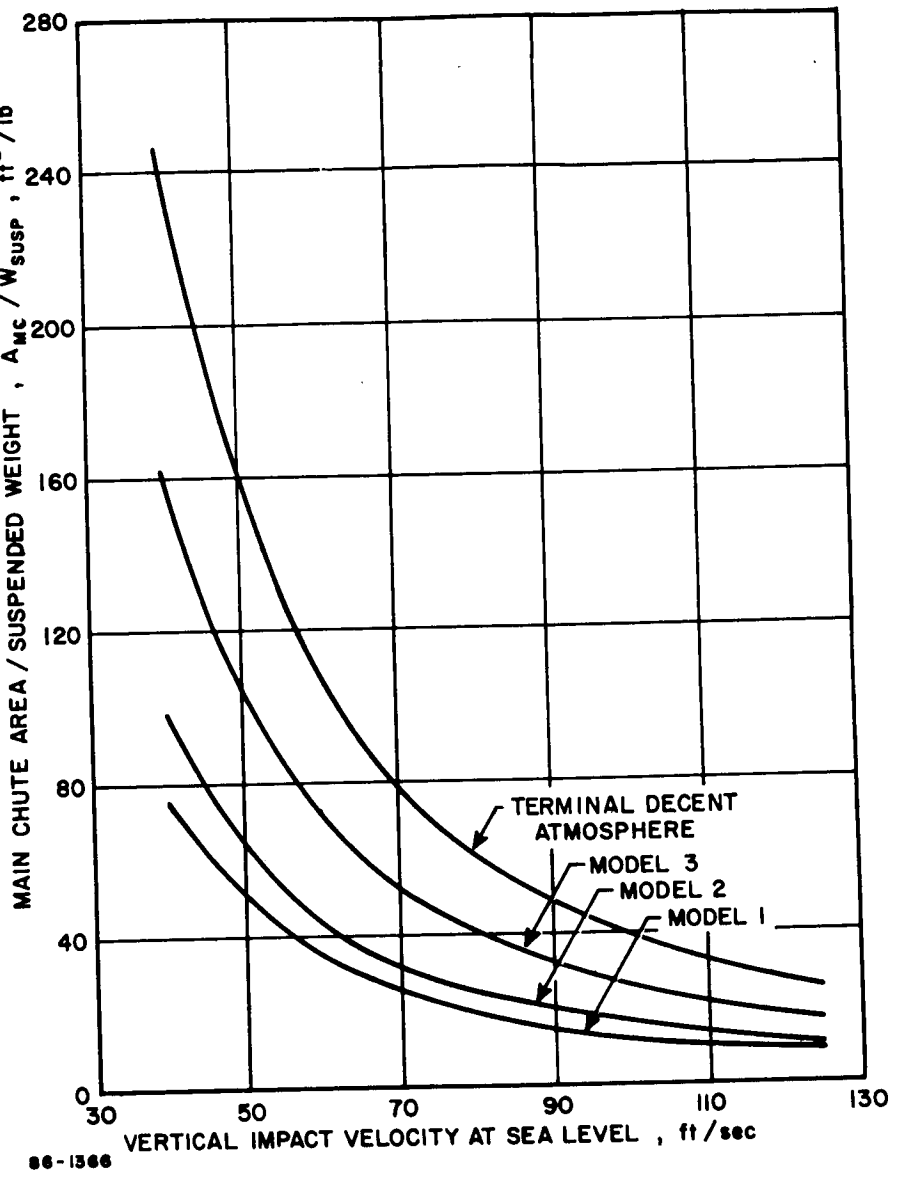

Figure 18 SINGLE PARACHUTE SYSTEM--IMPACT VELOCITY VERSUS MAIN CHUTE AREA/SUSPENDED WEIGHT

With the model 3 - terminal descent atmosphere established as the most critical from a system design weight standpoint, a discussion of parametric results as a function of impact velocity, parachute diameter and suspended weight will follow. Figures 19 and 20 show the required main parachute system weight and diameter for a range of suspended weight and impact velocities. Note that for a suspended weight of 1000 pounds and an impact velocity of 80 ft/sec (final design condition) the parachute system weight is 77 pounds and the nominal parachute diameter is 88 feet. Figure 21 shows the ratio of main parachute system weight to suspended mass (W_{mc}/W_{susp}) versus vertical impact velocity. For an impact velocity of 80 ft/sec, this ratio is 7.7 percent.

Figures 22, 23 and 24 are cross plots of Figures 19 and 20 and dipict main parachute weight and diameter versus suspended weight for a range of impact velocities.

2.4.2.2 Cluster Tradeoff

The utilization of a cluster of parachutes rather than a large single parachute of equivalent drag area must consider the following: 1) performance, 2) weight, and 3) reliability. Use of a cluster is dictated primarily by system considerations involving the above three factors.

1. Performance -- Four basic considerations exist in the comparison of cluster performance with single parachutes. These are 1) stability, 2) drag, 3) opening loads, and 4) short filling time potential.

The inherent stability of clusters, for even the most unstable canopy design, is markedly increased over the single-parachute configuration. In order to approach cluster stability with a single canopy, the porosity must be increased with an attendant loss of drag coefficient. The favorable characteristic of clusters is attributed to the effect of the intercanopy airflow pattern which forces each canopy to fly at a statically stable angle.

The drag coefficient of each parachute in a cluster is decreased due to the flow interactions but can approach that of the individual canopy if sufficient riser length is used.

Individual parachute opening loads of clustered parachutes are higher than for the equivalent single canopy for two reasons. First, shorter filling times, and secondly, nonuniform inflation pressure between parachutes creates higher loads for the first random parachute opening. While reefing is conventionally employed to reduce opening shock and minimize nonsynchronous inflation, the disreefing tolerances still allow high individual parachute opening loads. Parachutes having the most positive inflation characteristics are generally most susceptible to nonuniform loading when clustered.

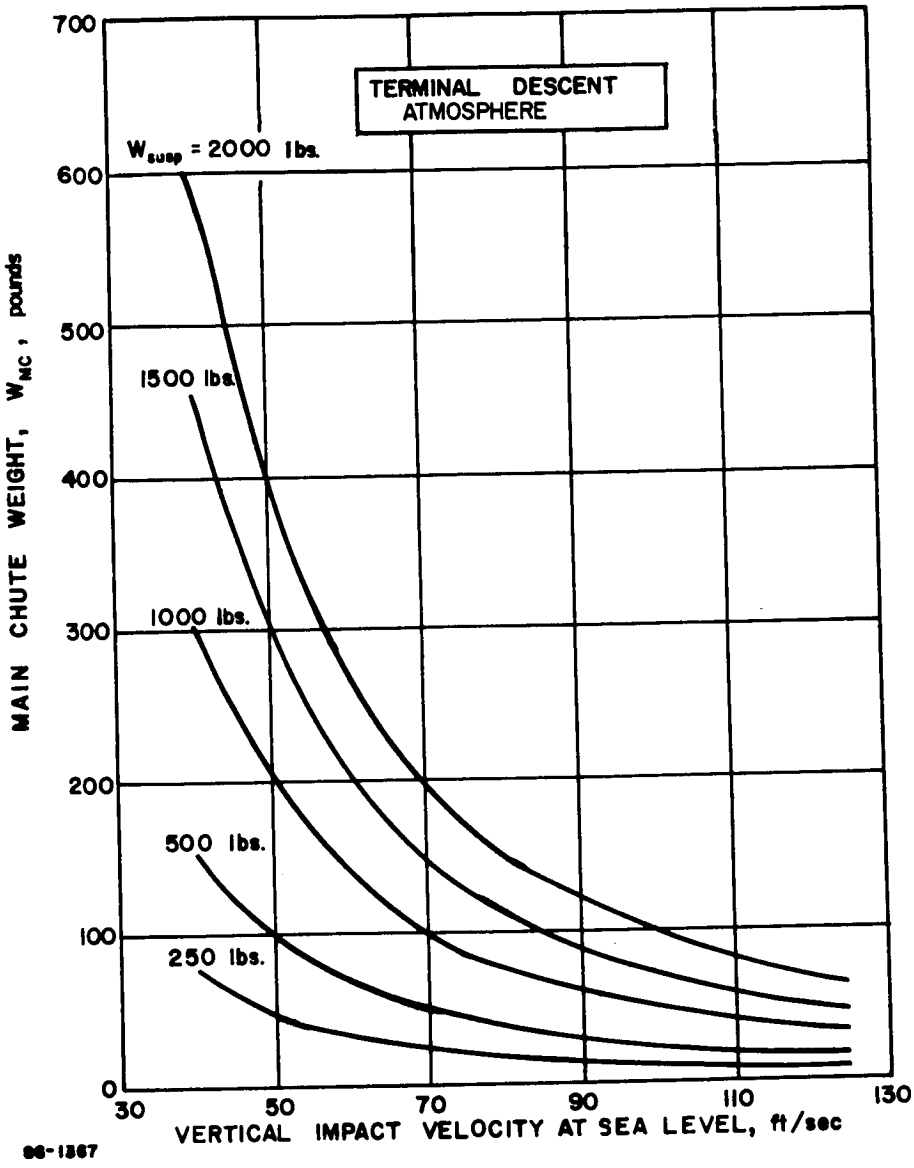

Figure 19 SINGLE PARACHUTE SYSTEM--MAIN PARACHUTE WEIGHT VERSUS IMPACT VELOCITY

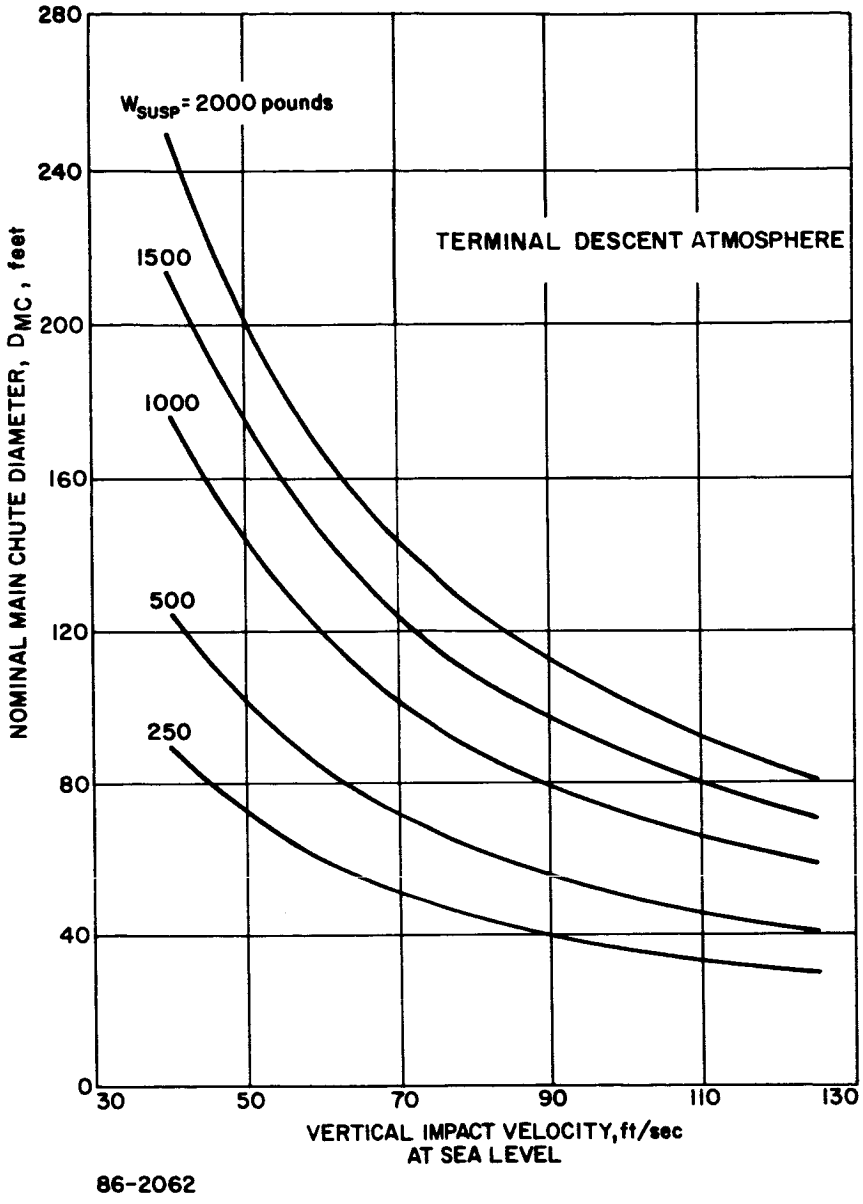

Figure 20 SINGLE PARACHUTE SYSTEM--MAIN PARACHUTE NOMINAL DIAMETER VERSUS IMPACT VELOCITY

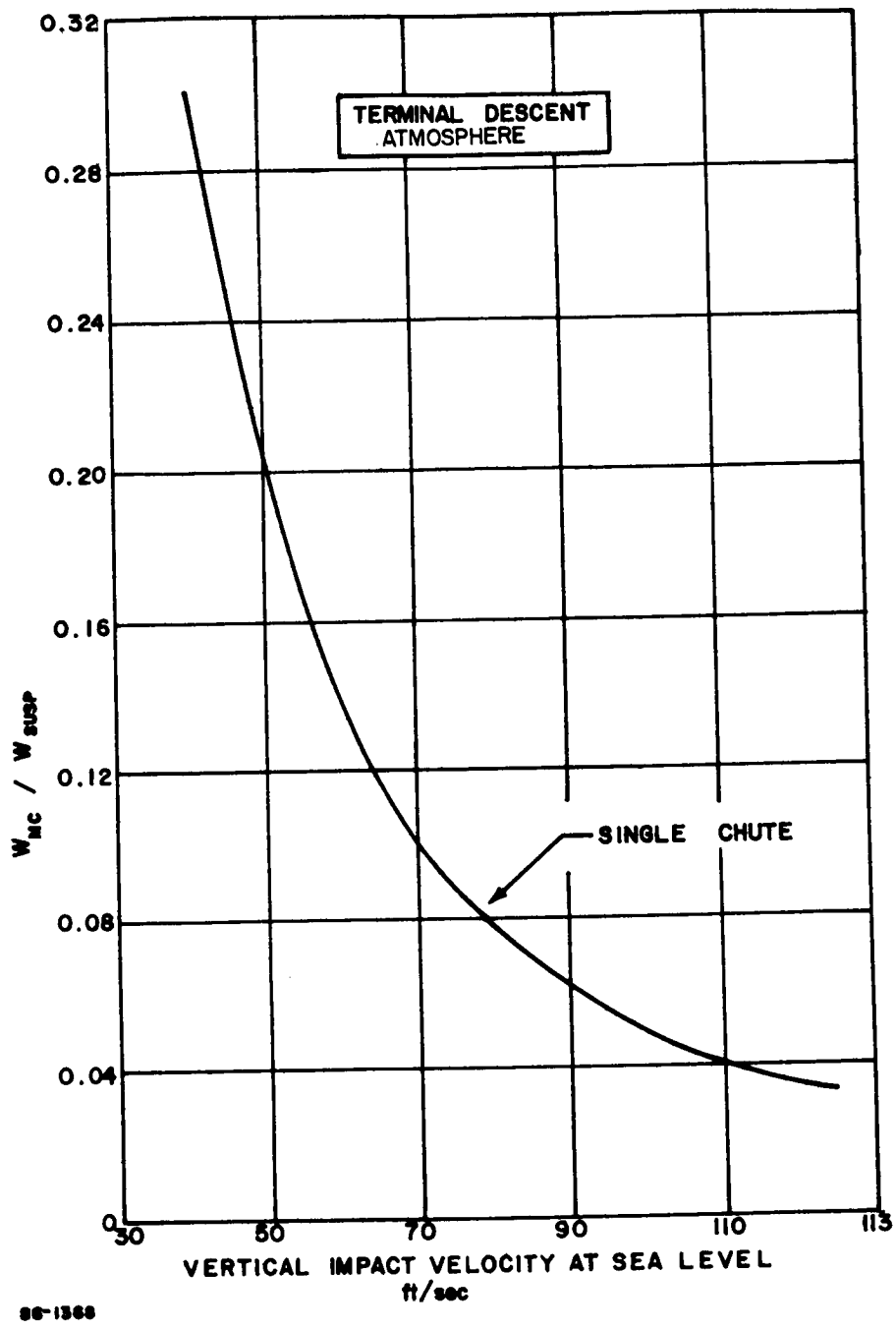

Figure 21 PERCENT MAIN PARACHUTE WEIGHT VERSUS IMPACT VELOCITY

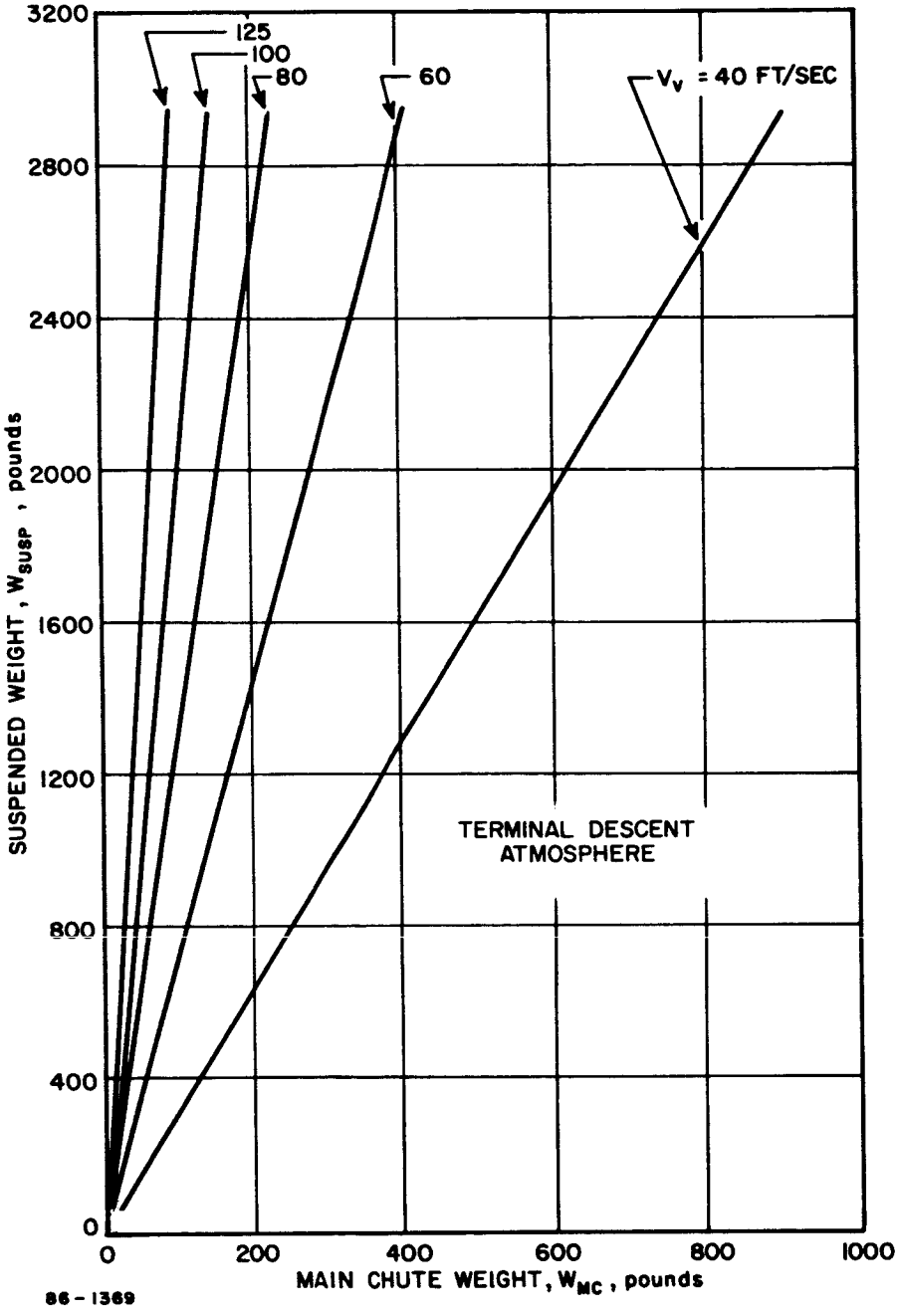

Figure 22 SINGLE PARACHUTE SYSTEM--MAIN PARACHUTE WEIGHT VERSUS SUSPENDED WEIGHT

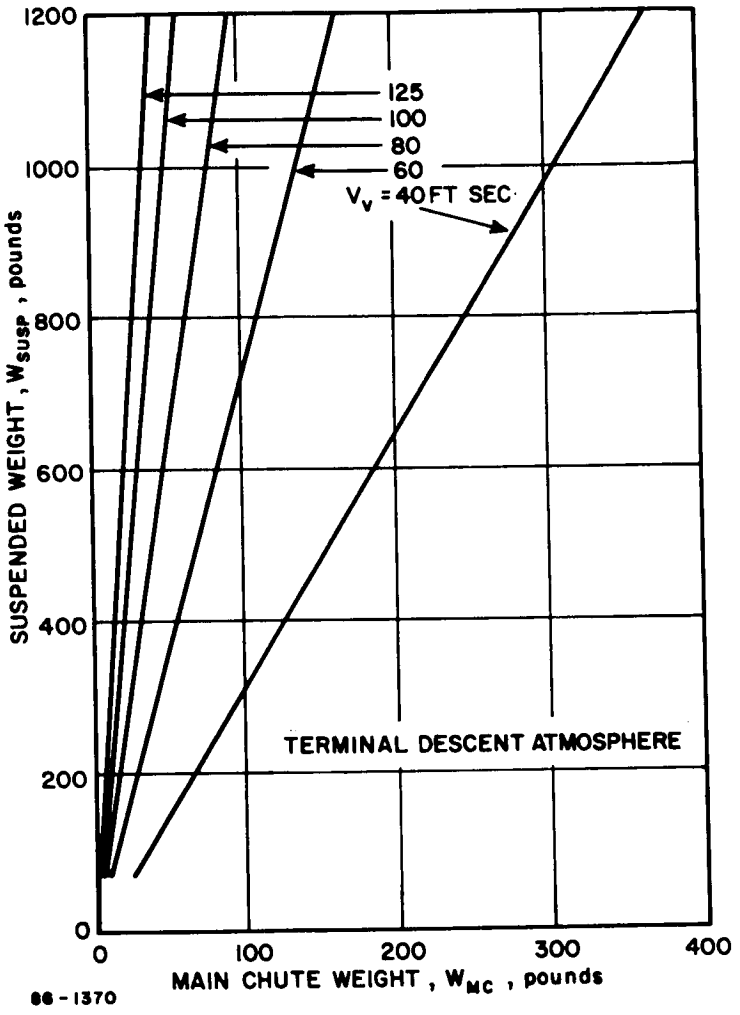

Figure 23 SINGLE PARACHUTE SYSTEM--MAIN PARACHUTE WEIGHT VERSUS SUSPENDED WEIGHT

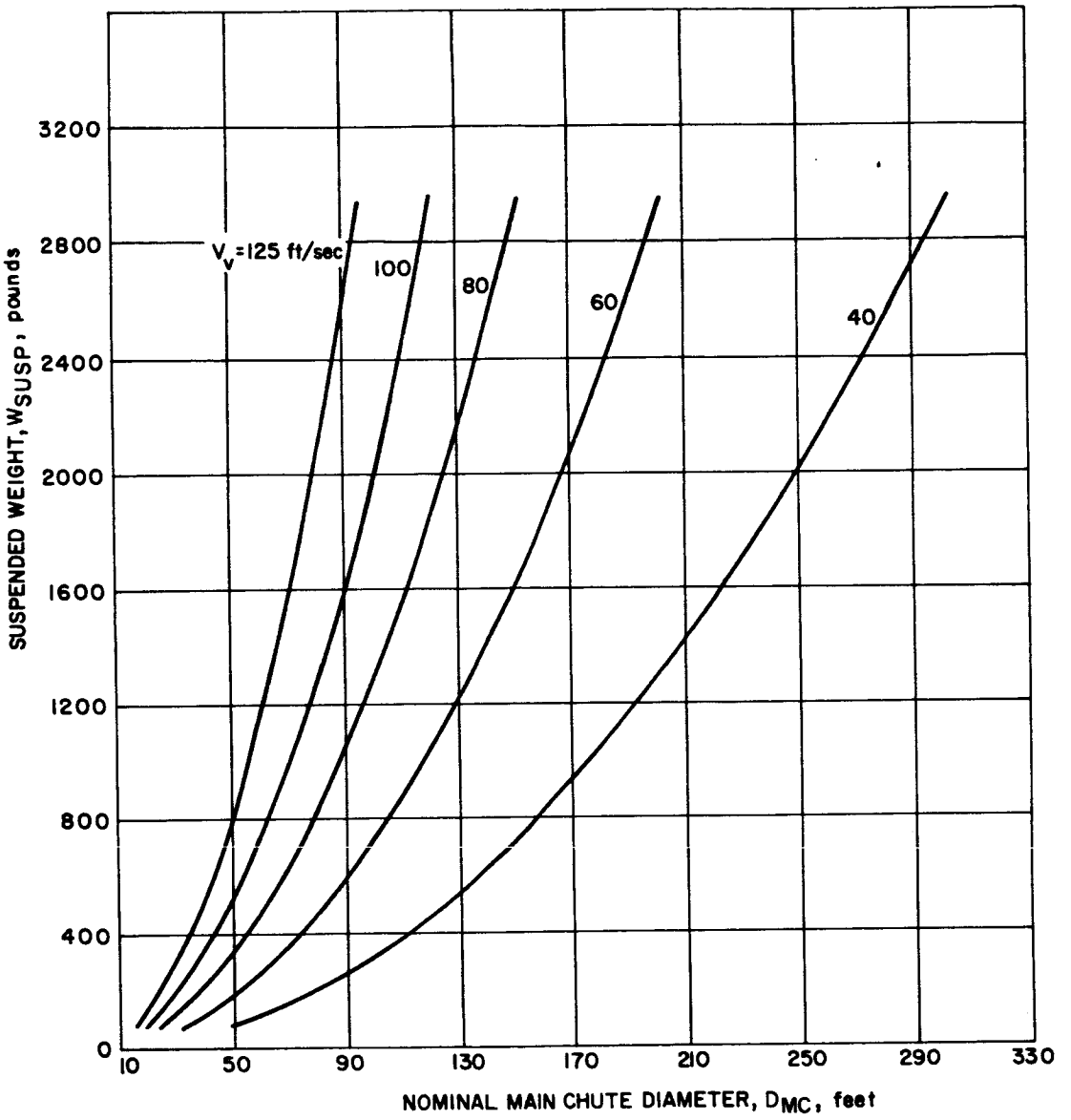

Figure 24 SINGLE PARACHUTE SYSTEM--SUSPENDED WEIGHT VERSUS MAIN PARACHUTE DIAMETER

2. Weight -- In general, there is a weight penalty associated with the use of clustered parachutes in comparison to an equivalent single parachute system.

For comparison, the weight penalties involved with cluster applications are illustrated by a current development program for large single parachute systems equivalent to the Apollo clustered system.

This program is aimed at utilizing a single ring-sail canopy 127 feet nominal diameter to provide the same descent conditions as two 88-foot parachutes. The design weight of the single parachute system, canopy, lines, links, and risers is 213.3 pounds. This is comparable to the weight of 249 pounds for two 88-foot diameter parachutes (a 15-percent weight penalty).

3. Reliability -- Reliability of clusters in spacecraft recovery applications typically typically tend to be quite favorable. Clusters of ring-sail parachutes provide an extremely high tolerance for damage since the primary performance characteristic, namely drag, is relatively insensitive to canopy damage. This trend relaxes sensitivity to manufacturing tolerance level as well as packing deviations.

Disadvantages with the use of clusters are found in the areas of subsystem requirements and in reliability testing. The extent of testing required to develop and qualify minimum weight clusters exceeds that of the single parachute due to the inherent inconsistencies in cluster performance.

With the present difficulties in the development of a descent system for a 1971 mission, clusters present many additional problems and will not be actively considered at this time. However, for comparative purposes, results for three and five parachute clusters are shown on Figures 25 and 26. On Figure 25 the main parachute system weight and diameter versus suspended weight are shown for a three parachute clustered system. Note that the results are shown for a three parachute clustered system, are for the reference 80 ft/sec impact velocity and that the diameter scale reflects the diameter of each parachute within the cluster. Figure 26 presents comparisons between single, three, and five parachute systems.

If one were to arbitrarily dictate that the maximum diameter of a single parachute be no greater than 100 feet (a reasonable constraint), then the maximum suspended weight would be 1300 pounds with the parachute system weight of 100 pounds. At this point, a three parachute cluster of 62-foot diameter parachutes could accomplish the required 80 ft/sec descent velocity, but the clustered system weight is 130 pounds, reflecting a 30-percent increase. From Figure 26, note that a reasonable

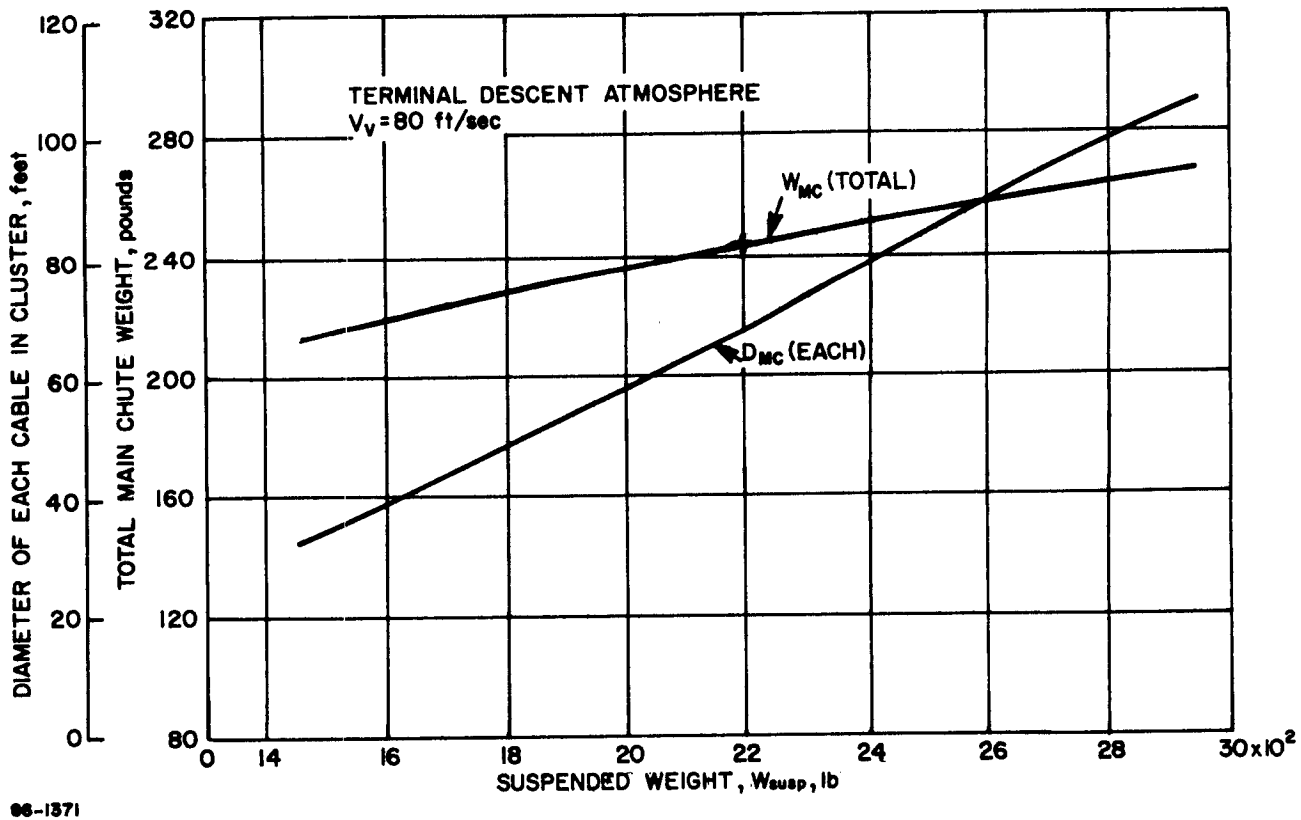

Figure 25 SUSPENDED WEIGHT VERSUS MAIN PARACHUTE WEIGHT--THREE PARACHUTE CLUSTER

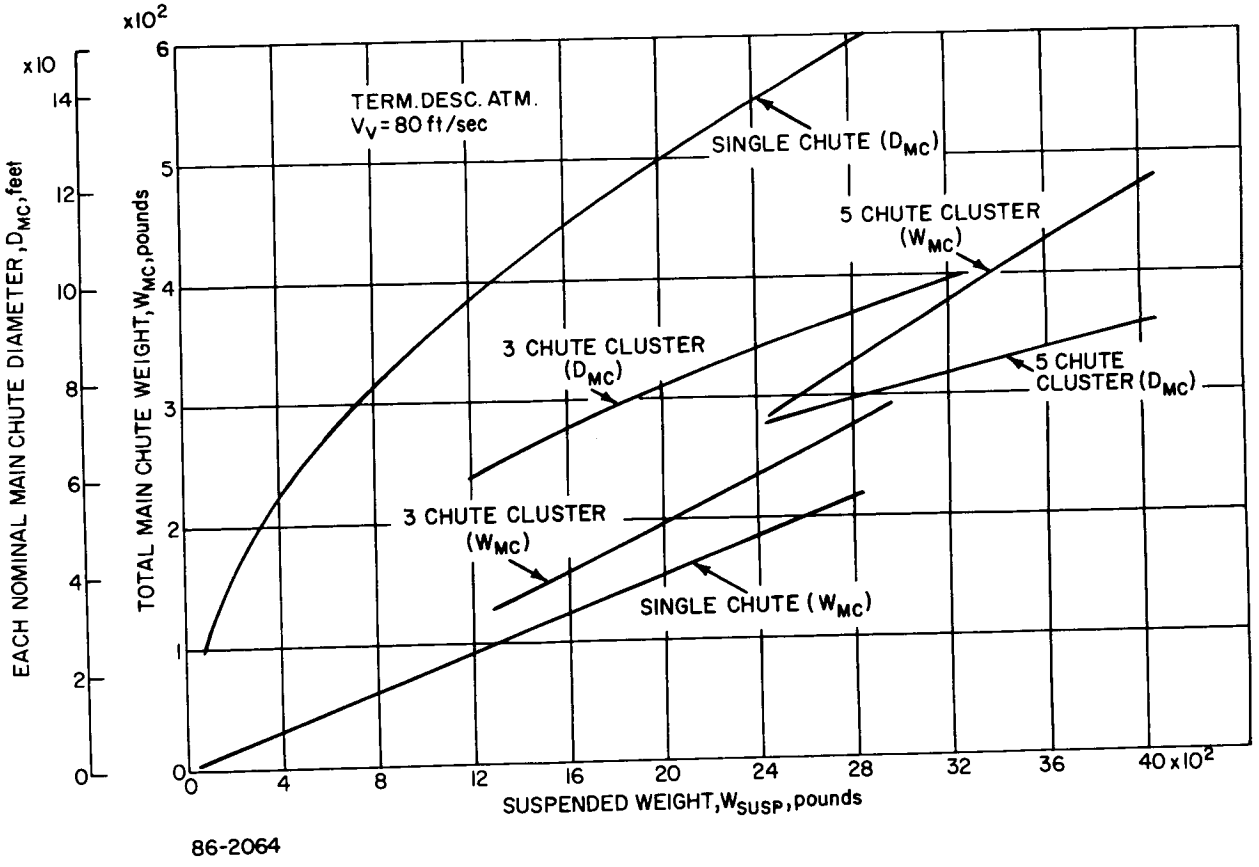

Figure 26 MAIN PARACHUTE WEIGHT AND DIAMETER VERSUS SUSPENDED WEIGHT FOR THREE AND FIVE PARACHUTE CLUSTERS

operating range for a three parachute cluster is between 1300 and 3300 pounds suspended weight, beyond this weight each parachute in the cluster exceeds a nominal diameter of 100 feet. For a suspended weight of 3300 pounds, five or more parachutes will be required.

2.4.2.3 Reefing

Reefing of self inflating decelerators is a technique used to control the inflated shape through the use of one or more sets of auxiliary lines, bands, and mechanical accessories. The application of reefing is generally suited to enhance parachute performance or effectiveness by:

1. limiting the opening shock force,

2. control of descent rate for a predetermined interval for trajectory or descent time/dispersion control,

3. increasing the lateral stability and minimizing the breathing (inflation instability) characteristic of the canopy,

4. minimizing nonuniformity of inflation time and loads, during the operation of parachute clusters.

Current design practice based on flight-test data indicates that the lower limit for reefed drag area is approximately 3 percent of the fully opened drag area, below which point stability becomes a critical problem. For single-stage reefing, the optimum reefed-area percentage tends to be 15 to 30 percent for balanced opening shock load, optimum parachute stress distribution, and minimum system weight.

The selected descent system design calls for deploying a reefed parachute at Mach 1.3 and then disreefing at 16,000 feet. A minimum weight system will be achieved (for both the parachute system and the suspended capsule structure) by equalizing the reefed and disreefed opening shock loads. This is dependent upon the percent of canopy reefing and also the opening dynamic pressures. For an M/C_DA of 0.15 slugs/ft^2 and entry angle of 90 degrees, the optimum design calls for 18 percent reefing of the full open area. This is shown on Figure 27 and corresponds to a disreefing Mach number of 0.42 and dynamic pressure of 1.8 lb/ft^2.

2.4.2.4 Descent Times

For deployment at Mach 1.0, 16,000 feet and using area to weight ratios from Figure 18, Figure 28 shows the descent time for all of the model atmospheres and for a range of main parachute area/suspended weight ratios.

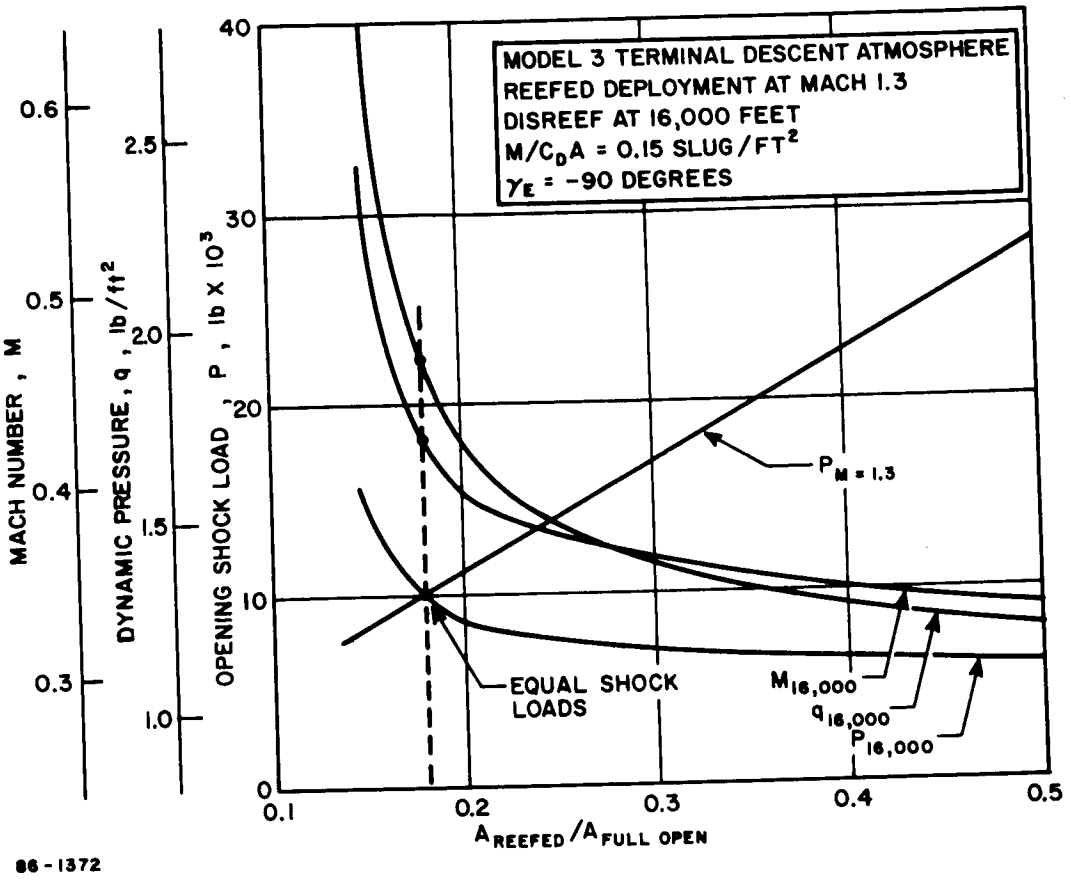

Figure 27 OPENING SHOCK LOAD VERSUS REEFED PARACHUTE AREA/FULL OPEN AREA

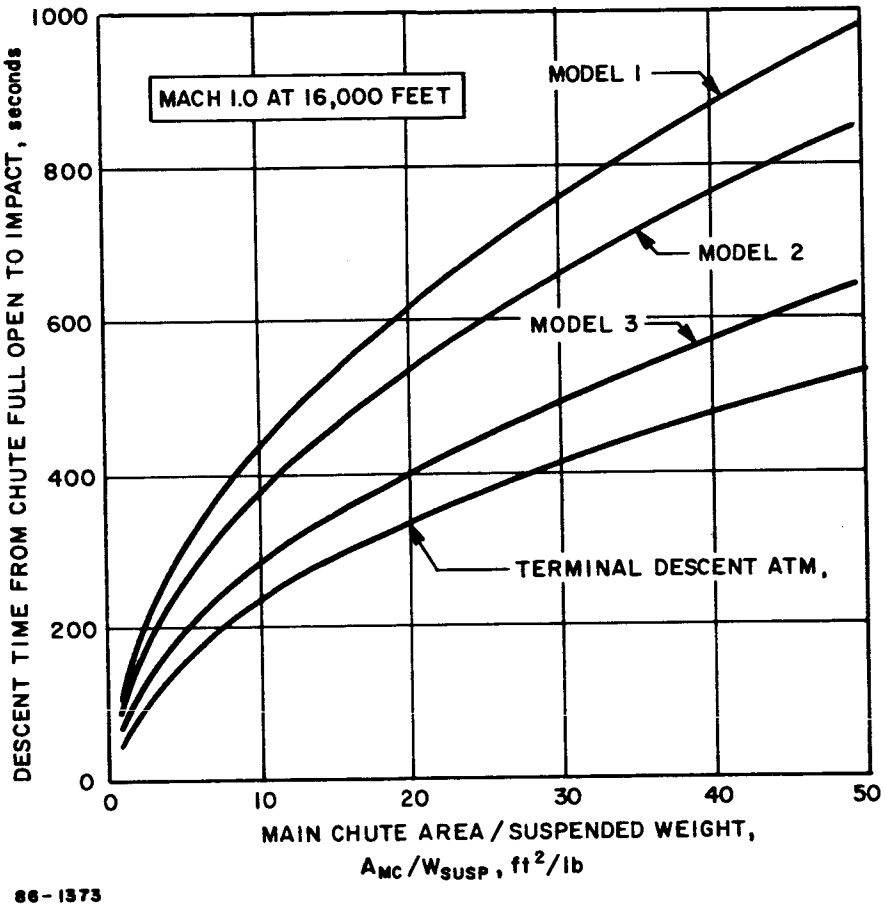

Figure 28 DESCENT TIME VERSUS A_{mc}/W_{susp}

Figure 29 depicts descent time for a range of deployment altitudes in the terminal descent atmosphere. Note that for an impact velocity of 80 ft/sec in the terminal descent atmosphere, the ratio of A_{mc}/W_{susp} is 6.1 ft^2/lb. Deployment at lower Mach numbers, as in the reefed chute case, will result in slightly longer descent times than those shown in Figures 28 and 29.

2.4.2.5 Weight Analysis

Overall system weights for the main parachute are based on experimental data and past experience. Data from Northrop Corporation/Ventura Division and Cook Electric Company were used. Parametrically, the total parachute system weight is expressed as,

$$W_{mc} = \frac{Kq\ A_p}{10}$$

where,

K = 0.013 for 0.8 oz/yd^2 Nylon canopy

q = deployment dynamic pressure, lb/ft^2

A_p = projected canopy area, ft^2

For the clustered parachute systems,

$$W_{mc} = \frac{Kq\ A_p\ n(0.98 + 0.045\ n)}{10}$$

where,

A_p = projected area of each parachute in the cluster, ft^2

n = number of parachutes in the cluster (must be greater than 1).

Utilizing the above equation, Figure 30 presents curves of the main parachute system weight versus opening dynamic pressure for a range of nominal parachute diameters. Note that the weight reflects only the parachute canopy and suspension lines, hence availing itself to quick parametric weight evaluation. Weights for other components within the system must additionally be included.

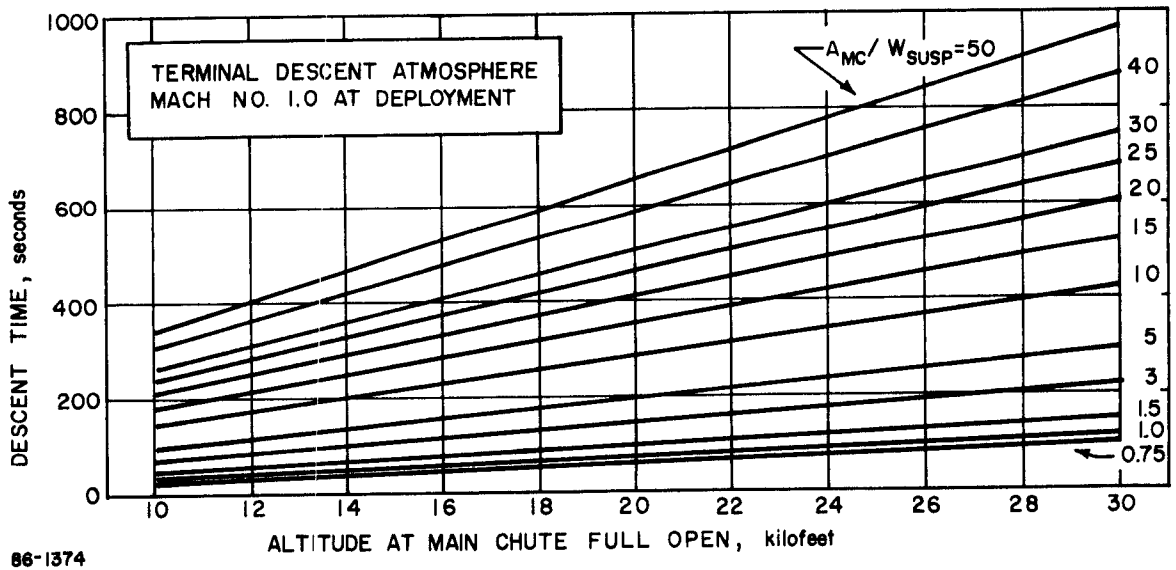

Figure 29 FULL-OPEN ALTITUDE VERSUS DESCENT TIME

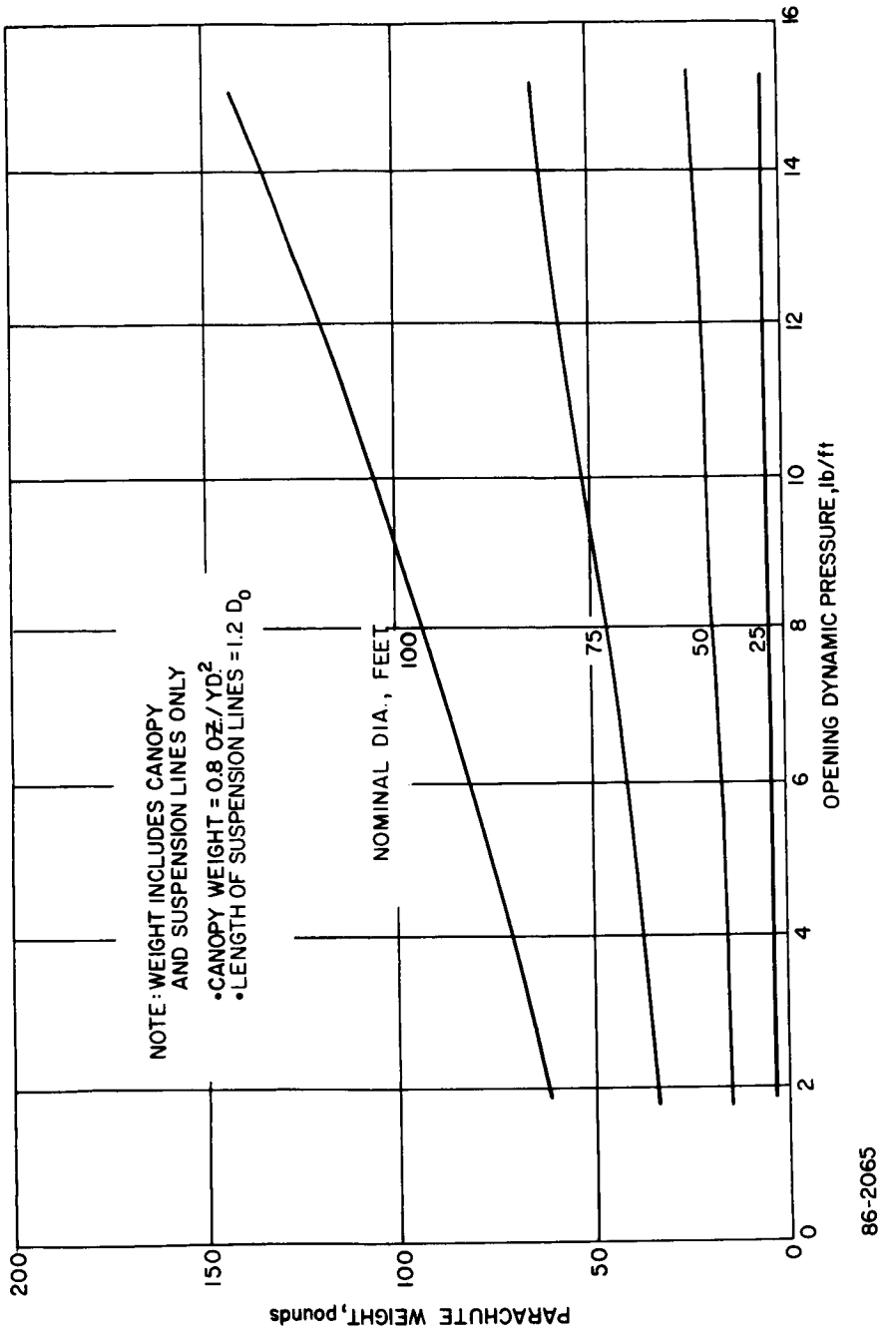

Figure 30 MAIN PARACHUTE WEIGHT VERSUS DYNAMIC PRESSURE

2.4.3 Drogue Parachute Analysis

2.4.3.1 Material Selection

Parachute fabrics for drogue parachute construction are selected on the basis of load and temperature limitations. The load criterion is set by the breaking strength of the fabric and is a function of the dynamic pressure and the parachute diameter. The stress on the canopy can be calculated by utilizing a thin-wall hemisphere approach, the expression for which is

$$S = \frac{qD_o}{4t} \quad lb/ft^2$$

where q is the pressure acting uniformly on the hemisphere, t is the thickness of the material, and D_o the nominal diameter of the parachute.

A more common parachute notation expresses the required fabric strength as:

$$L = \frac{qD_o}{4} \quad lb/ft$$

where the definitions are as given above.

The temperature limitation is set by the maximum wall temperature a particular fabric can withstand and is a function of the ratio of specific heats (γ), static free stream temperature (T_∞), and the free stream Mach number at a given altitude (M_∞).

Hence, the canopy wall temperature (T_S) can be expressed as

$$T_S = T_\infty \left[1 + \frac{\eta(\gamma - 1)}{2} M_\infty^2\right]$$

where η is the temperature recovery factor, assumed as 1.0 throughout the study. This expression is the adiabatic wall temperature and neglects the heat sink effect of the decelerator wall. Nylon and Nomex, the two fabrics investigated, have maximum temperature limitations of 1260 and 1760°R, respectively, for short time drogue parachute heating. Based on these temperature limitations, Figures 31 and 32 present the maximum possible deployment Mach numbers for all the model atmospheres and a range of deployment altitudes. Figure 33 shows the fabric temperature limited Mach numbers for Nylon and Nomex materials in model 3 atmosphere. These curves present the bounds on M/C_DA due to temperature limitations. The lowest limited Mach numbers (due to fabric temperatures) occur at sea level and are 3.5 and 2.75 for Nomex and Nylon, respectively. To avoid further complications, these conservative values are used as limits at all deployment altitudes.

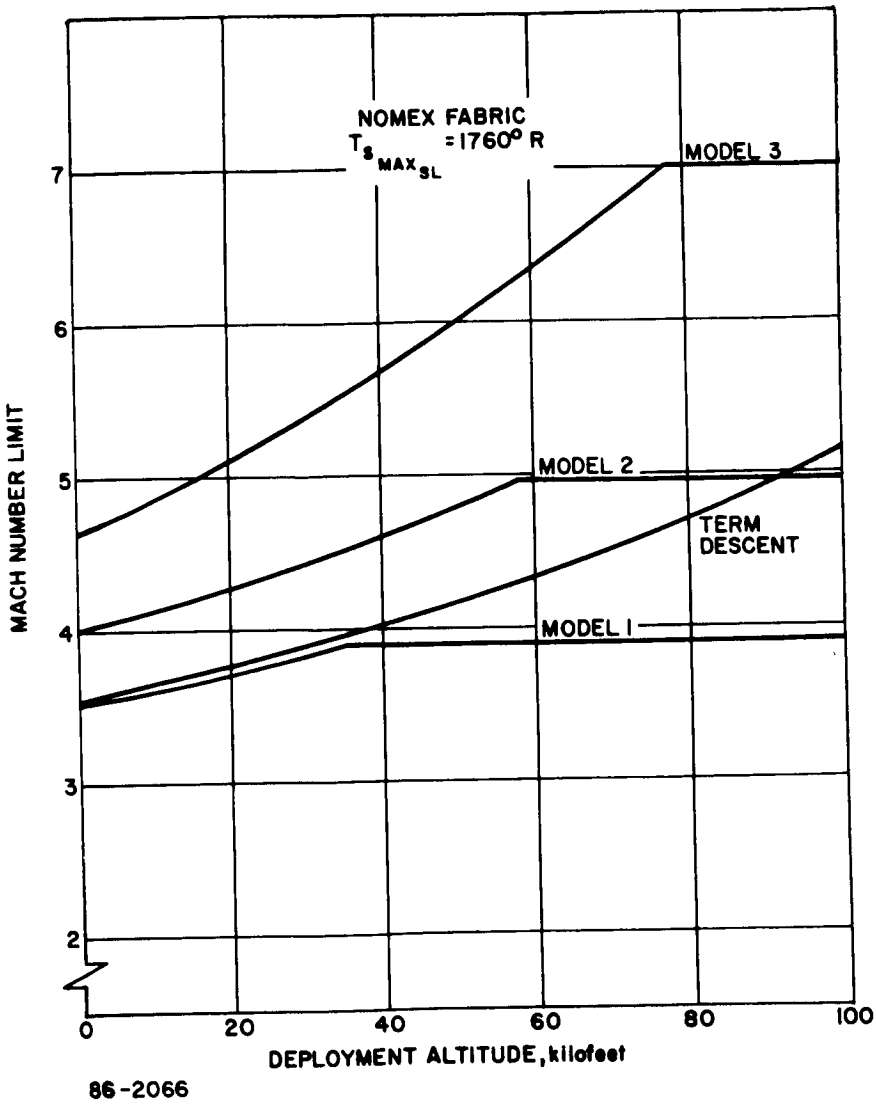

Figure 31 FABRIC MACH NO. LIMIT VERSUS ALTITUDE (NOMEX FABRIC)

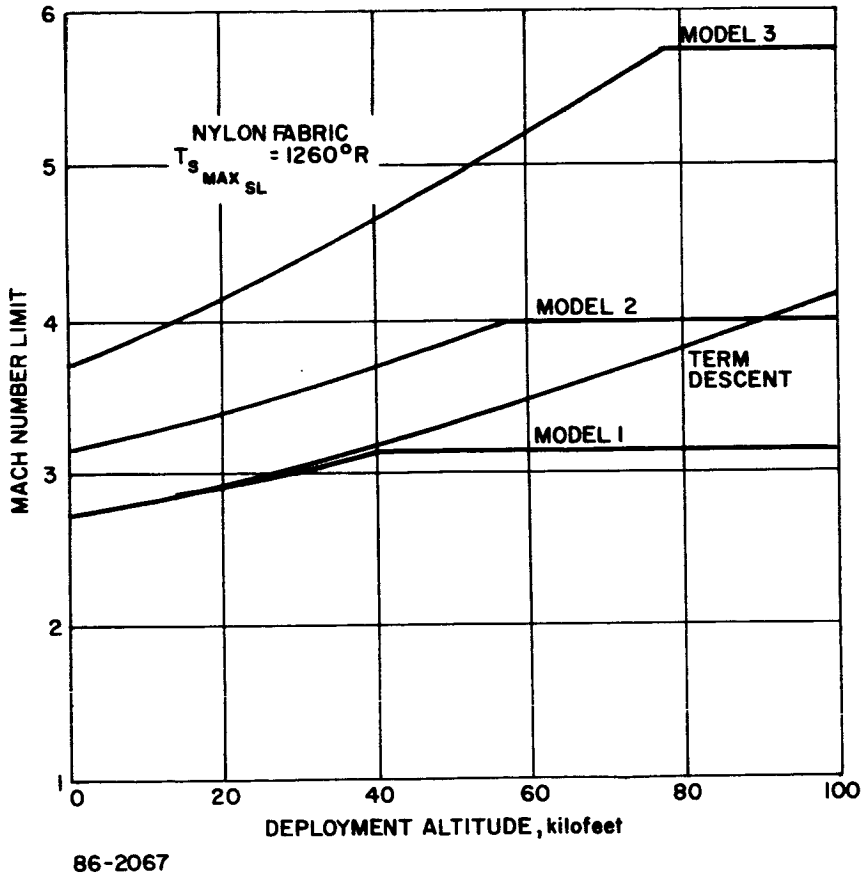

Figure 32 FABRIC MACH NO. LIMIT VERSUS ALTITUDE (NYLON FABRIC)

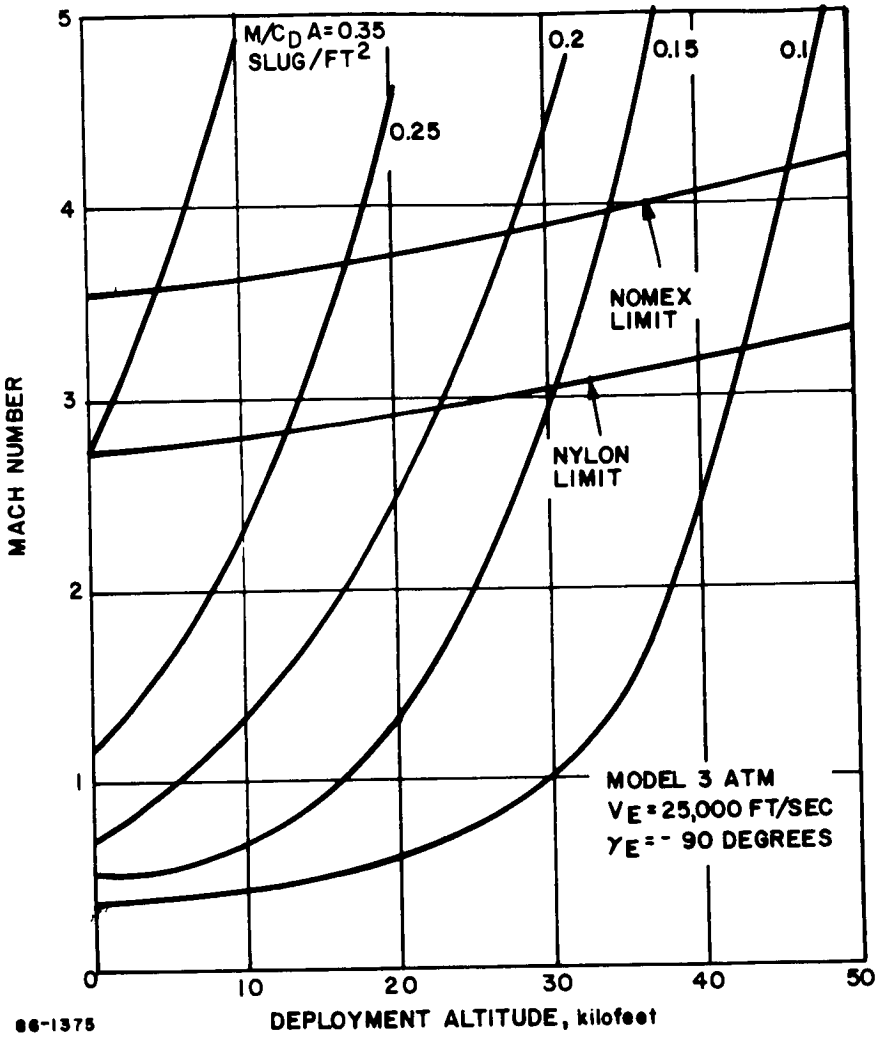

Figure 33 FABRIC TEMPERATURE LIMITED MACH NO. VERSUS ALTITUDE

2.4.3.2 Trajectory Data

Figures 34 and 35 present particle trajectory data of ballistic coefficients versus deployment altitude utilizing Nomex and Nylon fabrics, respectively. The limited Mach number values at sea level were used as the deployment criteria, namely 3.5 for Nomex and 2.75 for Nylon. The results are for deployment in the model 3 atmosphere and are shown for a range of entry angles. Note that all of the trajectory data is based on particle trajectories. Figure 36 shows the deployment dynamic pressure versus altitude for particle trajectory into each of the model atmospheres. These results are for the limit Nomex deployment Mach number (3.5) and limit Nylon deployment Mach number (2.75).

2.4.3.3 Optimization Results

The use of a two parachute (drogue-main) descent system allows one of two alternatives, namely, 1) increase the M/C_DA, or 2) increase the main parachute deployment altitude by maintaining the same M/C_DA as utilized in the single parachute system design.

It is of primary interest to increase the landed payload. Hence, an attempt was made to optimize the ballistic coefficient and/or suspended weight. For a given set of entry conditions and a range of M/C_DA's, the suspended weight can be maximized. The optimizing parameter is the drogue parachute weight.

As the ballistic coefficient increases, it becomes increasingly more difficult to achieve Mach 0.8 (main parachute deployment) at the given main parachute deployment altitude. In order to decelerate to Mach 0.8 at the given deployment altitude (for increased M/C_DA's) the drogue parachute diameter must increase. Finally, an M/C_DA is reached such that the drogue weight becomes greater than the increased entry weight; hence, the suspended weight starts to decrease and an optimum design point is reached.

Figures 37 and 38 demonstrate the required drogue area/vehicle area ratio such that for a given M/C_DA the vehicle will decelerate to Mach 0.8 at a given altitude in the model 3 atmosphere. The curves reflect results for Nomex and Nylon fabrics (i.e., Mach limit of 3.5 and 2.75, respectively). The trajectory curves utilize an effective drag coefficient such that,

$$(C_D)_{eff} = \frac{(C_DA)_V + (C_DA)_D}{A_V}$$

where the subscripts D and V refer to drogue and vehicle, respectively. The drag coefficient of the hyperflo parachute and the ring-sail main

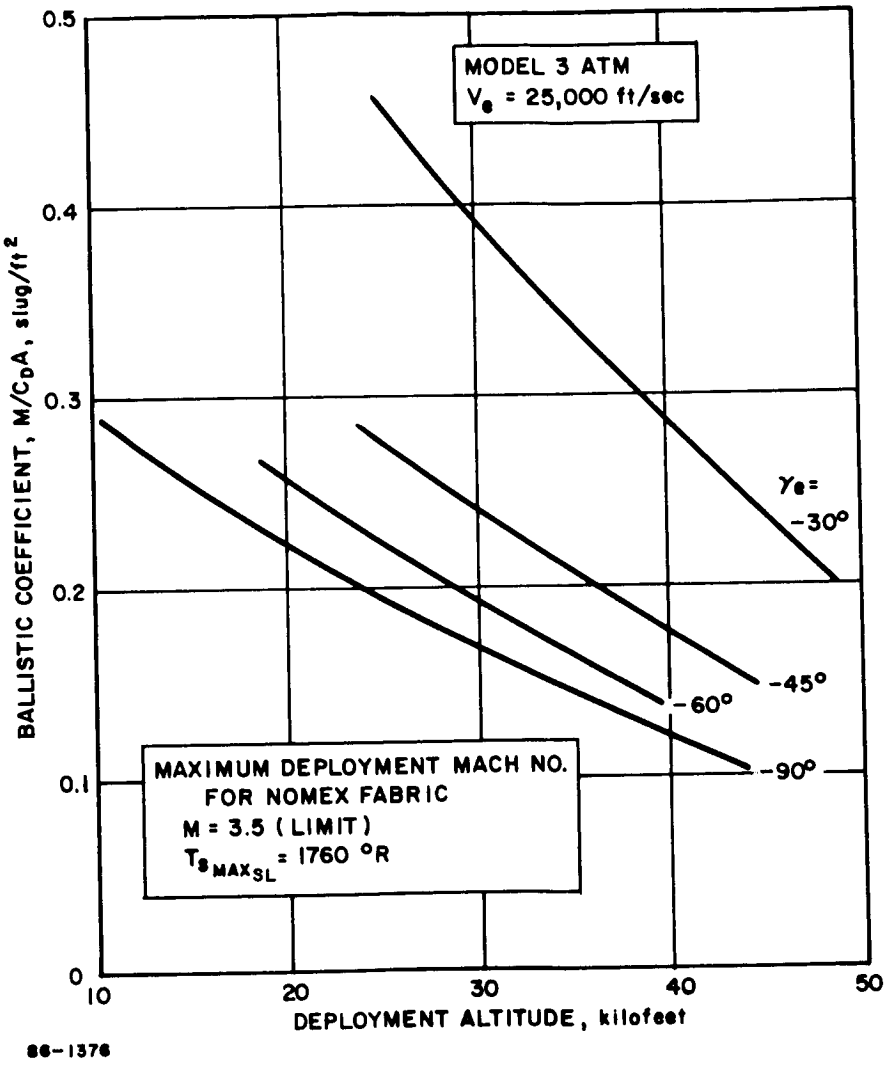

Figure 34 M/C_DA VERSUS DEPLOYMENT ALTITUDE (MACH 3.5 DEPLOYMENT)

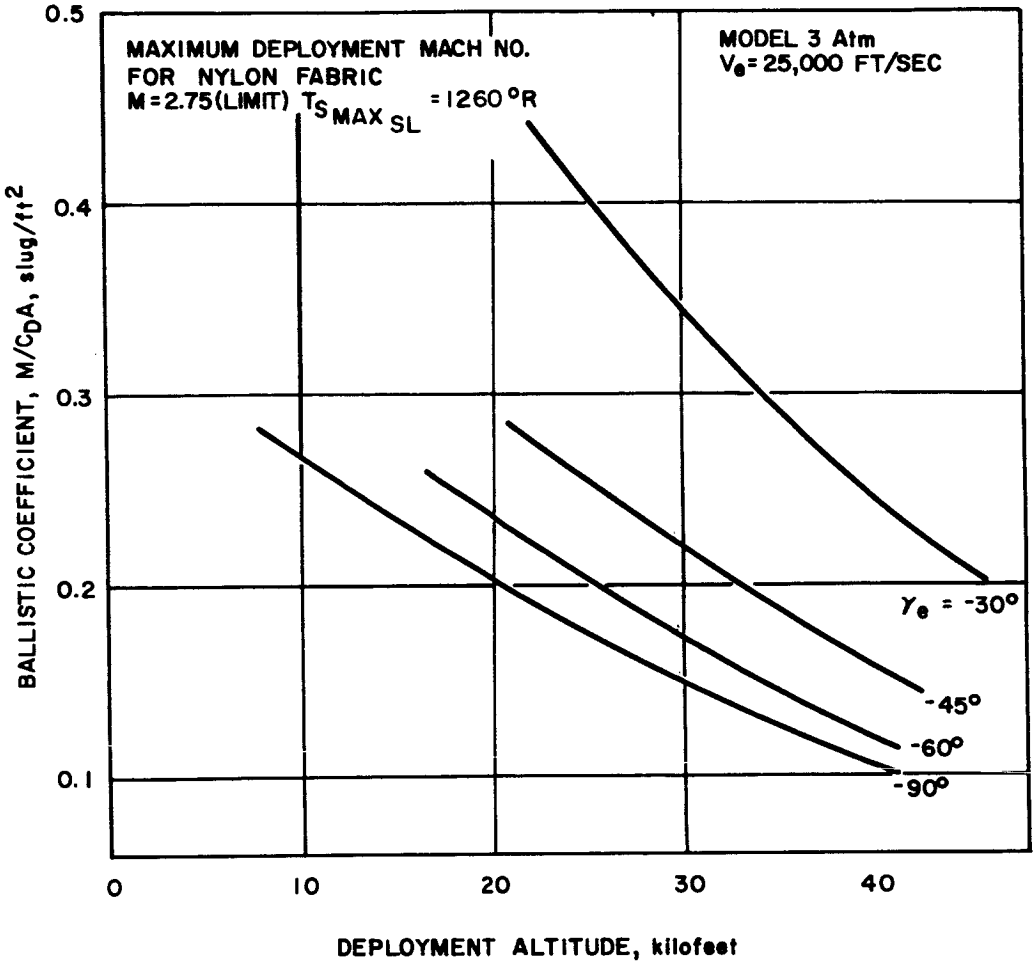

86-1377

Figure 35 M/C_DA VERSUS DEPLOYMENT ALTITUDE (MACH 2.75 DEPLOYMENT)

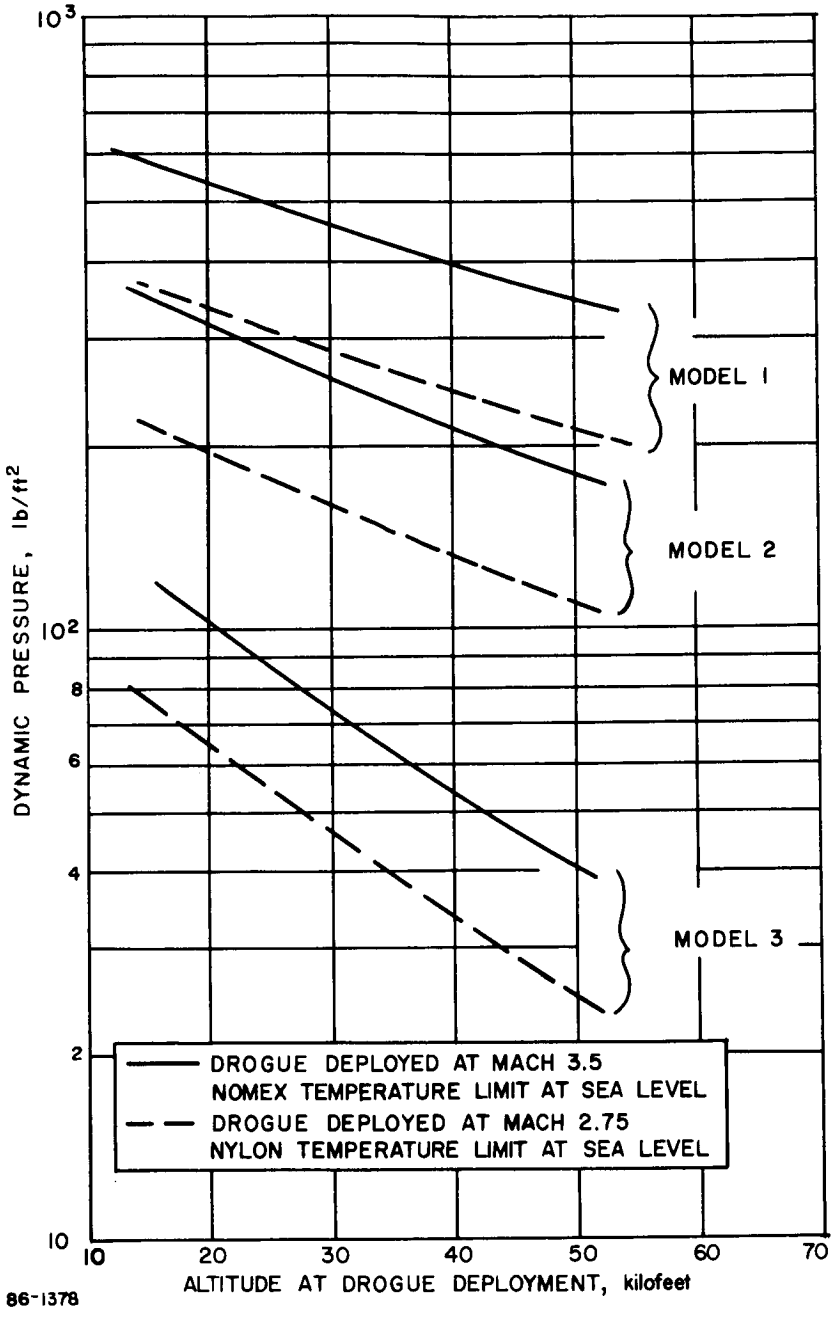

Figure 36 DYNAMIC PRESSURE VERSUS DEPLOYMENT ALTITUDE

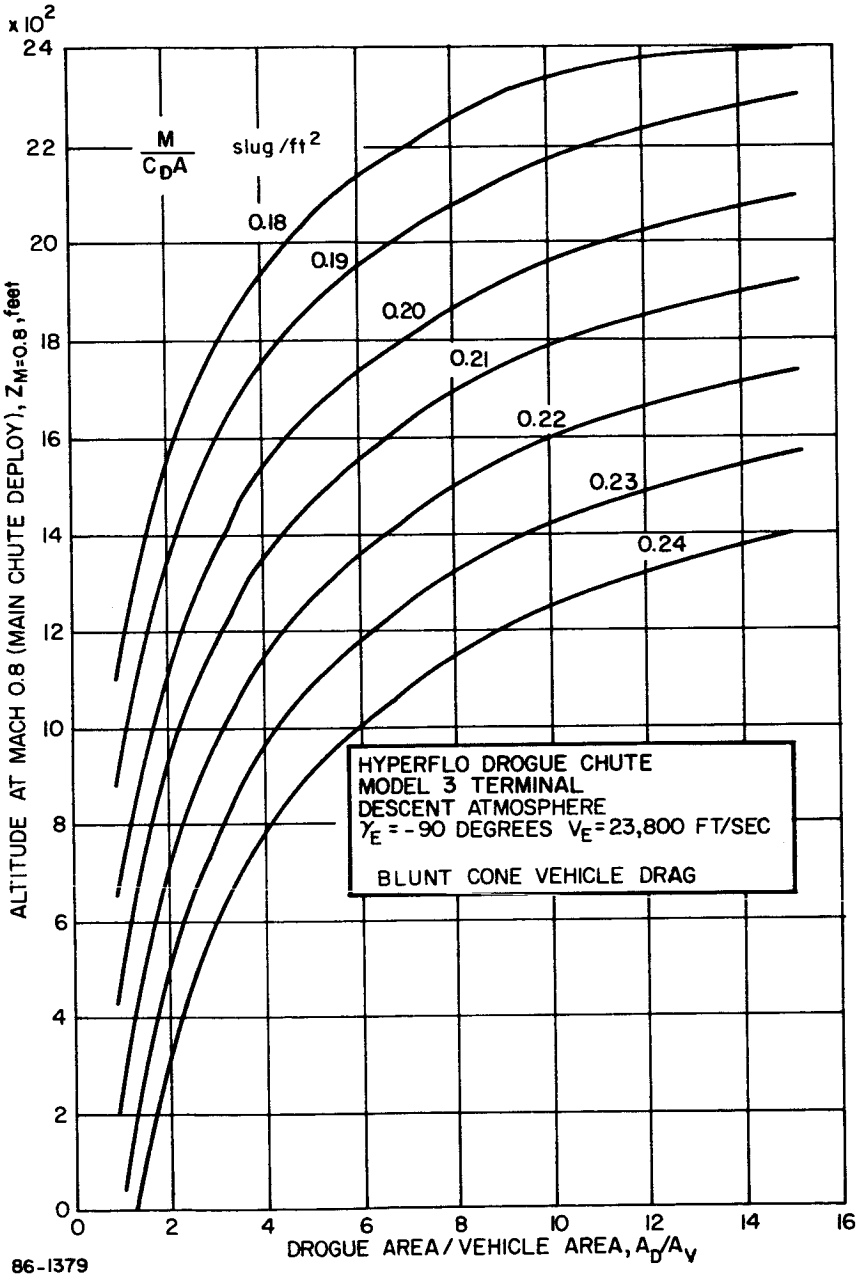

Figure 37 ALTITUDE AT MAIN PARACHUTE DEPLOYMENT VERSUS A_D/A_V (DROGUE DEPLOYMENT AT MACH 3.5 IN THE MODEL 3 ATMOSPHERE)

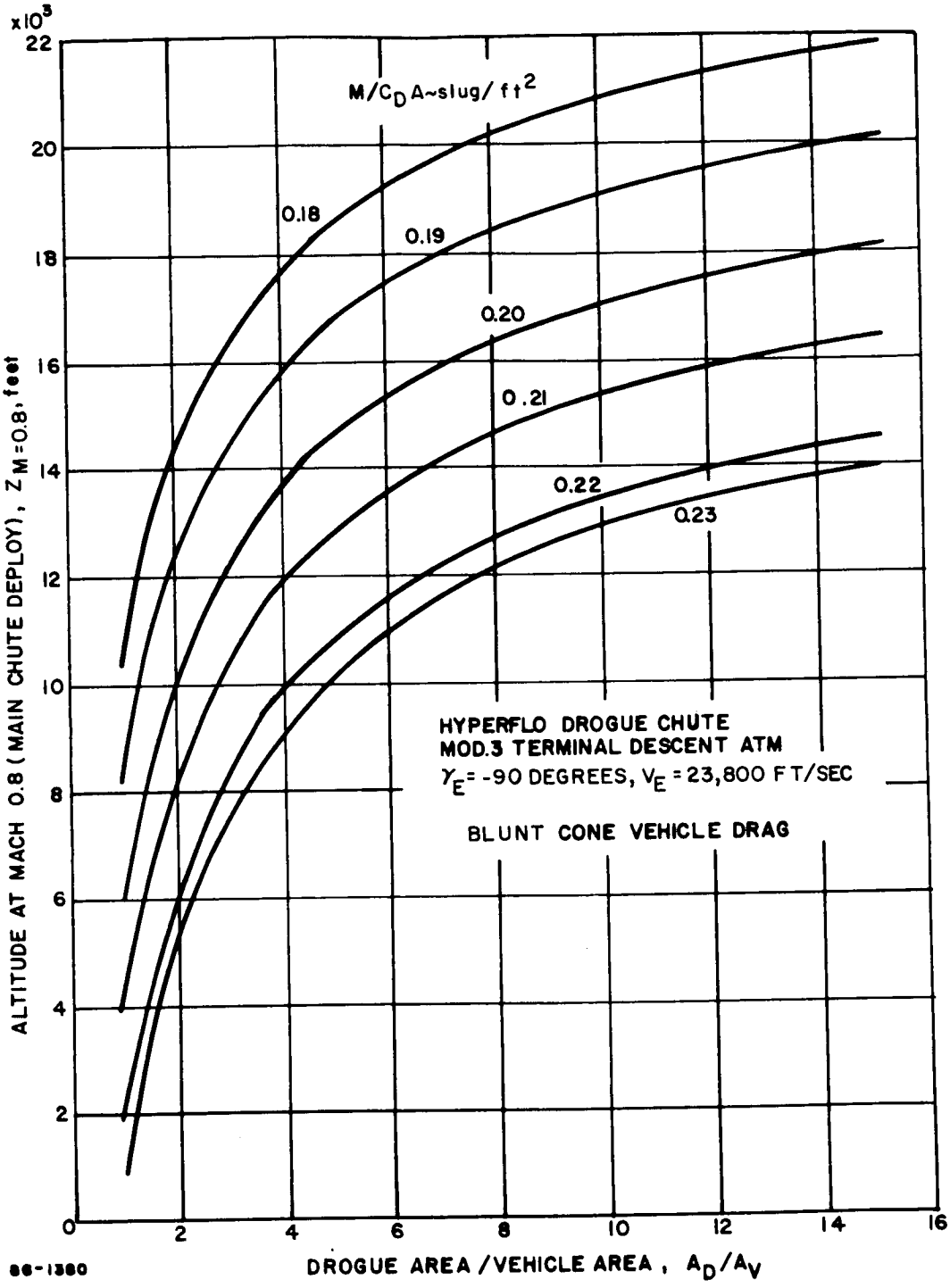

Figure 38 ALTITUDE AT MAIN PARACHUTE DEPLOYMENT VERSUS A_D/A_V (DROGUE DEPLOYMENT AT MACH 2.75 IN THE MODEL 3 ATMOSPHERE)

parachute are shown on Figure 39 (data obtained from Reference 5). The drag coefficient of the vehicle is that of the blunt cone. Note that results reflect particle trajectory data.

Figure 40 presents the optimization results of entry weight, minus drogue weight (optimizing parameter) as a function of M/C_DA for deployment at Mach 0.8 and 16,000 feet. An optimum M/C_DA of 0.195 is feasible utilizing Nomex fabric and 0.190 for Nylon fabric. However, since the available Nylon canopy fabric is lighter than presently available Nomex fabric, a greater suspended weight is obtained for Nylon.

Figure 41 indicates the required drogue diameter/vehicle diameter ratio for a range of M/C_DA's. Note that at the optimum M/C_DA, this ratio is approximately 2.0, which is presently considered the best operating range. A similar curve is presented in Figure 42, indicating the required drogue parachute diameters for a 197-inch diameter entry vehicle. For the optimum M/C_DA, the drogue parachute diameters range from 30 to 35 feet.

Similar drogue parachute optimization results for the model 2 atmosphere (25 mb) are shown on Figures 43 through 46 indicating that an optimum M/C_DA of approximately 0.60 slugs/ft^2 is possible. Note that the drogue-vehicle diameter ratio is around 2.0 as was previously experienced for the model 3 results shown on Figure 41.

2.4.3.4 Weight Analysis

To establish a parameteric weight model for tradeoff studies, a relation involving materials weight, opening dynamic pressure, and parachute diameter is required. From curve fits of Northrop Ventura, Cook Electric and in-house data, the following equation was evolved:

$$W_D = Kq D^3 \quad \text{(see References 5 and 6)}$$

where,

W_D = the drogue system weight, pounds

K = materials factor

5.1×10^{-5} for Nylon

7.2×10^{-5} for Nomex

q = opening dynamic pressure, lb/ft^2

D = drogue diameter, feet

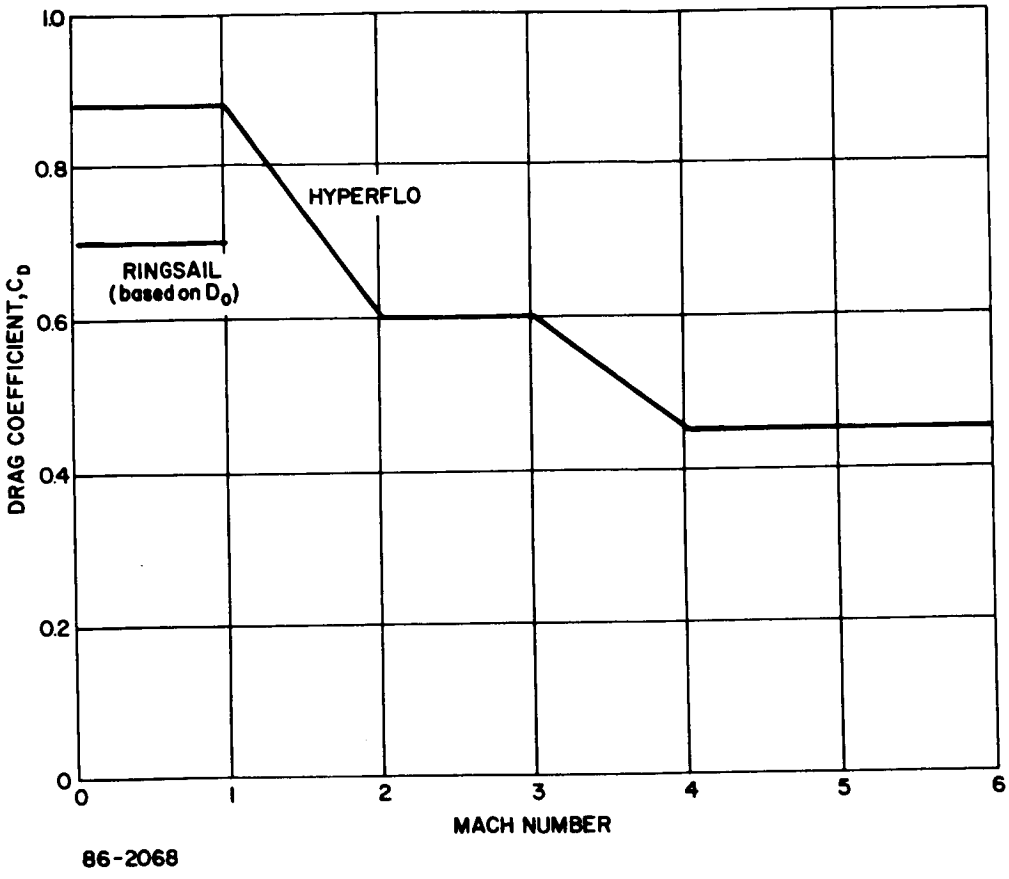

Figure 39 HYPERFLO AND RING-SAIL DRAG COEFFICIENTS VERSUS MACH NUMBER

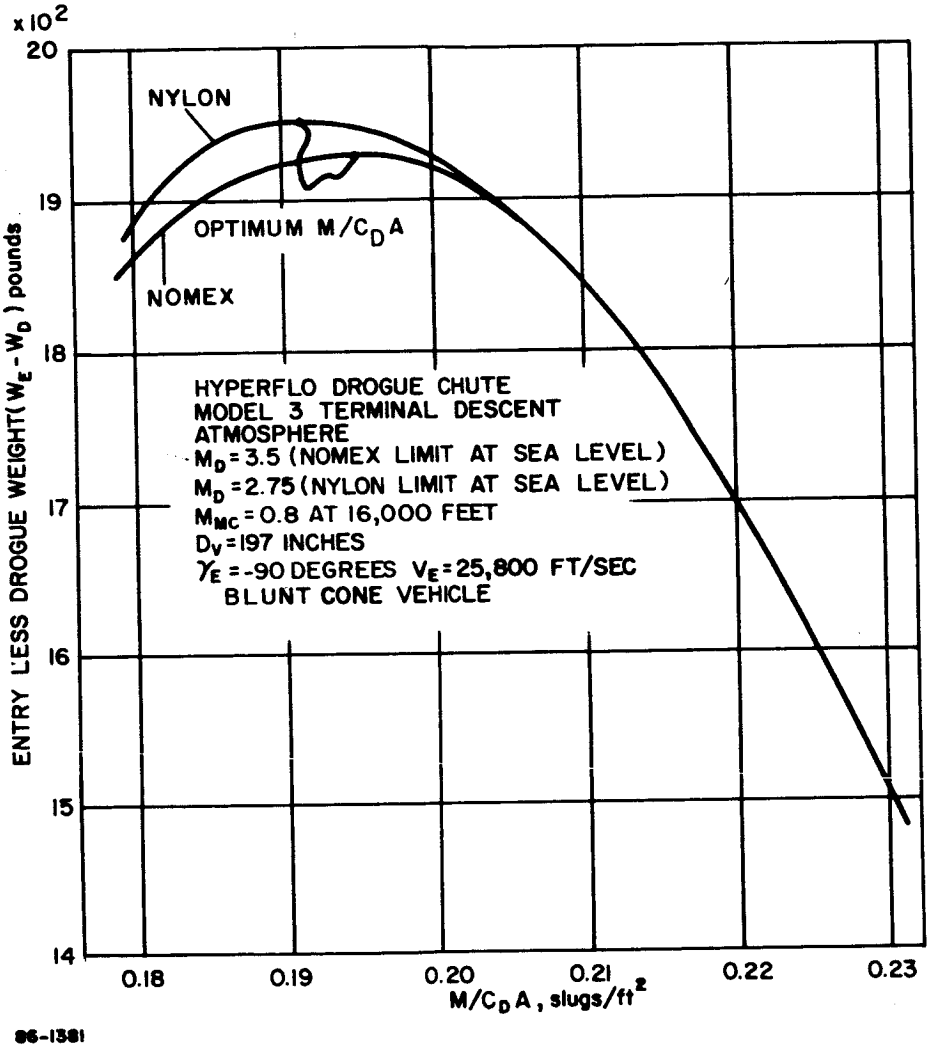

Figure 40 ENTRY WEIGHT LESS DROGUE PARACHUTE WEIGHT VERSUS M/C_DA

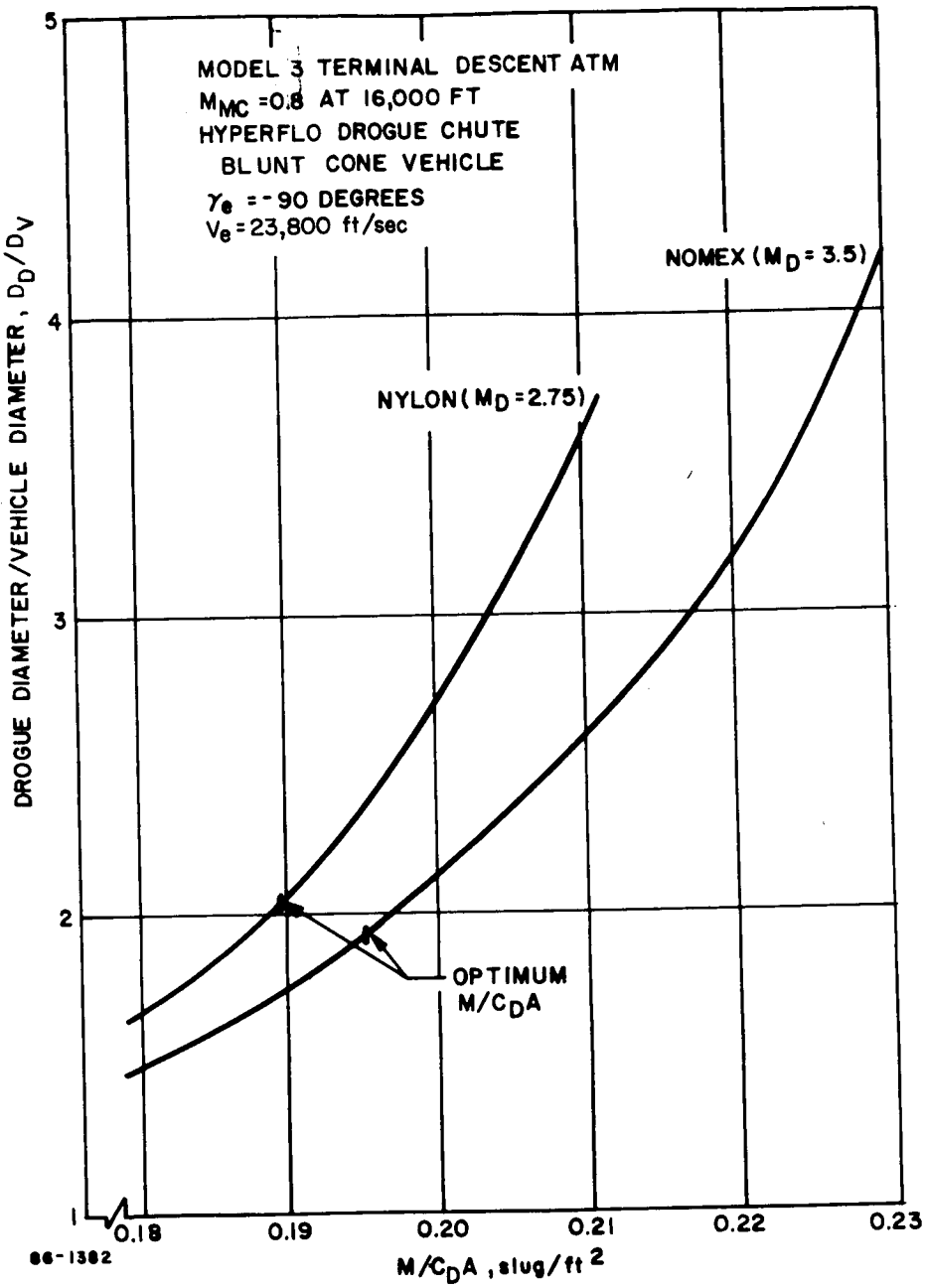

Figure 41 DROGUE DIAMETER/VEHICLE DIAMETER VERSUS M/C_DA

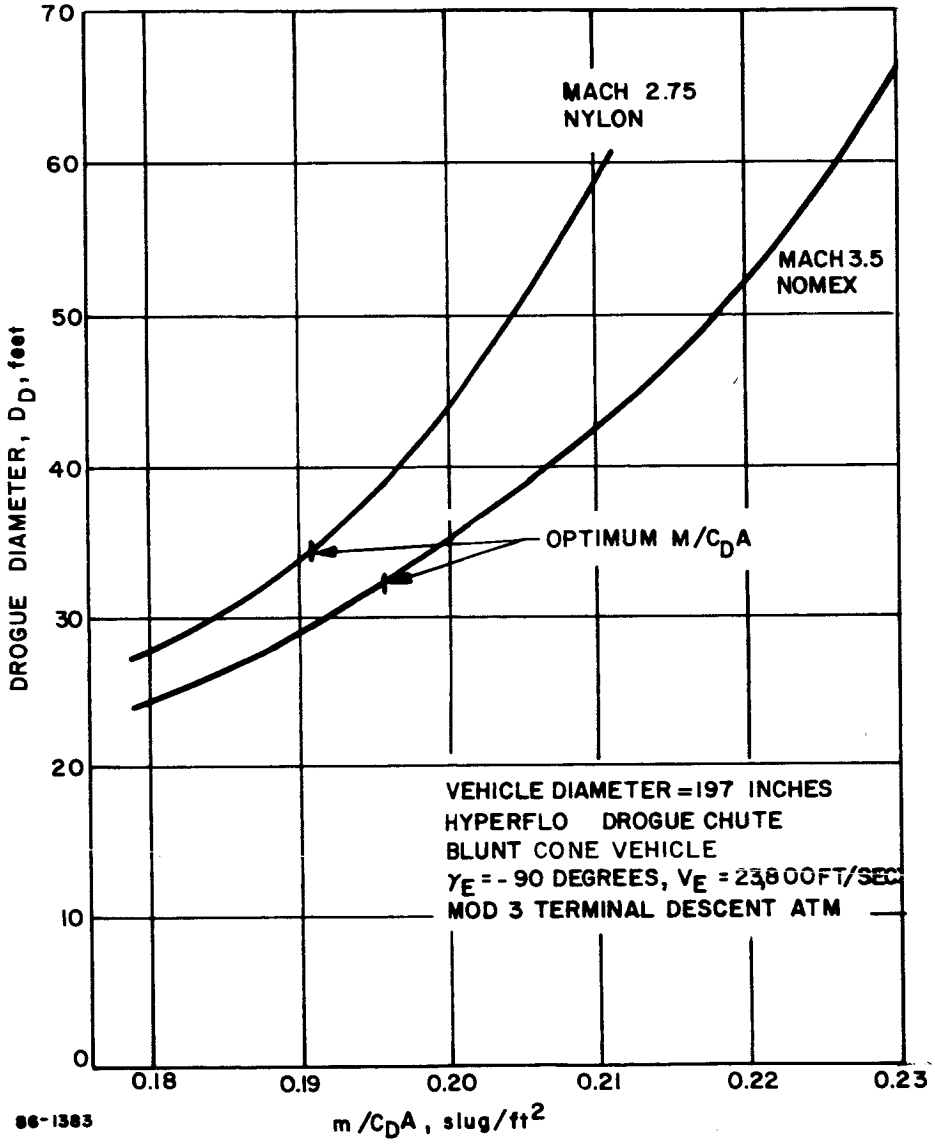

Figure 42 DROGUE DIAMETER VERSUS M/C_DA

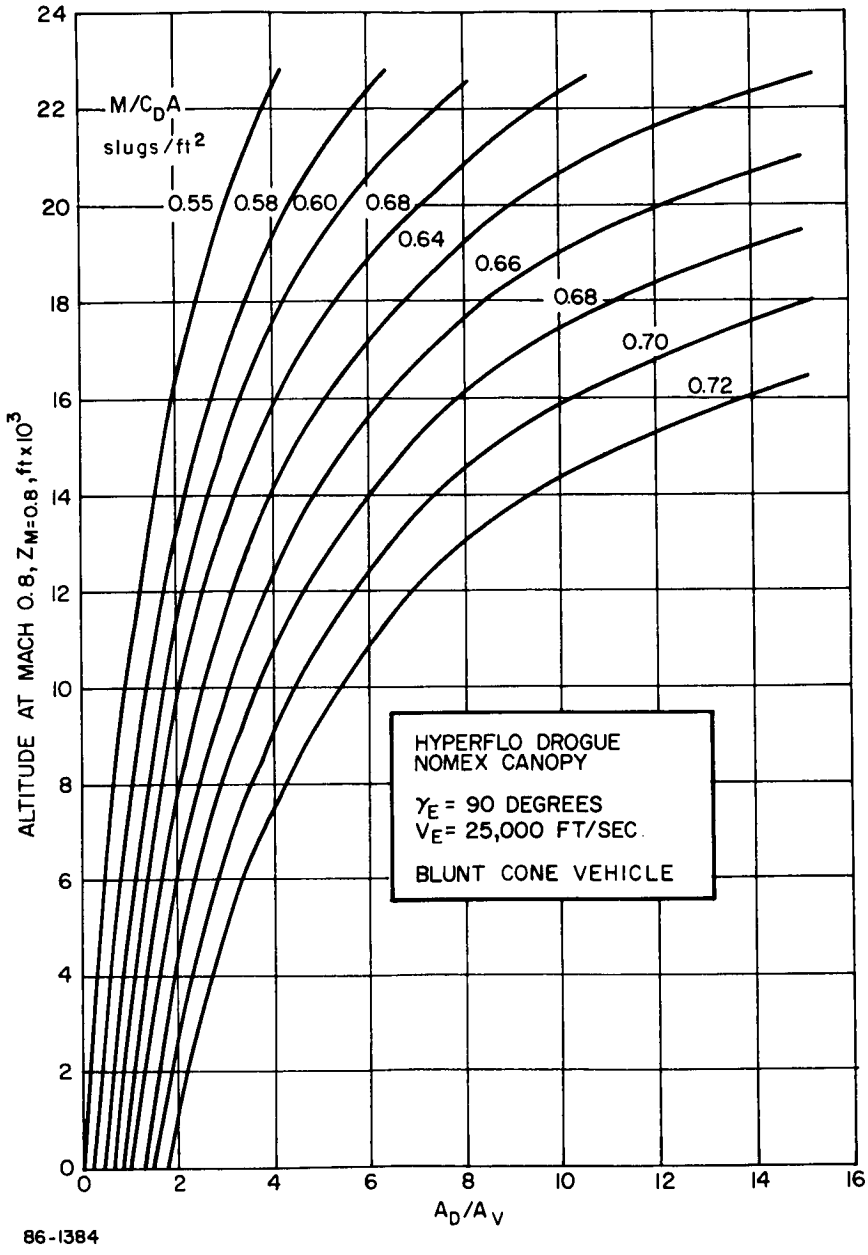

Figure 43 ALTITUDE AT MAIN PARACHUTE DEPLOYMENT VERSUS A_D/A_V (DROGUE DEPLOYMENT AT MACH 3.5 IN THE MODEL 2 ATMOSPHERE)

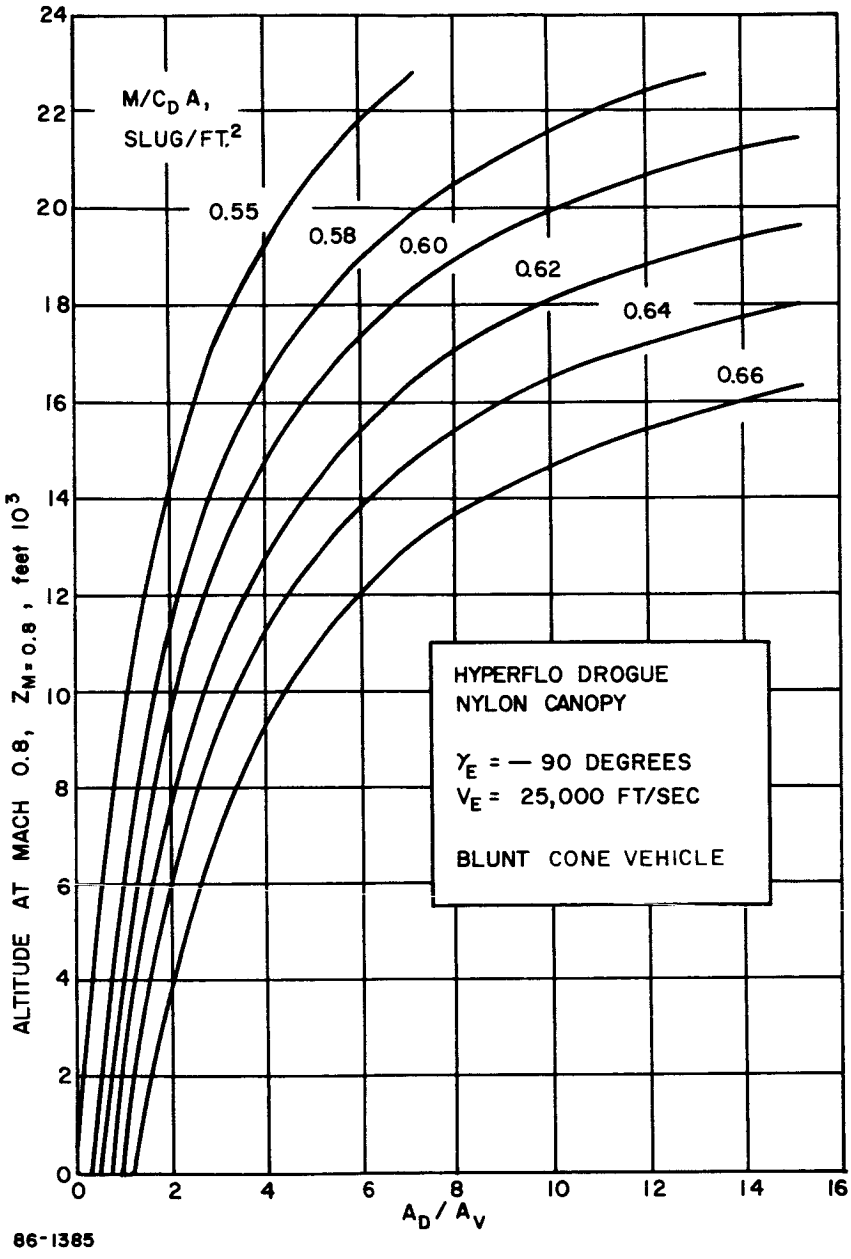

Figure 44 ALTITUDE AT MAIN PARACHUTE DEPLOYMENT VERSUS A_D/A_V (DROGUE DEPLOYMENT AT MACH 2.75 IN THE MODEL 2 ATMOSPHERE)

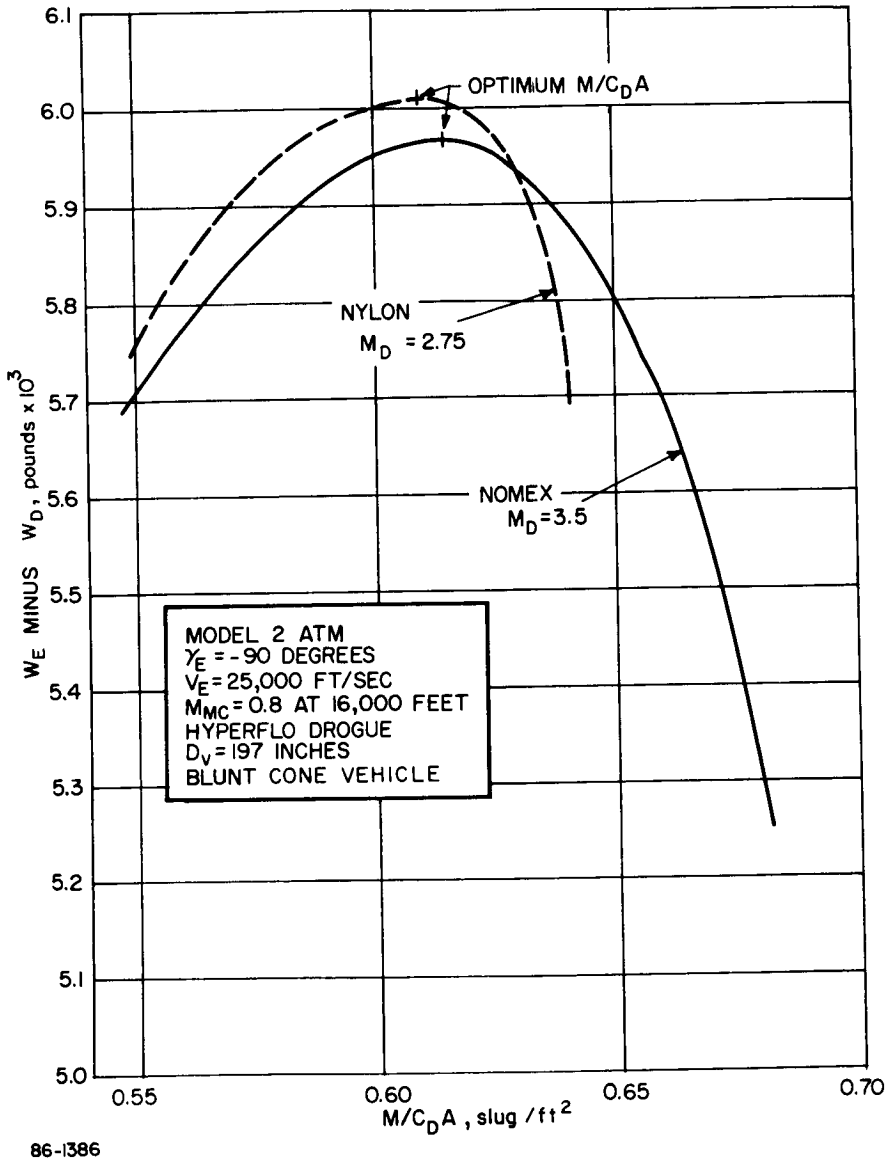

Figure 45 ENTRY WEIGHT LESS DROGUE WEIGHT VERSUS M/C_DA

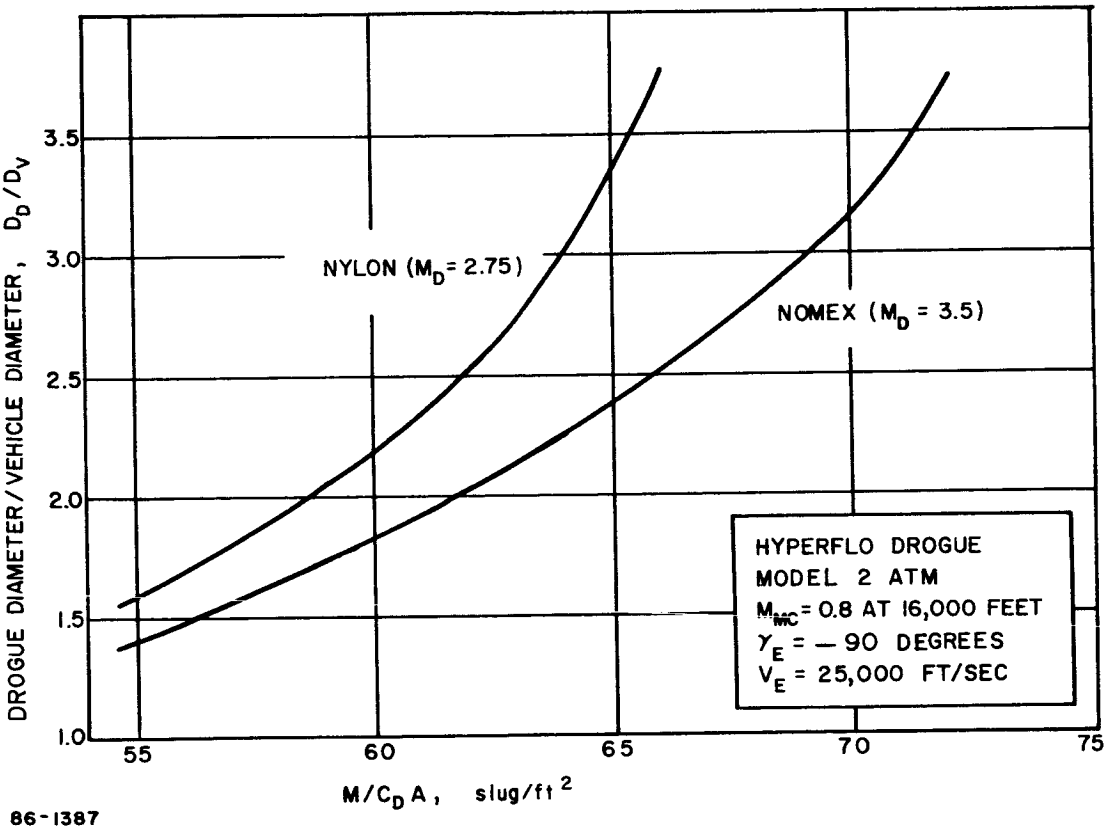

Figure 46 DROGUE DIAMETER/VEHICLE DIAMETER VERSUS M/C_DA

2.4.4 Selected Design

The selected reference design employs a reefed single parachute system. Based on a vertical sea-level descent velocity of 80 ft/sec (study ground rule), Figure 18 indicates that the required A_{mc}/W_{susp} ratio is approximately 6.1 ft^2/lb (Earth pounds) in the terminal descent atmosphere.

The reference design has a suspended capsule weight of 924 pounds. Based on this weight, Figure 19 indicates that a 85-foot nominal diameter ringsail chute is required. Trajectory results for the reference M/C_DA (0.15 slugs/ft^2) indicate that for deployment of the main parachute at Mach 1.3, the maximum opening dynamic pressure is approximately 10 lb/ft^2. For the reference 85 foot nominal diameter parachute and an opening dynamic pressure of 10 lb/ft^2, Figure 30 indicates a canopy and shroud line weight of 70 pounds. However, reefing the main parachute (18 percent of projected area) equalizes opening shock loads, lowers the extremely high descent times in the model 1 and 2 atmospheres and reduces the canopy and suspension line weight by 20 percent to 56 pounds. Finally, including the riser line, harness assembly, pilot parachute and deployment canisters, etc., the final total system weight is 74 pounds.

It is of prime importance to maintain parachute descent time within a reasonable minimum and maximum range in order to provide adequate communications time and also to ensure a relay link with the flight spacecraft. Figure 28 plots descent time versus A_{mc}/W_{susp} for parachute full open (disreef) at 16,000 feet. For the 4 atmospheres under consideration and the design A_{mc}/W_{susp} of 6.1 ft^2/lb, the descent time is bounded by a minimum of 175 seconds and a maximum of 332 seconds. This range of descent time combined with other considerations is within the overall system operational requirements.

2.4.5 Actuation System

The selection of a sensing system for parachute actuation presents a difficult problem due to the uncertainty of entry conditions and the range of atmospheric models to be considered. The sensing system must be capable of deploying the parachute at an accepted altitude for a worst combination of entry angle, entry velocity, and model atmosphere. The actuation system must also be such that it assures that the aerodynamic heating and loading remain within the design limits of the canopy fabric.

2.4.5.1 Selected Approach

The system selected utilizes 3-axial accelerometers which sense peak g and a timer which correlates peak g with the time from peak g to the

main parachute deployment Mach number of 1.3. The product $G_{MAX}\Delta t$ is a constant from peak g to a given velocity independent of entry velocity, entry angle, and atmosphere. The analysis assumes constant vehicle M/C_DA, a straight line trajectory, and an isothermal atmosphere. Mach number is the parameter of interest and not velocity, hence, a correction is needed for the speed of sound. Presented in Figure 47 is a theoretically derived curve of time from peak g to Mach 1.3 as a function of peak g (max deceleration). Shown also are actual trajectory points for the upper and lower bounds of entry angle and atmosphere combinations. A curve fit of these trajectory points is shown and based on this curve fit, which relates peak g and Δt, it is possible to evaluate the actual reefed main parachute deployment Mach numbers, altitudes, etc. Table III summarizes the predicted parachute deployment Mach numbers and altitudes for several combinations of entry angle, entry velocity, and atmosphere based on the selected actuation system.

The reefed chute actuation is such that with the use of a jerk meter and accelerometers, peak g through entry is determined. This value of peak g is correlated with a table of time intervals which have been established from trajectory data curve fits shown on Figure 47. Hence, a preset table of peak g versus Δt can be placed within the vehicle in the form of an analog computer. The timer starts its Δt excursion at peak g and at the end of the prescribed interval, reefed parachute deployment takes place. At 16,000 feet the onboard radar altimeter initiates disreefing so as to ensure parachute full open at 15,000 feet. A schematic of the sensing system is shown on Figure 48. If reefed parachute deployment does not take place by 18,500 feet minimum altitude, then the radar altimeter is used as a backup for reefed deployment.

2.4.5.2 Initiation Devices

Initiation of main parachute deployment is dependent on the sensing of peak g via onboard accelerometers. A timer, an analog circuit, and a radar altimeter are the other operational devices required for parachute initiation. Comparisons of various other initiation concepts, which were investigated, are detailed in Reference 4.

2.4.5.3 Error Analysis

The error analysis shown on Table III indicates that the selected activation system yields deployment conditions which are within parachute design limits and also within study constraints. Table III summarizes the predicted parachute deployment Mach numbers and altitudes and indicates that reefed parachute deployment occurs between Mach 0.97

TABLE III

REEFED MAIN PARACHUTE ACTUATION PERFORMANCE

(V_e = 23,800 Ft/Sec M/C_DA = 0.15 slug/ft^2)

Atmosphere Model	γ_e (degrees)	Time to G_{pk} (seconds)	Δt to dep. (seconds)	Altitude dep. (feet)	Mach dep.
3	-40	49.13	21.67	36630	1.30
	-50	40.67	19.53	29500	1.20
	-65	34.14	17.70	22400	1.13
	-90	30.82	16.77	18960	1.11
2	-40	43.17	32.00	98000	1.30
	-50	36.20	28.85	89700	1.13
	-65	30.60	26.30	77000	1.00
	-90	27.82	24.88	72000	0.97

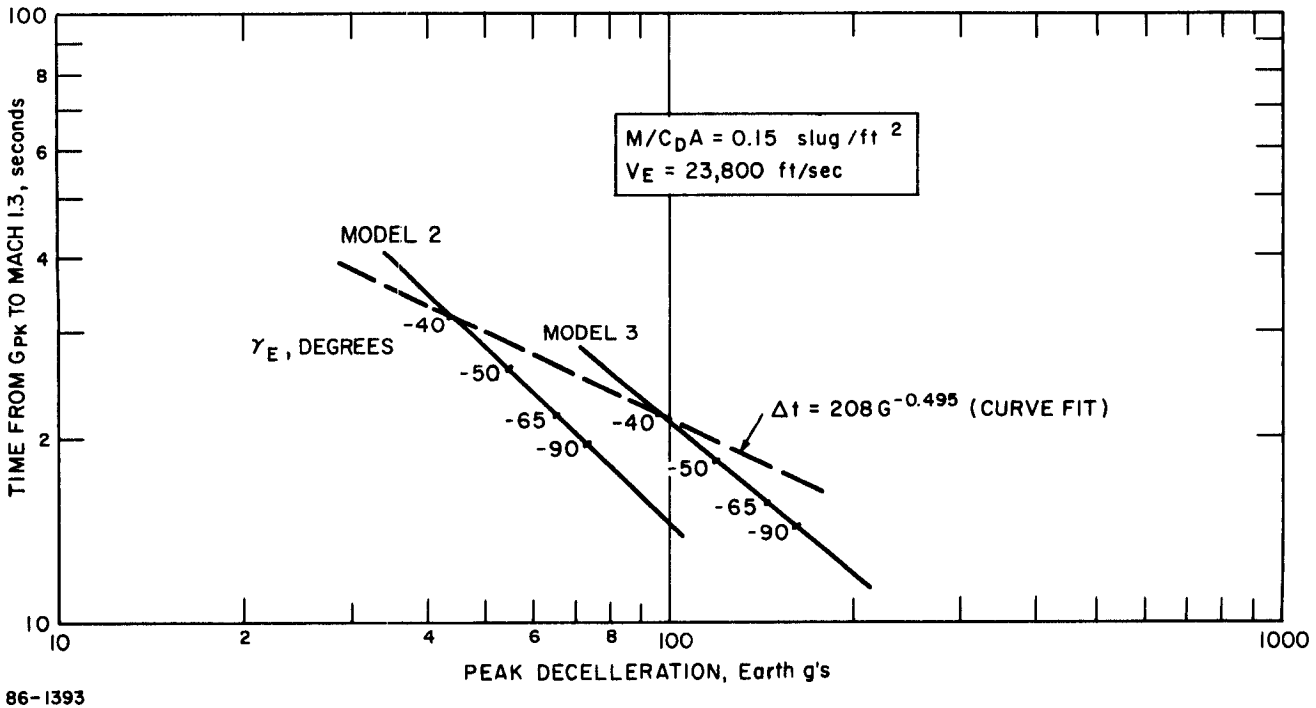

Figure 47 TIME FROM PEAK ACCELERATION TO MACH 1.3 VERSUS PEAK-g

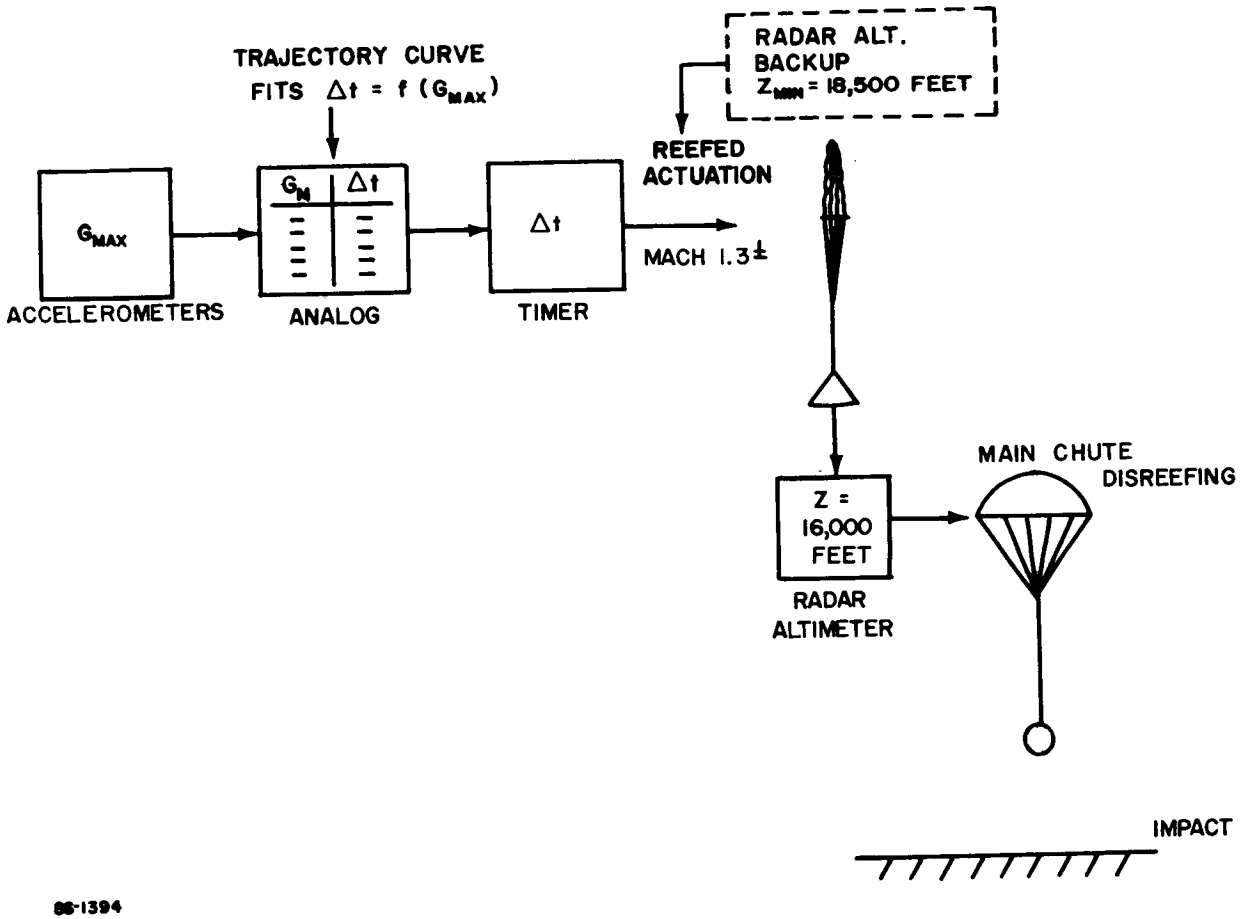

Figure 48 SENSING SYSTEM SCHEMATIC

and 1.30 with a minimum deployment altitude of 18, 960 feet or approximately 3, 000 feet above radar altimeter disreefing. Figure 46 and Table III present data for only one entry velocity.

Paragraph 2.5.3 of this book presents a summary curve utilizing this type of initiation system where entry velocity is expressed as part of the curve-fit equation.

2.4.6 Dynamic Analysis

A two-dimensional, three-degree-of-freedom, dynamics-analysis computer program developed by Northrop Corporation Ventura Division was utilized to determine the dynamic response of the parachute descent system (see Reference 7). The major emphasis was placed on determining the effect of a 50 ft/sec wind gust impinging on the descending main parachute system for a 10-second duration.

2.4.6.1 Calculation Model

The calculation model which has three degrees of freedom, includes two translational modes and one rotational mode. The two translational modes are with respect to the velocity vector, one being along the vector and the other at right angles to it. The rotational mode is about the center of gravity of the system. The equations of motion are written for both the capsule (suspended weight) and the parachute. Input parameters considered in the analysis include:

1. capsule mass, moment of inertia, and static and aerodynamic characteristics
2. elasticity of risers and suspension lines (spring constants)
3. riser line tension
4. parachute mass
5. inertia of the accelerated parachute air mass
6. parachute static and dynamic aerodynamic characteristics
7. capsule and chute dimensions and center of gravity positions
8. atmospheric environment
9. vertical and horizontal velocity components

A sketch of the parachute/capsule geometry and nomenclature are shown on Figure 49.

2.4.6.2 Wind Gust Environmental Effects

Vertical equilibrium descent conditions at an altitude of 5000 feet in the terminal descent model atmosphere were utilized to initiate the main parachute wind-dynamics analysis. An Apollo* payload (suspended weight) and a ring-sail main parachute were used in the analysis. The input parameters utilized in the analysis are listed below. The magnitude of most of the inputs are representative of a typical detailed conceptual design.

Capsule mass	M_c	31.1	slugs
Capsule c.g. location	Z_{cg}	2.80	feet
	X_{cg}	0.0	
Capsule moment of inertia	I_{cgy}	336.	slugs -ft^2
Capsule Diameter	D_c	12.8	feet
Initial flight path angle	γ_c	- 90.0	degrees
Capsule initial vertical velocity	V_v	80.0	ft/sec
Chute nominal diameter	D_o	84.0	feet
Chute projected diameter	D_p	58.2	feet
Chute effective drag area	(C_DS)	4150.	feet^2
Riser line length		8.4	feet
Suspension line length		88.8	feet

Results of the wind-gust dynamics analysis are presented in Figures 50, 51 and 52. The results indicated that, 1) the effects of wind gust

*At the time these results were generated, the Apollo vehicle was the reference shape.

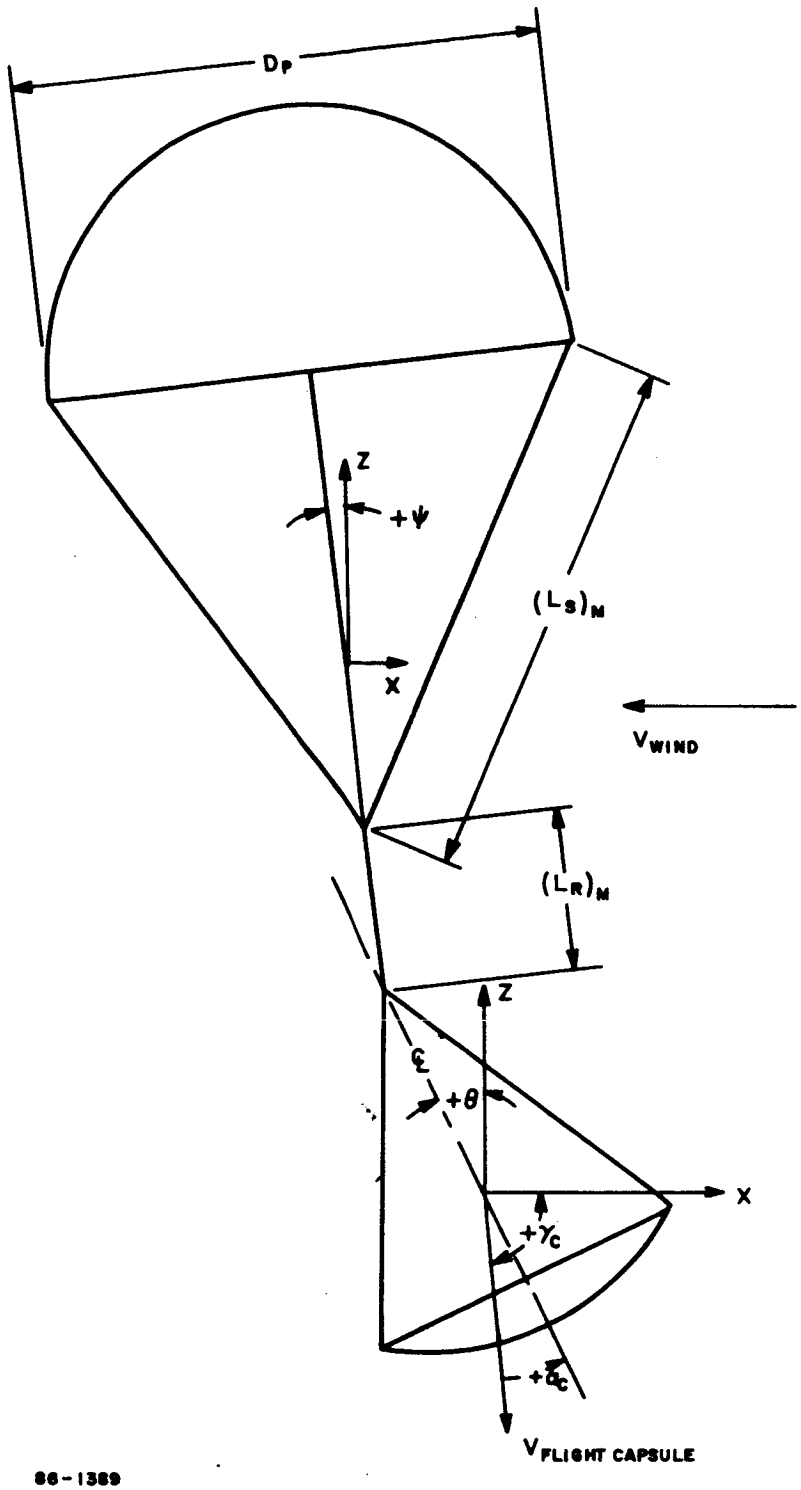

Figure 49 PARACHUTE/CAPSULE DYNAMIC GEOMETRY AND NOMENCLATURE

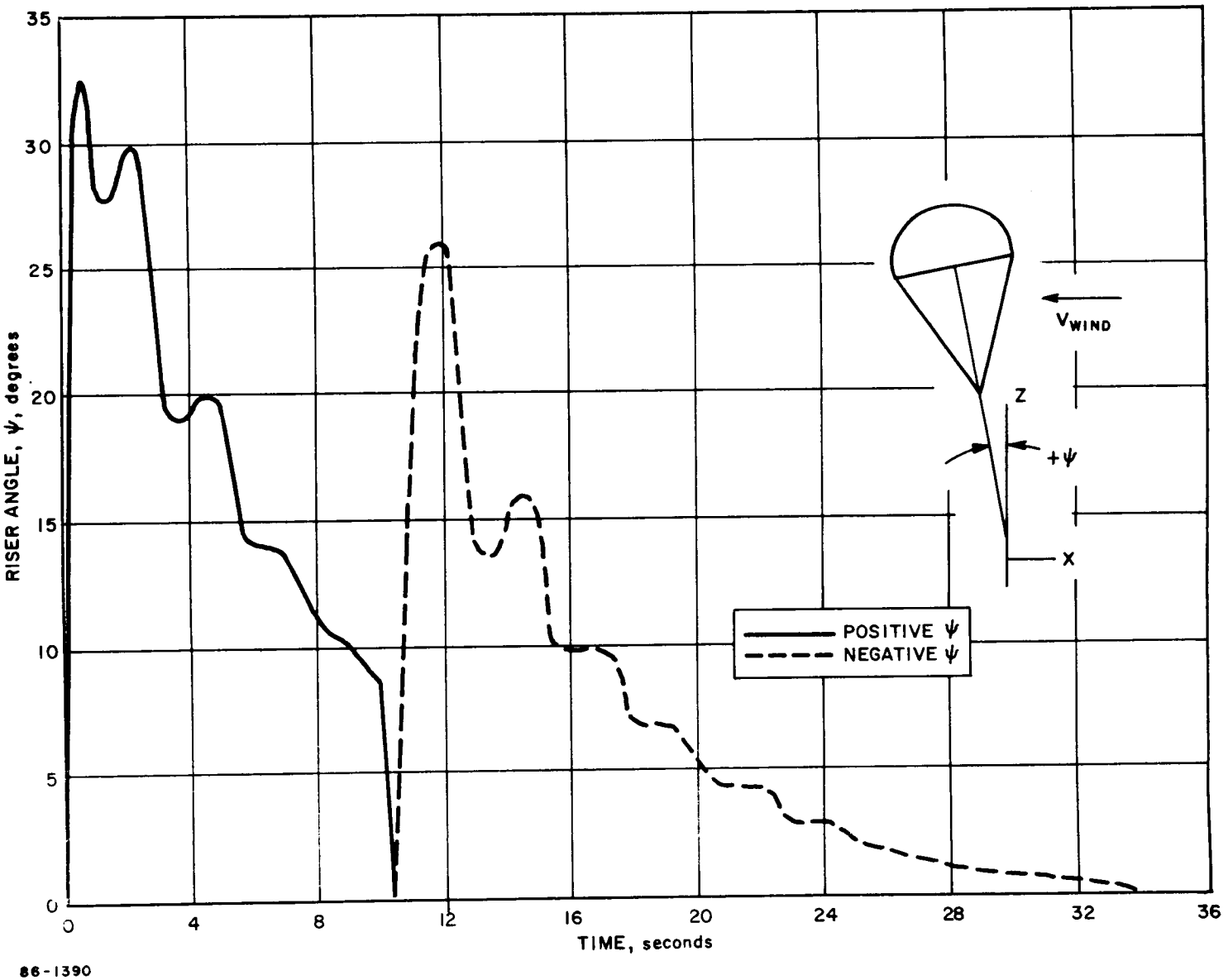

Figure 50 DYNAMIC RESPONSE OF MARS LANDER MAIN PARACHUTE SUBJECTED TO WIND GUSTS OF 50 FT/SEC FOR 10 SECONDS

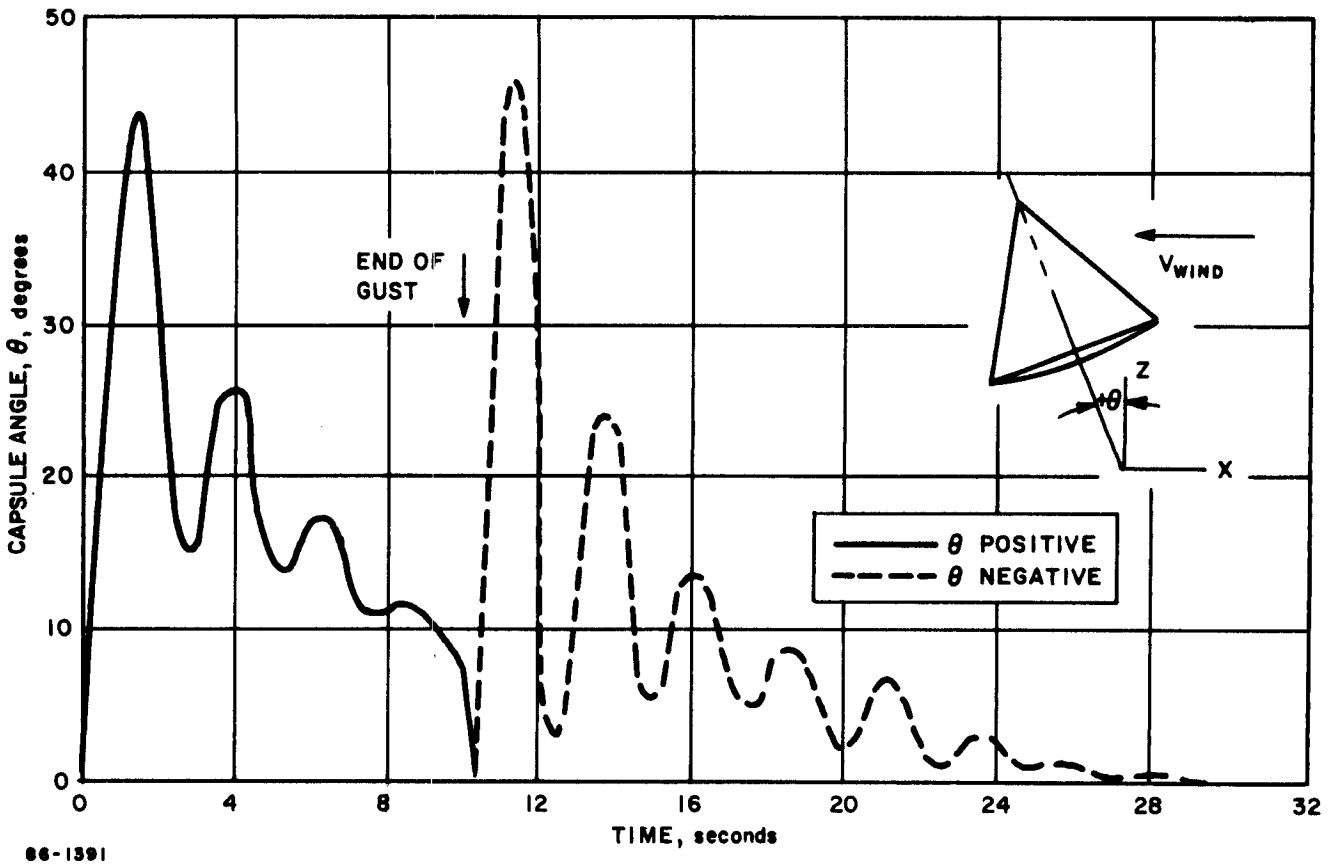

Figure 51 DYNAMIC RESPONSE OF MARS LANDER CAPSULE SUBJECTED TO WIND GUSTS OF 50 FT/SEC FOR 10 SECONDS

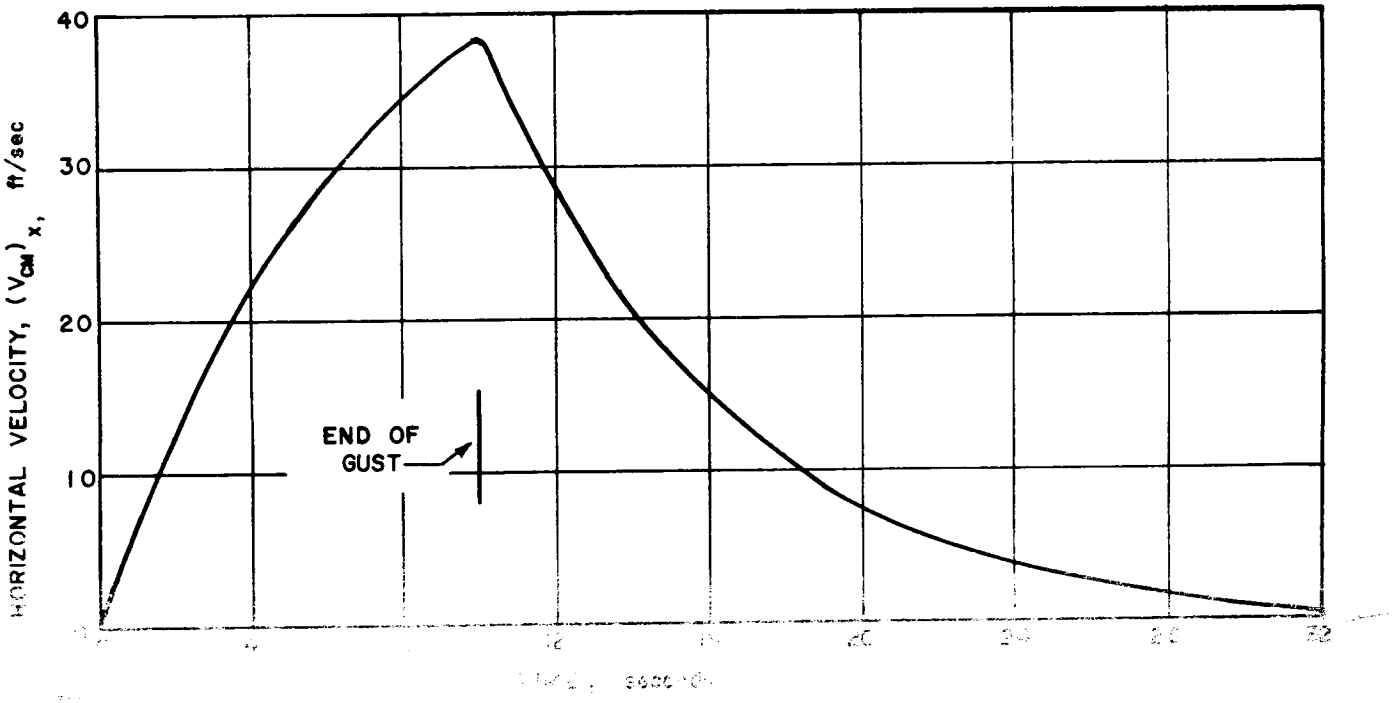

LA[illegible] WITH RESPECT TO MASS
[illegible] FOR 10 SECONDS

on the dynamic stability of the capsule and parachute are not detrimental to the performance of the descent system, 2) equilibrium with the horizontal wind is not attained during the 10-second gust, and 3) approximately 20-seconds are required to attain equilibrium after the gust has ceased. The large angular motions could present difficulties in atmospheric sampling.

More detailed results are shown in paragraph 2.5.4.

2.5 ENTRY FROM ORBIT DESIGN

2.5.1 Summary

The entry vehicle for the entry from orbit design must have enough drag to allow adequate communications time during the terminal phase of the flight. It would be desirable to use passive retardation for the probe eliminating the necessity for an active descent system. To achieve passive retardation, the probe must have sufficient drag area and stability after entry into the atmosphere to decelerate to a reasonably low impact velocity consistent with the required descent time for atmospheric sampling and communications playback. Such a vehicle would require a ballistic coefficient on the order of 0.025 slugs/ft^2, whereas high-drag configurations with a ballistic coefficient less than 0.15 slugs/ft^2 are difficult to achieve with sufficient weight reserve for mission objectives after meeting the structural and thermal protection requirements. Hence, a passive retardation concept is not feasible; an active parachute descent system or other similar device for retardation is necessary.

The primary objective of the parachute descent system is to decelerate the entry vehicle during post entry to allow adequate communications time at altitudes between the surface of the planet and 20,000 feet. The parachute descent system must satisfy both a minimum and maximum required descent time. A minimum of 160 seconds is required for data acquisition and playout and a maximum of 360 seconds is available before the flight spacecraft passes out of communications range. It is further required that the terminal descent parachute be fully inflated and subsonic at a minimum altitude of 15,000 feet.

The type of parachute system and allowable attendant deployment conditions dictate to a large degree, the maximum M/C_DA that can be achieved for a vehicle entering a given atmosphere with particular entry conditions. The final selection of the descent system should be based first on reliability, second on weight and then on performance and development.

The model atmospheres used in the entry from orbit study were the 5 to 10 mb surface pressure VM-3, 4, 7 and 8 atmospheres presented in

Table IV. It was established during the study that neither a two parachute drogue-main nor reefing of a single main parachute system is necessary to accomplish the intended mission under the design constraints. The selected reference descent system is a conventional single-stage ring-sail parachute deployed at a maximum Mach number of 1.2 (Mach 1.2 was selected as the upper limit for reliable deployment and operation).

For the range of entry conditions considered, the VM-8 atmosphere is least receptive to passive vehicle deceleration resulting in the lowest parachute deployment altitudes. However, for terminal descent deceleration, the VM-7 atmosphere requires a greater drag deceleration area than the VM-8 if all other conditions are equal. This cross-over in behavior between the two atmospheres is due to the larger scale height and lower sea-level density of the VM-7 atmosphere in comparison with the VM-8. In conclusion, the VM-8 atmosphere dictates the maximum allowable $M/C_D A$ for given parachute deployment conditions while an appreciably greater altitude is required in the VM-7 atmosphere in order to maintain a descent time equal to that achieved in the VM-8 atmosphere.

2.5.2 Main Parachute Analysis

The parametric analyses shown in this section are based on the ring-sail configuration utilizing a drag coefficient of 0.7 based on the nominal parachute diameter. The parachute weights and dimensions can be easily scaled for other configurations with different drag coefficients. The main parachute weights and dimensions are based on terminal descent velocity using the equation,

$$A_{mc} = \frac{2\, W_{susp}\, g_{\sigma}}{\rho\, C_D\, V_v^2\, g_{\oplus}}$$

where,

A_{mc} = main chute canopy area based on nominal chute diameter, ft^2

W_{susp} = suspended weight on the parachute plus the parachute system weight, pounds

g = gravitational acceleration, $ft/sec.^2$

ρ = sea level atmospheric density, $slugs/ft^3$

C_D = chute drag coefficient based on nominal chute diameter

V_v = vertical impact velocity at sea level, ft/sec

TABLE IV

SUMMARY OF MODEL ATMOSPHERE PARAMETERS FOR MARS

(Models VM-3, -4, -7, and 8)

Property	Dimension	VM-3	VM-4	VM-7	VM-8
Surface Pressure	mb	10.0	10.0	5.0	5.0
	lb/ft^2	20.9	20.9	10.4	10.4
Surface Density	$(gm/cm^3)\ 10^5$	1.365	2.57	0.68	1.32
	$(slugs/ft^3)\ 10^5$	2.65	4.98	1.32	2.56
Surface Temperature	°K	275	200	275	200
	°R	495	360	495	360
Stratospheric Temperature	°K	200	100	200	100
	°R	360	180	360	180
Acceleration of Gravity at Surface	cm/sec^2	375	375	375	375
	ft/sec^2	12.3	12.3	12.3	12.3
Composition:					
CO_2 (by mass)		28.2	70.0	28.2	100.0
CO_2 (by volume)		20.0	68.0	20.0	100.0
N_2 (by mass)		71.8	0.0	71.8	0.0
N_2 (by volume)		80.0	0.0	80.0	0.0
A (by mass)		0.0	30.0	0.0	0.0
A (by volume)		0.0	32.0	0.0	0.0
Molecular Weight	mol^{-1}	31.2	42.7	31.2	44.0
Specific Heat of Mixture	cal/gm°C	0.230	0.153	0.230	0.166
Specific Heat Ratio		1.38	1.43	1.38	1.37
Adiabatic Lapse Rate	°K/km	-3.88	-5.85	-3.88	-5.39
	°R/1000 ft	-2.13	-3.21	-2.13	-2.96
Tropopause Altitude	km	19.3	17.1	19.3	18.6
	kilo ft	63.3	56.1	63.3	61.0
Inverse Scale Height (stratosphere)	km^{-1}	0.0705	0.193	0.0705	0.199
	$ft^{-1} \times 10^5$	2.15	5.89	2.15	6.07
Continuous Surface Wind Speed	ft/sec	155.5	155.5	220.0	220.0
Peak Surface Wind Speed	ft/sec	390.0	390.0	556.0	556.0
Design Vertical Wind Gradient	ft/sec/1000 ft	2	2	2	2

2.5.2.1 Parametric Results

The effective drag area of the suspended weight is neglected since it is small compared with the drag area of the parachute system. Utilizing the above equation, Figure 53 depicts the required main parachute canopy area per pound of suspended weight (A_{mc}/W_{susp}) for each of the atmospheres under consideration. This parameter allows a quick evaluation of total parachute system weight for a given suspended weight. The results are plotted as a function of vertical impact velocity and indicate that the VM-7 atmosphere yields the highest impact velocity for a given parachute size and suspended weight. Figure 54 presents curves of nominal parachute diameter versus suspended weight for a range of A_{mc}/W_{susp} ratios. In order to calculate detailed weights for the parachute system such as canopy, suspension lines and riser line, it is necessary to establish the opening shock load. Figure 55 shows opening shock load versus dynamic pressure for a range of nominal parachute diameters. With the required parachute size and opening dynamic pressure established it is possible to fix the parachute weight. Figure 30 plots weight versus opening dynamic pressure for a range of nominal parachute diameters. Note that the indicated parachute weight reflects only the canopy and shroud lines hence, more readily availing itself to quick parametric weight estimates. The weight of the riser line, pilot parachute canisters, etc., must additionally be included.

2.5.2.2 Descent Time

Descent time curves as a function of full parachute open altitude are plotted on Figures 56 through 59 for each of the atmospheres considered. A range of A_{mc}/W_{susp} ratios are presented for each atmosphere. The initial conditions assume deployment at an entry angle of -50 degrees and Mach 1.0. For deployment within ±0.3 Mach number and ±10 degrees entry angle, the total descent time will vary only a few seconds. For the majority of the trajectories considered, the deployment entry angle was very close to -50 degrees.

2.5.2.3 Weight Analysis

Overall system weights for the main parachute are based on experimental data and past experience. Data from Northrop Ventura and Cook Electric were used. Parametrically, the overall main parachute system weight is expressed as

$$W_{mc} = \frac{K q A_p}{10}$$

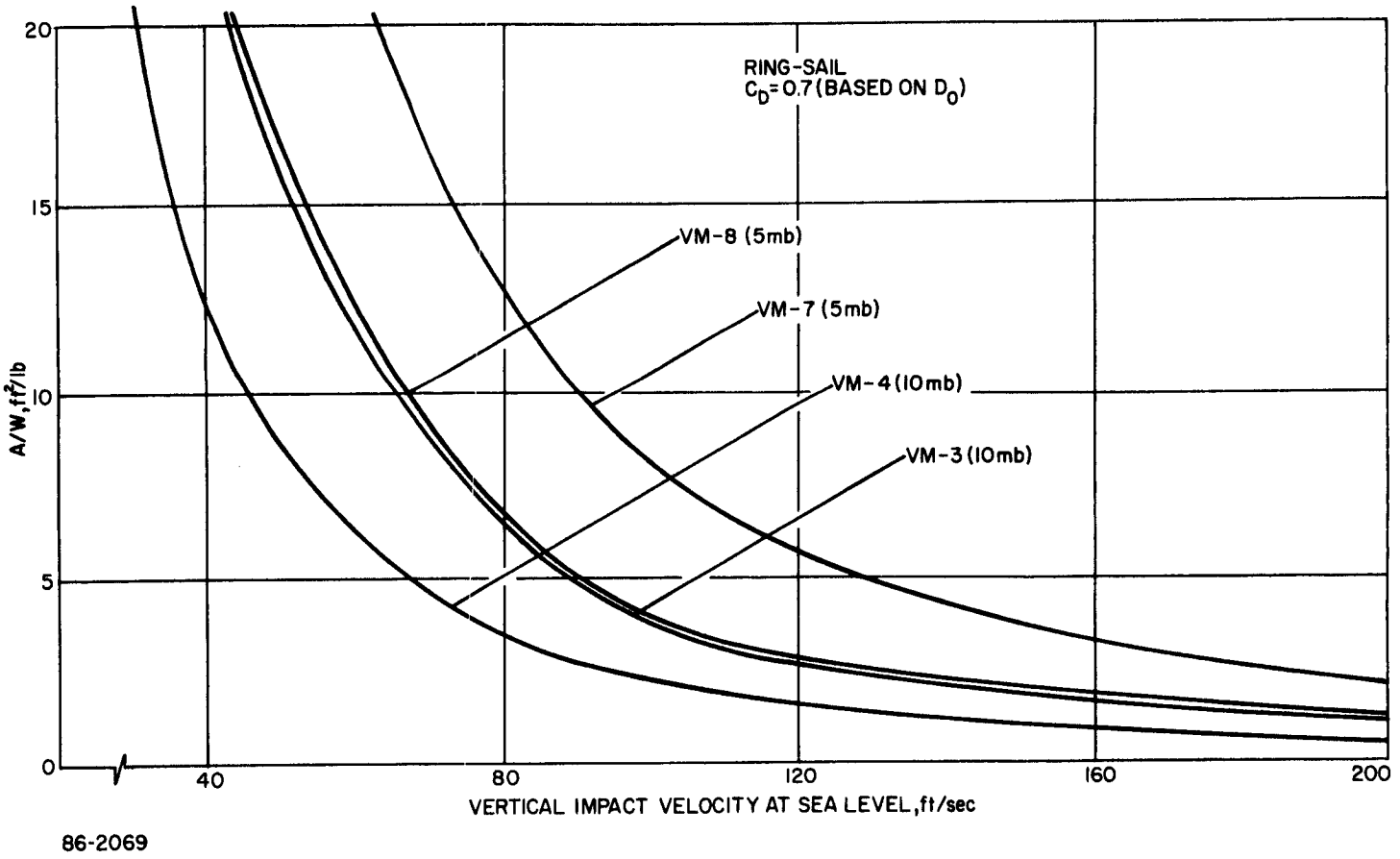

Figure 53 SINGLE PARACHUTE SYSTEM-IMPACT VELOCITY VERSUS MAIN PARACHUTE AREA/SUSPENDED WEIGHT

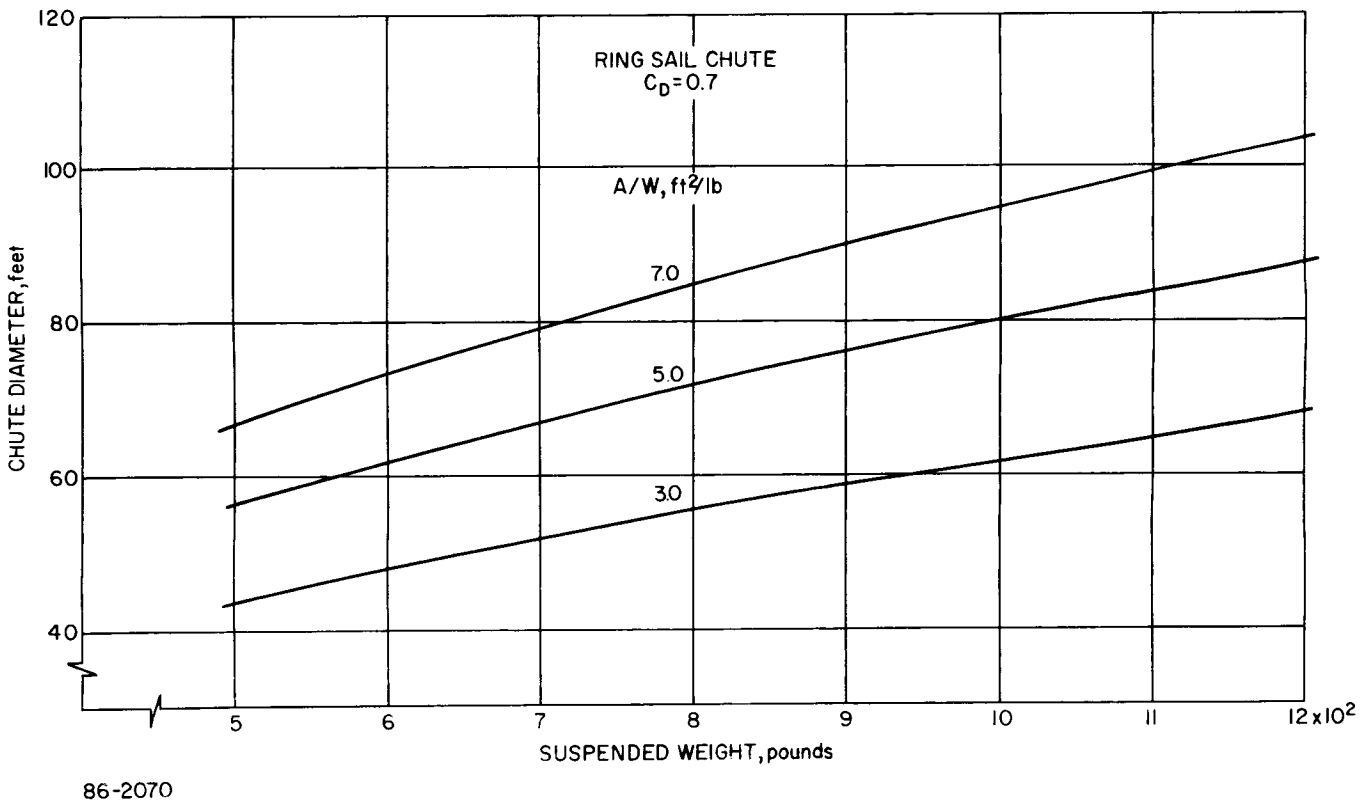

Figure 54 NOMINAL PARACHUTE DIAMETER VERSUS SUSPENDED WEIGHT

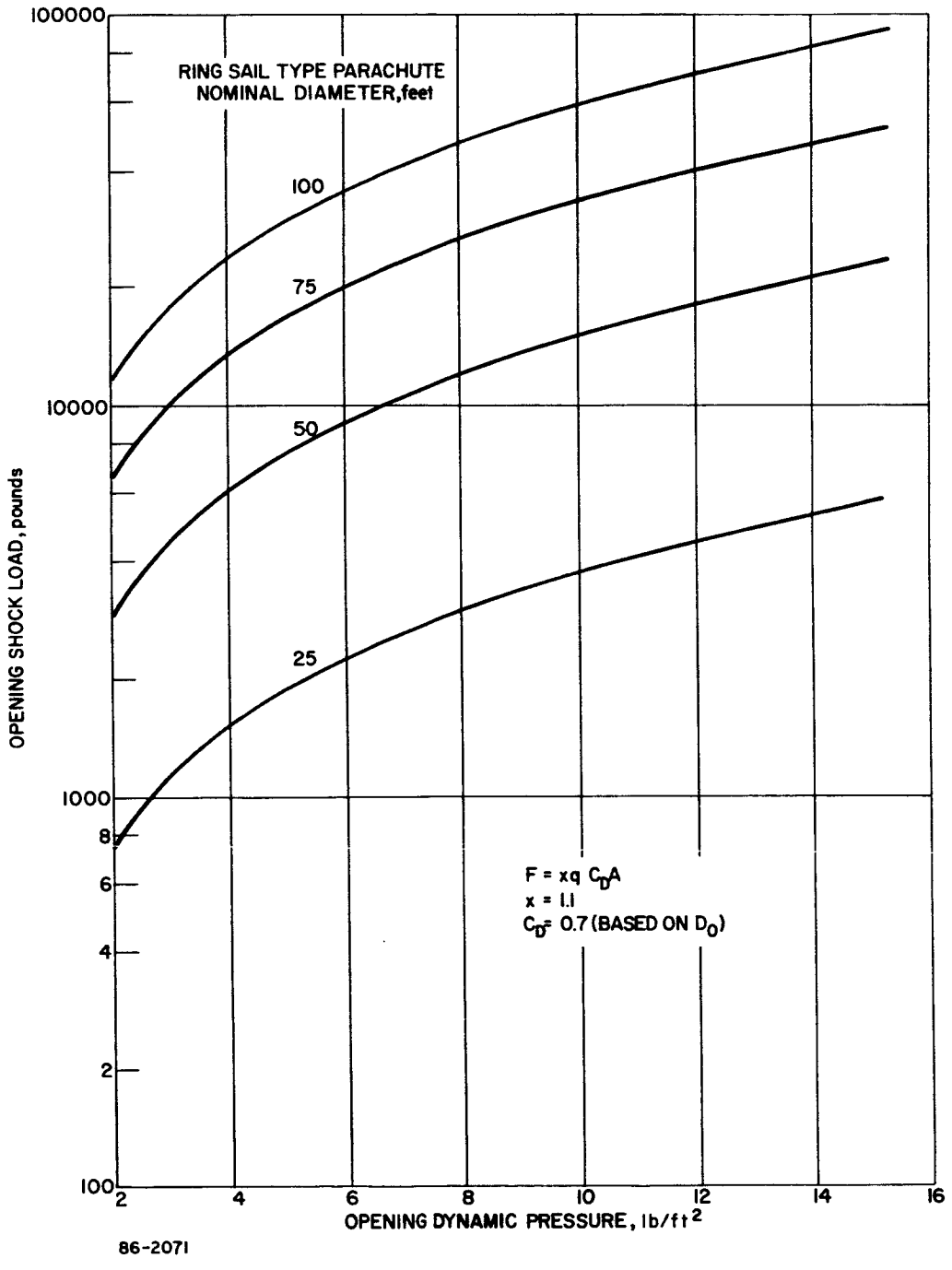

Figure 55 OPENING SHOCK LOAD VERSUS DYNAMIC PRESSURE

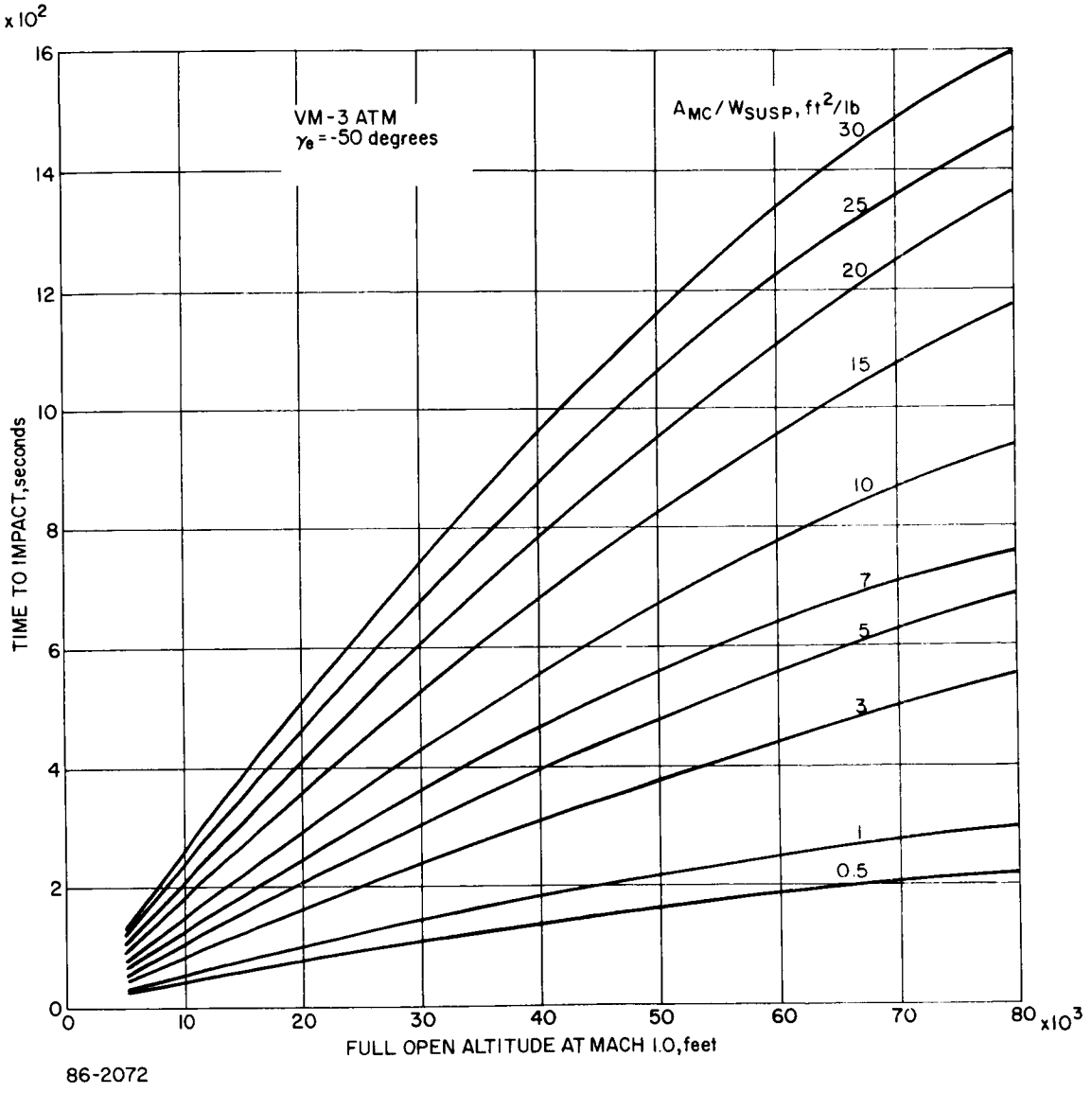

Figure 56 PARACHUTE DESCENT TIME VERSUS FULL-OPEN ALTITUDE IN THE VM-3 ATMOSPHERE

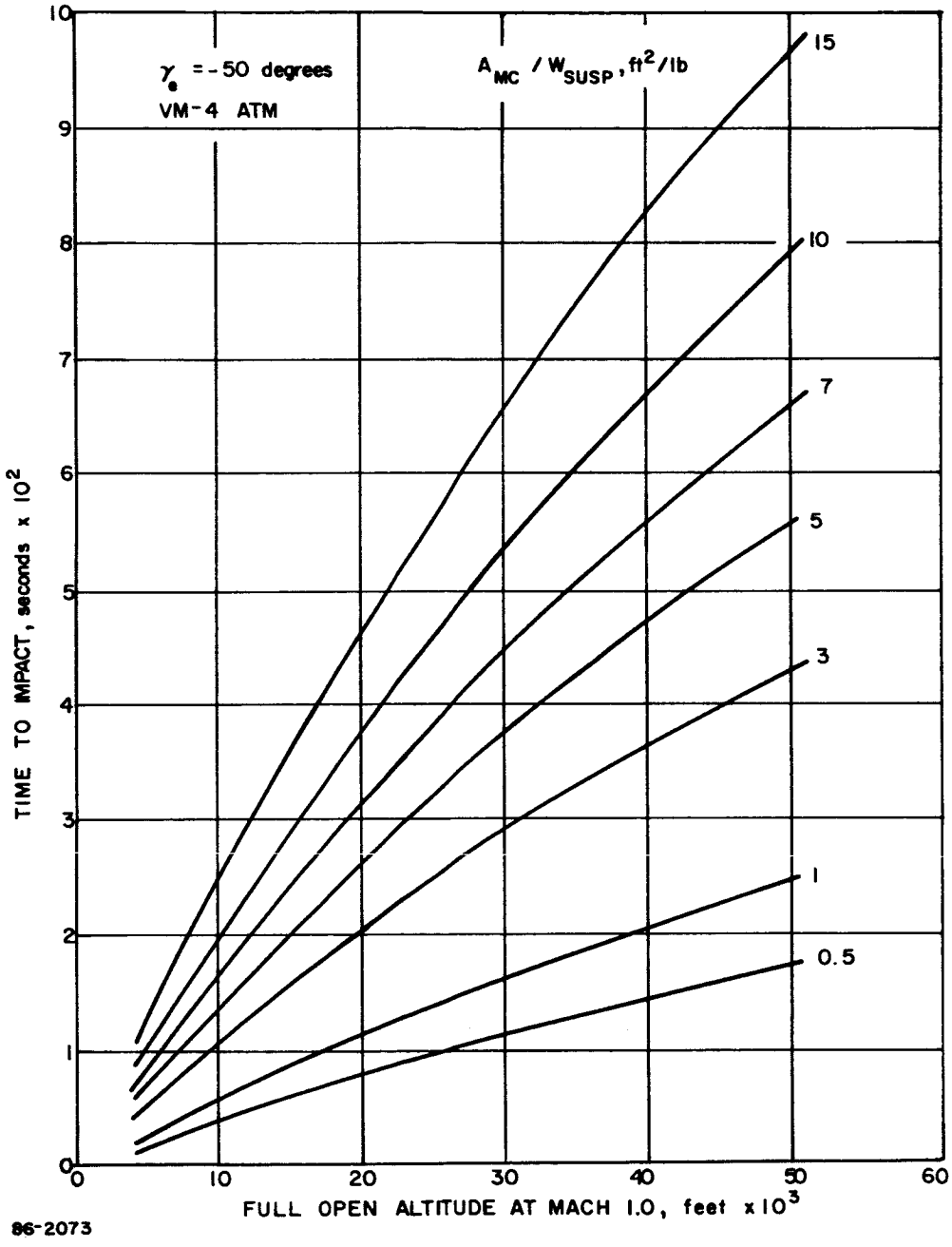

Figure 57 PARACHUTE DESCENT TIME VERSUS FULL-OPEN ALTITUDE IN THE VM-4 ATMOSPHERE

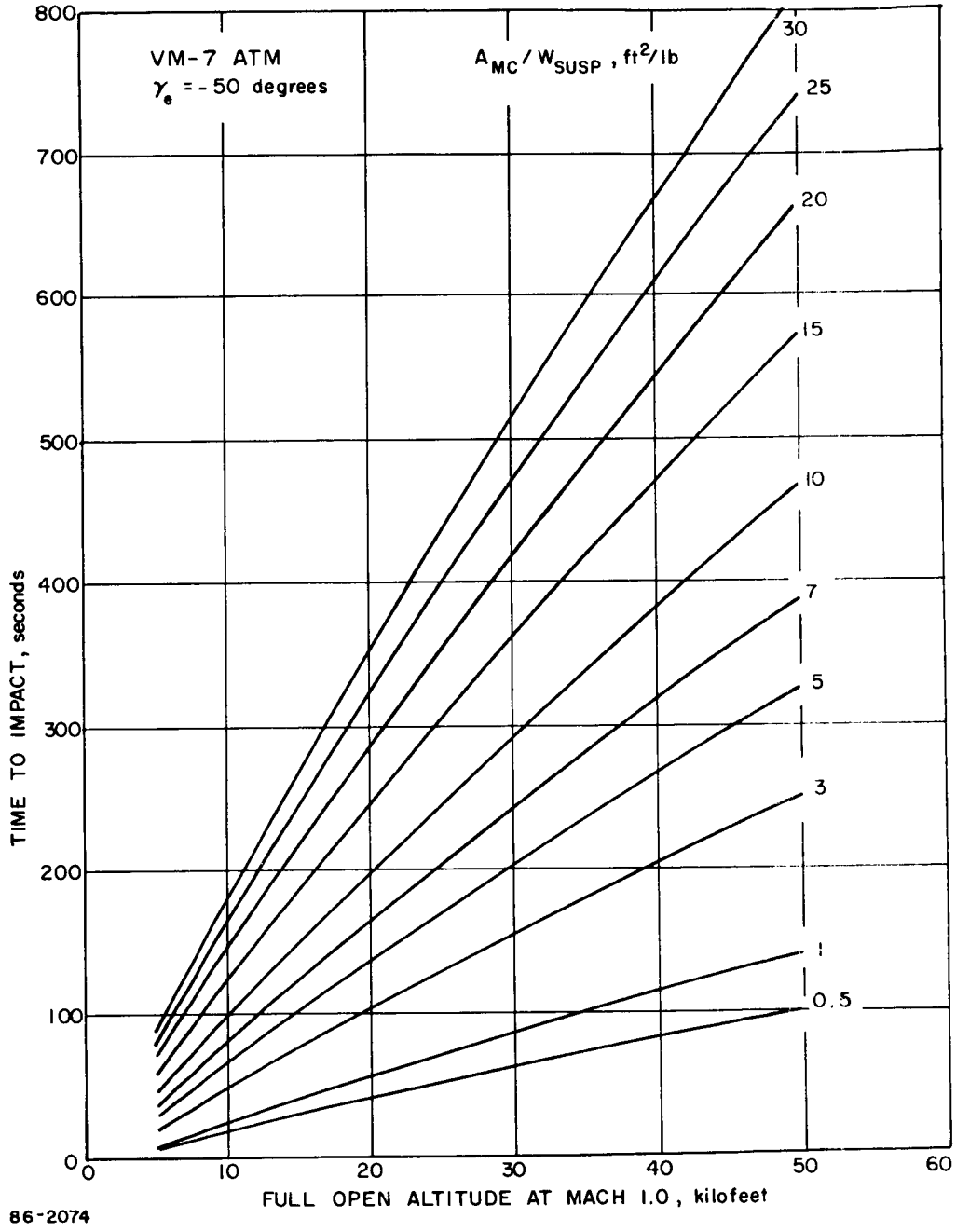

Figure 58 PARACHUTE DESCENT TIME VERSUS FULL-OPEN ALTITUDE IN THE VM-7 ATMOSPHERE

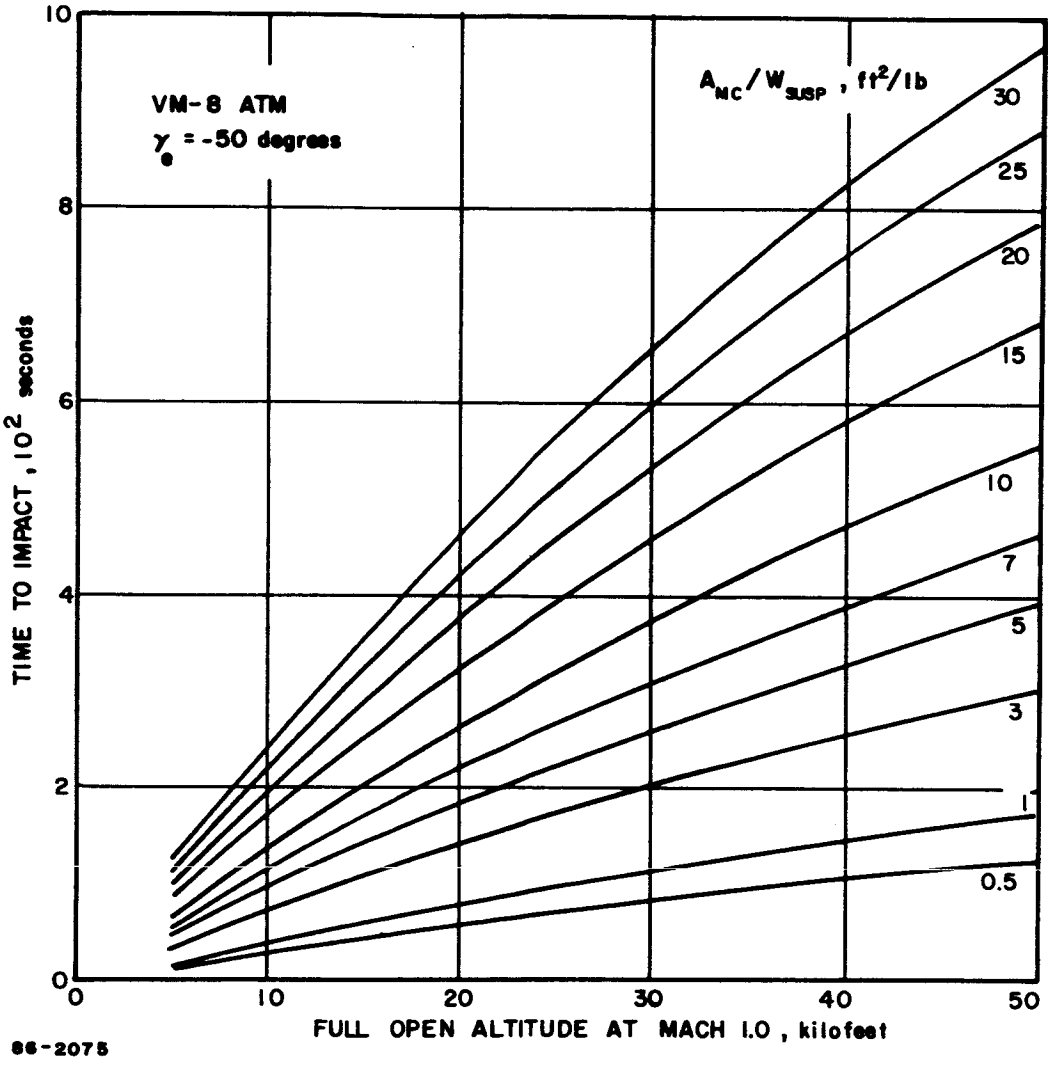

Figure 59 PARACHUTE DESCENT TIME VERSUS FULL-OPEN ALTITUDE IN THE VM-8 ATMOSPHERE

where

k = 0.013 for 0.8 oz/yd^2 Nylon canopy

q = deployment dynamic pressure, lb/ft^2

A_p = projected canopy area, ft^2

2.5.3 Actuation System

The selection of a sensing system for parachute actuation presents a difficult problem due to the uncertainty of entry conditions and the range of atmospheric models to be considered. The sensing system must be capable of deploying the parachute for a worst combination of entry angle, entry velocity, and model atmosphere. The actuation system must also be such that it assures parachute deployment within the aerodynamic heating and loading design limits of the canopy fabric.

2.5.3.1 Selected Approach

The selected system utilizes three axial accelerometers which sense peak entry deceleration and correlates the magnitude of the peak value with time from peak g to the main parachute deployment Mach number of 1.2. The product $G_{max}\,\Delta t$ is a constant peak g to a given velocity independent of entry velocity, entry angle, and atmosphere. The analysis assumes constant vehicle M/C_DA, a straight line trajectory and an isothermal atmosphere. Mach number is the parameter of interest and not velocity, hence a correction is needed for the speed of sound. A radar altimeter is combined with the acceleration-time correlation (Mach 1.2 deployment) to ensure deployment at an altitude equal to or less than 27,500 feet. Two conditions must be satisfied before initiation of the system takes place i.e., $Z \leq 27,500$ and $M \leq 1.2$. The value of 27,500 feet was chosen in order to maintain communications with the flight spacecraft during terminal descent on the parachute and also to ensure minimum descent time in the VM-7 atmosphere.

Based on these assumptions, Figures 60 through 63 were constructed to depict time from G_{max} to Mach 1.2 as a function of G_{max}. Data points are shown for each atmosphere and for a range of entry velocities (12,000 to 15,000 fps) and associated entry angles. A curve fit of the data points is shown on each figure relating G_{max} and Δt. In each case, the curve and resultant equation ensures deployment at or below Mach 1.2.

Figure 64 is a summary plot of G_{max} versus Δt for the entire range of entry velocities, angles, and atmospheres considered. The finalized curve-fit equation shown on this figure includes entry velocity, entry angle and atmospheric effects.

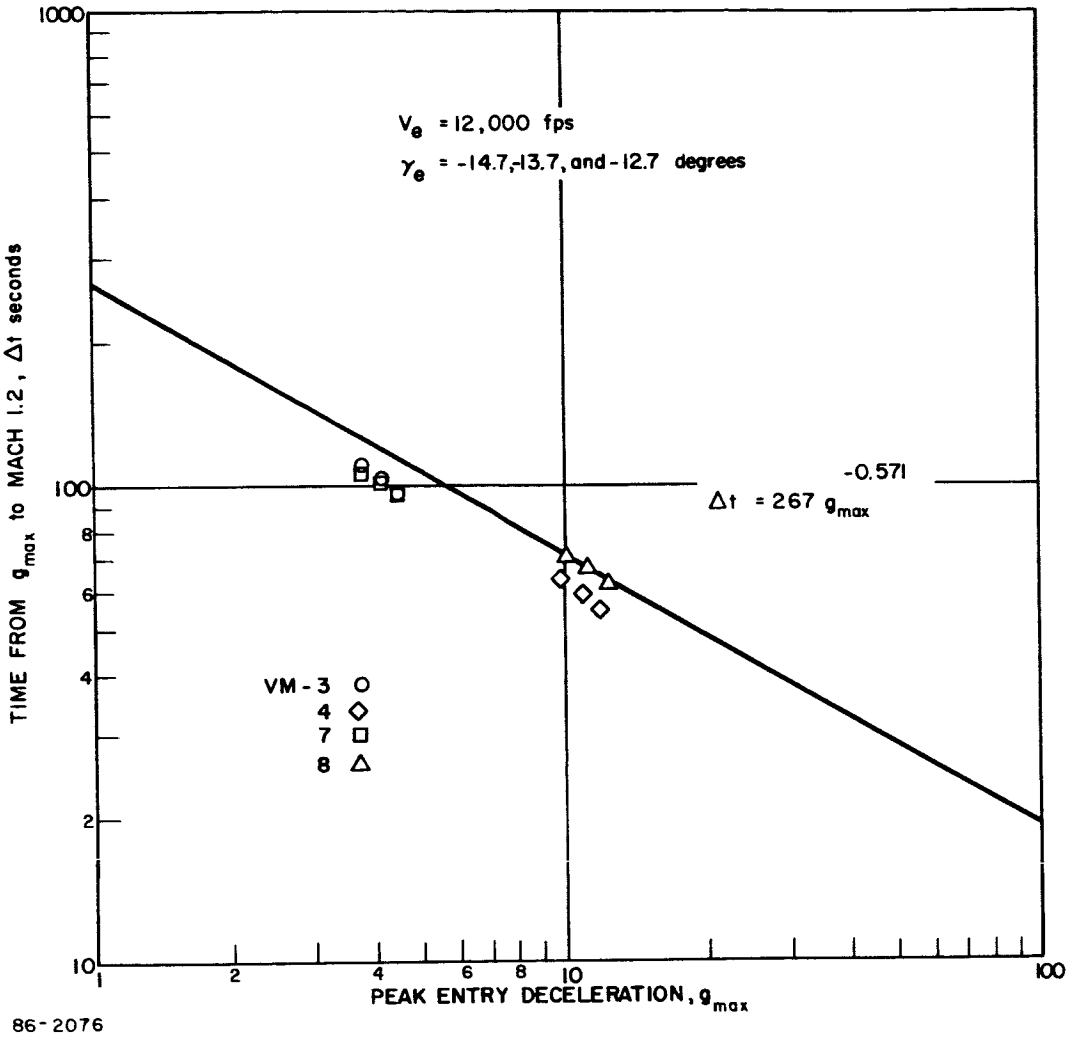

Figure 60 PEAK ACCELERATION VERSUS TIME FROM G_{max} TO MACH 1.2
(V_e = 12000 ft/sec)

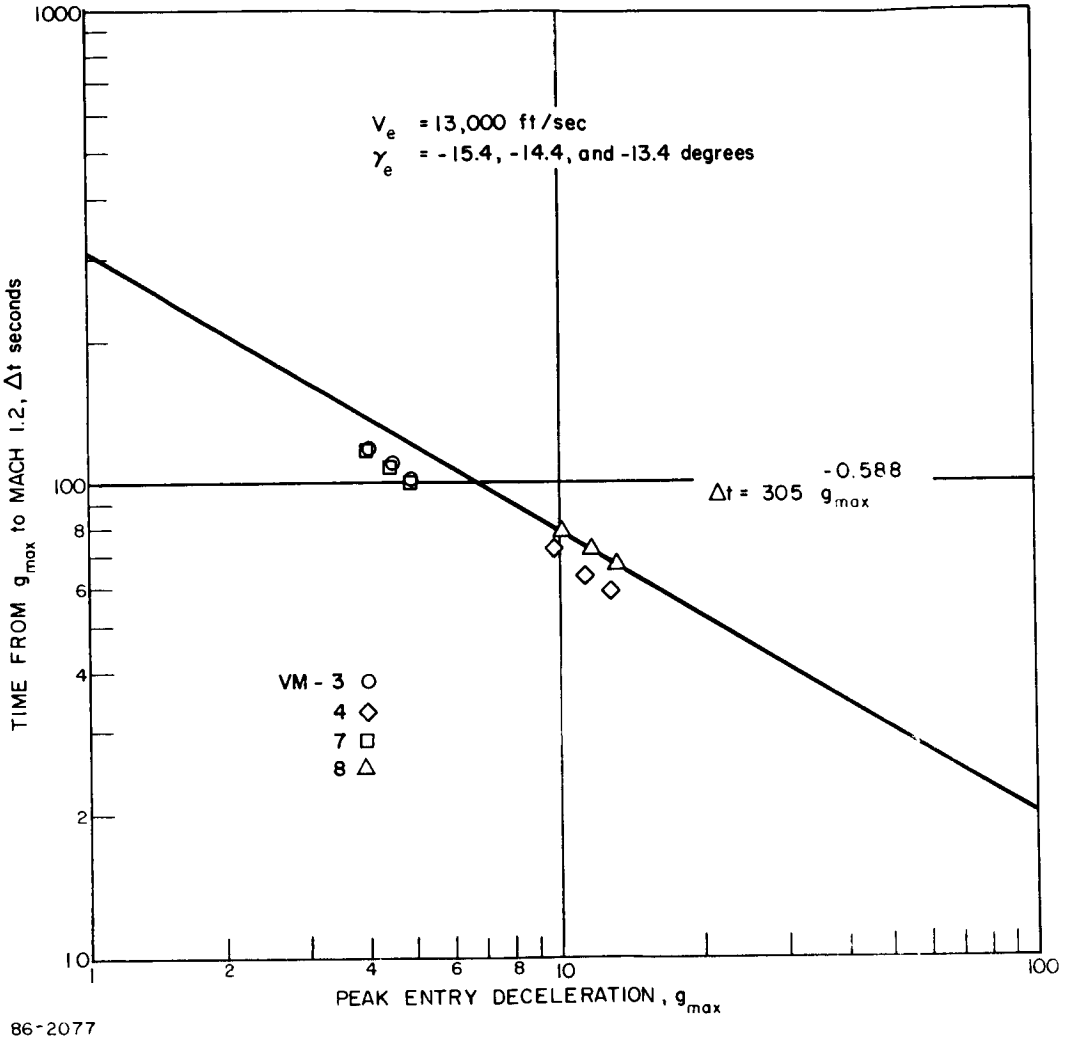

Figure 61 PEAK ACCELERATION VERSUS TIME FROM G_{max} TO MACH 1.2
(V_e = 13000 ft/sec)

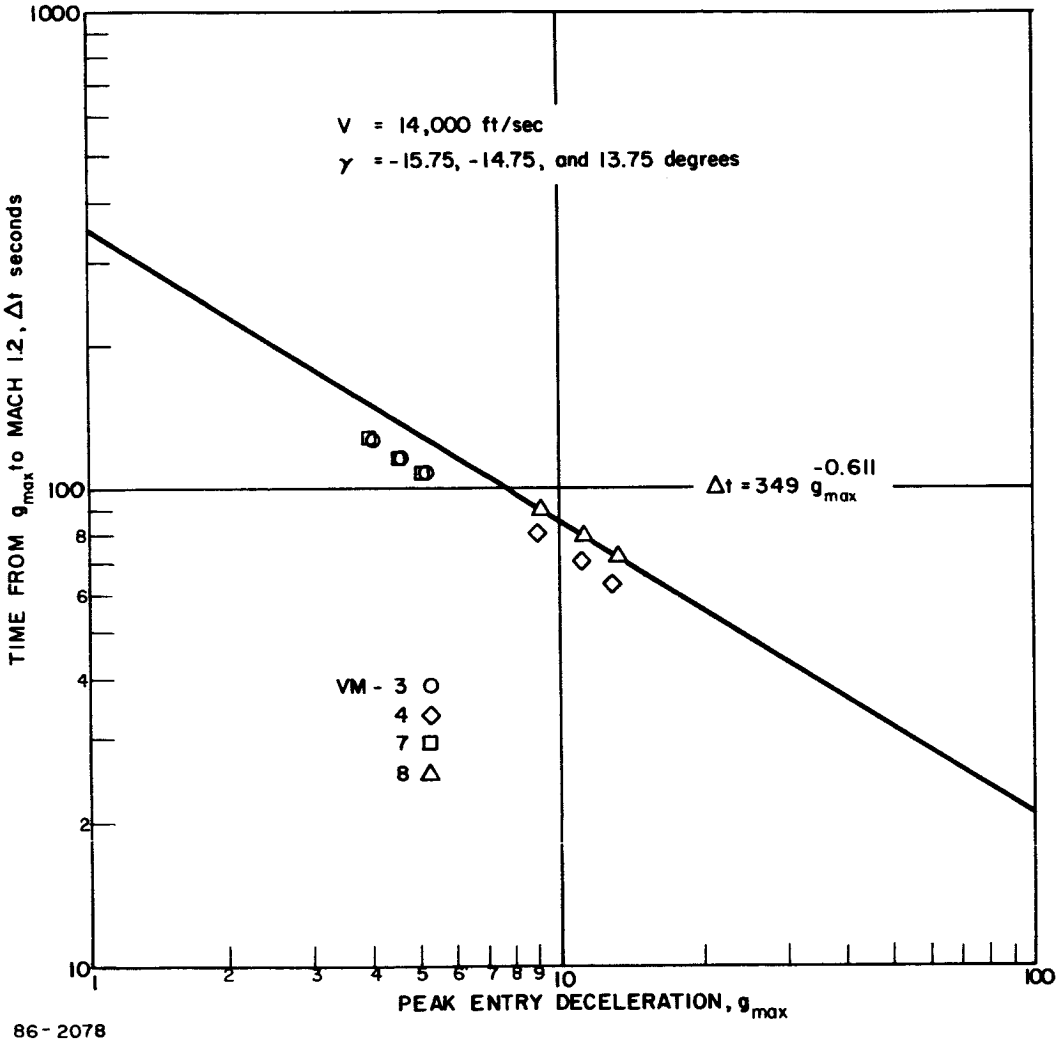

Figure 62 PEAK ACCELERATION VERSUS TIME FROM G_{max} TO MACH 1.2
(V_e = 14000 ft/sec)

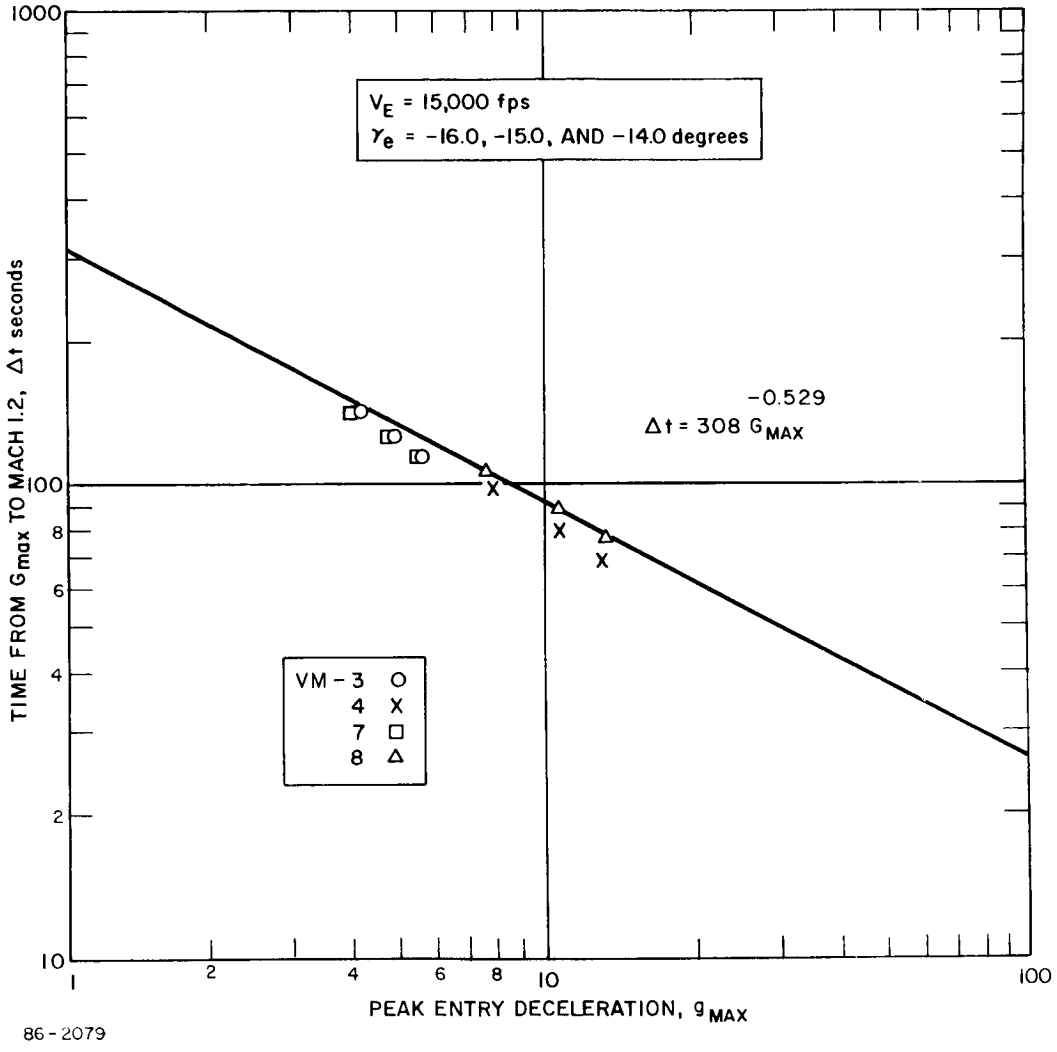

Figure 63 PEAK ACCELERATION VERSUS TIME FOR G_{max} TO MACH 1.2
(V_e = 15000 ft/sec)

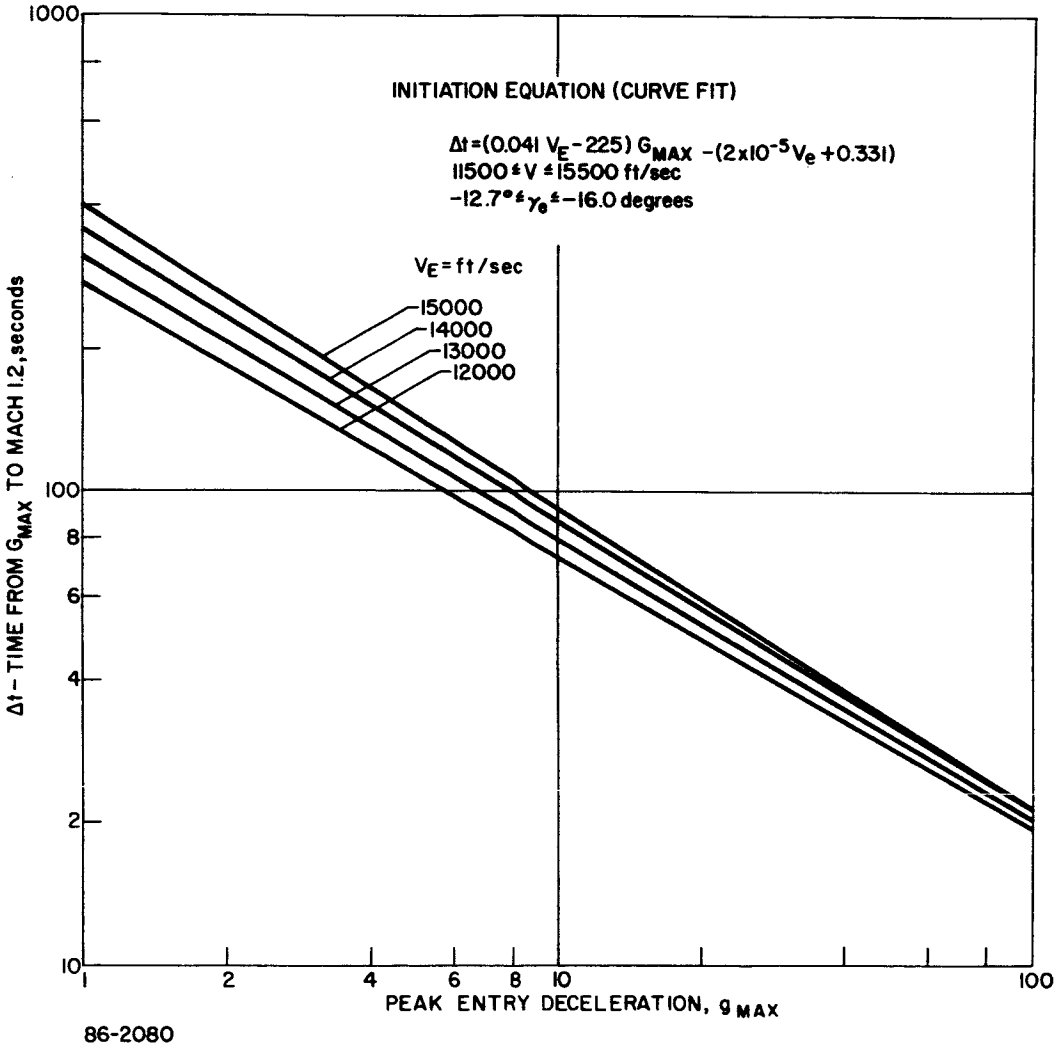

Figure 64 SUMMARY INITIATION DATA--PEAK ACCELERATION VERSUS TIME FOR G_{max} TO MACH 1.2 (ALL ENTRY VELOCITIES, ENTRY ANGLES AND ATMOSPHERE INCLUDED)

Peak entry deceleration is sensed via the onboard accelerometers. The magnitude of the peak value along with the entry velocity is fed into an analog circuit which contains the finalized equation shown on Figure 64. A value of Δt is determined and at peak g a timer is started. At the end of the prescribed Δt interval initiation of the system takes place only if the altitude is less than 27, 500 feet.

2.5.3.2 Initiation Devices

Initiation of the system is dependent on the sensing of peak g via onboard accelerometers. A timer, an analog circuit, and a radar altimeter are the other operation devices required for parachute initiation. Comparisons of various other initiation concepts which were investigated are presented in detail in Reference 4.

2.5.3.3 Error Analysis

Particle trajectory results for the reference M/C_DA of 0.22 slugs/ft^2 are shown on Tables V through VIII. The tables indicate the altitude at Mach 1.2, the altitude at which the parachute is initiated (based on the G_{max} computation), the actual deployment altitude and finally the Mach number and dynamic pressure for the entire range of trajectories considered. In all cases for the VM-3, VM-4 and VM-7 atmospheres, the Δt (based on G_{max} computation occurs above 27, 500 feet; hence, deployment takes place uniquely at 27, 500 feet via the radar altimeter signal. In the VM-8 atmosphere, the converse is true in all cases, i.e., Mach 1.2 occurs below 27, 500 feet, hence deployment takes place after the Δt excursion for all VM-8 trajectories. The reference system is such that it ensures deployment over the following ranges:

$$19,900 \leq Z \leq 27,500 \text{ feet}$$

$$0.70 \leq M \leq 1.2$$

$$4.14 \leq q \leq 4.96 \text{ lb/ft}^2$$

Six degree-of-freedom trajectories have been checked against the reference system and in all cases fall within the above deployment ranges; entry dynamics do not degrade the system to any significant degree. The primary system depends on proper operation of the radar altimeter, accelerometers, timers, and analog circuitry.

In the event of failure of the accelerometers and/or timers, a backup is provided such that deployment takes place at 19, 000 feet via a signal from the radar altimeter. In the event the radar altimeter fails, then initiation of the system takes place nominally at Mach 0.85 based on a similar peak g Δt correlation. Table IX shows the deployment conditions for each of the backup systems.

Figure 65 schematically shows the initiation circuit and deployment sequence. Figure 66 shows the data, curve fit, and resulting equation for the Mach 0.85 deployment backup.

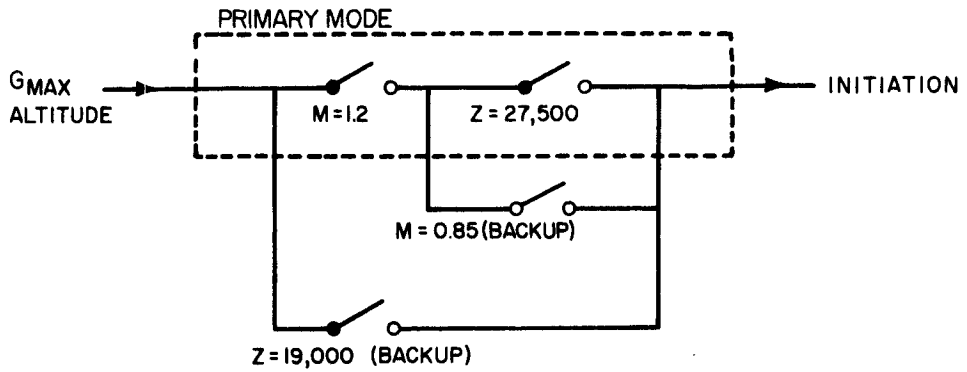

INITIATION LOGIC (ELECTRICAL ANALOGY)

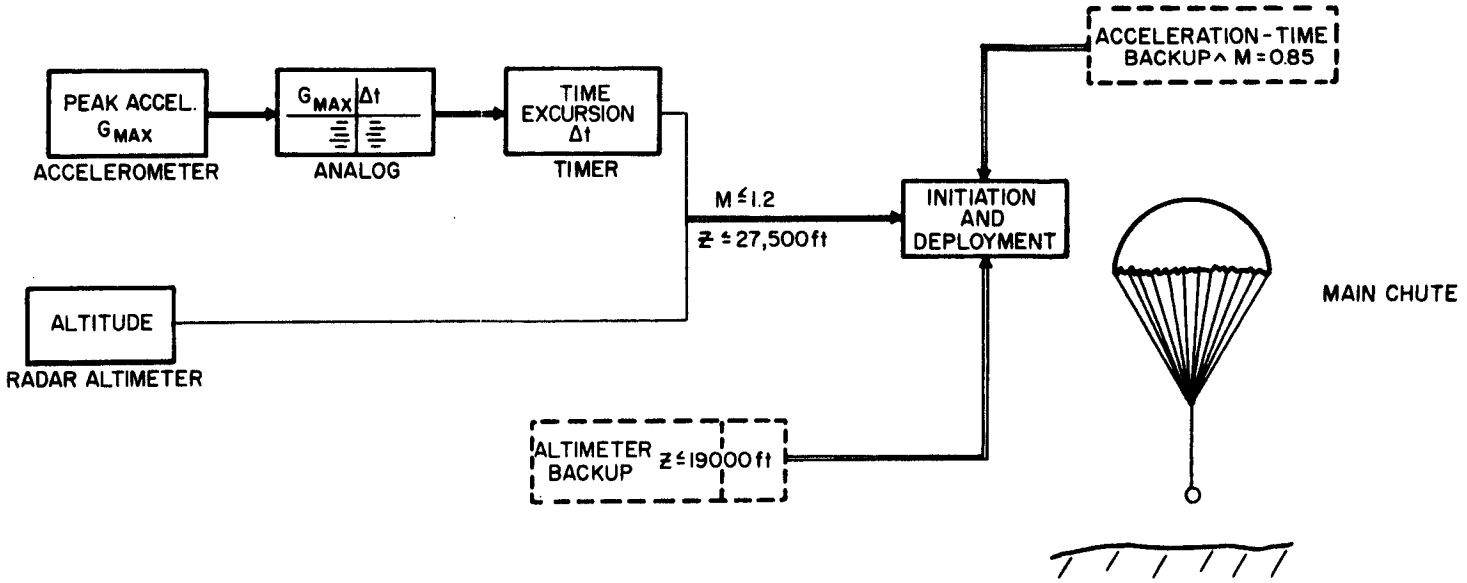

86-2081

Figure 65 DEPLOYMENT SCHEMATIC

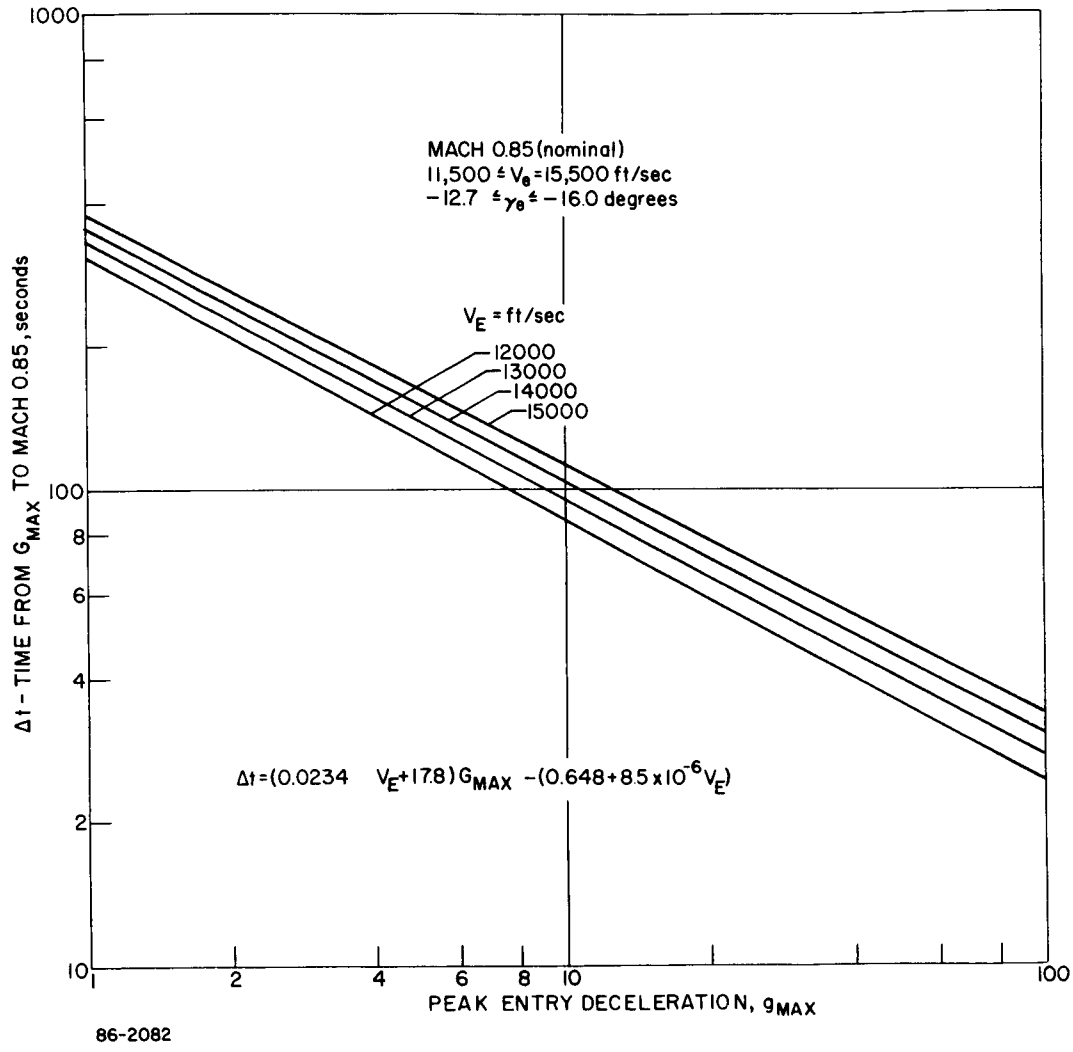

Figure 66 MACH NUMBER INITIATION BACKUP--PEAK ACCELERATION VERSUS TIME FROM G_{max} TO MACH 0.85 (NOMINALLY)

TABLE V

TRAJECTORY RESULTS AND DEPLOYMENT CONDITIONS IN THE VM-3 ATMOSPHERE (PARTICLE TRAJECTORY ~ Z_E = 800, 000 FT)

V_e (ft/sec)	γ_e (degrees)	t at g_{max} (seconds)	Z at g_{max} (feet)	G_{max}	Z at $M = 1.2$ (feet)	$\Delta t_{G_{max} \to 1.2}$ (seconds)	$q_{M=1.2}$ (lb/ft^2)	Z_{Deploy} (feet)	M_{Deploy}	q_{Deploy} (lb/ft^2)
12, 000	-14. 7	222	171, 017	4. 41	72, 556	96. 02	5. 45	27, 500	0. 71	4. 56
12, 000	-13. 7	238	175, 465	4. 07	73, 423	104. 00	5. 32		0. 71	4. 57
12, 000	-12. 7	257	180, 175	3. 72	74, 320	111. 00	5. 22		0. 71	4. 58
13, 000	-15. 4	205	176, 374	4. 81	73, 524	102. 34	5. 37		0. 70	4. 56
13, 000	-14. 4	221	181, 225	4. 37	74, 441	110. 34	5. 23		0. 71	4. 57
13, 000	-13. 4	241	185, 754	3. 92	75, 195	119. 00	5. 11		0. 71	4. 59
14, 000	-15. 75	194	180, 687	5. 15	74, 382	108. 00	5. 26		0. 70	4. 56
14, 000	-14. 75	211	185, 537	4. 59	75, 634	117. 00	5. 13		0. 71	4. 58
14, 000	-13. 75	234	188, 870	4. 00	76, 342	126. 66	5. 01		0. 71	4. 60
15, 000	-16. 0	184	185, 942	5. 48	75, 008	114. 66	5. 14		0. 70	4. 57
15, 000	-15. 0	201	192, 505	4. 79	76, 379	126. 34	5. 03		0. 71	4. 58
15, 000	-14. 0	223	200, 557	4. 06	77, 213	141. 66	4. 94		0. 71	4. 61

TABLE VI

TRAJECTORY RESULTS AND DEPLOYMENT CONDITIONS IN THE VM-4 ATMOSPHERE (PARTICLE TRAJECTORY ~ Z_E = 800,000 FT)

V_e (ft/sec)	γ_e (degrees)	t at g_{max} (seconds)	Z at g_{max} (feet)	G_{max}	Z at $M = 1.2$ (feet)	$\Delta t_{G_{max} \to 1.2}$ (seconds)	q $M = 1.2$ (lb/ft^2)	Z_{Deploy} (feet)	M_{Deploy}	q_{Deploy} (lb/ft^2)
12,000	-14.7	250	76,887	11.87	38,552	55.2	5.29	27,500	0.85	4.23
12,000	-13.7	270	78,956	10.84	39,255	59.5	5.09		0.85	4.20
12,000	-12.7	294	81,341	9.78	40,013	64.4	4.91		0.85	4.18
13,000	-15.4	234	80,605	12.55	39,229	59.6	5.13		0.85	4.19
13,000	-14.4	256	81,463	11.18	40,187	64.0	4.93		0.85	4.17
13,000	-13.4	282	85,059	9.67	41,014	73.5	4.75		0.85	4.16
14,000	-15.75	226	81,339	12.91	40,050	63.2	4.95		0.85	4.15
14,000	-14.75	250	83,561	11.04	40,897	70.5	4.71		0.85	4.16
14,000	-13.75	282	87,228	8.96	41,887	80.5	4.56		0.85	4.18
15,000	-16.0	219	83,708	13.01	40,756	68.5	4.77		0.85	4.14
15,000	-15.0	246	87,087	10.59	41,706	79.0	4.56		0.85	4.16
15,000	-14.0	286	93,399	7.62	42,438	97.0	4.44		0.85	4.21

TABLE VII

TRAJECTORY RESULTS AND DEPLOYMENT CONDITIONS IN THE VM-7 ATMOSPHERE (PARTICLE TRAJECTORY ~ Z_E = 800,000 FT)

V_e (ft/sec)	γ_e (degrees)	t at g_{max} (seconds)	Z at g_{max} (feet)	G_{max}	Z at M = 1.2 (feet)	$\Delta t_{G_{max} \to 1.2}$ (seconds)	q M = 1.2 (lb/ft^2)	Z_{Deploy} (feet)	M_{Deploy}	q_{Deploy} (lb/ft^2)
12,000	-14.7	233	139,080	4.42	40,404	96.3	5.17	27,500	1.00	4.54
12,000	-13.7	250	143,637	4.08	42,175	102.0	5.08		0.99	4.46
12,000	-12.7	272	145,730	3.73	43,211	107.2	4.97		0.99	4.42
13,000	-15.4	216	144,565	4.79	42,524	101.2	5.10		0.99	4.46
13,000	-14.4	234	144,995	4.34	42,979	108.4	4.96		0.98	4.39
13,000	-13.4	256	152,644	3.87	45,723	116.4	4.85		0.97	4.35
14,000	-15.75	205	149,487	5.07	42,735	107.4	4.99		0.98	4.38
14,000	-14.75	224	153,834	4.50	44,331	116.4	4.85		0.97	4.33
14,000	-13.75	247	160,823	3.90	45,346	129.0	4.75		0.97	4.31
15,000	-16.0	196	153,559	5.35	43,885	114.0	4.88		0.98	4.33
15,000	-15.0	215	160,570	4.63	45,007	127.0	4.74		0.97	4.29
15,000	-14.0	241	168,217	3.86	44,801	142.2	4.67		0.97	4.29

TABLE VIII

TRAJECTORY RESULTS AND DEPLOYMENT CONDITIONS IN THE VM-8 ATMOSPHERE
(PARTICLE TRAJECTORY ~ Z_E = 800, 000 FT)

V_e (ft/sec)	γ_e (degrees)	t at g_{max} (seconds)	Z at g_{max} (feet)	G_{max}	Z at g_{max} (feet)	$\Delta t_{G_{max} \to 1.2}$ (seconds)	$q_{M=1.2}$ (lb/ft^2)	Z_{Deploy} (feet)	M_{Deploy}	q_{Deploy} (lb/ft^2)
12,000	-14.7	254	65,304	12.24	20,631	62.5	5.08	19,903	1.17	4.96
12,000	-13.7	274	68,014	11.16	21,480	67.3	4.89	21,480	1.20	4.89
12,000	-12.7	300	68,220	10.04	22,327	71.0	4.73	21,950	1.19	4.69
13,000	-15.4	238	69,223	12.86	21,342	67.5	4.91	21,342	1.20	4.91
13,000	-14.4	260	70,908	11.42	22,574	72.7	4.72	22,574	1.20	4.72
13,000	-13.4	288	72,757	9.89	23,534	79.0	4.56	23,534	1.20	4.56
14,000	-15.75	230	70,337	13.18	22,411	71.5	4.75	22,150	1.19	4.72
14,000	-14.75	254	73,639	11.20	23,621	79.5	4.55	23,621	1.20	4.55
14,000	-13.75	288	76,371	9.03	24,425	90.0	4.37	24,200	1.19	4.35
15,000	-16.0	224	71,617	13.26	23,062	76.5	4.59	23,062	1.20	4.59
15,000	-15.0	252	75,524	10.64	24,503	87.5	4.39	24,300	1.19	4.38
15,000	-14.0	296	81,185	7.45	25,096	106.0	4.25	22,987	1.14	4.18

TABLE IX

BACKUP MODE DEPLOYMENT SUMMARY

					Accelerometer Backup			Altimeter Backup	
Atmosphere	V_e (ft/sec)	γ_e (degrees)	G_{max}	$\Delta t_{G_{max} \rightarrow 0.85}$ (seconds)	Z_{Deploy} (feet)	M_{Deploy}	q_{Deploy} (lb/ft^2)	$M_{19000'}$	$q_{19000'}$
3	12,000	-13.7	4.07	141	49,000	0.86	4.52	0.67	4.65
	13,000	-14.4	4.37	149	49,400	0.86	4.50	0.66	4.66
	14,000	-14.75	4.59	157	49,600	0.86	4.49	0.66	4.66
	15,000	-15.0	4.79	167	50,400	0.86	4.48	0.66	4.67
4	12,000	-13.7	10.84	86	29.400	0.89	4.21	0.74	4.34
	13,000	-14.4	11.18	92	29,460	0.88	4.16	0.74	4.35
	14,000	-14.75	11.04	100	28,500	0.85	4.14	0.74	4.36
	15,000	-15.0	10.59	109	28,200	0.85	4.15	0.74	4.39
7	12,000	-13.7	4.08	144	15,000	0.87	4.33	0.91	4.35
	13,000	-14.4	4.34	152	14,900	0.87	4.31	0.90	4.31
	14,000	-14.75	4.50	160	15,000	0.86	4.29	0.90	4.28
	15,000	-15.0	4.63	171	20,200	0.91	4.26	0.90	4.26
8	12,000	-13.7	11.16	99	15,200	1.01	4.36	1.12	4.63
	13,000	-14.4	11.42	106	15,300	1.00	4.25	1.10	4.43
	14,000	-14.75	11.20	114	15,300	0.99	4.16	1.07	4.26
	15,000	-15.0	10.04	124	13,900	0.96	4.12	1.06	4.16

2.5.4 Dynamic Analysis

A two-dimensional, three-degree-of-freedom dynamics analysis computer program (see Reference 7) was utilized to determine the dynamic response of the chute and suspended capsule as affected by wind gusts. The calculation model is outlined and described in paragraph 2.4.6.1 of this book.

2.5.4.1 Wind-Gust Environmental Effects

Figure 67 presents an illustration of the parachute and suspended-capsule dynamic oscillations. As indicated, the parachute has a long-term oscillation while the suspended capsule oscillates at a higher frequency about the riser-line suspension point. Figure 68 presents angle definitions which will be used for descriptive purposes in the following curves. The angle ψ defines the angular excursion of the parachute system center line with respect to the local vertical (called parachute swing angle), and θ_c is the angle between the suspended capsule longitudinal axis and the local vertical (called the capsule swing angle). The time rate of change of θ_c is the capsule swing rate, $\dot{\theta}_c$. It was found that the parachute was most seriously affected by wind gust while descending through the VM-4 atmosphere. Hence the results shown on the subsequent figures will be solely for VM-4 atmosphere. Shown in Figure 69 is the effect of wind gust on parachute swing-angle ψ. The results are for a fixed parachute area-suspended weight ratio (A/W) of 3.5 ft^2/lb (Earth). In each case the wind gust was of 10-second duration. It should be noted that doubling the wind gust velocity from 100 to 200 ft/sec increases from about 60 degrees to only 80 degrees. This is due to the parachute breathing effect as shroud-line tension increases. The results are sensitive to the simulation of parachute elastic effects. Figure 70 is similar to the curve presented in Figure 69 and shows results for the capsule swing angle, θ_c . The results indicate that for single capsule harness-riser line attachment, an independent oscillation of the capsule is induced with peak-to-peak amplitudes of 15 to 20 degrees about the parachute swing angle.

Capsule swing rates, $\dot{\theta}_c$, are illustrated in Figure 71. These reach more or less steady peak values after the first violent swing of about 20 to 45 deg/sec depending on the magnitude of the gust. More discussion and the effects of these results on the mission objective, particularly the television subsystem, are presented in paragraph 1.6.6.

Similarly, the effect of A/W on the parachute dynamics was considered and the results are illustrated in Figure 72 through 74. The results presented in Figure 72 (a constant wind velocity of 150 ft/sec) indicate that the parachute swing angle decreases as the A/W ratio decreases. This effect is primarily due to the smaller parachute sizes for the reduced A/W ratio's. Note that for the reference design A/W of 5.0 ft^2/lb,

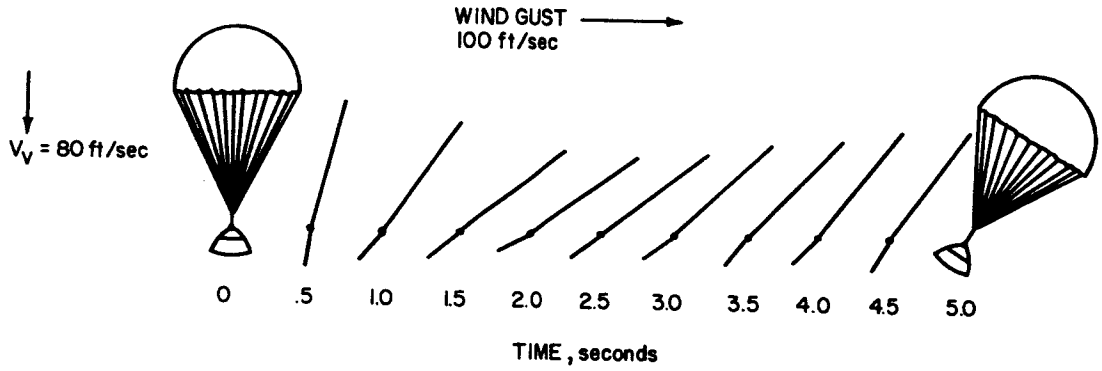

Figure 67 PARACHUTE DYNAMICS PICTORIAL

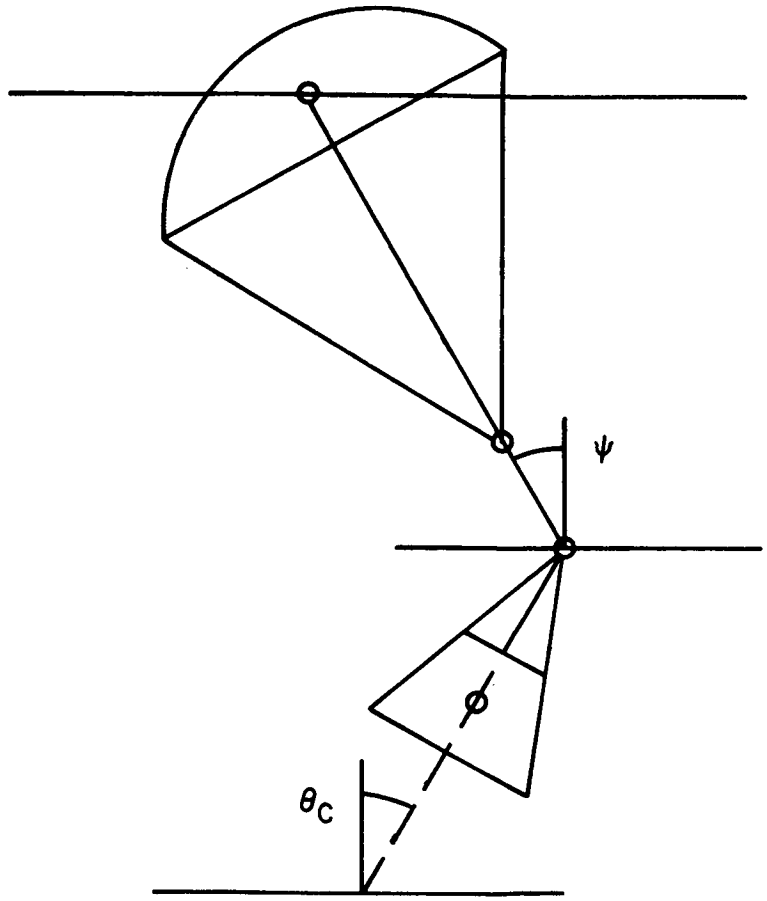

Figure 68 PARACHUTE DYNAMICS--ANGLE DEFINITIONS

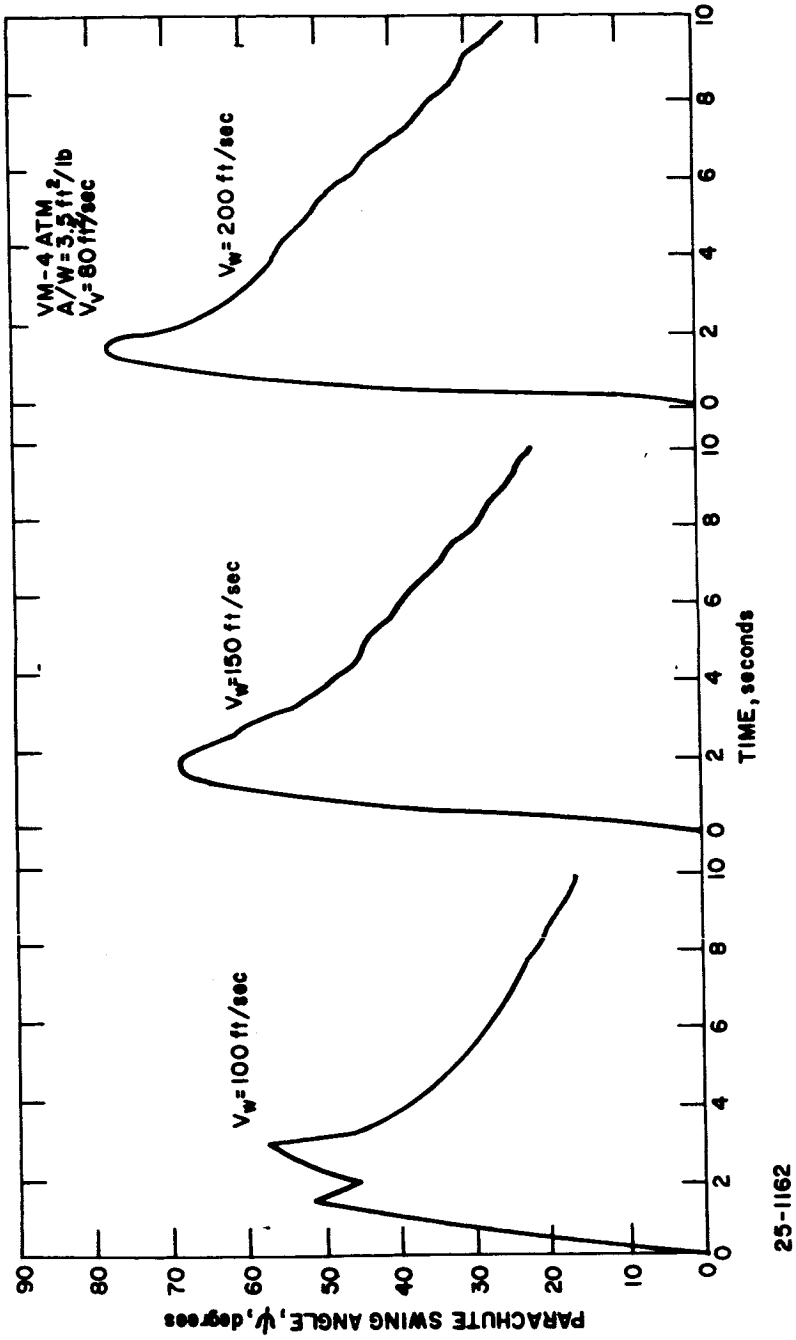

Figure 69 PARACHUTE SWING ANGLE VERSUS TIME (EFFECT OF GUST MAGNITUDE)

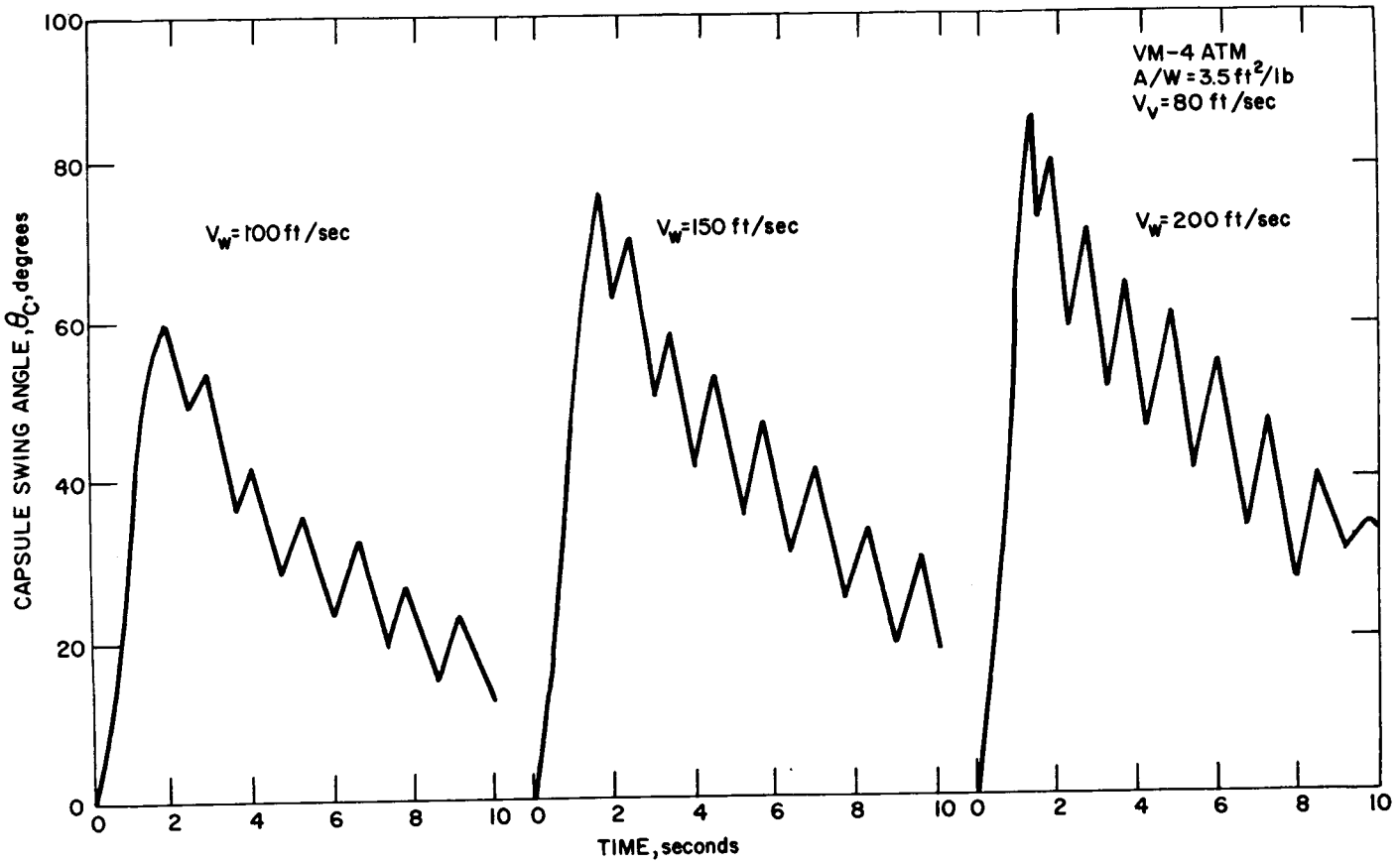

25-1161

Figure 70 CAPSULE SWING ANGLE VERSUS TIME (EFFECT OF GUST MAGNITUDE)

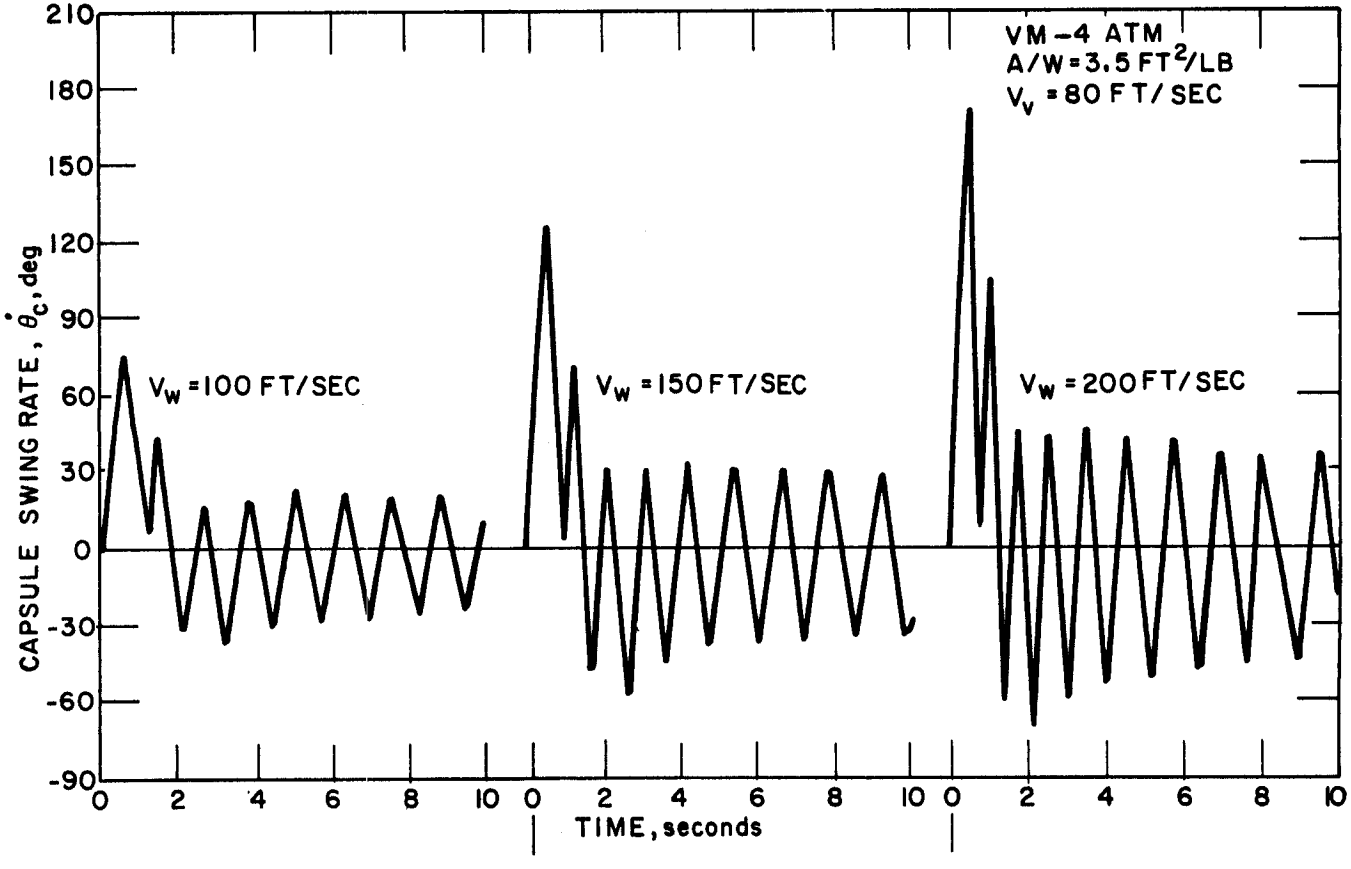

25-1163

Figure 71 CAPSULE SWING RATE VERSUS TIME (EFFECT OF GUST MAGNITUDE)

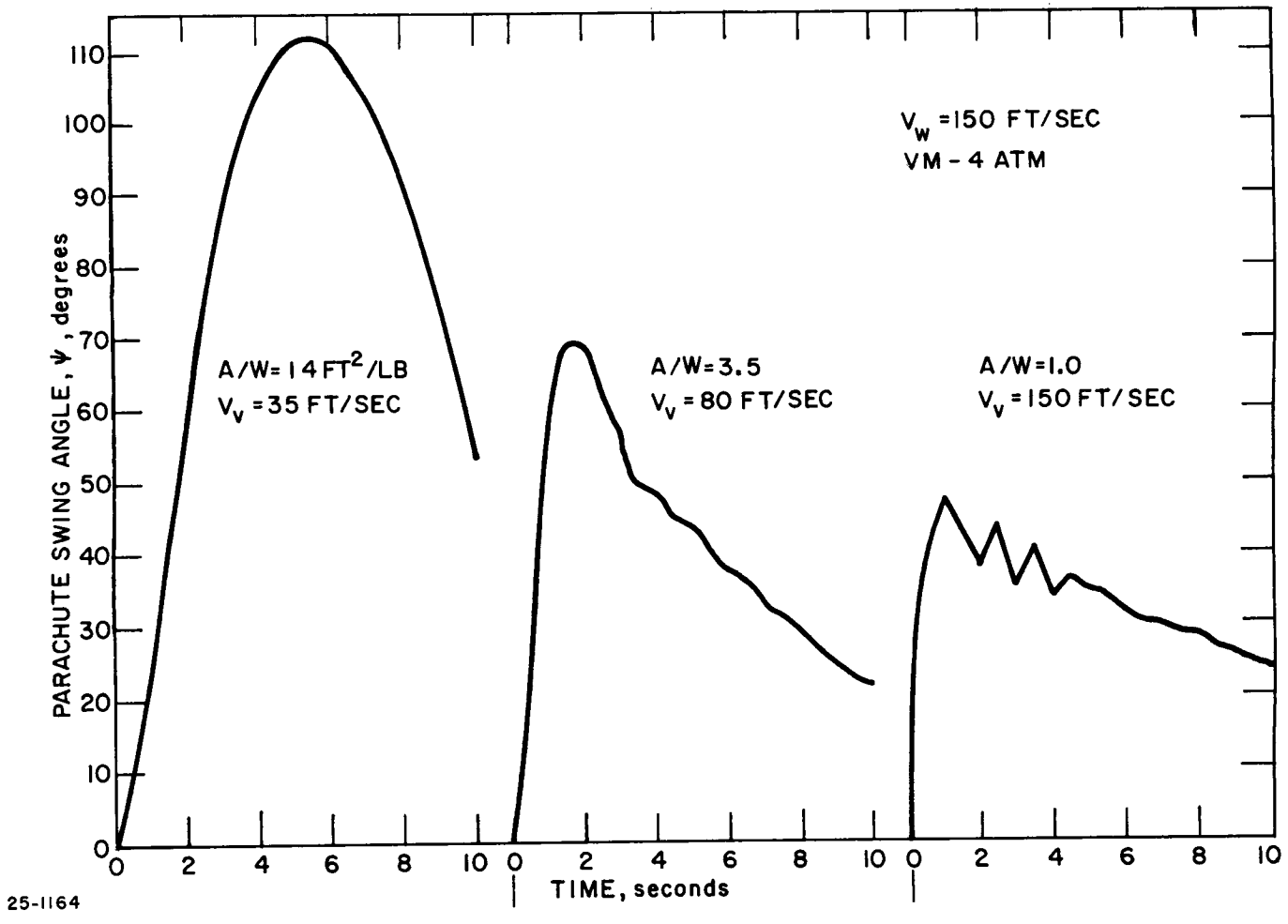

Figure 72 PARACHUTE SWING ANGLE VERSUS TIME (EFFECT OF A/W RATIO)

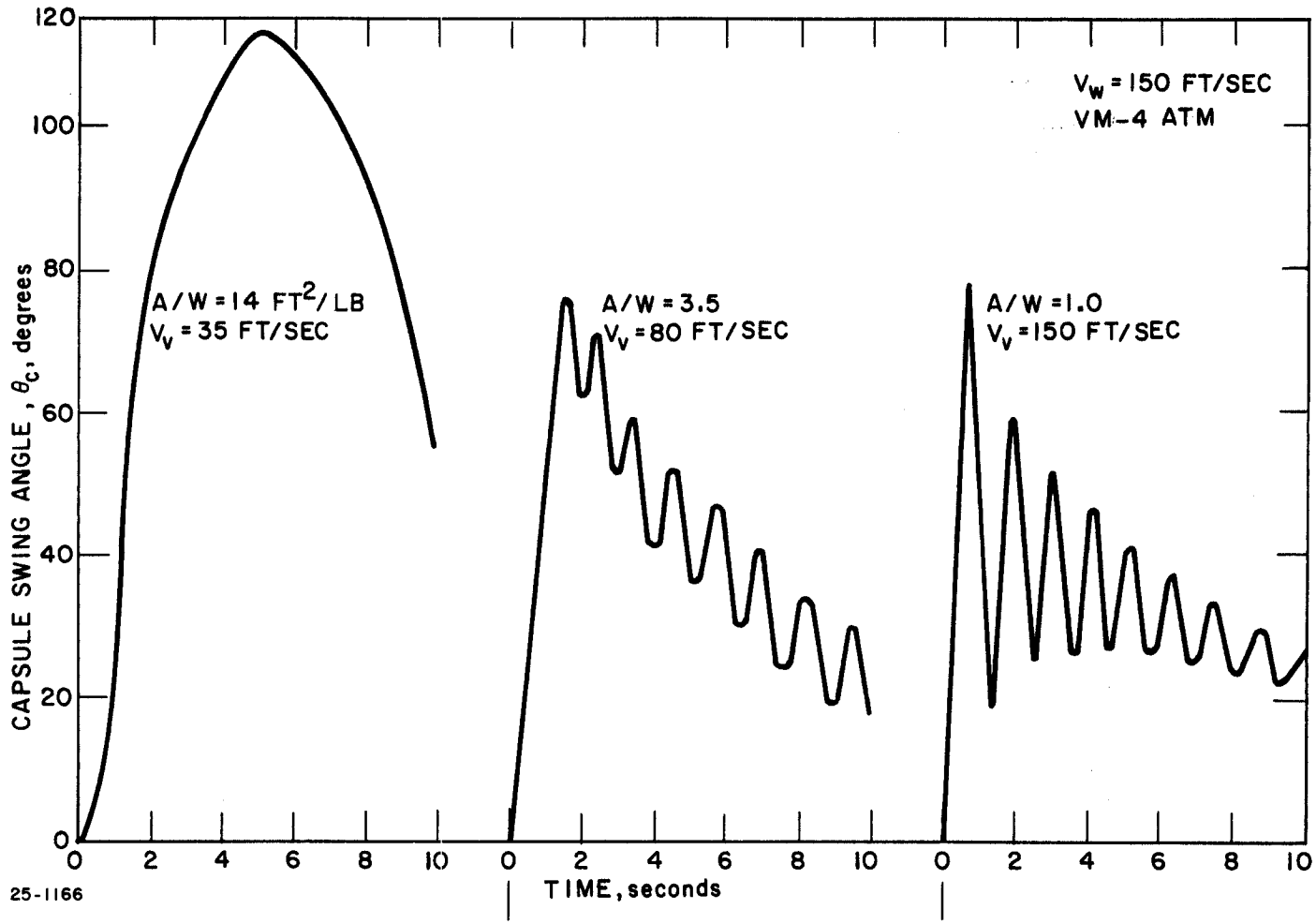

Figure 73 CAPSULE SWING ANGLE VERSUS TIME (EFFECT OF A/W RATIO)

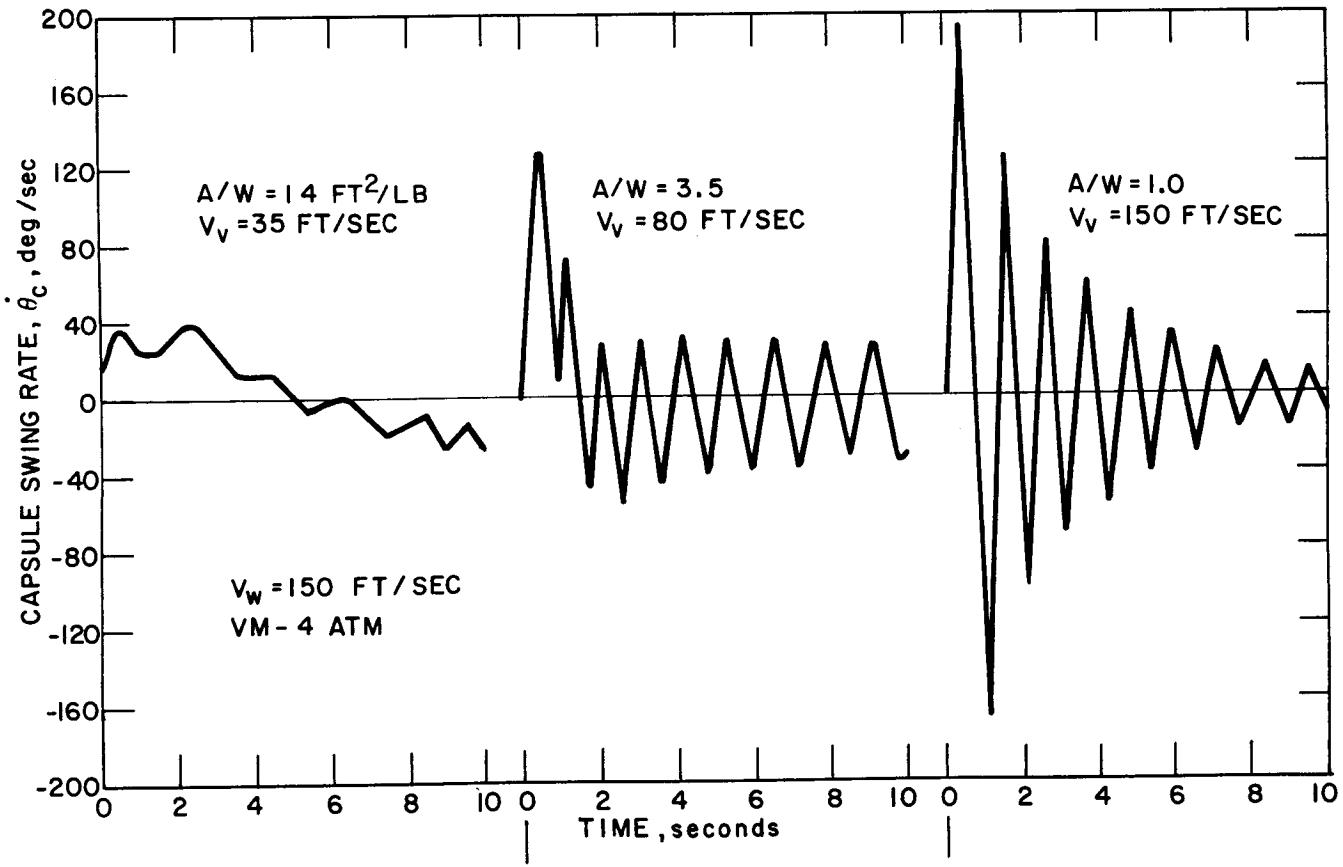

25-1165

Figure 74 CAPSULE SWING RATE VERSUS TIME (EFFECT OF A/W RATIO)

the parachute swing angle is approximately 80 degrees. Figure 73 indicates that for large values of A/W, the capsule swing angle is very high (going above the horizontal), and that as A/W decreases in value to somewhat in excess of 3.5, the minimum peak value of θ_c is reached. Below A/W of 3.5, the θ_c excursions actually increase somewhat, but seem to damp more quickly because of the poorer overall stability of the smaller parachute and coupling of the capsule oscillations into the parachute oscillations. Figure 74 (capsule swing rate $\dot{\theta}_c$) supports the conclusions discussed in Figures 72 and 73, and indicates that perhaps an optimum A/W of about 4.0 to 5.0 exists. Very large values of A/W yield values of ψ and θ_c which are too high and values of $\dot{\theta}_c$ which remain significantly high for too long a period of time. Figure 74 also indicates that very low values of A/W yield higher values of capsule swing rate, $\dot{\theta}_c$.

The above parachute dynamic analysis, showing the influence of a sudden wind gust, indicated angular motion of both the complete parachute system and the suspended capsule. The magnitudes of the angular motions are dependent upon the magnitude of the wind gust and the A/W ratio. A large component of the high angular rates for the suspended capsule is probably due to the attachment concept of a single riser line. Two types of harness attachments are shown in Figure 75; i.e., the single riser-line attachment (reference design) and a four point canopy line attachment. The high angular rates associated with the suspended capsule are due to a single riser-line attachment and can probably be significantly reduced by a different suspension attachment as indicated by the four point attachment illustrated in Figure 75. In this concept the suspended capsule is not hinged at a single point, which to a large degree could be responsible for the high angular rates previously noted.

In the final detailed design system, the single riser-line attachment was chosen since the television subsystem utilizes a two degree-of-freedom gimbal system to counteract the angular motion (see discussion in Volume V, Book 4, paragraph 6.1). In order to evaluate the possible advantages of the other attachment scheme shown in Figure 75, the dynamics computer program, utilized in the previous analysis, must be modified. Note that this type of attachment scheme will necessitate some changes in the deployment system which may be unfeasible. In conclusion, further studies to more fully evaluate the effect of wind gust on the parachute system are required before an optimum design can be established.

2.5.5 System Analyses

In this section, a presentation of the reference parachute system will be discussed. The design constraints, reference trajectories, deployment

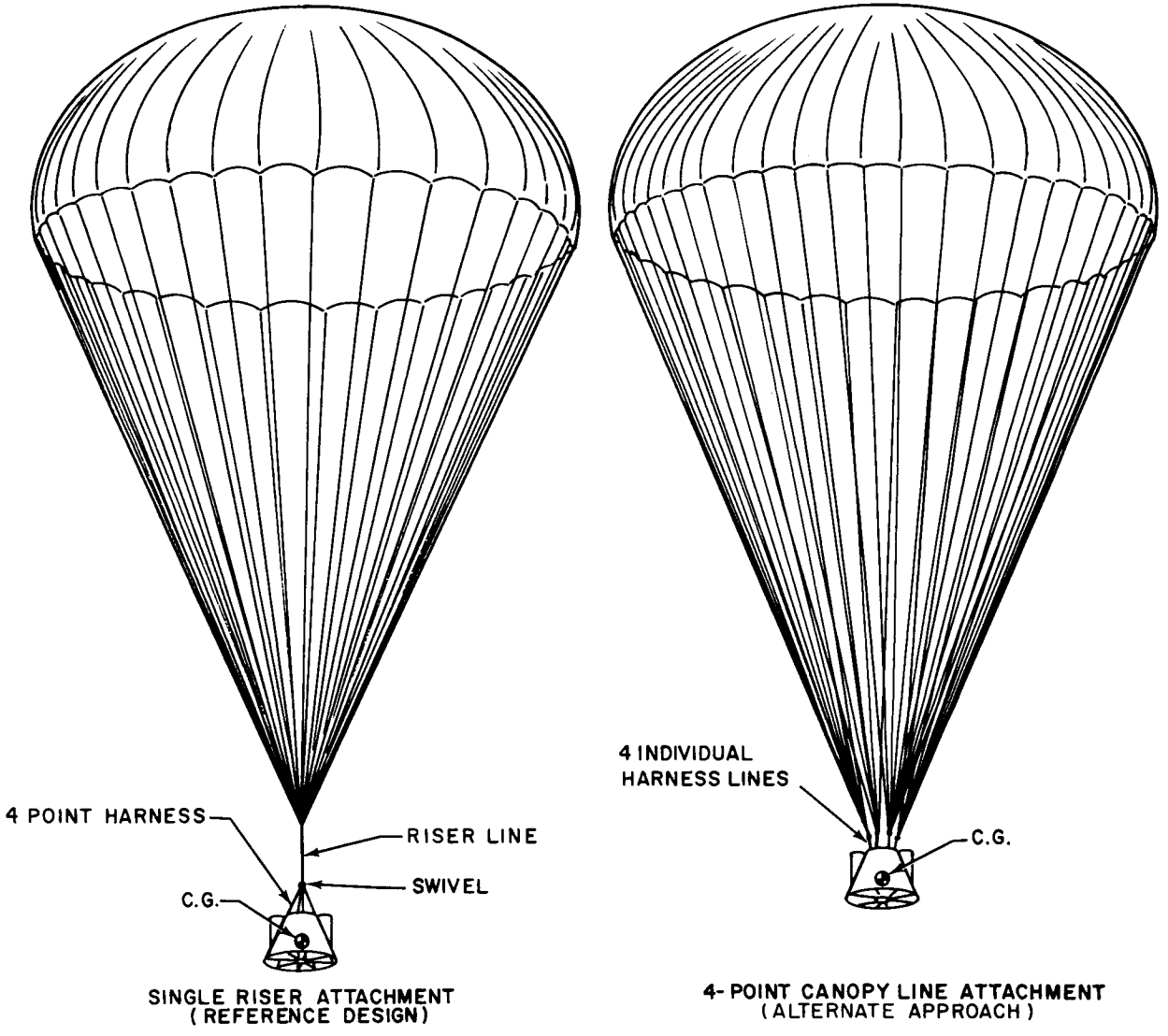

Figure 75 PARACHUTE ATTACHMENT CONCEPTS

conditions, system weights, and dimensions will be discussed in detail. Note that the reference parachute subsystem utilizes a single ring-sail configuration which is fully deployed at a maximum Mach number of 1.2.

2.5.5.1 Design Constraints

The design constraints require that the main parachute be fully deployed and subsonic at a minimum altitude of 15,000 feet. The communications system is such that the total parachute descent time must satisfy both a minimum and maximum requirement during terminal descent. A minimum of 160 seconds is required for atmospheric sampling, television picture taking and data playout. A maximum of 360 seconds is available before the flight spacecraft passes out of communication range in the worst case. The final constraint is opening Mach number which was set at a maximum of Mach 1.2 in order to ensure reliable deployment and operation of the parachute.

2.5.5.2 Reference Trajectories

The vehicle reference M/C_DA is 0.22 slugs/ft^2. For the range of entry velocities and associated entry angles necessary to achieve an entry from orbit, particle trajectories were computed for the various atmospheres considered. Presented in paragraph 2.5.3.3 are the particle trajectory results listed in Tables V through VIII. These tables tabulate the dynamic pressure, the altitude and time at Mach 1.2 for the entire range of trajectories and atmospheres considered. Also shown are the peak vehicle decelerations and the time from peak deceleration to Mach 1.2. Based on the primary initiation and sensing system (discussed in paragraph 2.5.3 of this book) the actual deployment altitudes, Mach numbers and dynamic pressures are shown. The maximum deployment altitude is 27,500 feet and the minimum is 19,900 feet. The deployment Mach number is between 0.70 and 1.2 and the deployment dynamic pressure is between 4.14 and 4.96 lb/ft^2. The parachute stress analysis will be based on a maximum dynamic pressure of 4.96 lb/ft^2.

2.5.5.3 Parachute Sizing

Figure 76 which is a plot of parachute descent time versus full-open altitude for a range of A_{mc}/W_{susp} ratios in the VM-8 atmosphere, indicates that in order to satisfy the minimum descent time requirement of 160 seconds, an A_{mc}/W_{susp} ratio of approximately 4.9 ft^2/pound is required. This ratio is based on the assumption that approximately a 2500-foot altitude loss will be incurred during sensing, initiation, deployment, and inflation of the main parachute. Hence an altitude of 17,400 feet is assumed as the full parachute open altitude based on

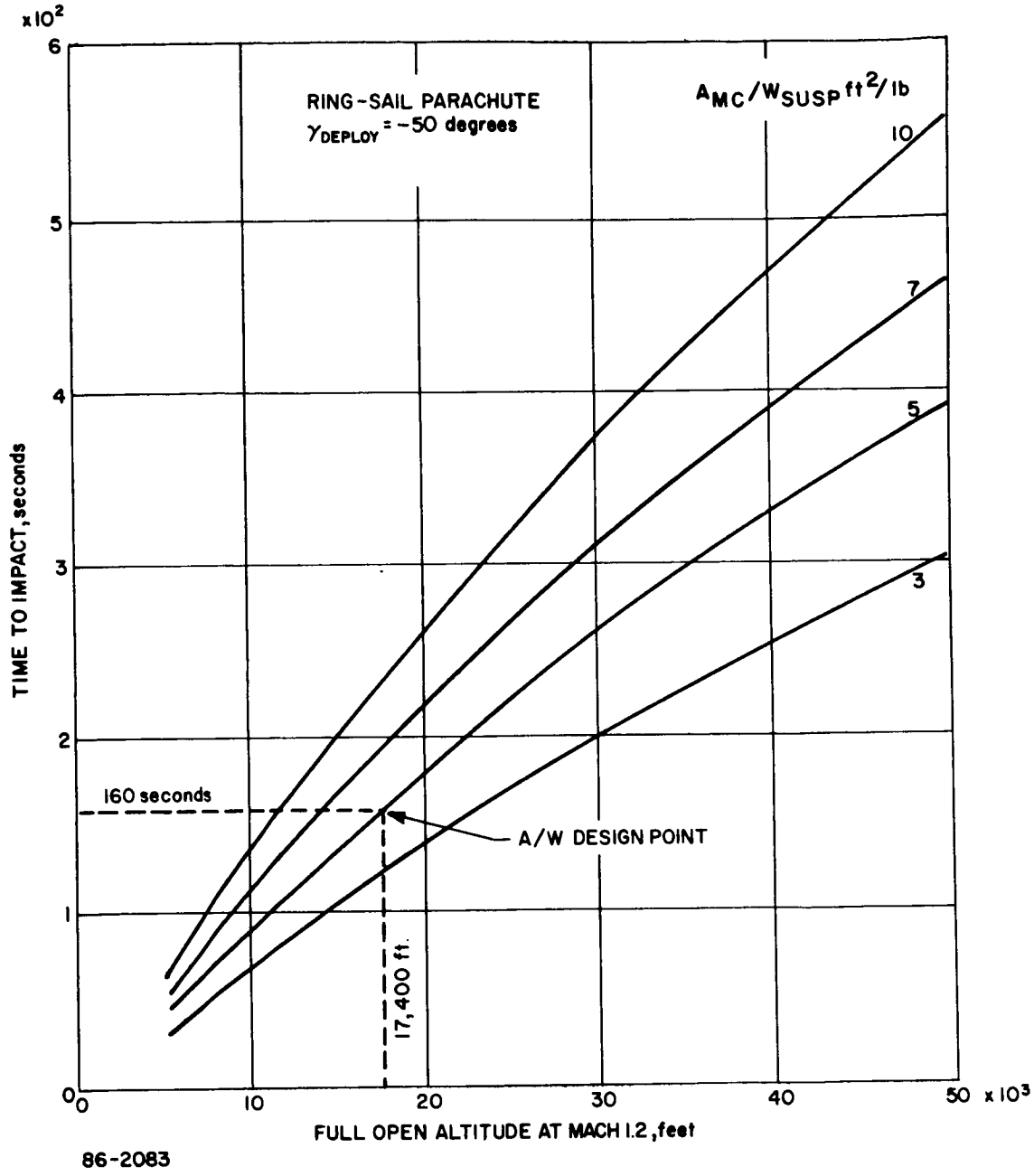

Figure 76 PARACHUTE DESCENT TIME VERSUS FULL-OPEN ALTITUDE IN THE VM-8 ATMOSPHERE

the minimum deployment altitude of 19,900 feet. An A_{mc}/W_{susp} of 5.0 ft^2/lb was chosen as the reference design to allow for additional dispersion in sensing, initiation, deployment, and inflation times.

The reference entry vehicle has a suspended weight of 1025 pounds. Based on this suspended weight and the reference A_{mc}/W_{susp} ratio, Figure 54 indicates that an 81-foot nominal-diameter ring-sail parachute is required. Utilizing these requirements, Table V indicates that for deployment at Mach 1.2 in the VM-3 atmosphere an altitude of approximately 75,000 will result. Under these conditions, a parachute descent time of 660 seconds will result. This exceeds the maximum required descent time by some 300 seconds (a requirement established to maintain communications with the flight spacecraft). Hence, in order to ensure descent times within the minimum and maximum range for all considered atmospheres and trajectories, a restriction on the deployment altitude must be imposed. For the VM-7 atmosphere, a deployment altitude of approximately 27,500 feet is required for minimum descent time considerations. Therefore, the radar altimeter and the peak g time computation are combined into an electrical circuit such that parachute deployment occurs when the altitude is less than 27,500 feet and the Mach number is less than 1.2 (both conditions must be satisfied).

Effect of the model atmosphere on the parachute descent time are presented in Figure 77 for the reference A_{mc}/W_{susp} of 5.0 ft^2/lb. Table X summarizes the minimum and maximum parachute descent times for both primary and backup deployment modes. Note that for the primary deployment mode, the minimum and maximum time constraint is satisfied and for the backup modes, at least 50 percent of the minimum required descent time is achieved in all cases and the maximum time is surpassed by approximately 100 seconds in only the VM-3 atmosphere.

The vertical impact velocities for the A_{mc}/W_{susp} ratio of 5.0 ft^2/lb are 90, 68, 128, and 89 ft/sec in the VM-3, 4, 7, and 8 atmospheres, respectively.

2.5.5.4 Stress Analysis and Weight Calculations

The following section is a presentation of the stress analysis and weight calculations for the reference design. The design parameters are as follow:

main parachute configuration	ring-sail
main parachute nominal diameter	81 feet

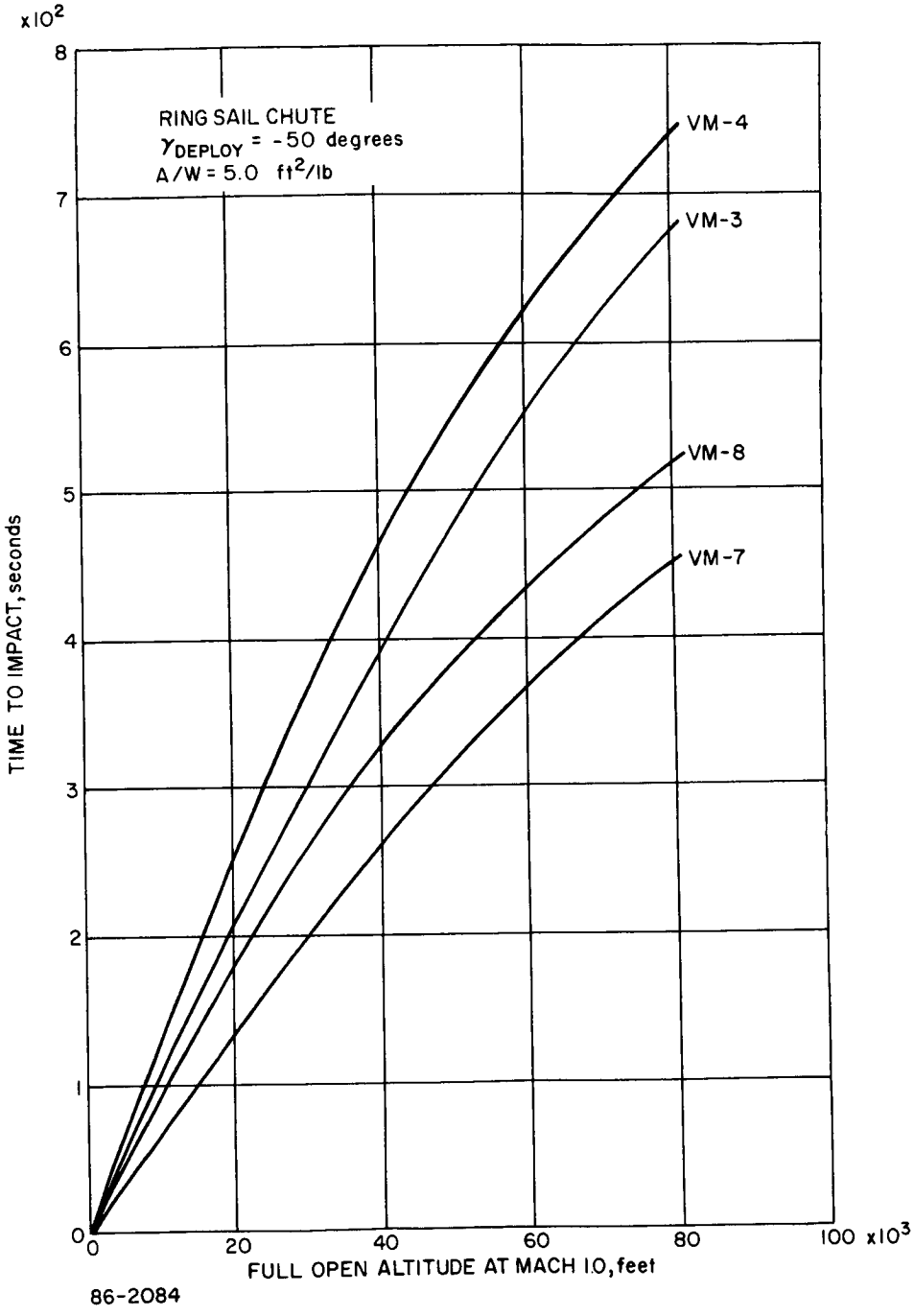

Figure 77 PARACHUTE DESCENT TIME VERSUS FULL OPEN ALTITUDE (A/W = 5.0 ft^2/lb)

TABLE X

MAIN PARACHUTE DESCENT TIME SUMMARY -- PRIMARY AND BACKUP MODES

			Primary (M = 1.2)		Accelerometer Backup (M = .85)		Altimeter Backup	
Atmosphere	V_e (ft/sec)	γ_e (degrees)	Z_{Deploy} (feet)	Descent Time (seconds)	Z_{Deploy} (feet)	Descent Time (seconds)	Z_{Deploy} (feet)	Descent Time (seconds)
3	12,000	-13.7	27,500	258	49,000	452	19,000	176
	15,000	-15.0	27,500	258	50,400	465	19,000	176
4	12,000	-13.7	27,500	322	29,400	343	19,000	221
	15,000	-15.0	27,500	322	28,200	331	19,000	221
7	13,000	-14.4	27,500	170	14,900	84	19,000	112
	15,000	-15.0	27,500	170	20,200	121	19,000	112
8	12,000	-14.7	19,903	163	15,300	112	19,000	153
	15,000	-15.0	24,300	199	13,900	109	19,000	153

main parachute effective drag area	3610 ft^2
main parachute shock load factor	1.05
pilot parachute configuration	ring-slot
pilot parachute nominal diameter	9 feet
pilot parachute effective drag area	44.5 ft^2
pilot parachute shock load factor	1.1
maximum opening dynamic pressure	4.96 lb/ft^2
packaging density	35 lb/ft^3
pilot parachute mortared velocity	100 ft/sec
main parachute ejection velocity (gas generator)	30 ft/sec
A/W ratio	5.0 ft^2/lb

In order to establish the component weights of the parachute assembly, it is necessary to calculate the maximum opening shock load on both the pilot parachute and the main parachute.

1. Maximum Opening Shock Load -- The maximum opening shock load on the ring-sail parachute is expressed as,

$$F_o = Xq\, C_D A$$

where,

X = opening dynamic shock load factor

q = opening dynamic pressure, lb/ft^2

$C_D A$ = effective drag area based on either nominal or projected diameter, ft^2.

$$F_o = 1.05\ (4.96)\ (0.7)\ 3610 = 18{,}800 \text{ pounds}$$

Similarly the maximum opening shock load for the pilot parachute can be calculated as,

$$F_o = 1.1\ (4.96)\ 44.5 = 243 \text{ pounds}$$

In addition to the shock load, an overall strength factor (k) must be included in order to make weight calculations for the canopy, suspension lines, and riser line. The strength factor (K) is expressed as,

$$K = \frac{je}{\mu ac}$$

where,

j = standard factor of safety

e = assymetric loading factor

μ = joint efficiency factor, strength loss at connection of suspension line and drag producing surface (canopy)

a = factor related to strength loss by abrasion

c = factor related to suspension line convergence angle

The following table summarizes the above factors for canopy, suspension line, and riser line design.

Design Component	j	e	μ	a	c	K
Canopy	1.3	1.5	0.8	0.95	0.95	2.7
Suspension lines	1.3	-	0.85	0.95	0.95	1.7
Riser line	1.3	-	0.85	0.95	0.95	1.7

2. Main Parachute Canopy Weight -- In calculating the stresses on the main parachute canopy (sail), a good approximation is to assume the model to be hemispherical in shape. Hence the stress on the canopy can be calculated by utilizing a thin-wall hemisphere approach, the expression of which is

$$S = \frac{Kq\,D_o}{4t} \text{ lb/in.}^2$$

where K is the overall strength factor, q is the pressure acting uniformly on the hemisphere, D_o is the nominal parachute diameter and t is the thickness of the material. A more common parachute terminology is to express the loading in lb/in. of length of cloth. This yields,

$$L = St = \frac{Kq\,D_o}{4} \text{ lb/in.}^2$$

therefore,

$$L = \frac{2.7\,(4.96)\,81}{4} = 27.1 \text{ lb/in.}$$

Nylon cloth fabric with a break strength of approximately 35.0 lb/in. weighs 0.8 oz/yd^2. Utilizing this canopy fabric material it is possible to sustain about a 25 percent strength degradation due to sterilization and other environmental effects. The total canopy weight can be closely approximated by assuming the total surface area to be hemispherical.

Hence,

$$\text{Area}_{\text{canopy}} = \frac{\pi D_p^2}{2} = \frac{\pi\,[0.7\,(81)]^2}{2} = 5050 \text{ ft}^2$$

and

$$\text{Weight}_{\text{canopy}} = \frac{0.8\,(5050)}{144} = 28.1 \text{ pounds}$$

3. Main Parachute Suspension Lines -- From past experience in the Mercury and Gemini programs, it has been established (reference Northrop/Ventura) that the optimum length of the suspension lines is 1.15 times the nominal parachute diameter; this is based on drag efficiency and weight penalty. It has also been established that the distance between suspension lines at the canopy outer edge should be no greater than 4 feet in order to avoid scalloping of the canopy and an attenant loss in drag coefficient. Utilizing 48 suspension lines, the distance between lines is 3.71 feet at the canopy outer edge. The load on each line is,

$$F = \frac{KF_o}{N} = \frac{1.7\,(18{,}800)}{48} = 667 \text{ lb/line}$$

The total length of line required is,

$$L_s = 1.15\ D_o N = 1.15\ (81)48 = 4470 \text{ feet.}$$

Nylon cord MIL-Spec-C-5040B (see Reference 8), utilized for the suspensions lines, has a break strength of 750 pounds and weights 0.00605 lb/ft (55 yds/lb). Hence, the total weight of the suspension lines is,

$$\text{Weight}_{\text{suspension lines}} = (4470) \text{ ft } (0.00605) \text{ lb/ft} = 27.1 \text{ pounds}$$

4. Main Parachute Riser Line -- A 10-foot riser line (L_R) has been selected in order to further alleviate the possibility of suspension line wrap-up with the suspended capsule and/or harness assembly. This dimension, combined with the suspension lines, more than satisfies flow field requirements which call for inflation of the canopy at a minimum of five vehicle diameters behind the primary body.

Eight Nylon webbings are placed together (as the riser) and then branch out such that each webbing picks up six suspension lines in a group (see Figure 78). The load on the riser line (each webbing) is,

$$F = \frac{KF_o}{N} = \frac{1.7\ (18{,}800)}{8} = 4000 \text{ pounds}$$

Nylon webbing MIL-Spec-W-27657 (see Reference 8), used for the riser lines, has a break strength of 4000 pounds and weighs 1.25 oz/yd. Hence, the total weight of the riser line is expressed as,

$$\text{Weight}_{\text{riser line}} = NL_R w$$

where w is the unit webbing weight of,

$$1.25\ \frac{\text{oz}}{\text{yd}}\ (0.0261 \text{ lb/ft}).$$

Hence, the riser line weight becomes,

$$\text{Weight}_{\text{riser line}} = 8(10)\ (0.0261) = 2.1 \text{ pounds}.$$

The weight of the collars and attachment fittings is approximately 0.5 pounds.

5. Pilot Parachute Canopy Weight -- The shock load on the ring-slot pilot parachute canopy is such that minimum weight nylon fabric can be utilized, i.e., 0.80 oz/yd^2. A nine-foot nominal diameter chute has been selected as having adequate drag force to pull the main chute from its canister. The total pilot chute canopy weight can be calculated similar to the main chute by assuming the total surface area to be hemispherical. Hence,

$$\text{Area}_{\text{canopy}} = \frac{\pi D_p^2}{2} = \frac{\pi [0.7\ (9)]^2}{2} = 62.4 \text{ ft}^2$$

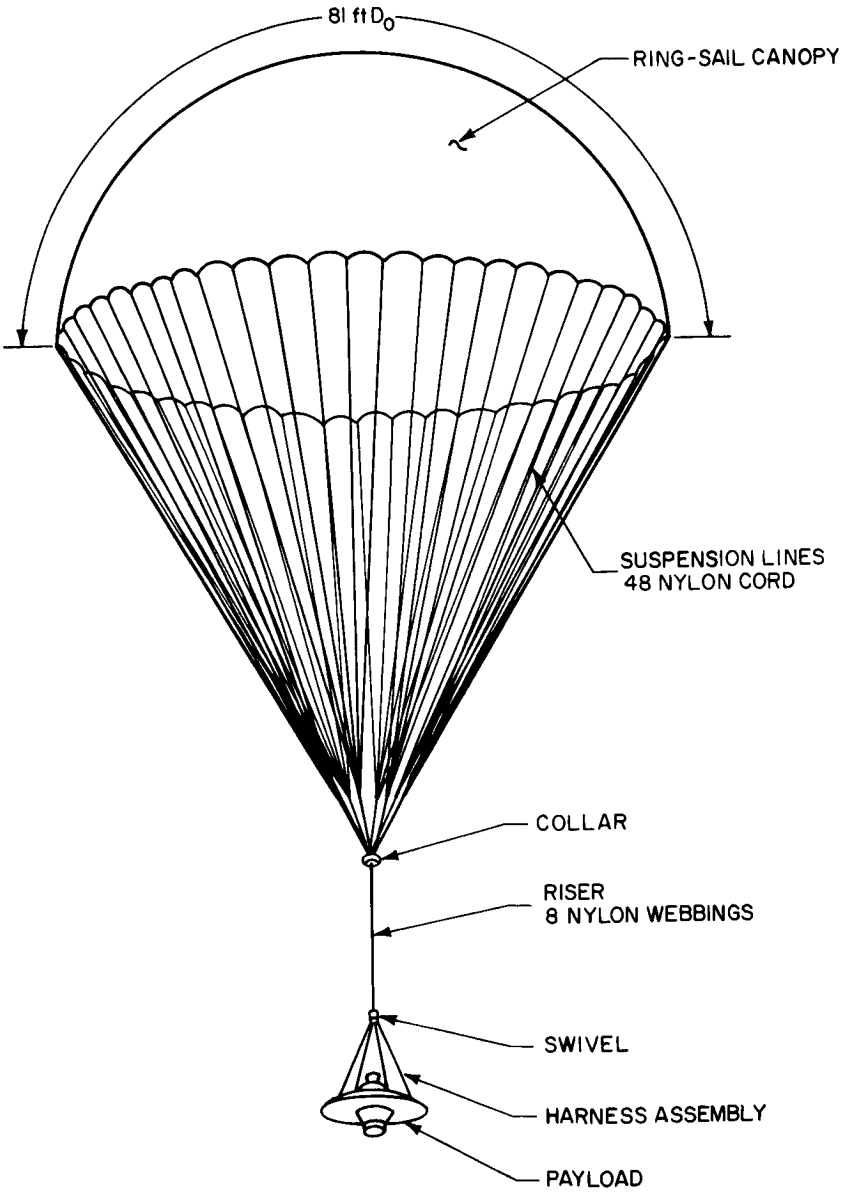

86-2085

Figure 78 MAIN PARACHUTE ASSEMBLY (RING-SAIL)

and

$$\text{Weight}_{\text{canopy}} = \frac{0.8(62.4)}{144} = 0.35 \text{ pounds} .$$

6. Pilot Parachute Suspension Lines -- Utilizing eight suspension lines results in approximately 2.43 feet between lines. The load on each line is,

$$F = \frac{KF_o}{N} = \frac{1.7(243)}{8} = 51 \text{ pounds} .$$

The total length of line required is,

$$L_s = 1.15 D_o N = 1.15 (9) 8 = 83 \text{ feet}.$$

Nylon cord MIL-Spec-C5040B (see Reference 8) used for the suspension lines, has a break strength of 100 pounds and weighs approximately 9.5×10^{-4} lb/ft (350 yd/lb). Hence, the total weight of the suspension lines is,

$$\text{Weight}_{\text{suspension lines}} = 83 (9.5 \times 10^{-4}) = 0.08 \text{ pounds} .$$

7. Pilot Parachute Riser Line -- The riser line of the pilot parachute must be long enough to allow for the main parachute to be pulled from its canister. It is recommended that it be at least five vehicle diameters behind the primary body inflation. Hence, a 75-foot riser line has been selected. Assuming the use of a single webbing, the load on the riser line is 413 pounds including an overall strength factor of 1.7. Nylon webbing MIL-Spec-W-4088D (see Reference 8), used for the riser line, has a break strength of 500 pounds and weighs 0.28 oz/yd. The total weight of the riser line is,

$$\text{Weight}_{\text{riser line}} = \frac{75(0.28)}{48} = 0.44 \text{ pounds} .$$

The total weight of the pilot chute including the canopy, lines and collars, etc., is 1.0 pound.

8. Swivel -- A standard swivel similar to Irvin swivel series SCD 3003 is capable of withstanding a basic load of 20,000 pounds and weights 2.0 pounds.

9. Harness Assembly -- The harness assembly, used to attach the suspended capsule to the main riser line, is made of Nylon webbing. The assembly is made up of four, 8-foot lines which come to a confluence point and tie into the bottom end of the swivel. Assuming that the total opening shock load of the main parachute will be resisted by a minimum of two lines, each line must be designed to sustain a 9400-pound load. the harness lines are constructed of Nylon webbing, MIL-Spec-W-27657 Type VI (see Reference 8), which has a break strength of 10,000 pounds and weighs 2.7 oz/yd. The total weight of the harness webbing is,

$$\text{Weight}_{\text{harness}} = \frac{2.7(32)}{48} = 1.8 \text{ pounds} .$$

Including attachment fitting, etc., the total weight of the harness assembly is 2.3 pounds.

10. Main Parachute Canister -- The main parachute canister contains the ring-sail canopy, shroud lines, deployment bag, and the gas generator bag. Based on a packing density of 35 lb/ft^3 an internal volume of approximately 1.75 ft^3 is required. Figure 79 shows the location of the canister and the approximate dimensions. The canister shell is made of 0.028-inch aluminum and the total weight of the assembly including the gas generator charge, bag, canister shell, and cover is approximately 5.0 pounds. In the event the main parachute is ejected by the gas generator (required ejection velocity of 30 ft/sec) the reaction load is 2400 pounds based on a 16-inch stroke.

11. Pilot Parachute Canister -- The pilot parachute canister is essentially a mortar tube. The canister contains the pilot parachute canopy, shroud lines and the sabot assembly. Figure 79 shows the location of the canister and the approximate dimensions. Based on a packing density of 35 lb/ft^3, an internal volume of approximately 0.03 ft^3 is required. The shell of the mortar tube is made of 0.028-inch aluminum. The total weight of the canister including the shell, sabot, charge (breech), cover and inertial weight (6 ounces) is 1.9 pounds. Based on an ejection velocity of 100 ft/sec and a 6-inch stroke, a 1250-pound reaction load can be expected.

12. Weight Summary -- The weight of each of the components is listed below and results in a total parachute subsystem weight of 70.0 pounds.

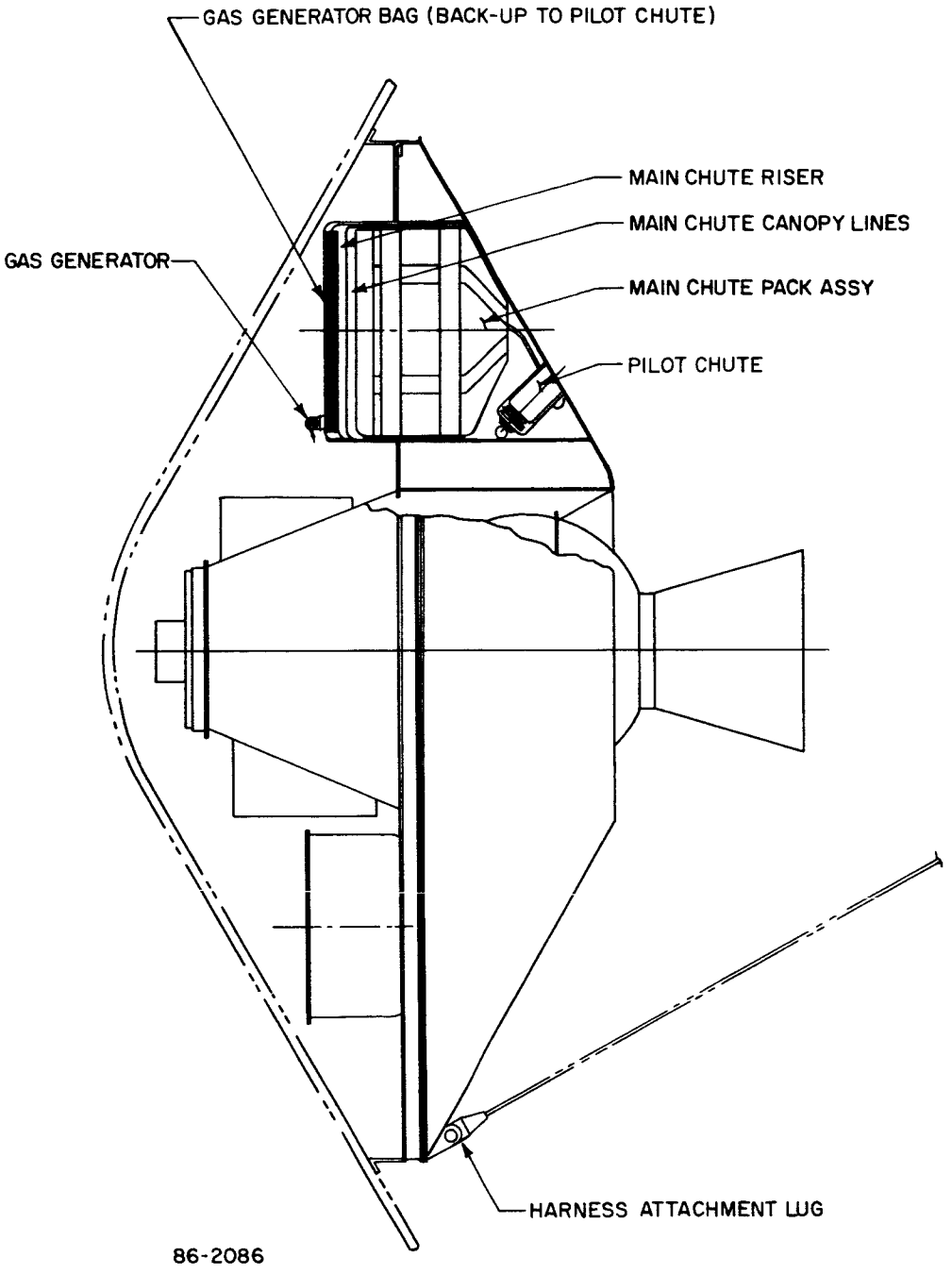

Figure 79 PARACHUTE CANISTER INSTALLATION

WEIGHT SUMMARY

Component	Component Weight (pounds)	Total (pounds)
Main Chute		57.80
ring-sail canopy	28.10	
suspension lines	27.10	
riser line	2.10	
collars and attachments	0.50	
Pilot Chute		1.00
ring-slot canopy	0.35	
suspension lines	0.08	
riser line	0.44	
collars and attachments	0.13	
Harness assembly	2.30	2.30
Swivel	2.00	2.00
Main chute canister	5.00	5.00
Pilot chute canister	1.90	1.90
Total subsystem weight		70.00

2.6 SIGNIFICANT PROBLEM AREAS

There exists five rather significant problem areas in the parachute descent system which could, for the most part, be resolved via early flight and ground-development tests.

2.6.1 Supersonic Deployment

Successful operational deployment of the ring-sail configuration at slightly above sonic velocities (Mach 1.2) has yet to be accomplished. One or two flight tests have deployed the ring-sail parachute at Mach 1.2 with slightly less than favorable results. The ring-sail canopy, which has been used in the Mercury, Gemini and Apollo programs, is basically a subsonic parachute having been most successfully deployed between Mach 0.3 and 0.6.

It is believed that Mach 1.2 operation is possible provided the parachute is properly designed from a strength standpoint. However, early flight test to prove the operational deployment of this configuration at Mach 1.2 is necessary.

2.6.2 Low Inflation Pressures

In light of the latest model atmospheres it is estimated that the opening inflation pressures for the parachute could be as low as 4.0 lb/ft^2. These low inflation pressures combined with Mach 1.2 deployment could create inflation problems for the large proposed main parachute (81 feet nominal diameter). Flight test combined with those indicated in paragraph 2.6.1 are necessary.

2.6.3 Wind Gust Oscillations

Dynamic computer results have indicated that severe oscillations of the main parachute and suspended capsule exists for wind gust above 150 ft/sec. These oscillations could greatly effect the performance of the entire suspended capsule, particularly the television and communications subsystems. Paragraph 2.5.4 of this book discusses the effects of wind gust in some detail. More work is needed in this area with a clearer definition of the wind environment, magnitude, application and duration.

2.6.4 Blunt Body Effects

The flow field behind a blunt body could be very turbulent for an extended distance and may seriously affect the inflation and performance characteristics of the chute. Wind-tunnel testing is necessary to evolve the optimum shroud line lengths necessary to negate any possible effects due to deployment behind a blunt forebody.

2.6.5 Parachute Materials

One of the most pressing problems is the selection of a light-weight canopy material which will withstand all of the prelaunch, flight, and descent environments. The thermal sterilization criterion is the most critical of these environments with respect to canopy material strength. Present indications are such that thermal sterilization degrades the tensile strength of some of the candidate materials such as Nylon, Dacron, and to some extent Nomex.

Present available thermal sterilization data, on the current candidate materials, is incomplete and does not afford the designer enough information to select the most efficient lightweight canopy material. As an example, a specially heat-treated Nylon (type 330) has not been thoroughly tested under the proper environment of thermal sterilization. It is quite possible that

this material would degrade only slightly. (Northrop Ventura has an in-house program which recently indicated that type 330 nylon degrades only 20 to 25 percent under thermal sterilization).

A complete development and test program is required in the area of thermal sterilization in order to firmly establish the selected canopy material. The test program should also, to a lesser extent, include the effects of chemical sterilization (ethylene-oxide bath), radiation and vacuum.

2.7 FUTURE CONCEPTS

Future concepts in the area of recovery systems for Martian landers is quite dependent upon the actual surface pressure and density of the atmosphere. For surface pressures of 7 to 10 mb, present parachute designs and configurations for single parachute systems would not be useful for landed capsules above 1200 to 1500 pounds if the maximum impact velocity were 50 ft/sec in the least dense atmosphere.

New parachute configurations are appearing which may result in increased performance and system weight savings. The annular configuration (Northrop Ventura) is presently entering development and shows promise of weight savings with improved low density performance compared to present candidate configurations.

An additional configuration which warrants serious considerations is the Clover-Leaf concept which is also in the development stage. The results of the current Air Force development program being conducted by Northrop Ventura shows definite promise of substantial weight savings. The Clover-Leaf parachute with its gliding capability would provide a means of negating the wind shear prior to touchdown by including a drift meter hookup in the control system. Negating the wind velocity would result in weight savings in the impact system. However, one should note the additional complication with accompanying reduction in reliability in utilizing such a system.

3.0 IMPACT ATTENUATION SUBSYSTEM FOR LANDED CAPSULE (ENTRY FROM APPROACH TRAJECTORY)

3.1 SUMMARY

Of the various methods of attenuating the landing impact shocks of landers, the use of crushable materials appears to offer distinct advantages over other methods. In particular, the requirement for essentially omnidirectional protection, in turn brought about by the 100 ft/sec horizontal wind velocity condition, eliminated or rendered infeasible most other schemes, with the possible exception of air bags. Air bags were investigated and found to be heavier and much less reliable than crushable material designs.

The candidate materials for use in the system included balsa wood and various honeycombs. Plastic honeycombs were preferred over metal, since it is desirable that the impact attenuator be transparent to radio frequency signals. This characteristic would eliminate the necessity for removing the impact attenuator after impact in some designs.

The particular material chosen for this application is a flass-cloth reinforced plastic honeycomb with polyurethane foam-filled cells; this composite crushes during impact, dissipating the energy in the crushing process. This material accomplishes the energy dissipation while limiting the peak deceleration level experienced by the internal payload to 500 g at the nominal impact velocity of 130 ft/sec (80 ft/sec vertical descent velocity with the 100 ft/sec horizontal wind speed) for a landed capsule in an oblate spheroid configuration. The foam-filled fiberglass honeycomb material accounts for more than 30 percent of the total landed weight. The use of balsa wood instead would result in more payload weight but at the expense of much higher g levels. In fact, the g level for the reference design would exceed the 1000-g maximum which was the ground rule established for this study.

Several lander geometries were considered in the parametric study, including spherical, prolate and oblate spheroids. The oblate spheroid is the reference geometry, but this decision was not made on the basis of the parametric results reported below. Considerations of stability and orientation after impact, as well as compatibility of the shape with the various entry vehicles, were more influential in making this decision than were the tradeoffs in impact attenuation system characteristics.

The most critical problem area encountered at the present time is the very low density crushable material which is required to obtain the desired performance. This low density material may prove difficult to manufacture and may not perform as well as tests on higher density samples would lead one to expect. Sould this problem be insurmountable, balsa wood, with its attendant high g levels, may be used in the design.

3.2 ANALYSIS METHODS AND RESULTS

3.2.1 Introduction

In arriving at the present choice of method and material for the impact attenuation system, many alternative approaches were considered. The necessity for omnidirectional protection eliminated many schemes such as penetration spikes and liquid shock absorbers. Most of the parametric study effort was directed towards crushable materials and air bags. Study results of these investigations are presented below.

3.2.2 Survey of Crushable Materials

The first step in this program involved the gathering of data on presently available crushable materials. Figure 80 summarizes these data; it is a plot of crushing stress versus bulk density (Reference 9 through 23.

One other parameter used to characterize these materials is the usable strain, ϵ. This parameter indicates the extent to which a material can be deformed at essentially constant stress. For balsa wood and for most honeycomb materials, the usable strain is of the order of 70 to 80 percent; for plastic foams, on the other hand, ϵ is typically 50 to 60 percent.

Several interesting features are exhibited by Figure 80. First, the materials tend to group themsleves into three broad categories. The first can be termed the balsa wood class (which includes some honeycombs, as can be seen). The second may be called the honeycomb class and the third the plastic foam class. If, instead of crushing stress, the product of crushing stress and usable strain were used as the ordinate for this curve, the gap between the honeycomb class and the plastic foam class would be much more pronounced, due to the difference in usable strains discussed above. This product (stress x strain), is a useful one for many applications, incidentally, since it represents the energy absorbed per unit volume of material.

Another interesting feature is the fact that while most aluminum, paper and glass-cloth reinforced plastic honeycombs lie in a narrow band of properties, several honeycombs are in the balsa wood class.

It should also be noted that there is considerable scatter in the balsa wood results.

All of the commonly used crushable materials exhibit anisotropic behavior to some degree. Honeycombs are strongest when loaded in a direction parallel to the cell axes, and balsa wood is strongest under loads aligned with the grain. Even many plastic foams tend to be stronger in the direction of foam rise. Some data on anistropy of various materials are presented on Figure 81. It should be noted that for some materials, the only data available are for crushing stress in the strongest direction and normal to this direction.

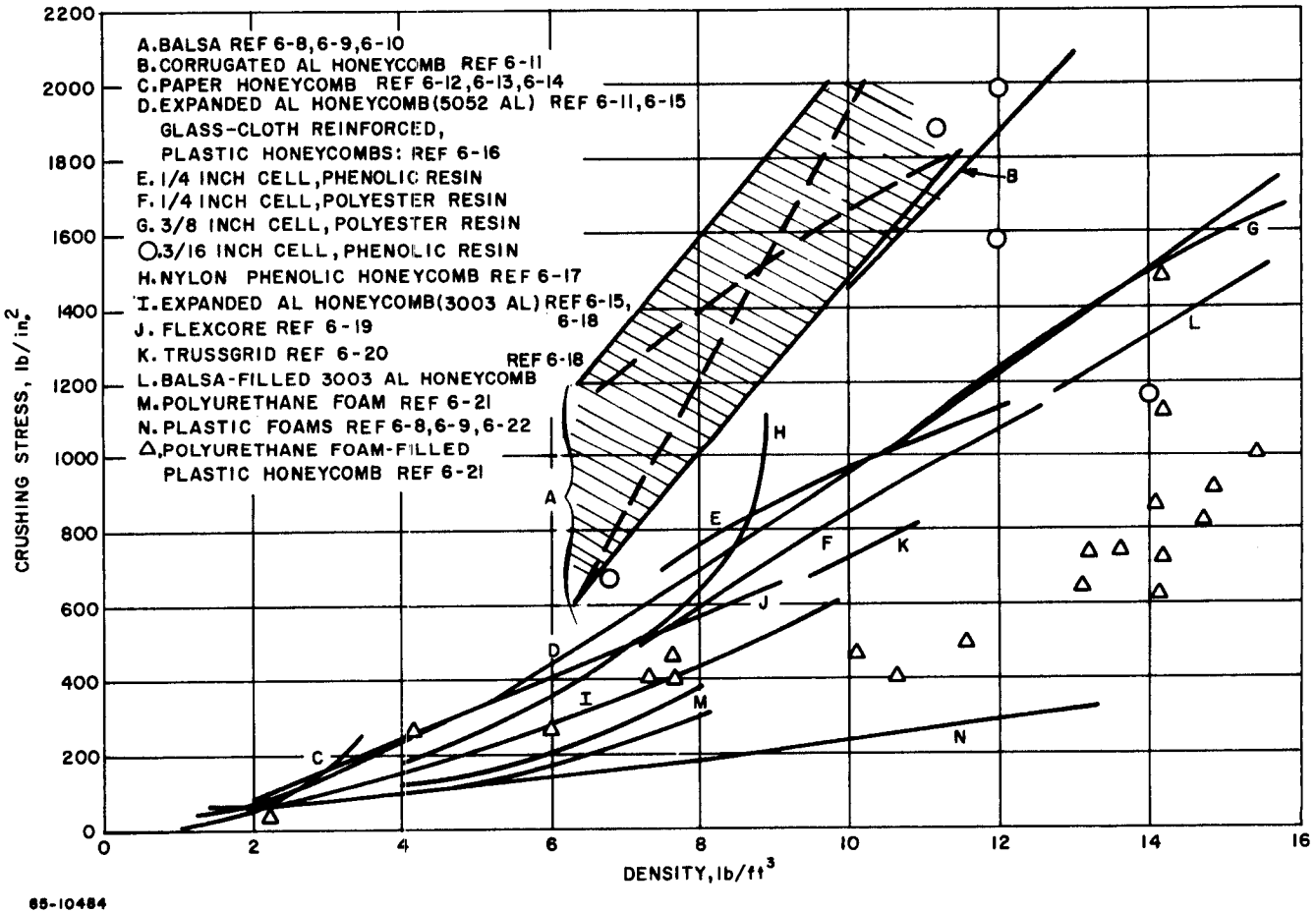

65-10484

Figure 80 PROPERTIES OF CRUSHABLE MATERIAL

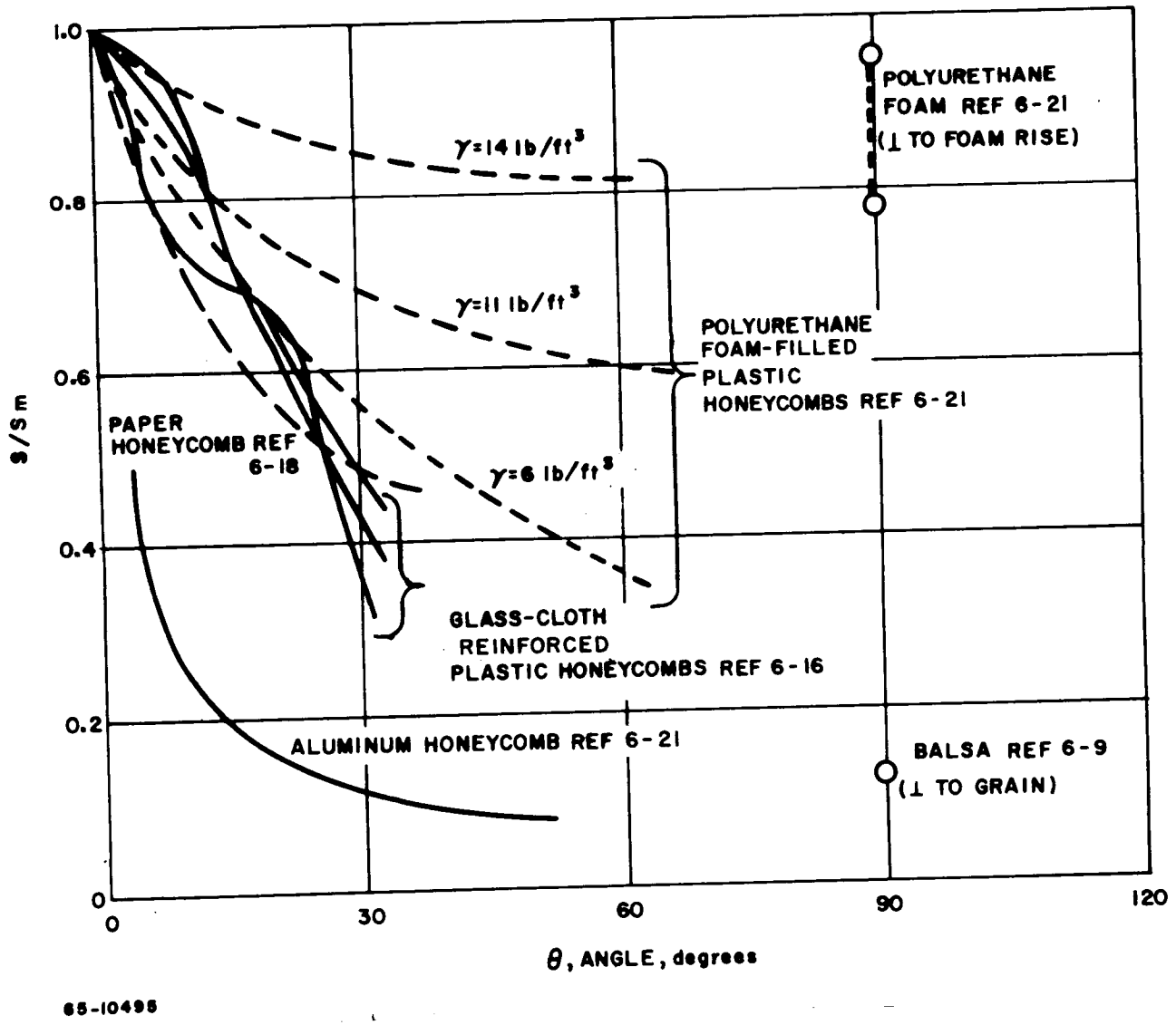

Figure 81 ANISOTROPHY OF CRUSHABLE MATERIALS

In the parametric study portion of this program, plastic foams used alone were not considered, as the efficiency of this material is too low for the present application.

The particular material chosen from the honeycomb class of materials is a polyurethane foam-filled, glass-cloth reinforced, plastic honeycomb, which was developed recently at Avco/MSD under company-funded research. The highlights of this test program are described in the following section.

Some balsa wood samples were also tested in-house in order to determine some properties, particularly in regard to anisotropic behavior, which have not been reported in the literature. Pertinent information from this test program are described in the following sections.

3.2.3 Foam Filled Fiberglass Honeycomb

In the first part of this section, the company-funded experimental program which led to the development of this impact attenuation material is outlined, while the second part deals with the parametric studies which were performed using the properties determined from the test program.

3.2.3.1 Experimental program

Impact tests were performed on polyurethane foam filled fiberglass honeycomb. The principal advantage of foam filling was shown to be the marked improvement in angular impact energy absorption characteristics as compared to the performance for glancing impact in unfilled systems.

An objective of this program was to suggest the possibility of manufacturing impact energy absorption materials to predetermined performance levels using, in particular, materials which would exhibit good radio frequency transparency. In order to delineate the potential of this type of material, some of the effects of honeycomb cell size, the variation of foam density, and the influence of additional resin dipping on mechanical behavior have been studied. In addition, preliminary tests were conducted to determine the effects of long time exposure to temperatures of +300° F, the sterilization temperature. Tests were performed while holding the specimen at temperatures of -100° F and +200. F since these represent typical limits for space vehicles.

All of these materials were tested on the high speed universal test equipment shown in Figure 82. Specimen sizes were nominal 2 x 2 x 1-1/4 blocks and no end plates were bonded to the samples. Specimen size may be expected to influence the observed performance.

Even more pronounced influences would be encountered in comparing crushing response of honeycomb materials with and without bonded end plates since this could considerably alter the buckling behavior of the samples.

Figure 82 HIGH STRAIN RATE TESTER (SHOWING TEMPERATURE CHAMBER IN POSITION)

A recently completed facility at Avco/ MSD is the device shown on Figure 83. In this ultrahigh strain rate loading device, explosives are used to propel a bar of material which impacts the crushable material sample. The sample, in turn, is mounted on another bar of metal or plastic, to which are attached two semi-conductor strain gages. The dynamic outputs of these gages are used to measure crushing load. This device is capable of propelling a 30 pound projectile up to 1000 ft/sec.

A test was performed using this device on a sample of polyurethane foam filled plastic honeycomb to determine the effect of very high velocity (250 ft/sec) on crushing stress of this material.

The bulk of this test program involved the testing of reinforced plastic honeycombs using the high speed universal test equipment illustrated on Figure 82. In most of the tests, the honeycomb cells were filled with polyurethane plastic foams of various densities.

Three different honeycombs were used: a 1/8-inch cell fiberglass phenolic, a 3/8-inch cell fiberglass pehnolic, and a 3/16-inch cell Nylon phenolic. Most of these data are illustrated on Figure 84, 88, and 90. On these figures, for reference purposes, dotted lines are shown, marked D, I, and N, which are taken from Figure 80. They represent 5052 aluminum honeycomb, 3003 aluminum honeycomb, and plastic foams, respectively.

The usable strains of practically all the specimens were in the neighborhood of 80 percent; the 1-1/4-inch thick specimens were crushed approximately 1 inch.

A comparison was made between static and dynamic (10, 000 in/sec) loadings on 1/8-inch cell fiberglass phenolic honeycomb of nominal density 7-7.5 lb/ft.^{3} No essential difference was found in the crushing stress at this rate (Figure 84) and all subsequent testing was done under dynamic conditions. This is actually more convenient than static loading in many ways; e.g., the stress history is obtained on the Polaroid pictures of the oscilloscope traces, simplifying the data reduction problem.

It can be seen from Figure 84 that this material is better than 3003 aluminum honeycomb (line I).

A 14.2 lb/ft^3 specimen of the 1/8-inch cell fiberglass phenolic honeycomb with polyurethane foam-filled cells was tested in the ultrahigh strain rate loading device shown in Figure 83 at an impact velocity of 250 ft/sec.

A high-speed film sequence of the impact is shown in Figure 85. The projectile can be seen approaching the target from the right. In this test, the entire specimen was reduced to a fine dust, since it was not of sufficient thickness to attenuate the complete energy of the projectiles.

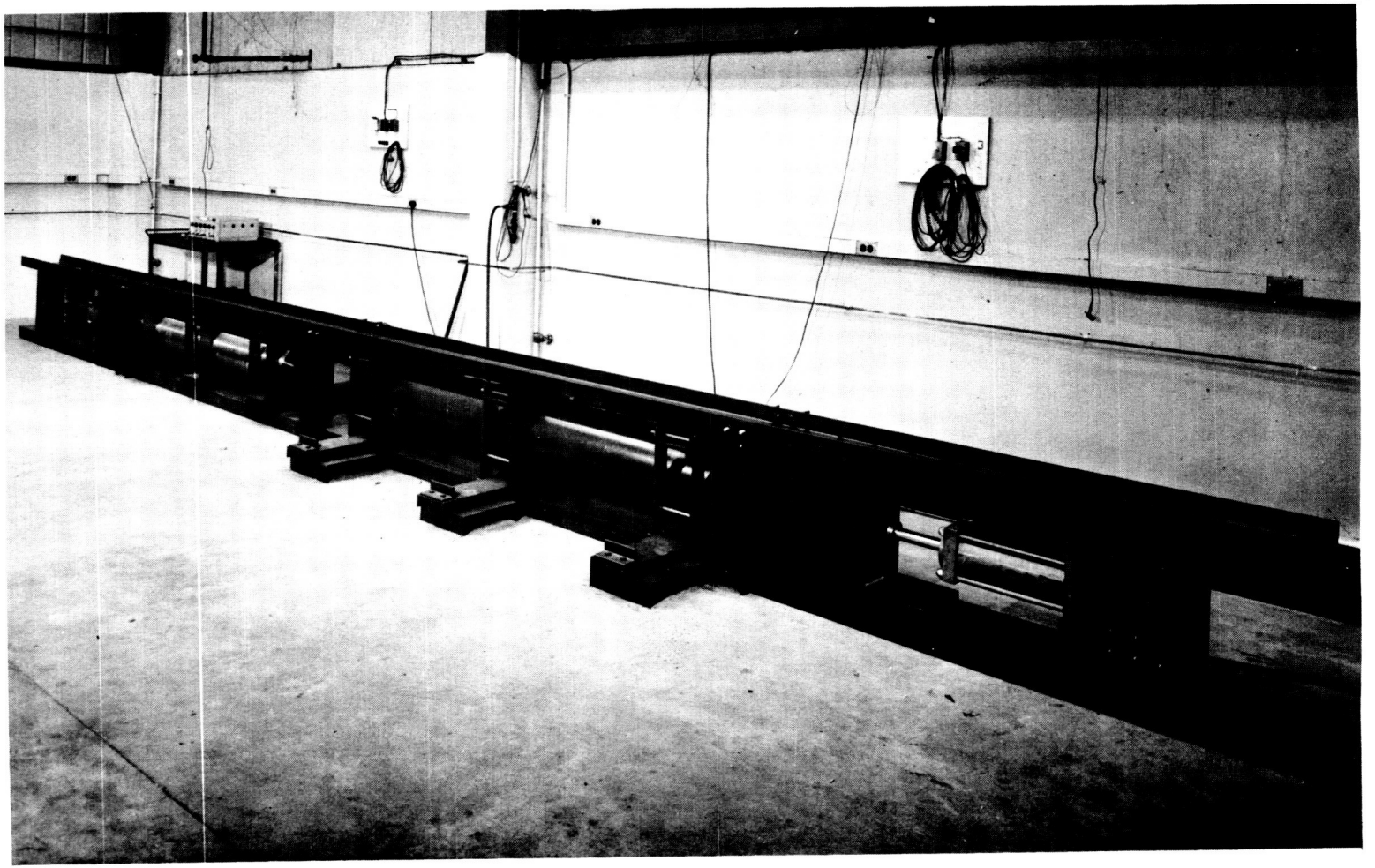

Figure 83 ULTRAHIGH STRAIN RATE LOADING DEVICE

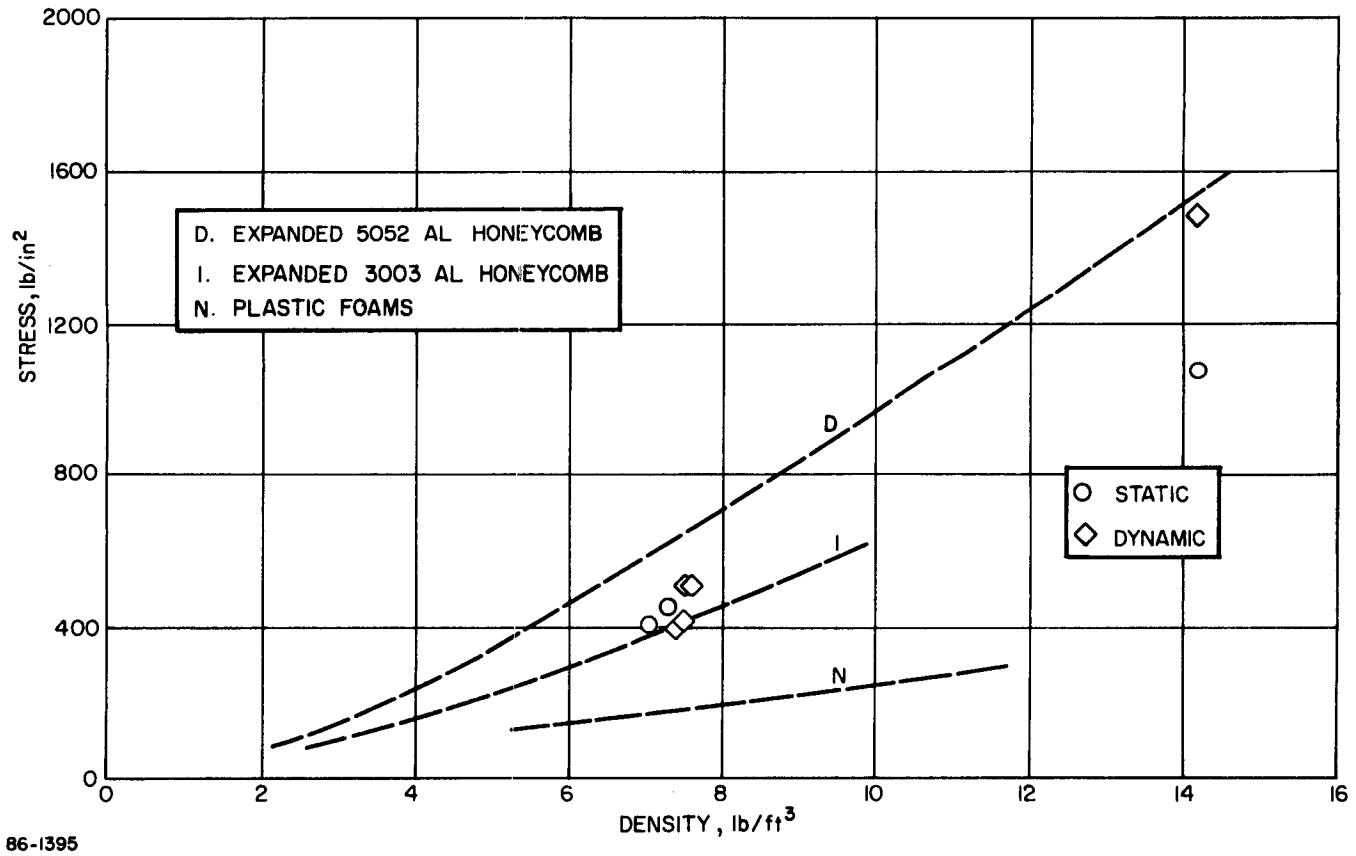

Figure 84 FIBERGLASS PHENOLIC HONEYCOMB 1/8-INCH CELL--POLYURETHANE FOAM FILLED

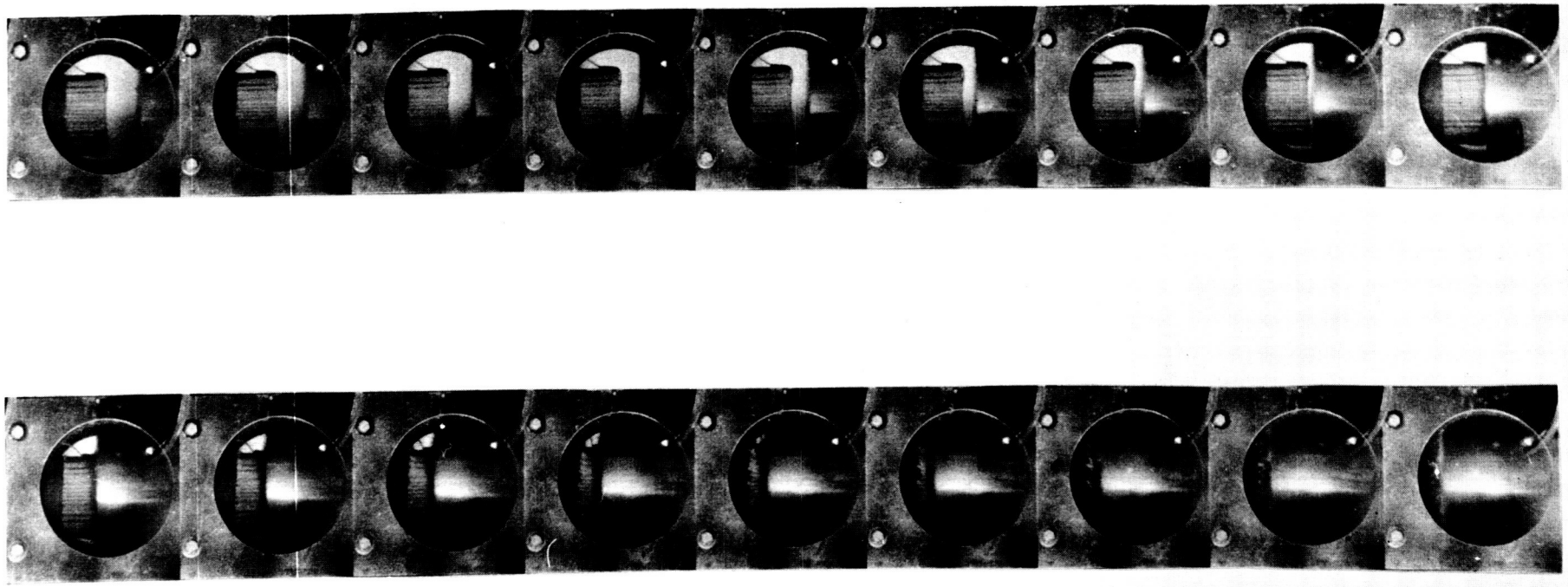

Figure 85 FILM SEQUENCE OF IMPACT IN ULTRAHIGH STRAIN RATE LOADING DEVICE

A schematic of the test set-up is shown on Figure 86. Oscilloscope trace of the strain gage outputs are shown in this figure. These outputs read from right to left. The output of gage 2 is cut off part way through by the shock wave which has reflected from the end of the bar.) The crushing stress of the material was found to be of the order of 1480 lb/in^2 as compared to 1075 lb/in^2 found in a static test on a specimen of the same geometry cut from the same original sample (Figure 87.) This tentatively indicates that this material does exhibit a velocity-dependent behavior for velocities of hundreds of feet per second. These results are also plotted on Figure 84.

Polyurethane material tends to behave as purely cellular structure. In this foam, the air is entrapped in small holes. Thus the resistance to flow of air offered by the walls is quite small at low rates, while the air flow impedance tends to increase at high strain rates. This phenomenon may accout for the velocity-dependence effect; a dynamic test under vacuum conditions would be quite interesting to test whether or not a strong velocity effect would be observed.

Figure 88 gives the results of dynamic tests on the 3/8-inch cell fiberglass phenolic. The properties of this material lie between those of 3003 aluminum honeycomb and plastic foams. This material is not as good as the 1/8-inch cell fiberglass phenolic.

Some pieces of 3/8-inch cell fiberglass phenolic honeycomb were epoxy resin-dipped in an attempt to increase the crushing stress and energy absorption capability of this material. However, upon being filled with polyurethane foam to yield a final bulk density in the range 22 to 26.5 $lb/ft.^3$, the crushing stress was determined to be not significantly greater than that of polyurethane foam of this density taken alone. Polaroid pictures of the oscilloscope traces, taken during these tests, are shown on Figure 89. There should still be some promise in this technique, as illustrated by some of the results described in Reference 17. In this same reference, it is pointed out that too much resin-dipping may make the honeycomb too brittle, and this may be what happened in this instance.

The 3/16-inch cell Nylon phenolic honeycomb test results are shown on Figure 90. The unfilled honeycomb is as strong as 5052 aluminum honeycomb (line D), but when foam-filled, the crushing stress level lies between the 3003 aluminum honeycomb and the plastic foams.

As expected, the foamed honeycomb was considerably stiffened by reduced temperatures (-100° F) and weakened at high temperatures (+200° F). Sterilization of specimens resulted in weight losses of the order of 4 percent and the character of crushing failure tended to be more brittle

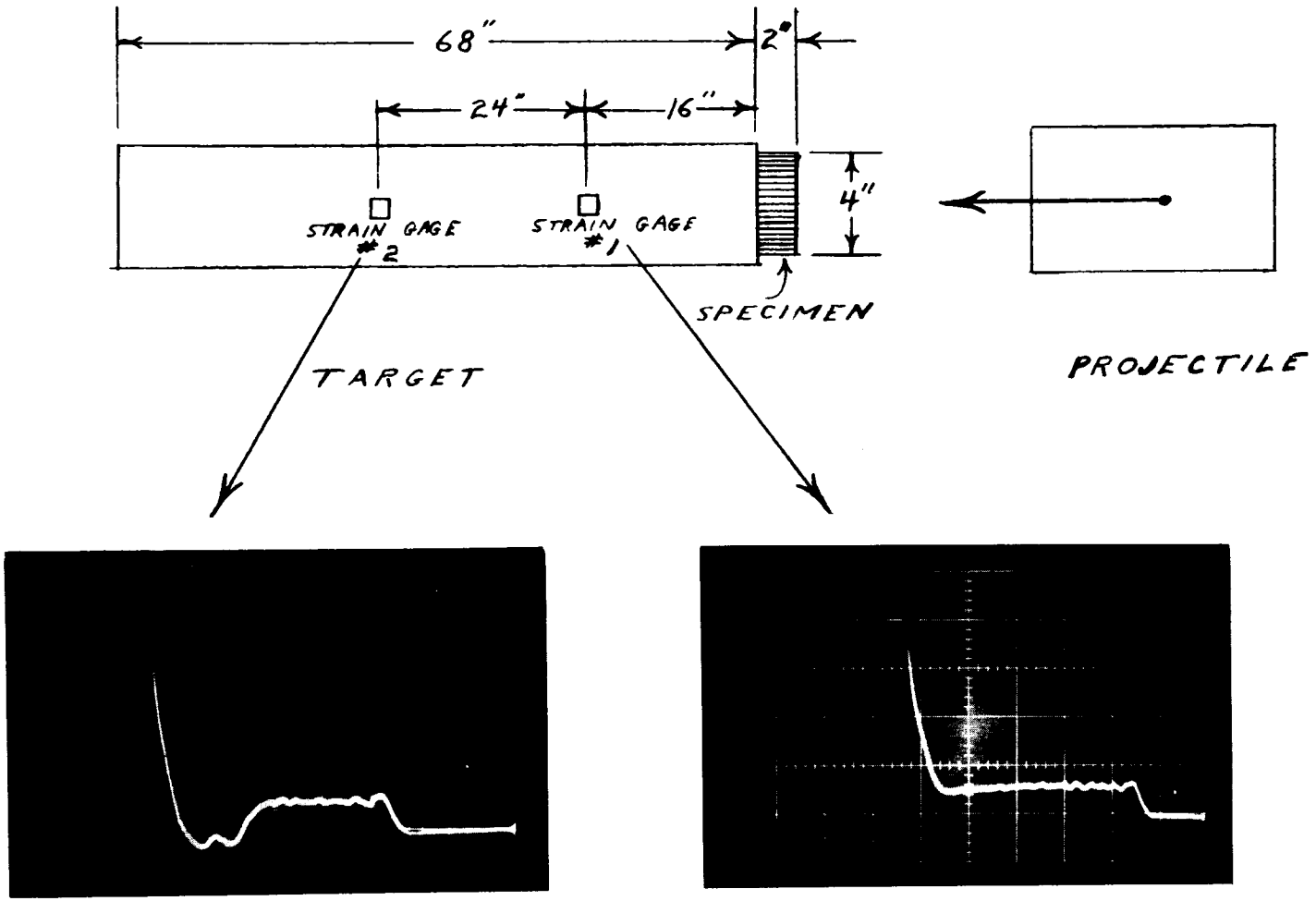

Figure 86 SCHEMATIC OF ULTRAHIGH STRAIN RATE LOADING DEVICE

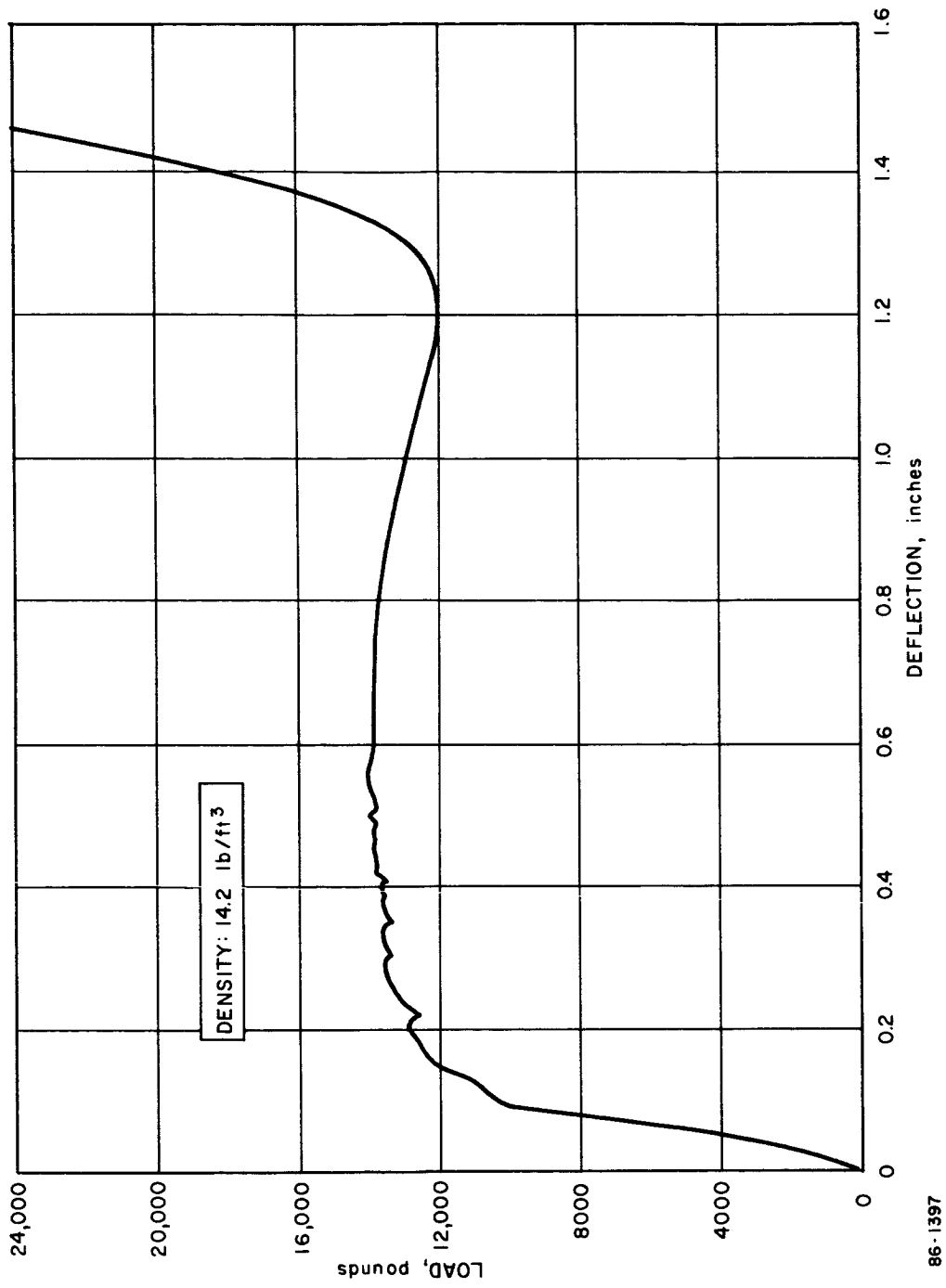

Figure 87 STATIC LOAD DEFLECTION CURVE--FIBERGLASS PHENOLIC

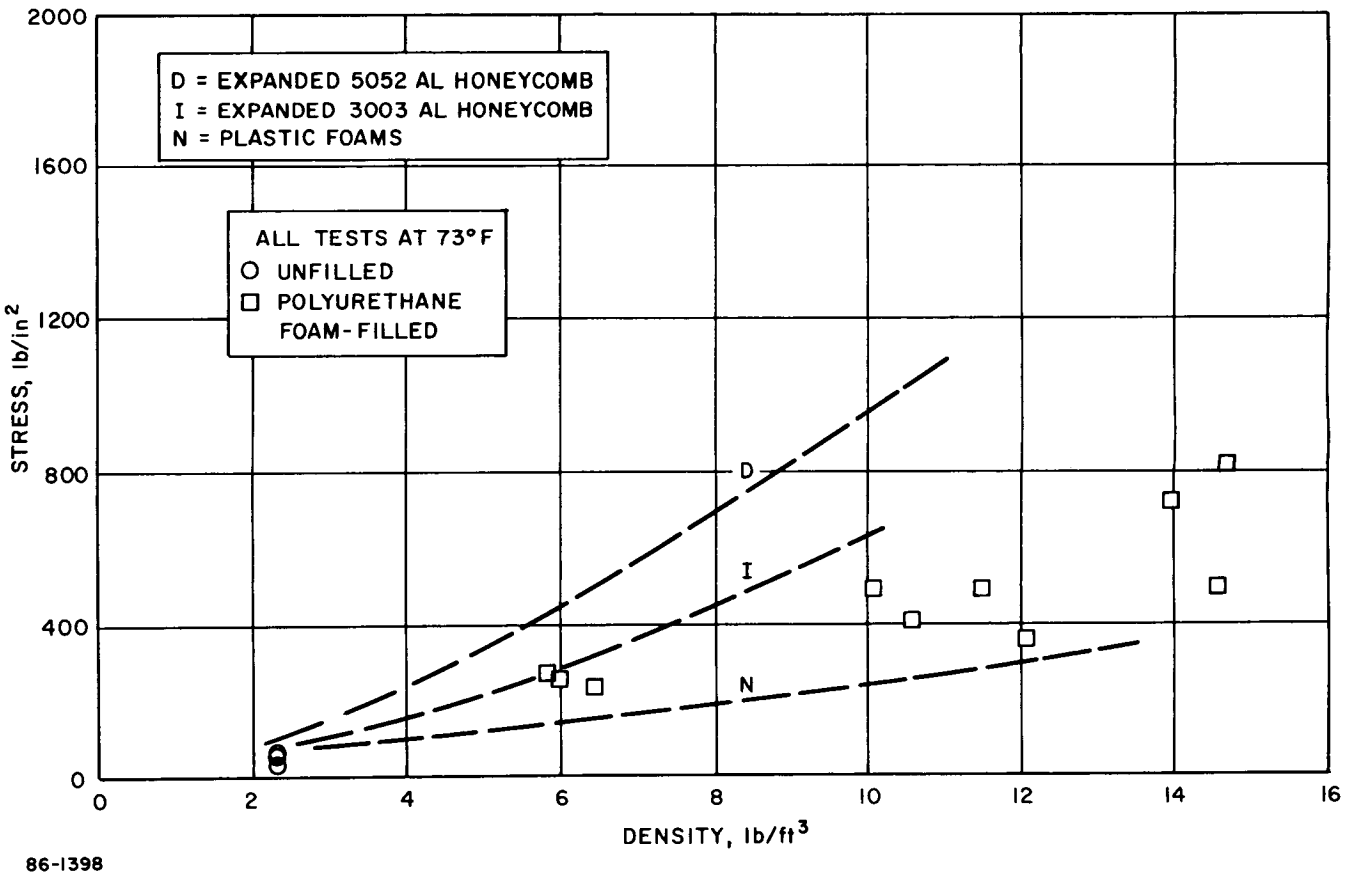

Figure 88 FIBERGLASS PHENOLIC HONEYCOMB--3/8-INCH CELL

PARALLEL TO HONEYCOMB CELL AXIS

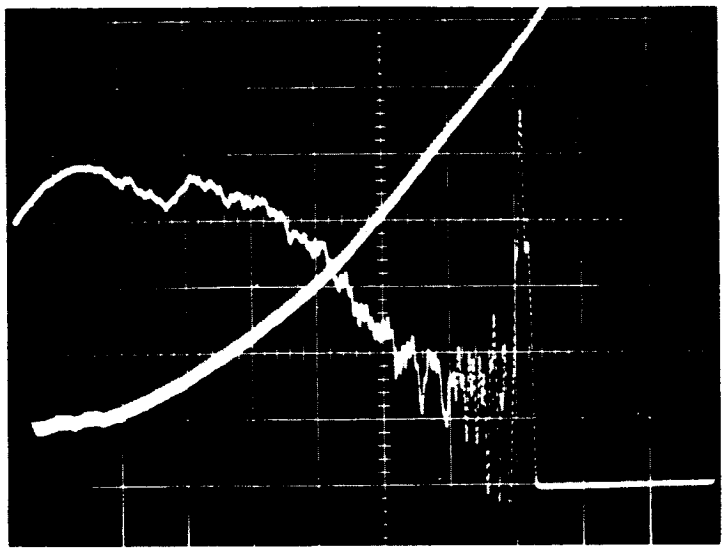

PERPENDICULAR TO CELL AXIS

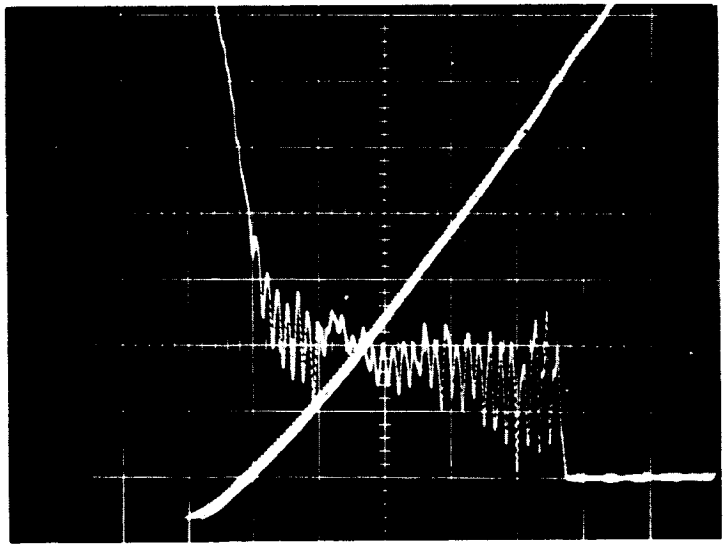

Figure 89 IMPACT TEST ON RESIN-DIPPED POLYURETHANE FOAMED--3/8 INCH CELL HONEYCOMB

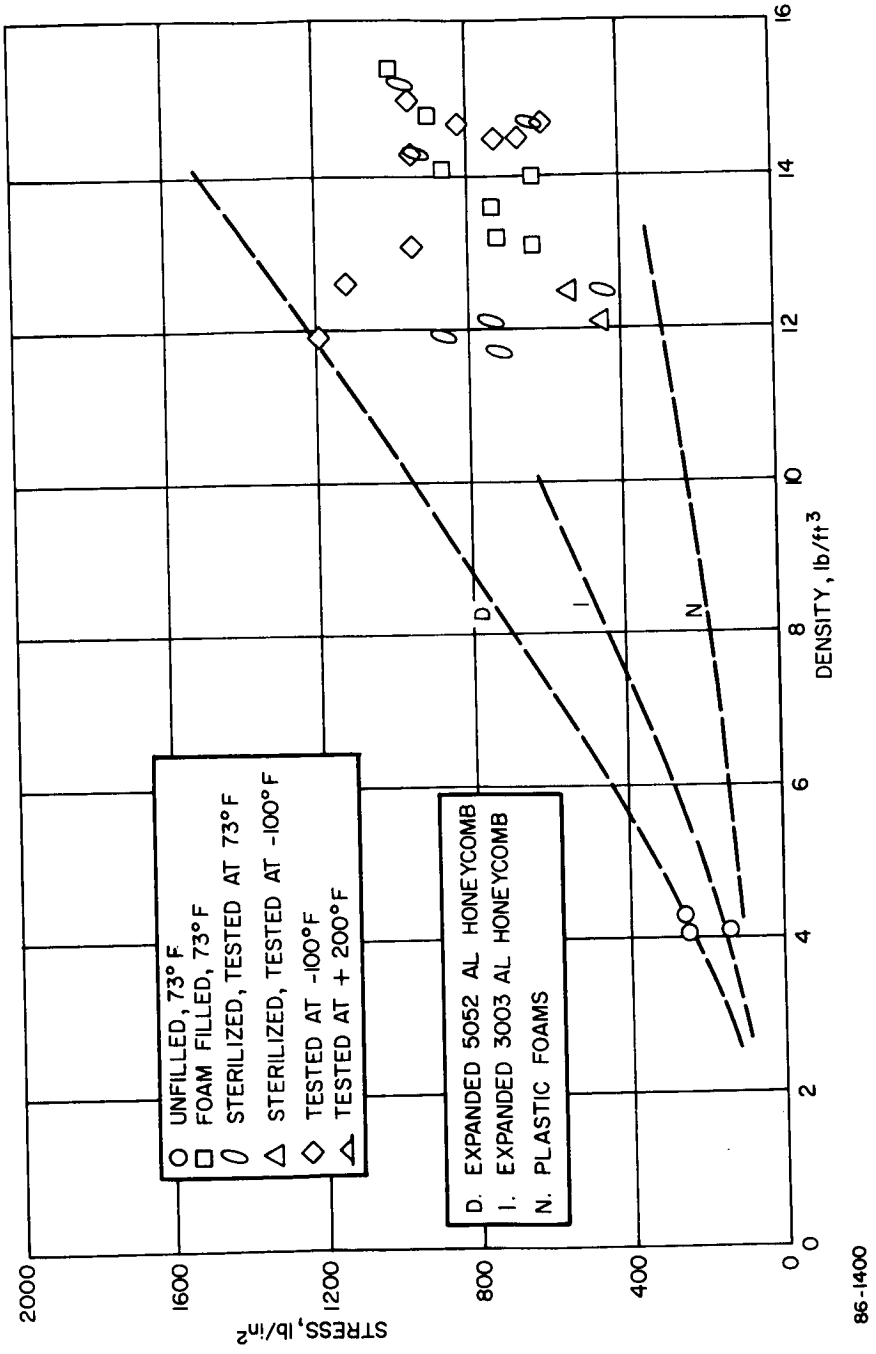

Figure 90 NYLON PHENOLIC HONEYCOMB--3/16-INCH CELL

after such exposure. Reducing temperature to -100° F after prolonged +300° F environment did not appear to increase the stiffness as much as in the thermally uncycled samples.

Load-deformation-time observations typical of polyurethane foam-filled plastic honeycombs are illustrated by Figure 89. For certain impact cushioning requirements, the existence of the initial peak stress is not a desirable feature. In applications utilizing aluminum honeycomb, the initial spike may be eliminated by pre-crushing the honeycomb. Elimination of the initial peak for plastic honeycomb has been achieved by precutting the honeycomb nodes to a slight depth. (Reference 17).

It has been suggested that the first crushing node is responsible for this sharp initial stress rise, and that pre-slitting tends to start the buckling in a manner similar to pre-crushing.

A fact not apparent in the illustrations is that with increasing foam density, the behavior of the material changes and at the highest density used, the honeycomb no longer seems to buckle, but tends to shatter in a brittle fashion.

The effects of density and angle of impact incidence on the dynamic response of foamed honeycombs are summarized on Figure 91. The shapes of the curves shown can be contrasted with the shapes shown on Figure 81, particularly those applying to unfilled plastic honeycombs. The foam-filling is of obvious benefit in reducing drastically the anisotropic behavior of the honeycomb.

3.2.3.2 Parametric analysis

The principle tools for performing the parametric studies were two digital computer programs; Avco/MSD program Nos. 1882 and 196B. These programs are based on the analyses of impact dynamics which are presented in (Reference 24).

The analyses in Reference 24 are, for the most part, restricted to landers in the shape of spheres or in a lenticular shape (here, lenticular is defined as composed of two spherical segments, see Figure 92. Early in the program, the analysis was extended to include prolate spheroids and oblate spheroids. This analysis is presented in Appendix A.

The various shapes treated in the study are shown on Figure 92. For the foam-filled fiberglass honeycomb under consideration here, its crushing stress versus density characteristics can be assumed to be given by $\gamma = S_m^{0.554}/4.15$ with γ in lb/ft^3 and S_m in lb/in^2. (This equation is an empirical curve fit to test results). A conservative value of 0.75 was used for the usable strain, ϵ.

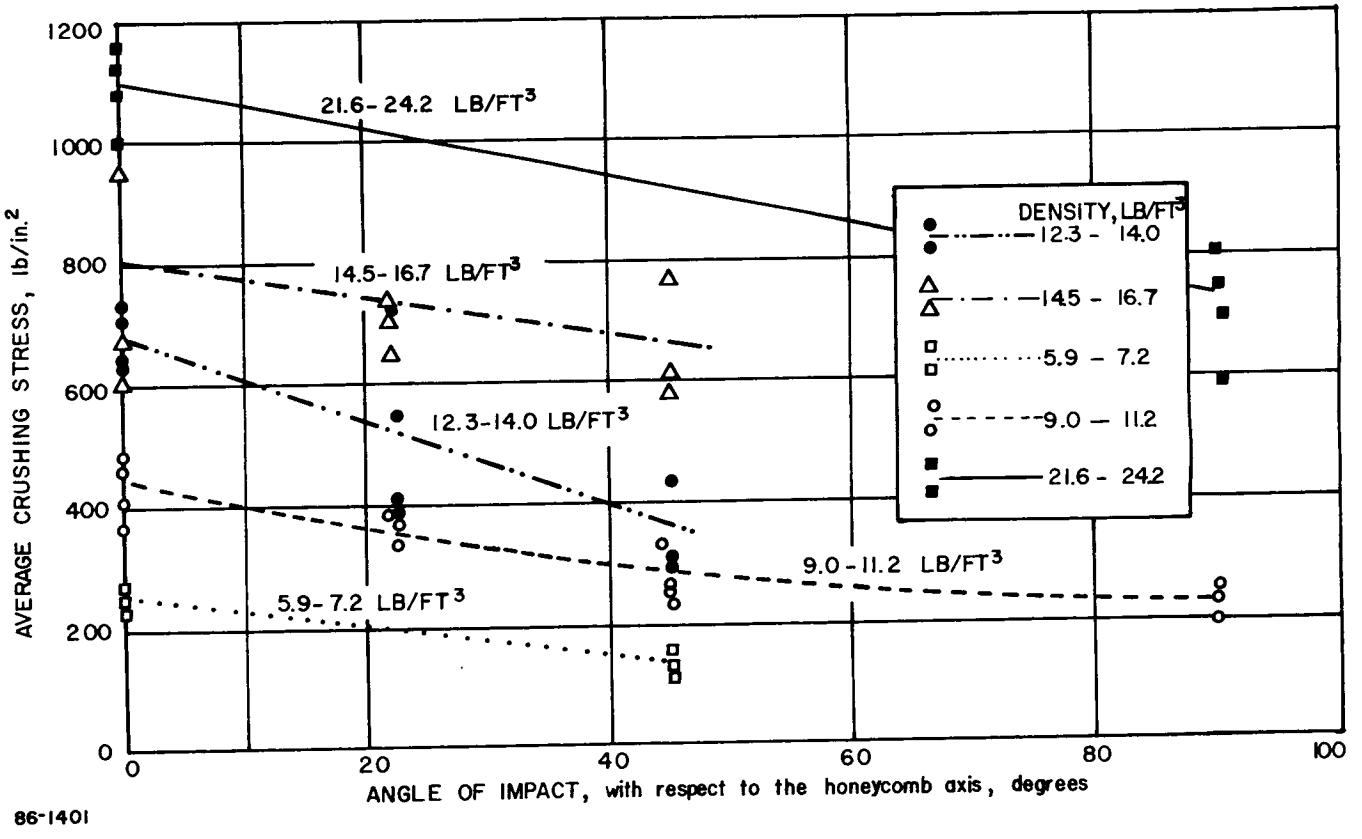

Figure 91 EFFECT OF DENSITY AND ANGLE OF IMPACT ON DYNAMIC RESPONSE OF POLYURETHANE FOAM-FILLED HONEYCOMB

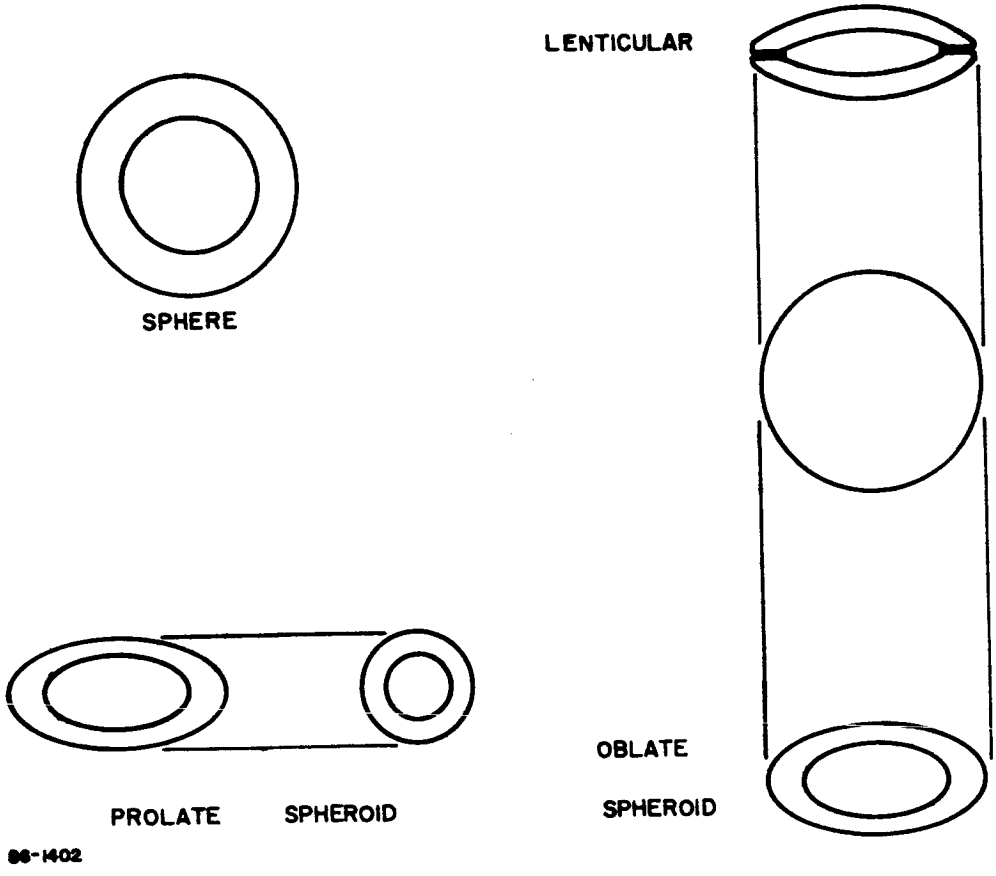

Figure 92 LANDER GEOMETRICS

A most important property of crushable material is anisotropy. The analyses of prolate and oblate spheroids are simplified by neglecting anisotropy; this simplication, as explained in Appendix A, allows these shapes to be analyzed using the existing digital computer program without modification. Valid comparisons can still be made by comparing these shapes with isotropic spherical results.

Some data was generated for spherical and lenticular geometries in which anisotropy was accounted for. This particular anisotropic behavior assumed for the foam-filled fiberglass is shown on Figure 93. and was obtained from test results reported in the previous section. Analytically, the anisotropic behavior is assumed to be given by:

$$S/S_m = 1 - 0.6\theta + 0.2\,\theta^2$$

where S/S_m is the normalized crushing stress and θ is the angle of crushing, measured from the direction of the honeycomb cell axes. This function represents an average anisotropy and is assumed to hold over the entire density range of interest. However, since the results of the parametric study indicate that the particular material required in this application is quite low in density, the anisotropic function above may prove to be too optimistic.

Figures 94 through 100 present the essential results of the parametric study. These figures are curves of total landed weight, W_T , versus principal radius of curvature, R_2, (for the sphere and lenticular shapes) or semi-minor axis, b, (for the prolate and oblate spheroids). On the curves are lines of constant peak deceleration and constant internal payload weight. Also drawn in on each of the figures is a line representing a crushable material density of 2 lb/ft^3. To the left of this line, the material density is higher. This particular density is considered to be the minimum which can be manufactured satisfactorily at this time. Hence, designs which lie to the right of this line are considered unattainable.

All of these curves exhibit the asymptotic behavior of the lines of constant internal payload weight. The reason for this behavior is explained in some detail in Reference 24; the salient point is that this results in these curves possessing minimums, which represent optimum designs.

To carry this a little further, consider Figure 94. As can be seen, the optimum design points lie a bit above the 1000 g line. However, note that the W_i curves are quite flat in moving to lower g levels. Further, the gains in usable payload due to the lighter supporting structure required at the lower g levels may more than compensate for the loss in total internal weight. In fact, cursory studies indicate that if the weight of impact-load-dependent supporting structure and bracketry

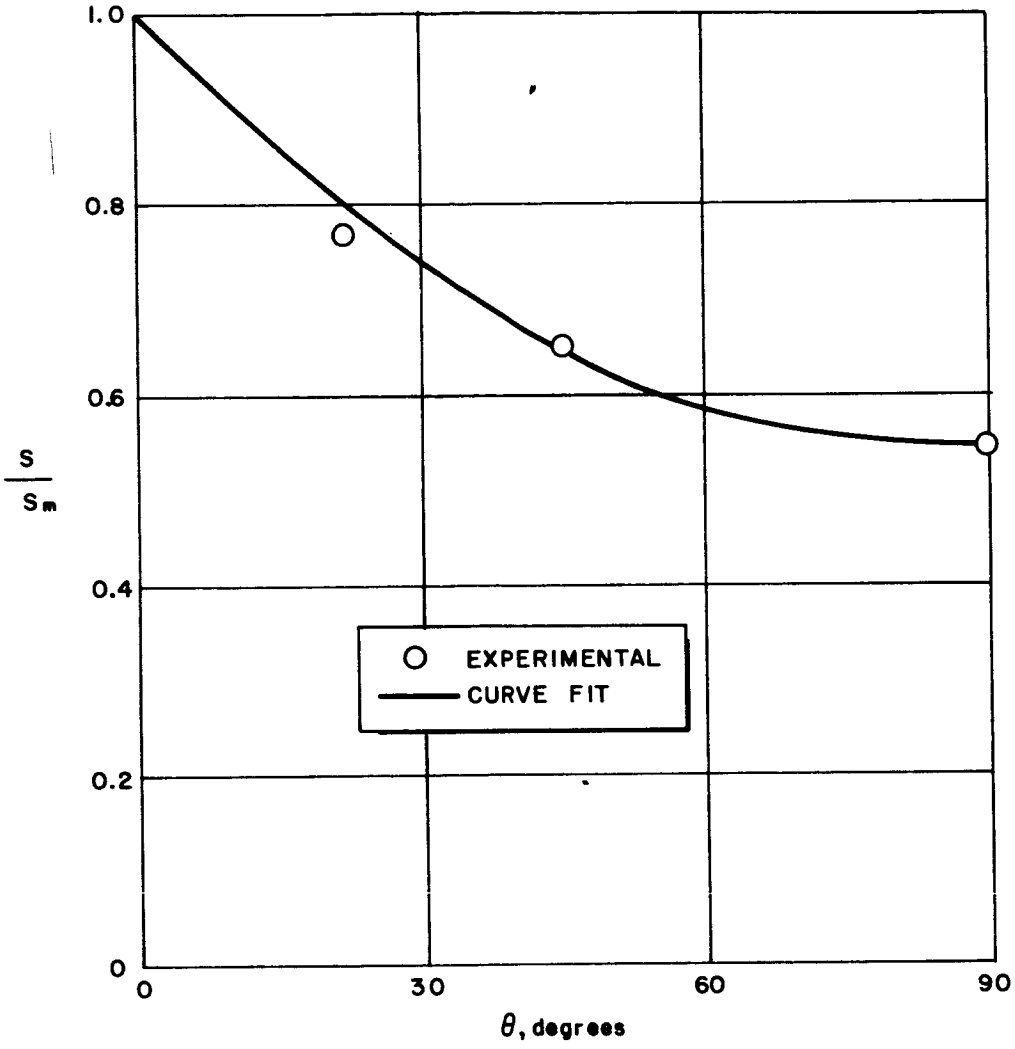

Figure 93 CURVE FIT TO ANISOTROPIC MATERIAL PROPERTIES

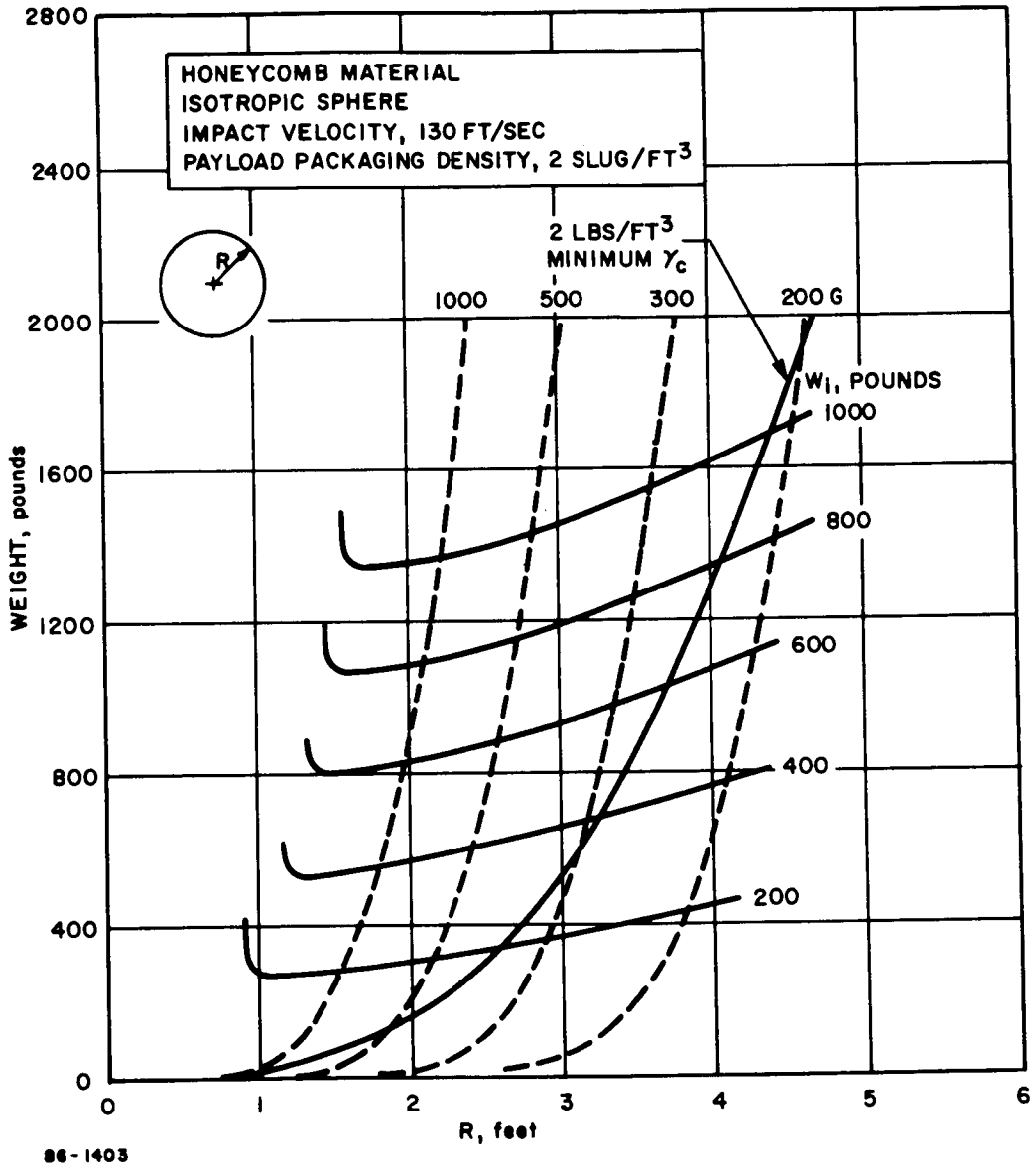

Figure 94 TOTAL WEIGHT VERSUS RADIUS-ISOTROPIC SPHERE LANDER

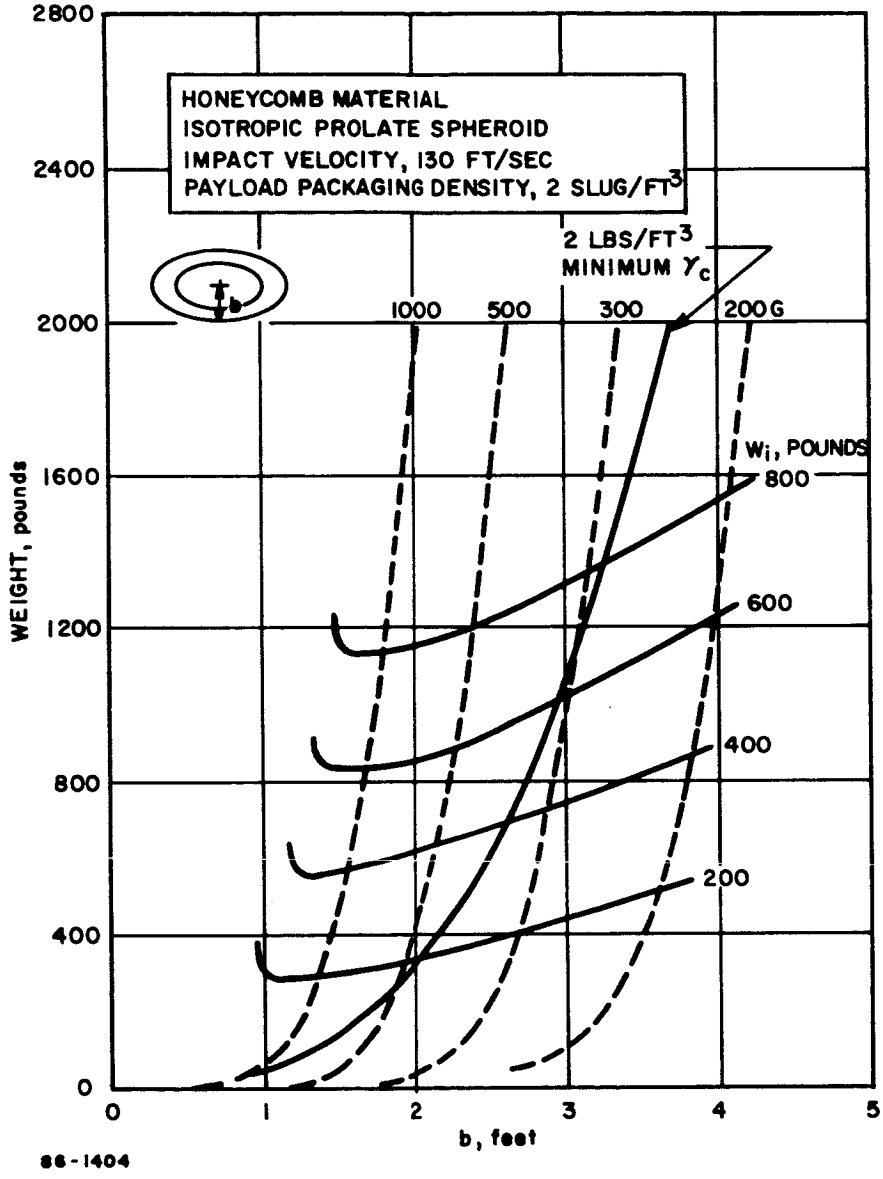

Figure 95 TOTAL WEIGHT VERSUS SEMI-MINOR AXIS-ISOTROPIC PROLATE SPHEROID LANDER

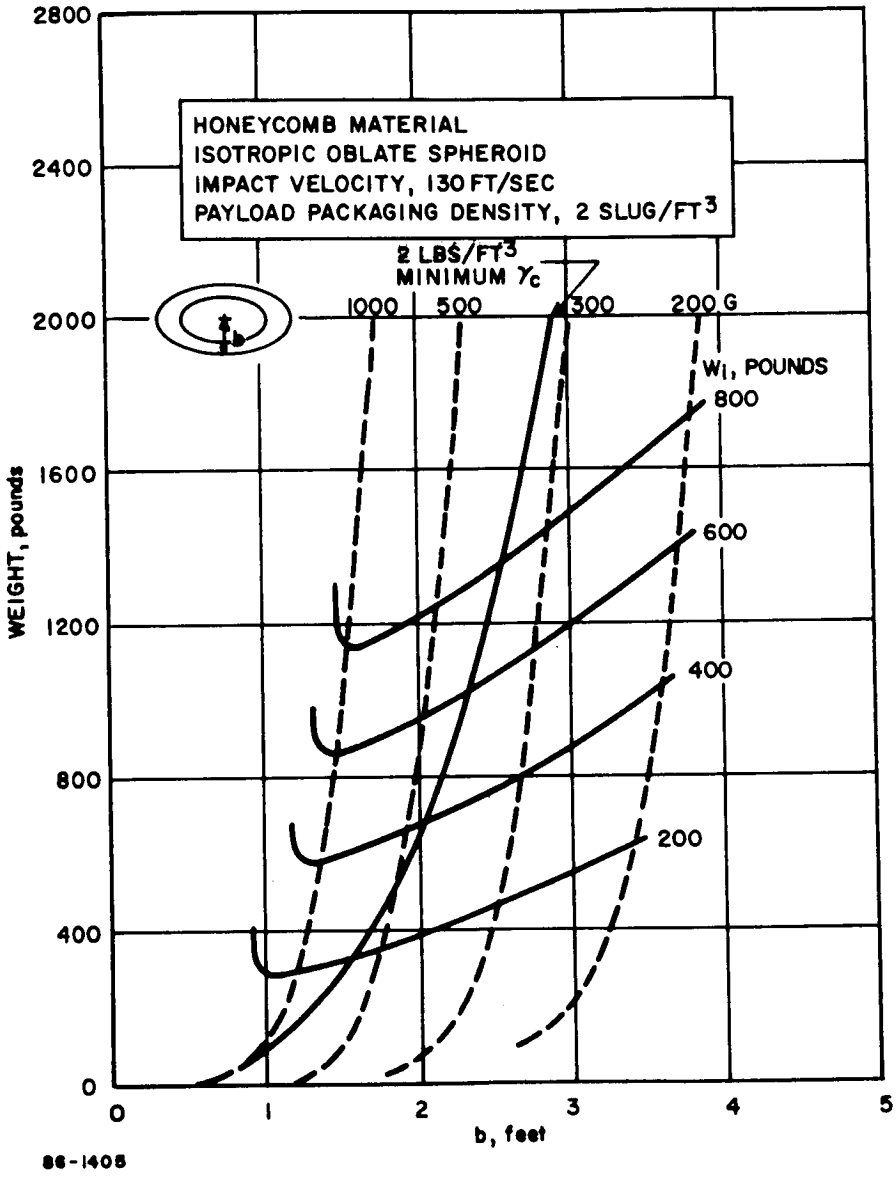

Figure 96 TOTAL WEIGHT VERSUS SEMI-MINOR AXIS-ISOTROPIC OBLATE SPHEROID LANDER

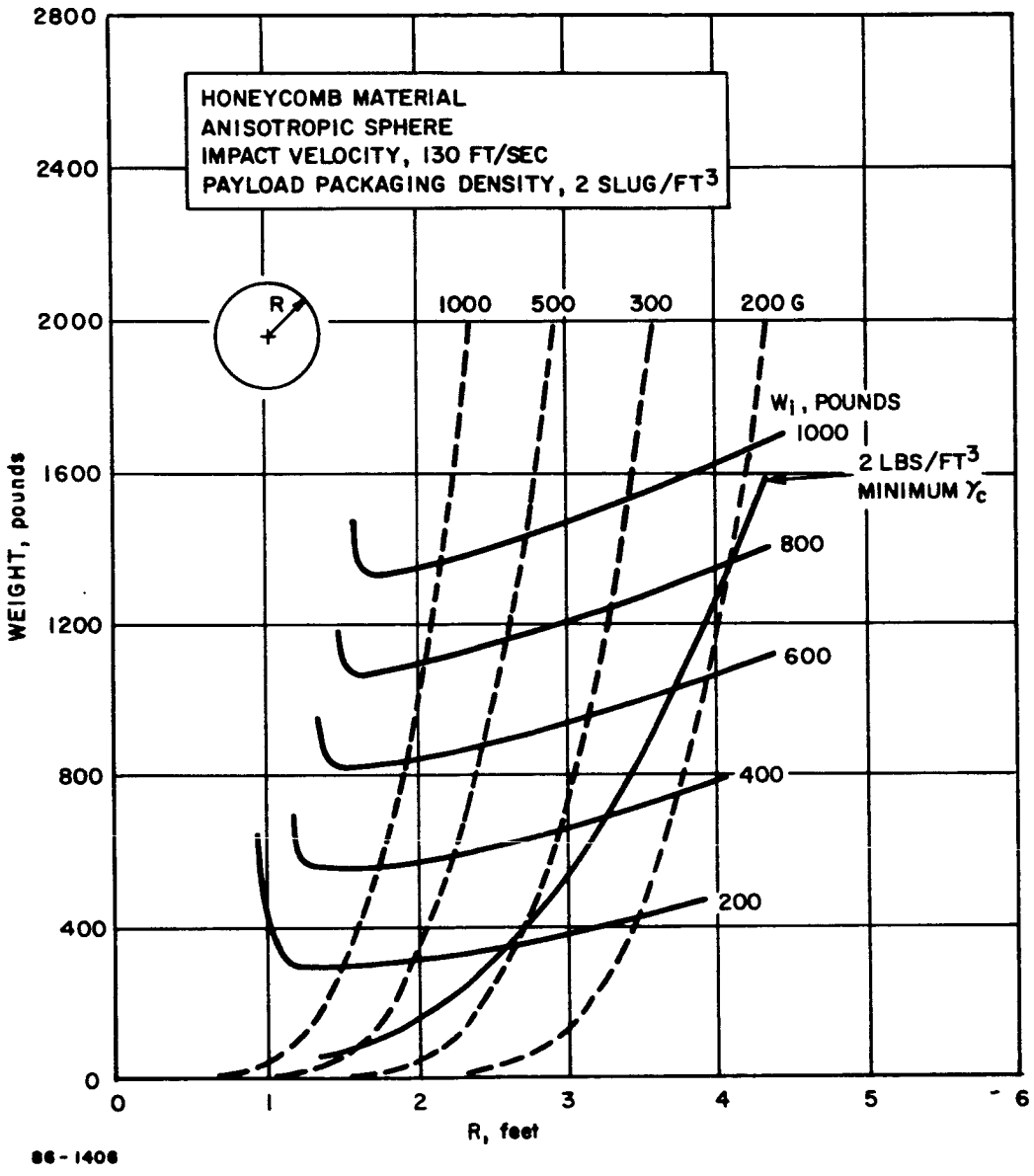

Figure 97 TOTAL WEIGHT VERSUS RADIUS-ANISOTROPIC SPHERE LANDER

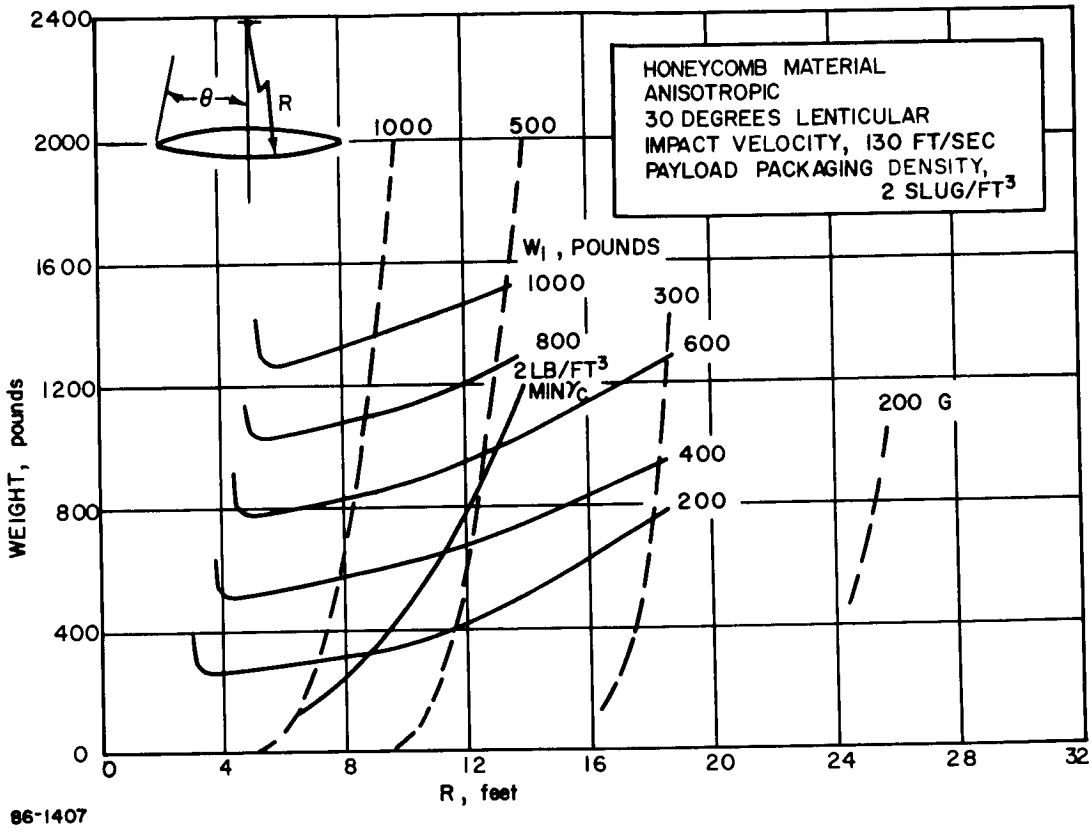

Figure 98 TOTAL WEIGHT VERSUS RADIUS--30-DEGREE LENTICULAR LANDER

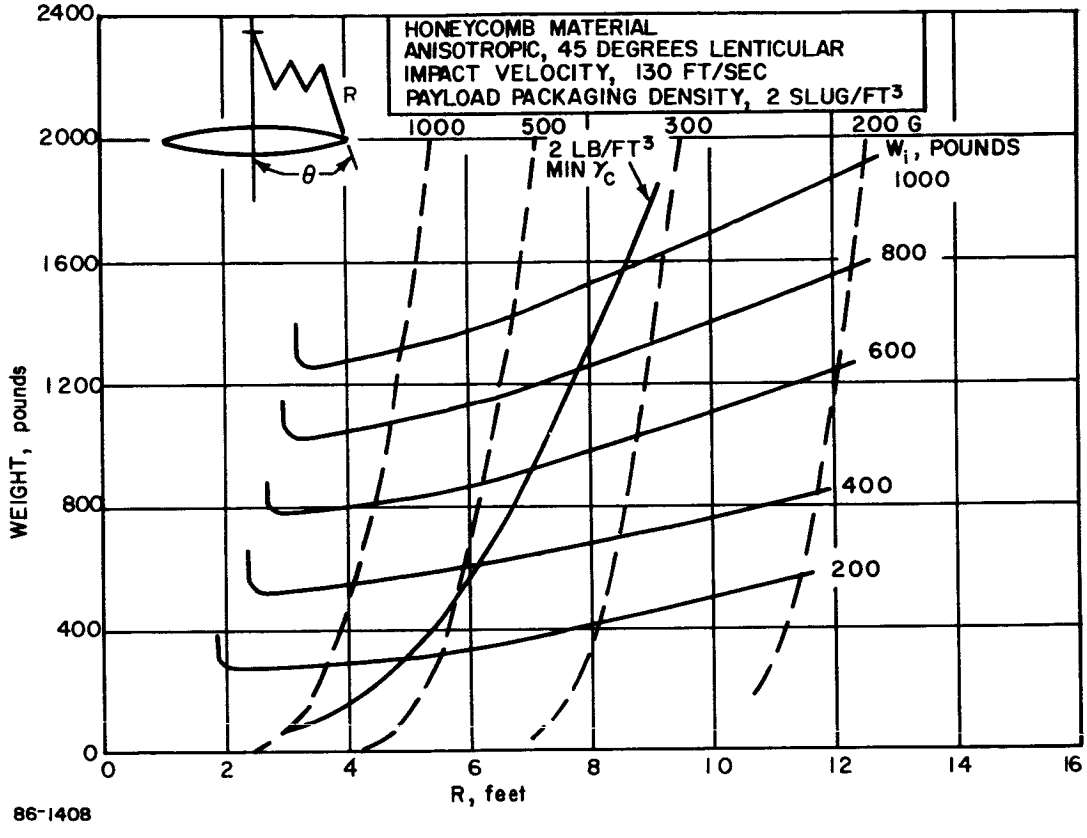

Figure 99 TOTAL WEIGHT VERSUS RADIUS--45-DEGREE LENTICULAR LANDER

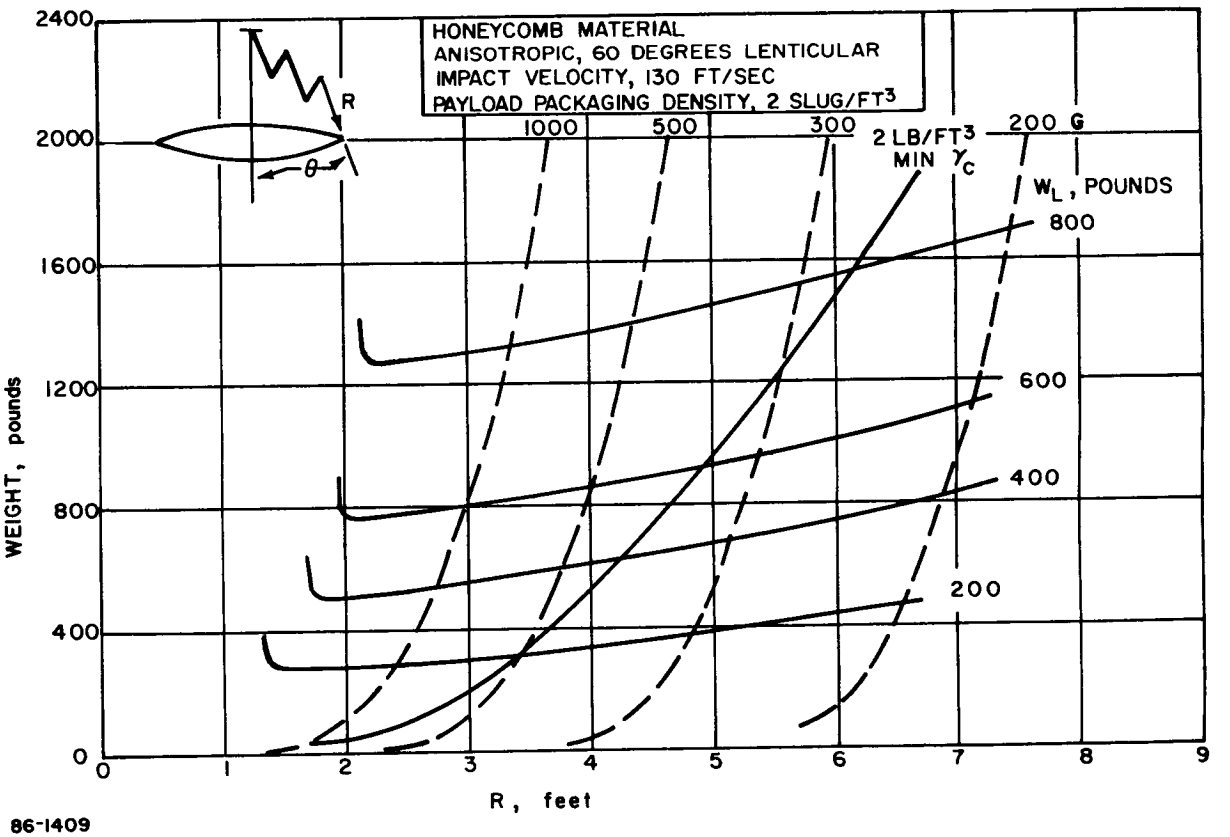

Figure 100 TOTAL WEIGHT VERSUS RADIUS--60-DEGREE LENTICULAR LANDER

exceeds 5 percent of the internal weight, then this is indeed the case. In other words, there will actually be a gain in useful payload in going to the lower g levels. Figures 94 through 100 were all drawn for an impact velocity of 130 ft/sec and an internal payload packing density (every thing internal to the impact alternator) of 2 slug/ft^3. Figure 101 is intended to illustrate the way in which these two parameters affect the results.

Using the results shown on Figure 94 through 96, a study was made comparing a (isotropic) sphere, prolate spheroid, and oblate spheroid packaged in the three candidate entry vehicle shapes (see Figure 102). It was assumed that the c. g. of the landers, as packaged in each entry vehicle, coincided; this fixed the relative geometries. A typical comparison, which illustrates the important conclusions reached as a result of this study, is given in the table below.

ENTRY-VEHICLE--LANDER SHAPE TRADEOFF
TOTAL LANDED WEIGHT: 800 POUNDS

	Tension Shell			Cone			Apollo		
	Sphere	Prolate	Oblate	Sphere	Prolate	Oblate	Sphere	Prolate	Oblate
W_i (lbs.) (Internal payload weight)	475	500	505	475	560	420	475	400	310
G	290	425	540	290	770	345	290	250	225
R_2, b (in.) (Semi-minor axis)	40	30	23	40	23	30	40	40	40

For the Tension Shell and Apollo entry vehicle shapes, it can be seen that a definite tradeoff exists among the lander shapes, higher payloads being attained at the expense of higher g levels. For the cone, the same type of tradeoff exists between the sphere and prolate spheroid; the oblate spheroid gives higher g levels and less internal weight than the sphere for this particular entry vehicle.

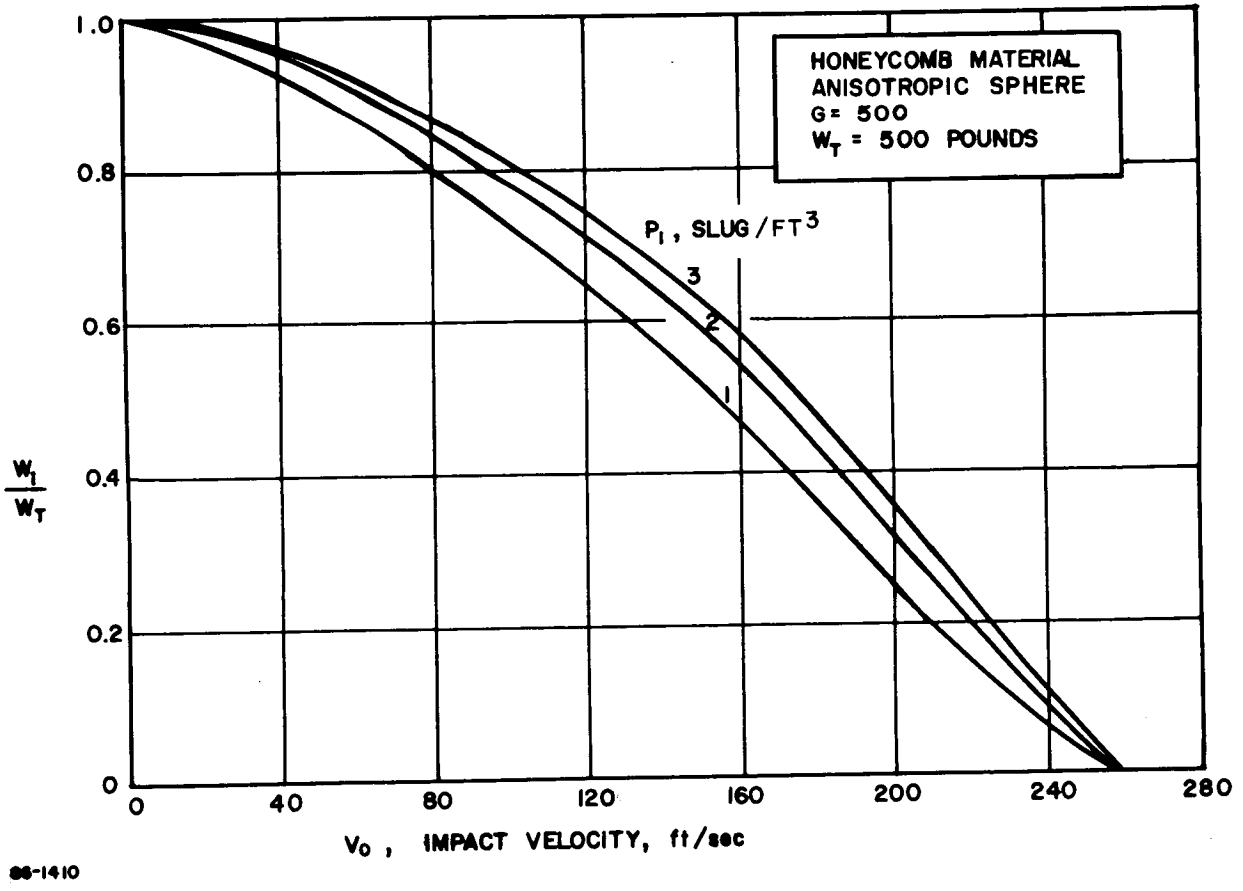

Figure 101 PAYLOAD WEIGHT FRACTION VERSUS IMPACT VELOCITY -- ANISOTROPIC SPHERE LANDER

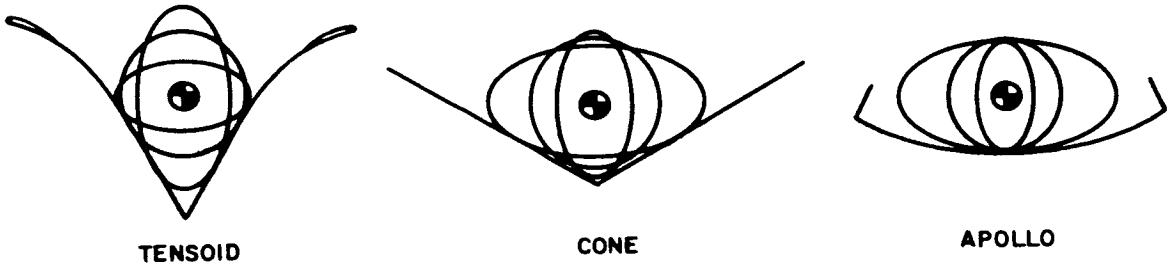

86-1411

Figure 102 LANDER GEOMETRICS FIT INTO ENTRY VEHICLES

Of course, the tradeoff discussed here refers strictly to the impact characteristics. Post-impact considerations of stabilization, orientation, and instrument deployment led to the choice of the oblate spheroid shape over the sphere.

3.2.4. Balsa Wood

3.2.4.1 Experimental program

The summary of the balsa wood data which was obtained from the literature search (see References 9, 10, 11, and 25) and which was shown on Figure 80 is expanded and detailed on Figure 103. The wide scatter of data on this material is strikingly illustrated by this figure.

It is apparent from this figure, and from Figure 80, that the density range of balsa wood is much narrower than that of honeycombs. In fact, for this parametric study, a single density of balsa was chosen, i.e., 6 lb/ft^3, with a crushing stress assumed at 1200 lb/in^2. This would be a material at the upper bound of the data shown on Figure 103.

This anisotropic behavior of balsa wood is extremely critical in determining its usefullness in this application, but published data on this behavior was found to be quite scanty, as evidenced on Figure 80. For this reason, a company-funded test program was conducted in the early part of this study, concurrent with the analysis in which the anisotropy of balsa wood was treated as a variable parameter. The results of the test program are shown on Figures 104 and 105. Figure 106 illustrates the somewhat different stress histories of balsa when crushed parallel to, and perpendicular to the grain; this behavior indicates that different modes of failure are operating in each case.

3.2.4.2. Parametric studies

Since the parametric studies were begun before the results of the test program were available, the anistropic behavior of the balsa wood was treated parametrically. In particular, it was assumed that the anisotropy of balsa could be represented by the function.

$$\frac{S}{S_m} = \cos^n \theta$$

where S/S_m is the normalized crushing stress, θ the angle relative to the grain direction, and n the degree-of-anisotropy parameter. Typical plots of this equation are shown on Figure 107.

A spherical lander geometry was analyzed using the balsa, not only at the design impact velocity of 130 ft/sec, but also at the parachute failure velocity of 425 ft/sec (i.e., $M/C_DA = 0.15$ in model 3 atmosphere). The results of this study are shown on Figures 108 and 109.

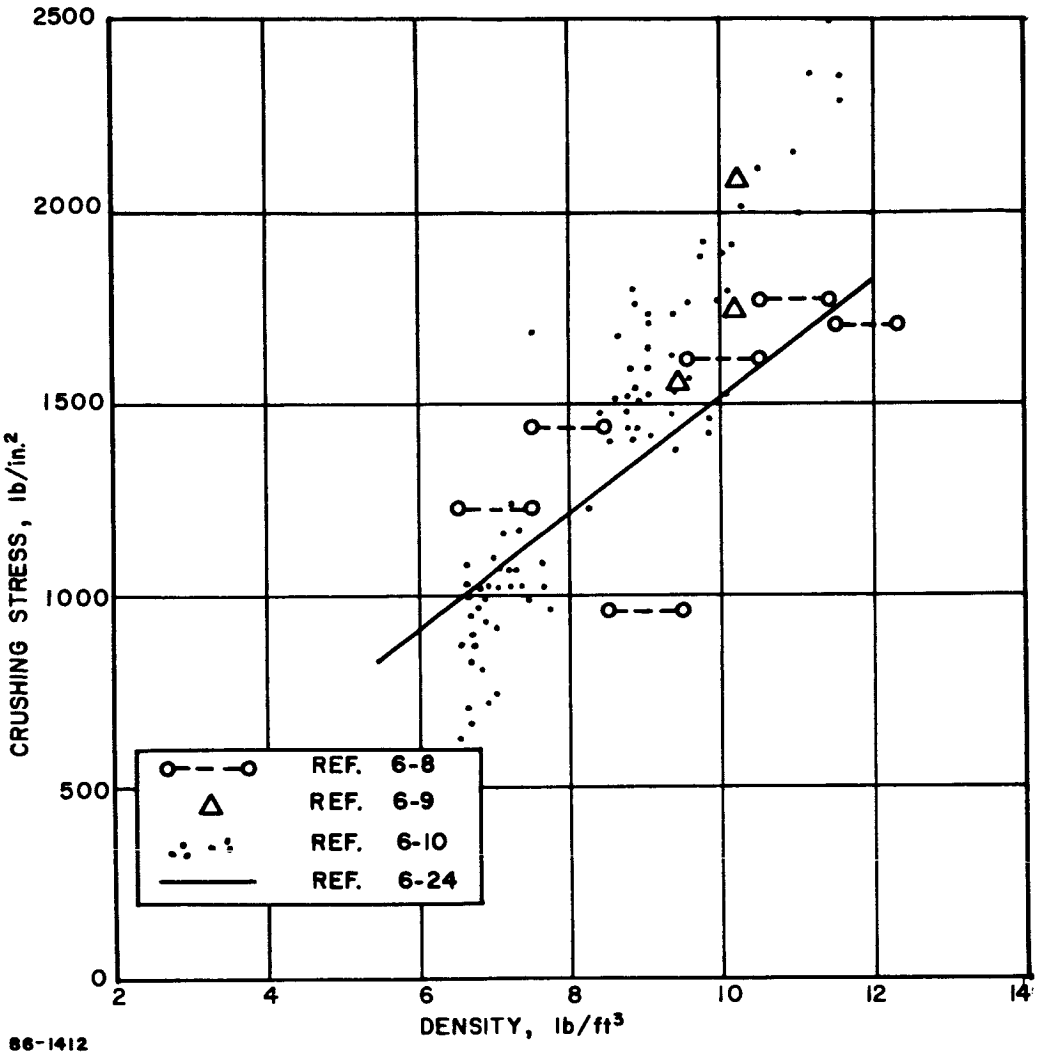

Figure 103 BALSA WOOD--CRUSHING STRESS VERSUS DENSITY LITERATURE SEARCH

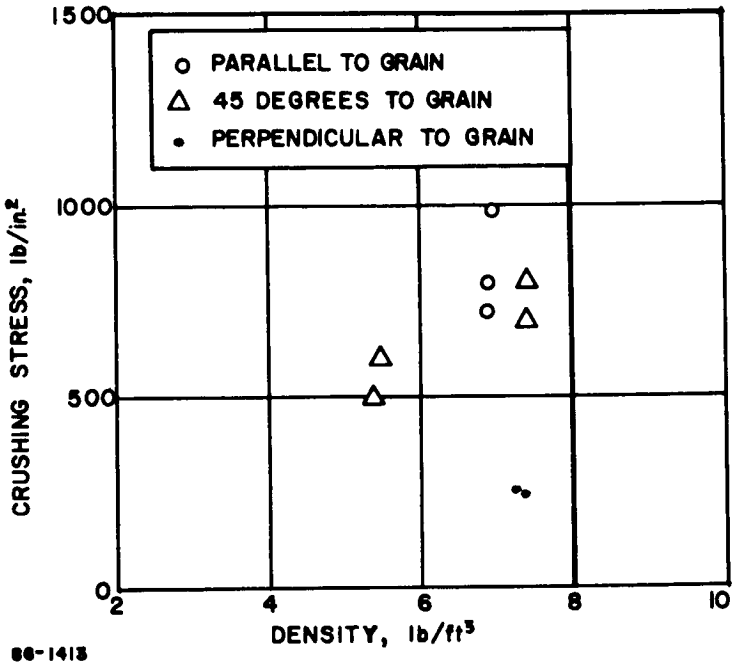

Figure 104 BALSA WOOD--CRUSHING STRESS VERSUS DENSITY--TEST

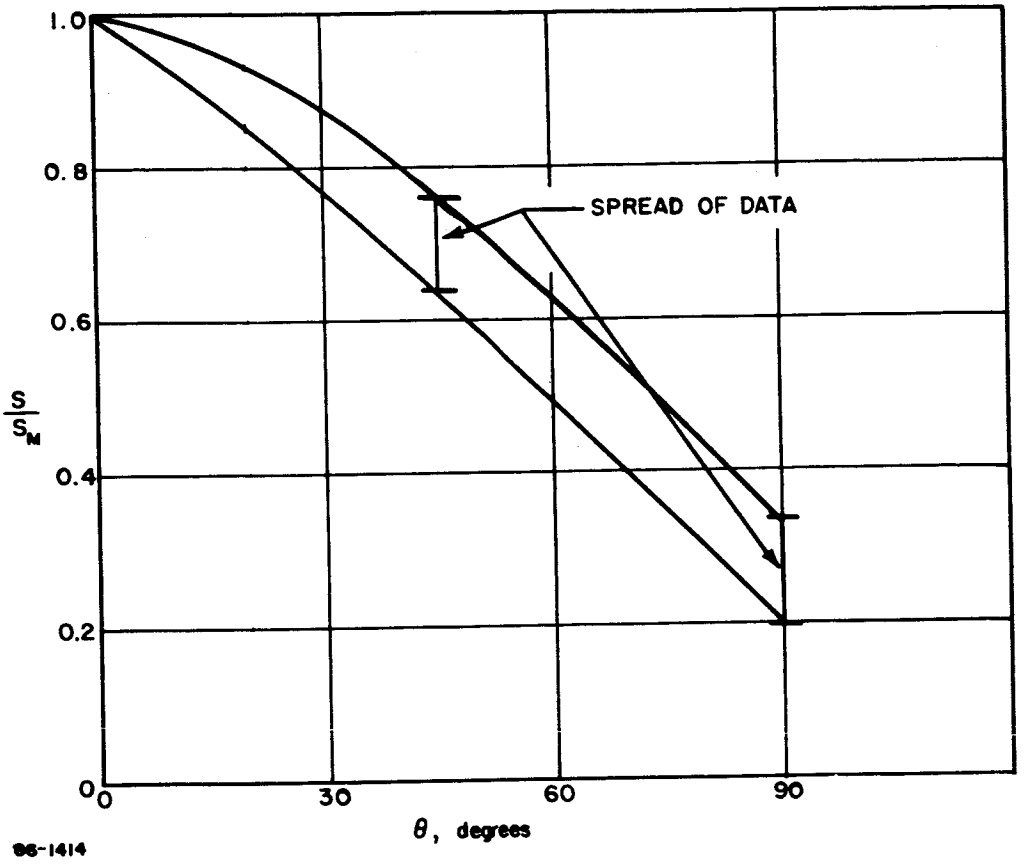

Figure 105 BALSA WOOD--ANISOTROPY--TEST

PARALLEL TO GRAIN

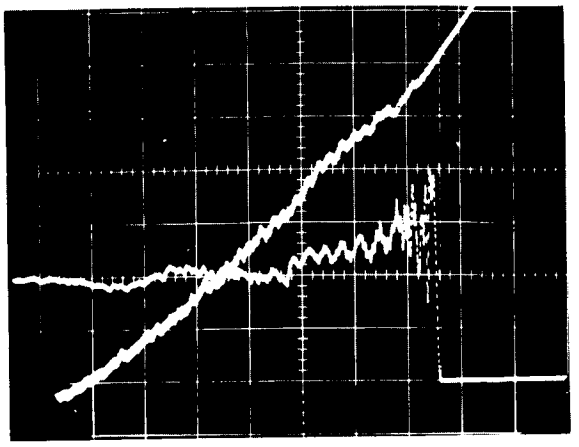

deformation

.125 in.

494 psi

stress

time

.002 sec.

PERPENDICULAR TO GRAIN

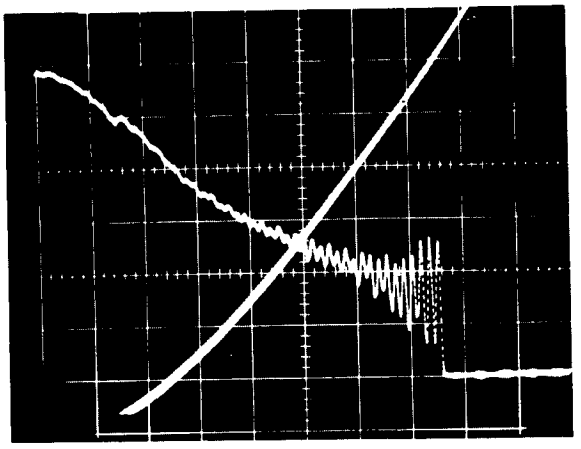

deformation

.125 in.

99 psi

stress

time

.002 sec.

Figure 106 IMPACT TESTS ON BALSA WOOD

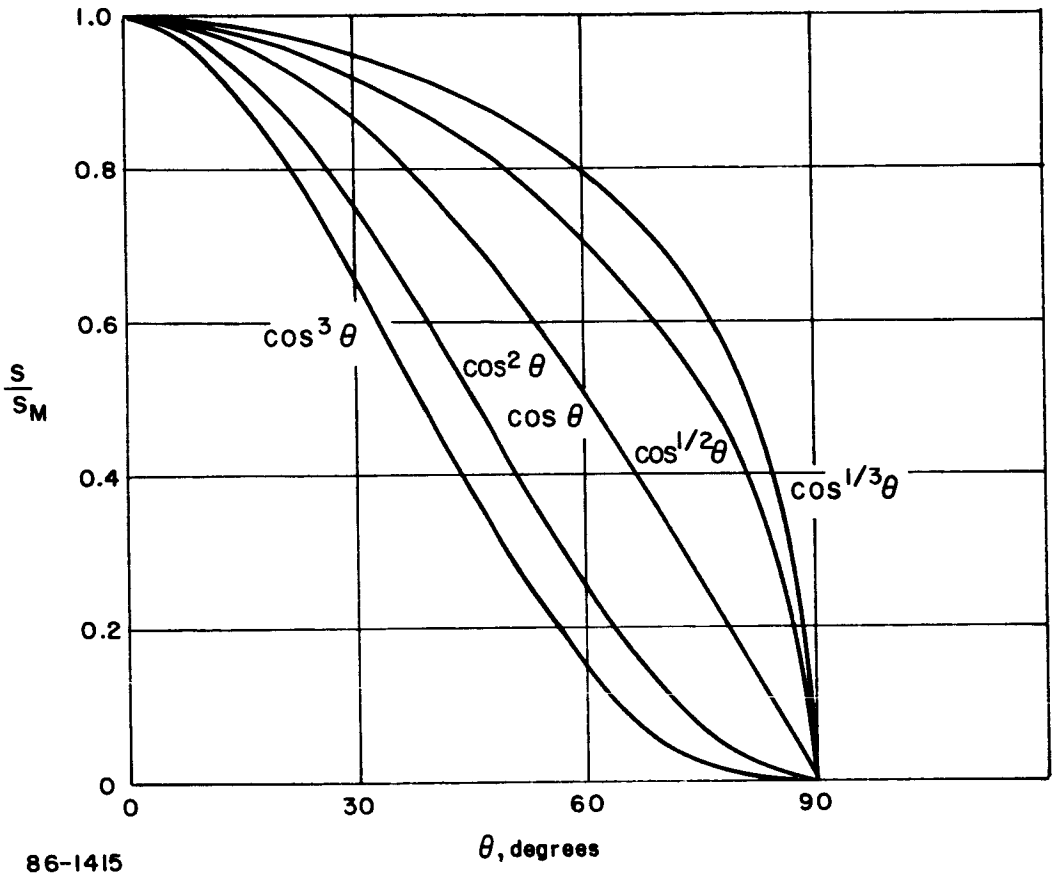

Figure 107 ANISOTROPIC COSINE FUNCTIONS

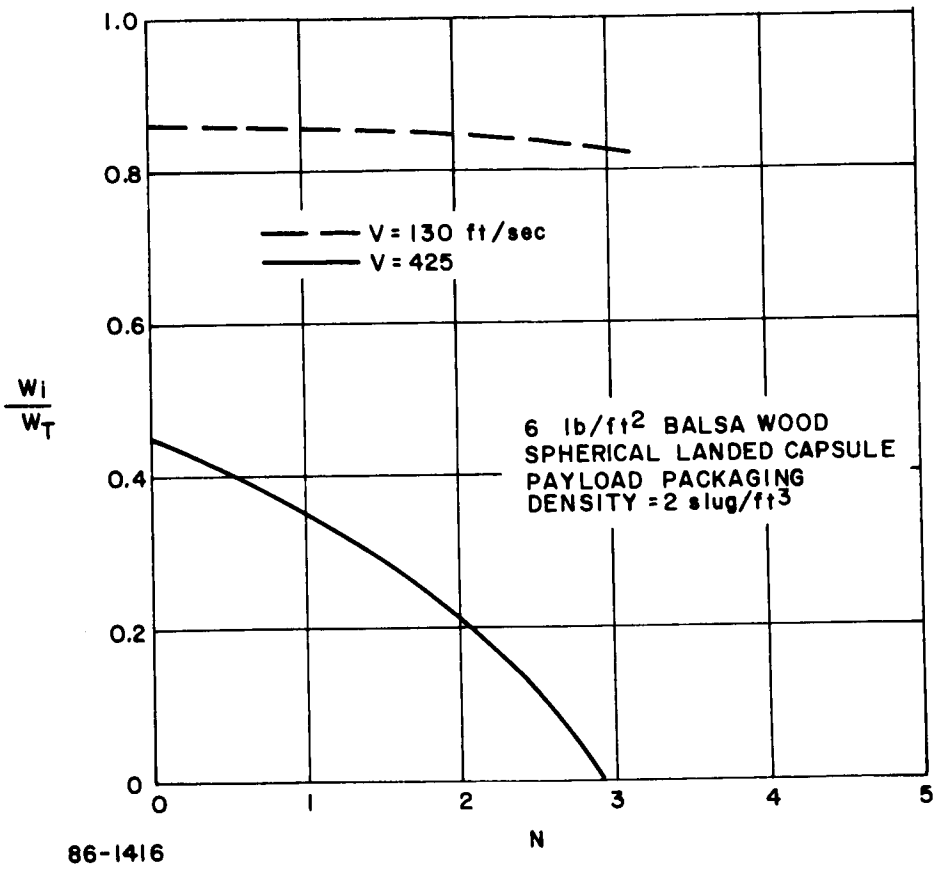

Figure 108 PAYLOAD WEIGHT FRACTION VERSUS n--BALSA WOOD

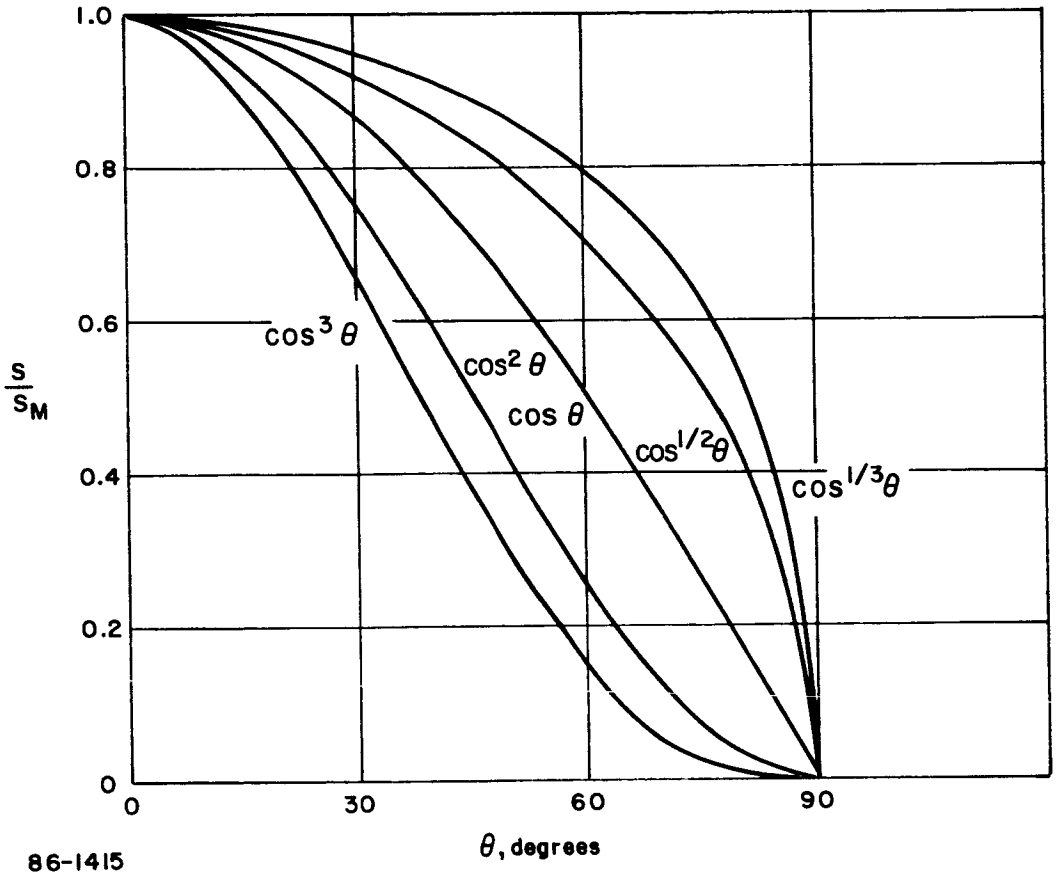

Figure 107 ANISOTROPIC COSINE FUNCTIONS

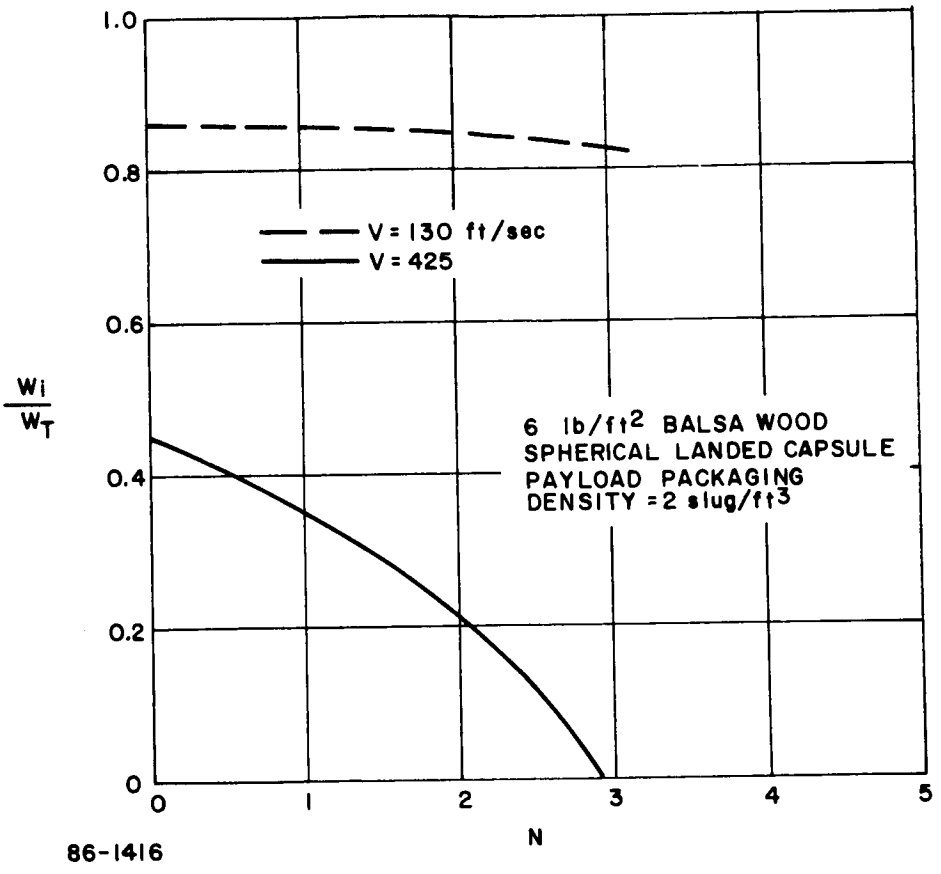

Figure 108 PAYLOAD WEIGHT FRACTION VERSUS n--BALSA WOOD

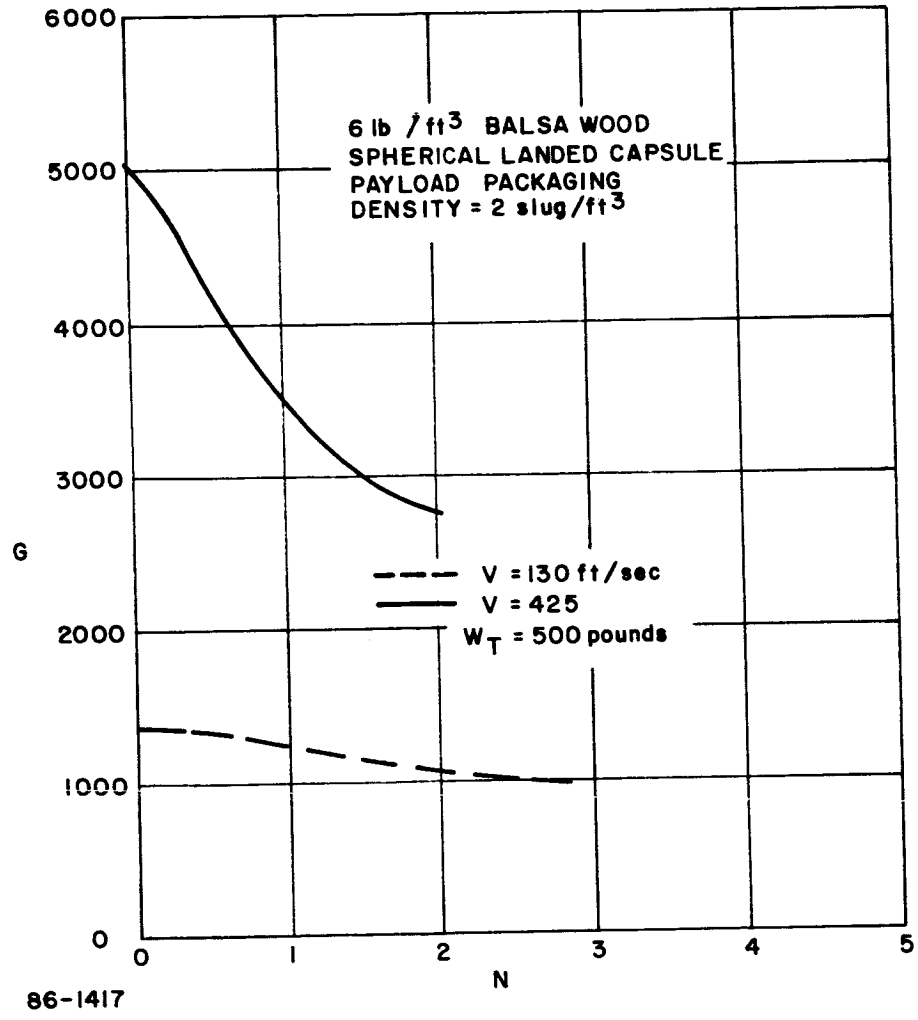

Figure 109 PEAK DECELERATION VERSUS N--BALSA WOOD

The degree of anisotropy has little effect on the 130 ft/sec design, but is crucial in determining if the parachute failure mode design is even possible. (This study used Avco/MSD digital computer program 1882, which takes account of the variation of decelerating mass during the impact (see Reference 24).

At this point in the parametric study, the results of the balsa wood test program became available. Comparison of Figure 105 with Figure 107 shows that a value of $n = 1$ would be conservative. Thus even the failure mode design at 425 ft/sec appears possible, yielding a payload weight fraction of about 35 percent. If the system is designed to accommodate only the 130 ft/sec nominal impact velocity, then a payload weight fraction of about 85 percent becomes possible. This is quite a bit higher than is attainable using the foam-filled fiberglass honeycomb, but the price is the high (1200 to 1300 g) deceleration level which must be accepted. (These numbers, it should be remembered, are for a spherical lander geometry.)

A possible way out of this dilemma may be to mechanically weaken balsa wood, by drilling a series of holes parallel to the grain. In this way, it may be possible to maintain the high energy absorption efficiency of balsa (i.e., foot-pounds of energy absorbed per pound of material crushed), while reducing the deceleration level, which is proportional to the crushing stress. Some preliminary in-house testing has been done on this concept, but the data is not sufficient to indicate whether or not there is promise in this approach.

In any event, the high-g balsa design may be forced upon us because of the results of the parametric studies of foam-filled fiberglass honeycomb designs which indicate that a very low density material is required. If the low density representatives of this material exhibit even more anisotropy than was assumed in the parametric study, then the internal payload weights which result may be too low to yield meaningful instrument packages.

3.2.5 Air Bags

3.2.5.1 Introductory remarks

Air or gas filled bags have been used as impact attenuators on many payload recovery systems in the past and several characteristics of them appeared to offer advantages for use in this application. Among these advantageous characteristics is the fact that an air bag can be stored in a relatively small volume. Further, very low deceleration levels are attainable if the bags are made large enough.

The principal disadvantage of air bags is that they are active impact attenuation systems in contrast to the passive crushable material systems.

Interestingly, a survey of the literature indicates a wide disparity between analysis and tests. (See References 26 through 42.) For the most part, the testers fail to generate parametric data or even to give typical weights while the analysts fail to use tests to obtain realistic values for many of the parameters they use. References 32, 41, and 42 are notable exceptions to this distressing trend, and most of the parametric data presented below is based on these references.

3.2.5.2 Typical Designs

Some designs which were investigated are illustrated on Figures 110 and 111. For the toroidal configuration, a set of five spheres was used (see Figure 110) rather than a doughnut shape for several reasons. Principal amoung these was the fact that a pure torus under internal pressure has a stress concentration at the inner surface; the smaller the opening in the torus is, the higher the stress concentration. Thus, even if varying fabric thicknesses were used at various sections of the torus, the inherently higher stresses in the torus make the five-sphere design significantly lighter.

It is assumed that variable orifices are used to vent the gas during an impact; typical design of this type of orifice can be found in Reference 36.

Properties of materials commonly used for air bags are tabulated below (from Reference 36).

Material	Weight		Tear Strength
	$oz./yd^2$	lb/ft^2	lb/in.
Neoprene coated Nylon	7.5	0.052	170
Raft Bottom MIL-R-009131 (USAF)	13.0	0.091	280
Neoprene-coated Nylon "Lite-Kote"	19.5	0.1354	400

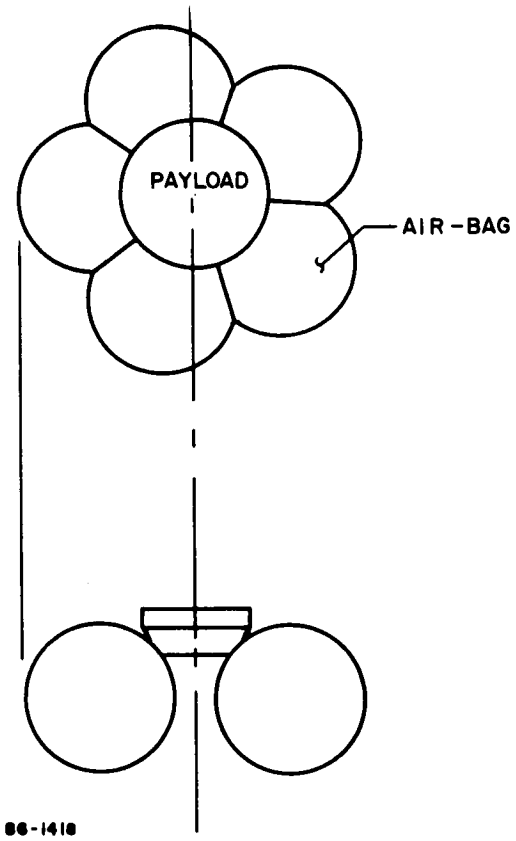

Figure 110 FIVE SPHERE TOROIDAL AIR-BAG DESIGN

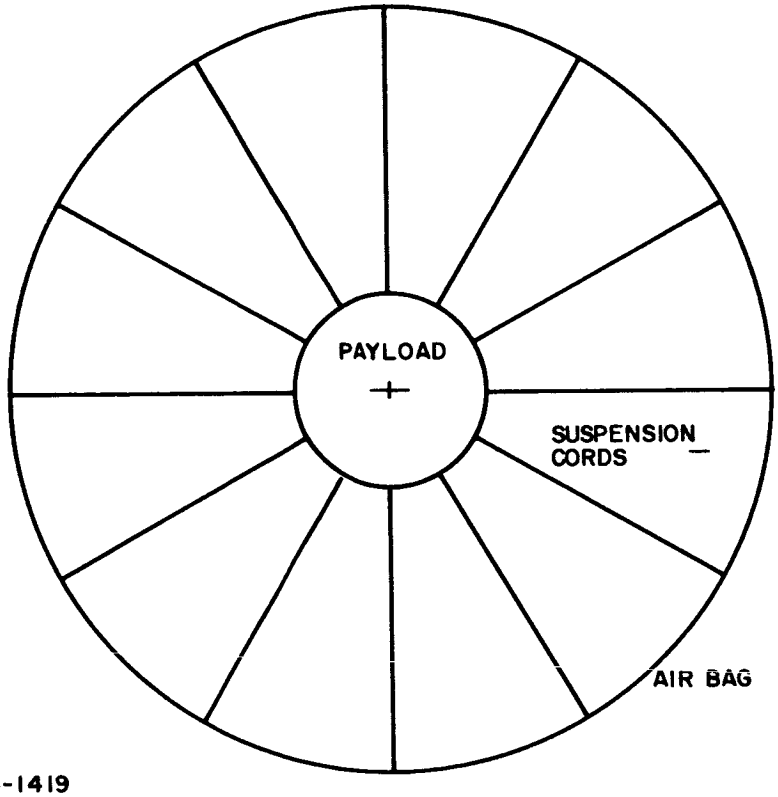

Figure 111 SPHERICAL AIR-BAG DESIGN

3.2.5.3 Design Data for Spherical Air Bags

Five-sphere design, Figure 50 of Reference 36 was adapted for generating parametric data for this study. The modified curve is shown on Figure 112. This is a curve of spherical bag diameter versus peak pressure. (Note that these curves are for a spherical bag which is wholely under the payload, not for a payload suspended inside a sphere.) Curves of constant total landed weight and of constant g are given on the curve. From page 41 of the reference, an equation can be obtained giving the bag weight as a function of pressure and diameter,

$$W = 0.0097\ PD^3 \quad (W \text{ in pounds, P in lb/in. and D in feet})$$

where a factor of 1.5 has been used to account for reinforcing girts and seams. Upon plotting this equation on Figure 112, the dotted lines result. An interesting feature of these lines is that they indicate that an optimum design exists in the neighborhood of 50 to 55 psi peak internal pressure. For higher pressures, the increase in fabric thickness overshadows the decrease in surface area and the bag weight increases. For lower pressures, the increase in surface area brought about by the larger size bag required more than compensates for the decreased skin thickness, again resulting in higher bag weights. At the optimum design point, the bag accounts for 22 to 23 percent of the total landed weight. Adding in the bag inflation system weight will increase this ratio to about one-quarter.

Now, in the five-bag design, it will be assumed that in the case of a canted impact, two of the bags must be sufficient to land the package. This assumption introduces a factor of 5/2 into the discussion, so that now the total air bag system weight would be of the order of 63 percent of the landed weight. Thus, the payload weight fraction attainable with this air-bag concept is significantly lower than can be obtained using crushable materials.

Spherical Design--Some discussion is in order concerning the spherical air bag concept presented in References 26 through 30. In this concept, the payload is suspended at the center of a large sphere. This concept provides the omnidirectional protection which is lacking in the toroidal or five-sphere designs.

From Reference 28, Figure 3, it can be found that a payload weight fraction of 90 to 95 percent is predicted at 130 ft/sec. This curve is based on a stress-density parameter of the bag material; the stress used in this parameter is that induced in the material by the internal pressure and is the stress prior to impact. Reference 28 uses a value of 10^6 ft^2/sec^2 (i.e., stress in lbs/ft^2 divided by density in $slugs/ft^3$)

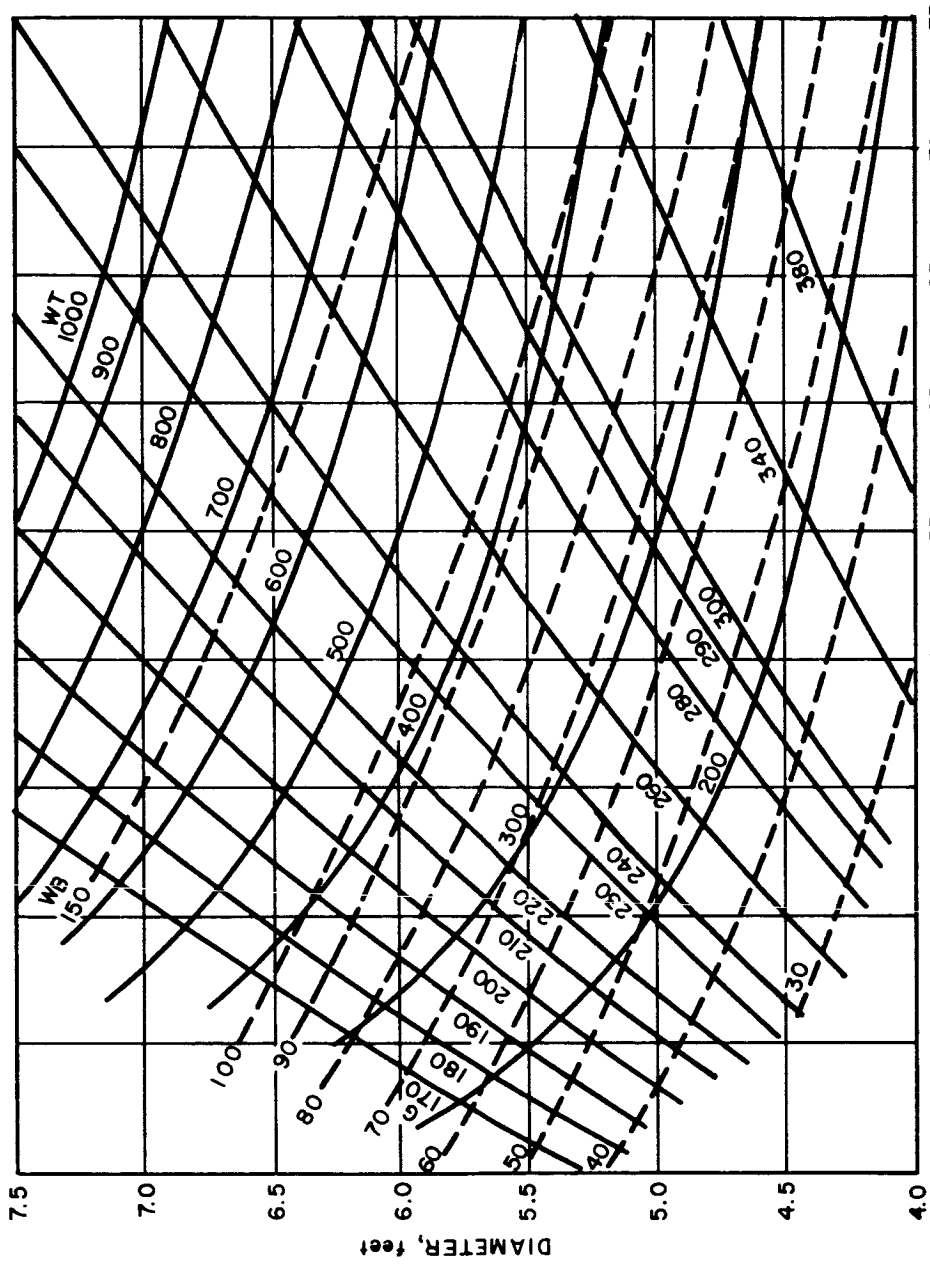

Figure 112 AIR-BAG PARAMETERS

for generating the curves. However, in Reference 29, it is shown that the peak stress in the bag fabric during impact can be 5 or 6 times the initial stess. Thus, a material has been implicitly assumed in the above references with a stress-density parameter of 5×10^6 ft^2/sec^2. The materials listed in the table above (see paragraph 3.2.5.2) have strength-density parameters of about 10^6. Thus Reference 28 has underestimated bag weights by at least a factor of 5. Adding in a safety factor, a factor to account for reinforcements and seams (1.5 is recommended by Reference 36, and the weight of an inflation system will bring the weight of this concept up to at least 40 to 50 percent of the total landed weight.

Further, the behavior of this system is analyzed by a quite idealized model in which the bag is assumed to suddenly rupture at the instant at which the payload has been arrested. Any deviations from this ideal will, of course, degrade the performance of this system.

Thus, in summary, this spherical air bag concept does not appear to offer a weight advantage over a crushable material system, and the added complexity of an air bag system make it less attractive than the passive, crushable material impact attenuation system, particularly when omnidirectional protection is desired.

3.2.6 Terrain Feature Management

An attempt at defining a model of terrain features of the Martian surface for engineering purposes has been made in Reference 43. The principal assumptions made in this reference are that the light areas of Mars are sandy deserts and the dark areas are volcanic rock. The results of the recent Mariner IV flyby mission to Mars cast doubt on both of these assumptions. The presence of a large number of craters on both the light and dark areas, (Reference 44) seems to preclude the possibility of fine sand, since such sand would eventually fill in most of the craters, at least in the light areas. (This interpretation then brings up the question of what the yellow clouds observed through the telescope might be, since these clouds were usually attributed to dust stores). Further, the Mariner IV photos show no evidence of tectonic activity (e.g., mountain chains) which implies that volcanism has not taken place.

Nevertheless, the criteria put forth in Reference 43 represents, in many cases, rather extreme conditions and could well serve as useful ground rules for estimating how well the lander can accommodate terrain features. Three criteria in particular were culled from those in Reference 43 being especially important. The first is the value assumed for the minimum bearing strength of Martian rock, namely 1 lb/in.^{2} (Reference 43.) This number is based on volcanic rock froth found on Earth. The second condition is a rock, approximated by a hemispherical hump whose radius is 1/2 that of a spherical lander. The third condition is a 30-degree slope. The implications of these three criteria on the lander are discussed in some detail below.

3.2.6.1 Low Bearing Strength Rock

The serious implication of the extremely low bearing stress of rock is that the impacting vehicle may imbed itself deeply in such a material. The classical reference for such terradynamics problems is Reference 45. It can be shown that the techniques developed in Reference 45 lead to an equation for depth of penetration into the medium of:

$$S = \frac{m}{C_D A \rho} \ln \left[1 + \frac{C_D \rho V_o^2}{2 \left(p_c - \frac{m}{A} g_m \right)} \right]$$

where S = penetration, feet

m = mass, slugs

C_D = drag coefficient in medium - 2 to 4

A = cross-sectional area of lander, ft^2

ρ = bulk density of medium, $slugs/ft^3$

V_o = impact velocity, ft/sec

p_c = crushing strength of medium, lb/ft^2

g_m = Martian gravity - 12 ft/sec^2

This formula was initially derived from a Poncelet resistance law ($F = \alpha + \beta V^2$) which was determined from experiments with sand. It has been found that the same type of resistance holds for impacts into granite, concrete, and clay (See Reference 46, p. iii).

Using a C_D of 2, V_o of 130 ft/sec and a bulk density of 2.32 $slugs/ft^3$ (based on 1.2 gms/cc.; see Refence 43, p. 46) yields:

$$S = \frac{1}{4.64} \frac{m}{A} \ln \left[1 + \frac{39{,}200}{p_c - 12 \frac{m}{A}} \right]$$

Now, the crushing stress, p_c, cannot be easily related to the bearing strength in the case of soils since soil bearing strengths are governed by shearing failures in the soil, rather than crushing (see Reference 47, pp 108-112). However, in the case of a rock froth, such as has been postulated here, the failure mode is indeed crushing; therefore, p_c in the above equation will be assigned the value 144 lb/ft^2 (1 psi from Reference 43). Finally, the value of m/A for typical oblate spheroid landers is close to 1/2. This gives

S = 0.61 feet

For spherical landers, m/A would probably increase to 1.5 to 2, which would increase the penetration by a factor of 3 to 4. Thus, a sphere could sink in as much as 2.5 feet. The same values would also hold for an oblate spheriod striking the ground edgewise. Since such vehicles are typically 6 or 7 feet in diameter, the results of this analysis indicate that, upon striking the hypothetical low bearing strength rock, the lander could penetrate 1/3 to 1/2 its length into the rock, but it would not bury itself.

3.2.6.2 Hemispherical hump

This criteria, as set forth in Reference 43, p. 49) attempts to set up a model of low scale surface contour as a series of hemispherical humps and holes. Humps whose radii are between 1/2 and twice the lander radius are excluded. It appears that the worst case of this terrain model would involve the payload landing on a hump whose radius was just 1/2 that of the lander (or in the case of an oblate spheroid, 1/2 the semi-minor axis), as illustrated in Figure 113. Since much less crushable materials is crushed in this case than is crushed on impact with a flat, smooth surface, not all of the kinetic energy will be absorbed before the hump begins interacting directly with the internal payload. This can lead to extremely high loadings on the payload.

There are several possible design alternatives which could be employed to attempt to accommodate such a terrain feature. One idea is to provide a layer of balsa wood between the internal payload and the honeycomb to absorb some of the shock. Another possibility is to harden some, but not all, of the payload to survive this worst case condition. That is, all of the payload would be designed to survive nominal impact conditions while only a minimum of instruments (perhaps only diagnostic instruments) would be hardened enough to survive the rare situation of landing directly on a hump. Of course, there exists the alternative of adding more of the foam-filled fiberglass honeycomb, but this procedure, would more than double the crushable material required. In this case, there would practically no weight left for payload.

3.2.6.3. Thirty-Degree Slope

The recommended maximum slop for design purposes, arrived at in Reference 43, is 30 degrees. This was arrived at by consideration of volcanic slopes on Earth and of sand dune angles. It is quite interesting to note that the same recommended design slope was arrived at during a previous study at Avco/RAD (see Reference 48) by consideration of entirely different phenomena, namely radar studies of the moon and of Mars and slope distribution studies of various areas on Earth.

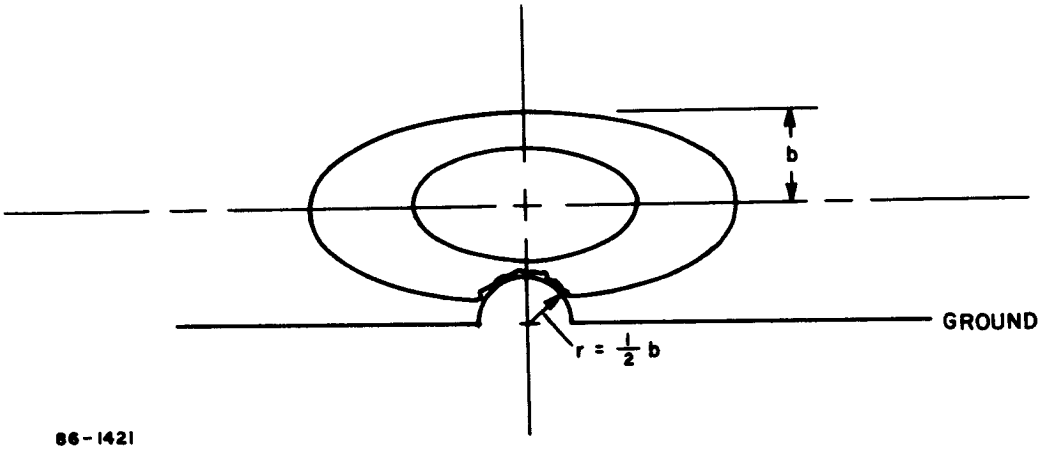

Figure 113 LANDER HITTING HEMISPHERICAL HUMP

Such a slope poses serious problems of stability, static and dynamic. Dynamically, a 30-degree slope will defeat almost any lander designed to land in an erect position, such as the design shown on Figure 110 especially with a further design condition of a 100 ft/sec horizontal velocity. The static problem arises in connection with the stable position assumed by a lenticular or ellipsoidal lander. Figure 114 illustrates the manner in which an ellipsoid tilts in order to be stable on a slope (of course, if the coefficient of friction between the ground and the lander is less than tan 30 degrees = 0.577, the lander will slide to the bottom of the hill, which would probably be desirable). If the coefficient of fraction is high enough, the lander will assume a position as indicated on Figure 114. A relationship between the variables can be found from geometry in the form:

$$\tan\psi = \frac{\left(\frac{a}{b}\right)^2 - 1 + \sqrt{1-(2+4\tan^2\theta)\left(\frac{a}{b}\right)^2 + \left(\frac{a}{b}\right)^4}}{2\tan\theta}$$

The plus sign in front of the radical leads to an unstable solution, so that the minus sign gives the solution of interest here.

For a slope angle, θ, of 30 degrees, the quantity under the radical is negative for values of $a/b < \sqrt{3}$, which leads to a complex value for ψ. Thus, if the lander is designed with an a/b ratio less than 1.732 it will not assume a stable position on the slope (except possibly on a flat created by crushing), but will flip-flop down the slope to flatter ground. The relationship between ψ and a/b for several slopes is shown on Figure 115. For a/b ratios a little bigger than 1.732, the angle ψ can be as much as 60 degrees. This is a severe condition with regard to antenna pointing considerations. It would be desirable to have the vehicle as near vertical as possible. Hence, if a 30 degree slope is accepted as a valid design condition, the a/b ratio of the lander ought to be as large as possible.

3.3 SIGNIFICANT PROBLEM AREAS

The most significant problem area at present is the very low density of the crushable material required for the oblate spheroid design (of the order of 2 lb/ft^3) as determined in the parametric study for typical lander weights of interest. Not only will this low a density material be difficult to manufacture, but its anisotropic behavior will probably be more severe than was assumed in the parametric study.

One possible way out of this dilemma is to raise the design deceleration level above 500 g. At higher g levels, the material required will be denser and, probably, less anisotropic. A level of 700 or 800 g would probably be sufficient, for payloads under consideration at this time, to bring the material density up to

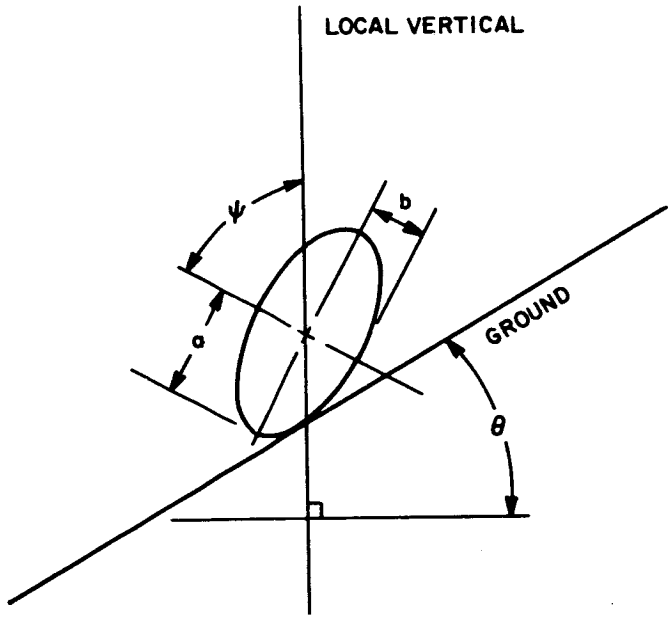

86-1422

Figure 114 OBLATE SPHEROID LANDER ON SLOPE

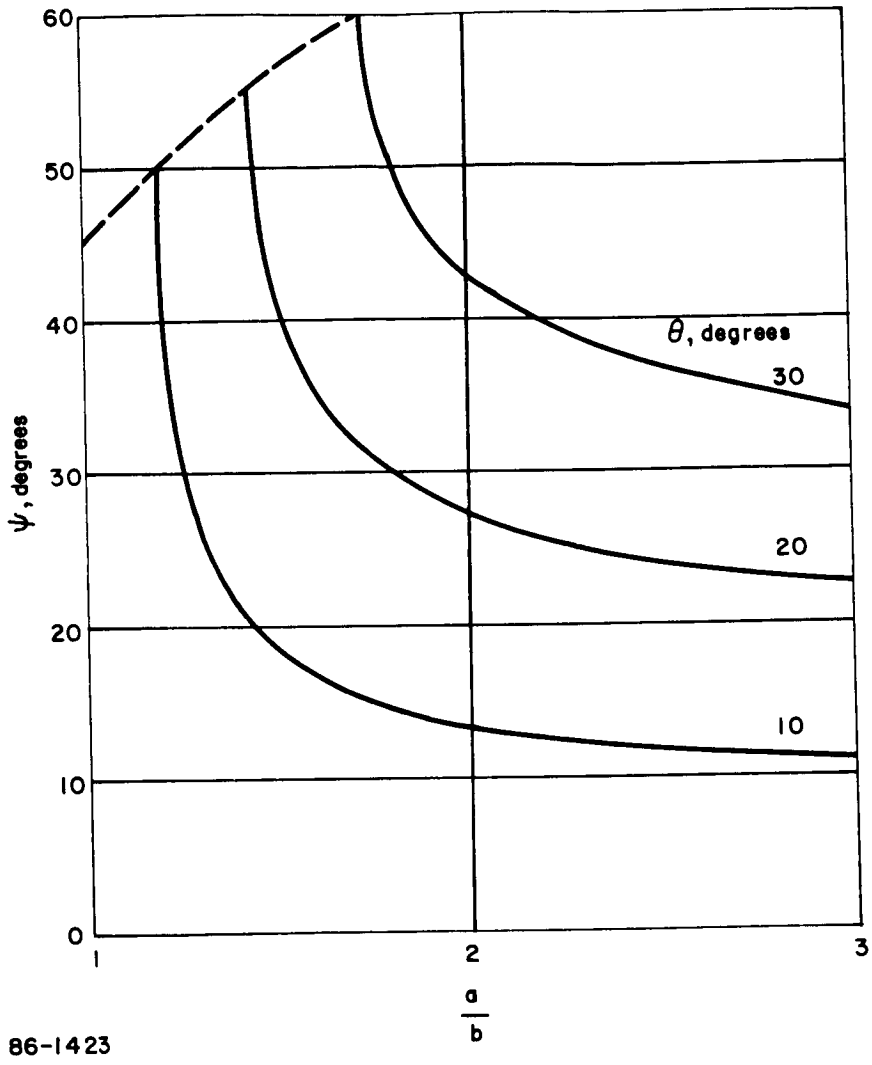

Figure 115 LANDER ANGLE VERSUS a/b RATIO

achievable values. Heavier payload would also mitigate this problem, as can be seen from Figure 94.

If the g-level is raised any more than this, then balsa wood becomes quite competitive, since its high g-level is compensated for by its very high payload weight fraction. The main problem with balsa wood is one of quality control, evidenced by the very wide spread in material properties obtained on samples (see Figure 104).

The technique for fabricating the impact attenuator will involve a great deal of development, particularly in reducing the weight of non-energy absorbing materials in the system (i.e., bonds, cover fabrics, etc.). The tradeoff between bending or cutting the honeycomb to the desired curvature will have to be studied, from the point of view of ease of fabrication and of maintaining the gross material properties.

3.4 FUTURE CONCEPTS

As was discussed in reference to Figure 80, presently available crushable materials are grouped into three rather distinct classes on the basis of their crushing strength-density characteristics. It would be desirable to fill in some of the resulting gaps in available materials, particularly the gap between balsa wood and honeycombs. One possible way to accomplish this may be to mechanically weaken balsa wood; e.g., by drilling holes in it or by using pencils of balsa wood to partially fill a low-density honeycomb. A brief set of tests was performed at Avco/MSD on the former concept, that of drilling holes in the specimens. In these tests, the density of the balsa wood was reduced by only 10 to 15 percent, not enough to draw general conclusions about the workability of this concept.

Nevertheless, it presently appears that this concept of weakened balsa wood is the most promising idea for improving the performance of the crushable material impact attenuation system.

The next evolutionary step, as landers become larger and more sophisticated, now appears to be a retrorocket system with some sort of terminal guidance. Even in this type of lander, the final touchdown shocks will most likely be attenuated by strategically placed crushable material pads, in the manner of the present LEM or Surveyor design, for example.

4.0 STERILIZATION CANISTER PRESSURIZATION SUBSYSTEM

4.1 SUMMARY

In the entry from approach trajectory design, a positive pressure within the sterilization canister was maintained from the time of sterilization until just prior to opening the canister in the vicinity of Mars. However, for the entry from orbit design the sterilization canister was vented during the Earth orbit phase of the mission due to the possible puncturing of the canister and the subsequent perturbation of the Planetary Vehicle's flight path by the escaping gas.

This change in the time of depressurization eliminated the requirement for an internal resupply system to maintain the pressure. Instead, the internal pressure will be regulated by ground equipment after sterilization. The ground equipment will be disconnected just prior to mating with the launch vehicle. Remaining components of the pressurization subsystem are a fill valve, through which the ground equipment is attached and a depressurization-relief valve for dumping the internal gases during the launch ascent and for maintaining a vent during the remaining portion of the flight to prevent a build-up of pressure due to slow outgasing from internal components.

This section will discuss the requirements of the subsystem and the major tradeoffs leading to the reference design. It will also discuss the methods used to meet the requirements. Finally, the problem areas that require more study are discussed. Only the entry-from-orbit design concept will be presented herein, due to the similarity of the subsystem for both entry from orbit and entry from approach trajectory design concepts.

4.2 REQUIREMENTS

The main function of the canister pressurization subsystem is to maintain a pressure inside the canister higher than that of the ambient conditions. Because of the size and construction of the canister and the desire to minimize weight, the differential pressure was restricted to 1.0 lb/in^2.

Since the pressurization profile was changed to include depressurization in Earth's parking orbit rather than at Mars orbit injection, the internal resupply was omitted and no pressurization control except relief and depressurization need be included in the subsystem. For long ground storage after sterilization, an external tank with a sterile gas supply and a regulator must be provided. Means must be designed into the subsystem to disconnect the external control and supply prior to mating with the launch vehicle. In case of a long prelaunch hold time, there must also be means of resterilizing the connection and reconnecting the external supply.

The relief system must open if the internal pressure exceeds the maximum allowable, however, during ground storage the ground equipment should provide this function to assure maintaining a good seal on the canister unit. During launch phase the canister internal gas volume must be dumped at a rate sufficient to keep the differential pressure under the required 1.0 lb/in.^{2} maximum.

All units of the pressurization control subsystem with connections to the outside must conform to the mission requirement that the probability of contamination of Mars with a viable Earth microorganism will be less than 10^{-4}.

4.3 MAJOR TRADEOFFS

The resupply and venting during storage on the ground will be by ground equipment with the attachment through a fill valve. This valve is necessary to allow the positive-acting (and probably heavy) regulating valves and sufficient sterilized gas supply for long storage periods to be mounted in one package away from the flight unit. By using ground equipment, the flight equipment need not be operated with the risk of developing leaks prior to installation on the launch vehicle. Also, the relief valve on the canister can be an explosive valve to be opened at lift off.

The relief valve requires a large dumping area to allow the internal volume of gas to escape during the short time from lift off to Earth parking orbit. However, even with filters in the relief line, it appears desirable to reduce the opening and provide a labyrinth exit for continuous venting during Earth orbit (and possibly longer) to protect from external contaminated products and to allow for outgassing of internal equipment and materials. The opening for Earth orbit venting can be accomplished by puncturing a hole in the main relief valve when the relief valve is actuated. This will allow continuous venting through a smaller hole when the relief valve is closed after launch phase venting.

4.4 METHODS AND RESULTS

4.4.1 Leakage Rate

The leakage rate of the canister and seals are determined primarily by the requirement that the entry vehicle be maintained in a sterile condition. Microorganism that can cause contamination are as small as 0.3 or 0.4 microns (a low probability exists that the canister be exposed to smaller organisms). The canister is pressurized to help prevent the influx of microorganisms, but, since the flow through very small leaks or pores will be molecular flow, the internal pressurization cannot prevent a microorganism from diffusing through the leak from the outside while the internal pressure is positive, i.e., particles striking the hole from either side could get through. In order to assure that microorganisms do not

penetrate the barrier, the largest leakage holes must be smaller in size than the anticipated microorganisms. Thus, the maximum hole size in the canister should be from 0.1 to 0.2 microns. This design goal appears to be compatible with current state-of-the-art in seal design and the construction of weldments.

It is shown in a concurrent Avco study (see Reference 49) permeability through an aluminum weldment (6061, TIG welded) is less than 1.0 percent per year, with an external vacuum of 6×10^{-6} mm Hg and an internal pressure of 1.0 atmosphere. The study also concluded that the most important contributors to leakage rates are the seals, with their inherent leakage, seal construction inaccuracies, and assembly procedure sensitivity. Proper selection of seal design and materials, along with careful assembly procedures, can reduce these rates sufficiently so that permeation of the gas through the seal material becomes the predominant leakage effect (see Reference 50).

Methods for leak rate calculations are included in Appendix B. With a 1.0 $lb/in.^2$ pressure differential across the canister wall, the reference design (6.56×10^4 $-in^2$ surface area for a 188 inch Flight Capsule) gives an initial leak rate of 2.17×10^{-7} lb/sec (18.75×10^{-3} lb/day). After a 300-day storage period the pressure will drop to approximately 0.1 $lb/in.^2$ gage. This calculation for the pressure range does not take into consideration changes in environmental temperatures and pressures. and for this reason, external control and resupply is discussed in paragraphs 4.4.2 and 4.3.

4.4.2 Resupply Method

A resupply method is required to replace the internal gas during the cooling period of the sterilization cycle and during the ground storage phase prior to launch vehicle mating (resupply may be required after mating if assembly and checkout procedures are too long). The replacement gas is stored in an attached auxiliary tank included in the sterilization process.

Immediately after the final assembly, the flight capsule should be purged with nitorgen and maintained at a positive pressure to avoid gas influx at any time. Since the pressure limits for the canister are a positive differential of from 0 to 1.0 $lb/in.^2$ (due to structural limitations) pressure will be maintained at approximately 0.5 $lb/in.^2$ to allow for some environmental temperature and pressure variations. Thus, at the start of the sterilization cycle, the canister will contain 38.7 pounds of nitrogen gas in a canister volume of 517 ft^3 (using an assumed Florida mean temperature of 70° F and an ambient pressure of 14.7 $lb/in.^2$). During the heating cycle the pressure can go up to 15.7 $lb/in.^2$(14.7 + 1.0) and then must be vented. With 15.7 $lb/in.^2$ and a sterilization temperature of 135°C (275°) the canister will contain 28.8 pounds of nitrogen, the excess gas (9.9 pounds)

having been vented off. Now, as the temperature returns to normal (70°F) the internal pressure will return to 11.3 lb/in.^{2}. Because of this, the external supply must return the 9.9 pounds of gas to the system as the temperature is reduced.

By adding the above gas loss to that from leakage (discussed in paragraph 4.4.1), the size of the external supply can be determined. There are two periods in which this leakage occurs. The first period is the storage from the end of sterilization to mating with the launch vehicle or spacecraft. During this period, the supply tank is attached to the canister. The second period is from the mating to the time of lift off. Due to canister leakage, this period must be considered in the sizing of the tank because it may be desirable to start the period with a higher differential pressure than 0.5 lb/in.^{2}

Both periods are of unknown length but a conservative assumption can be made of 300 days for the first period (storage) and one launch window period, or 60 days for the second (from mating to launch). The environmental conditions must be considered when determining the canister pressure differential.

The major objective in the pressurization control subsystem is to reduce the cycling requirements of the pressure control equipment and, especially, to eliminate opening the relief valve vents to the ambient atmosphere. The 3σ yearly pressure range in the vicinity of the Florida launch pads is approximately 14.6 to 100°F (see Reference 51). The variation in atmospheric pressure can be easily handled for the allowable pressure range by keeping the internal absolute pressure between a maximum of 15.6 lb/in.^{2} (14.6 + 1.0) and a minimum of 15.0 lb/in.^{2}

The temperature variation must be monitored more closely unless the canister is in a temperature controlled room and shielded from radiating heat sources. Figure 116 shows the relationship between the canister and the environmental temperature and pressure. The environmental temperature and pressure 3σ ranges in the vicinity of the Florida launch pads is shown outlined by dotted lines. The sloped lines represent the variation of pressure versus temperature at a constant internal gas volume.

At the top of the graph is a line representing 1.0 lb/in.^{2} over the minimum ambient pressure. As the gas temperature increases, the tank pressure will approach the limit pressure of 1.0 lb/in.^{2} over ambient. This line is the lower value of the limiting pressure. Exceeding the limit pressure will allow the relief valve to vent the canister, which is undesirable. As ambient temperatures decrease, the supply system will have to add gas to the canister if the internal pressure reaches the level of the ambient pressure (hence, zero differential). It is advisable to maintain a 0.1 lb/in.^{2} minimum differential as a safety precaution.

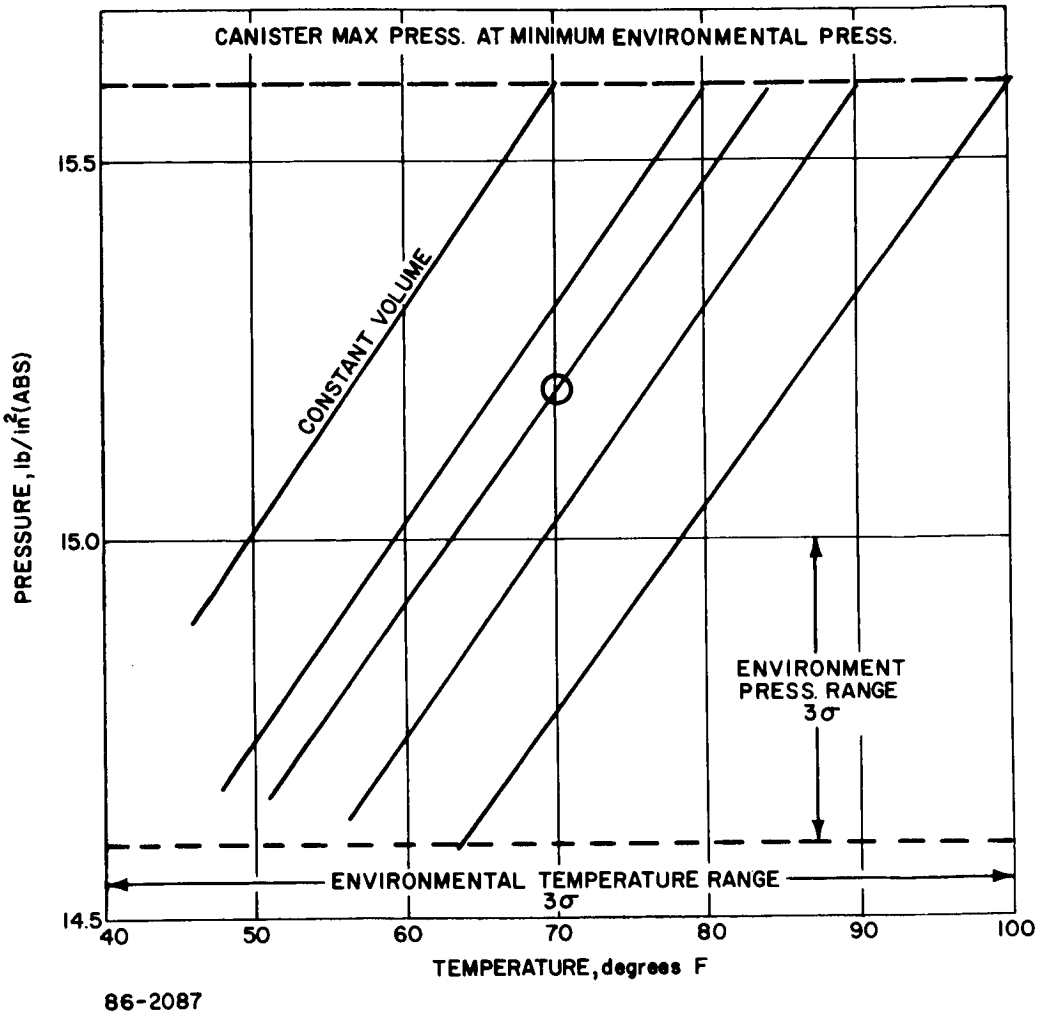

Figure 116 STERILIZATION CANISTER GAS TEMPERATURE--PRESSURE VARIATION

For sizing the resupply tank, an arbitrary temperature of 70°F (mean January temperature in vicinity of Florida launch pad) and, for conservatism, an atmospheric pressure of 14.7 lb/in.^{2} are assumed. The canister pressure, for a differential of 0.5 lb/in.^{2}, is then 15.2 lb/in.^{2} absolute. Due to the leak rate, the differential pressure will decay as an exponential function (see Appendix B). However, for conservatism, the regulator should be set at a minimum differential pressure of 0.1 lb/in.^{2} and assumed to operate at this value above the maximum 3σ value of the ambient pressure (15.0 lb/in.^{2}, Figure 116).

The ratio $\Delta P / \Delta P_{initial}$ (final differential pressure to initial differential pressure) is calculated as 0.11 at the end of a 300 day cycle (see Appendix B). Using this valve, the graph in Figure 117 was constructed which shows $\Delta P / \Delta P_{initial}$ plotted as a function of the cycle length in days. From the graph the cycle in days from an initial differential pressure of 15.2 lb/in.^{2} to a final one of 15.1 lb/in.^{2} ($\Delta P / \Delta P_{initial} = 0.8$) is found to be 30 days. The gas loss from this pressure change is 0.2 pounds and in 300 days the cycle will occur 10 times making the total gas loss 2.0 pounds. Since this is replaced by the resupply tank, the final sterilization canister pressure will be 15.2 lb/in.^{2}

Since the launch period (from launch vehicle mating to lift-off) was assumed to be 60 days long, the resupply tank must fill the canister to a sufficient pressure to avoid reaching ambient pressure through the leakage. This pressure is found by using Figure 117. For a 60-day cycle, $\Delta P / \Delta P_{initial}$ is 0.64. Assuming the final pressure as 15.2 lb/in.^{2}, the canister pressure must be brought up to 15.33 lb/in.^{2}, thus adding 0.7 pounds of gas.

The total gas supply, therefore, is the sum of the sterilization cycle replacement (9.9 pounds), the first storage period (2.0 pounds) and the second launch hold period initial refill (0.7 pounds) or 12.6 pounds total. This value has been arrived at by a cursory investigation of the conditions to which the sterilization canister will be exposed, therefore, a factor of safety of two on the gas supply required (25.2 pounds of gas) is used to determine the resupply tank size.

Assuming an initial pressure of 500 lb/in.^{2} in the resupply tank and a final pressure of 30 lb/in.^{2} the tank will hold 26.8 pounds of nitrogen (at the 70°F) and the tank volume required is 10.9 ft^3. By maintaining the canister in a temperature controlled environment, the initial pressure can be closer to the upper limit and actuation of the resupply valve can be reduced.

4.4.3 Venting and Relief Approach

Pressure relief during the sterilization cycle and ground storage phases will be accomplished by the ground equipment resupply system. The

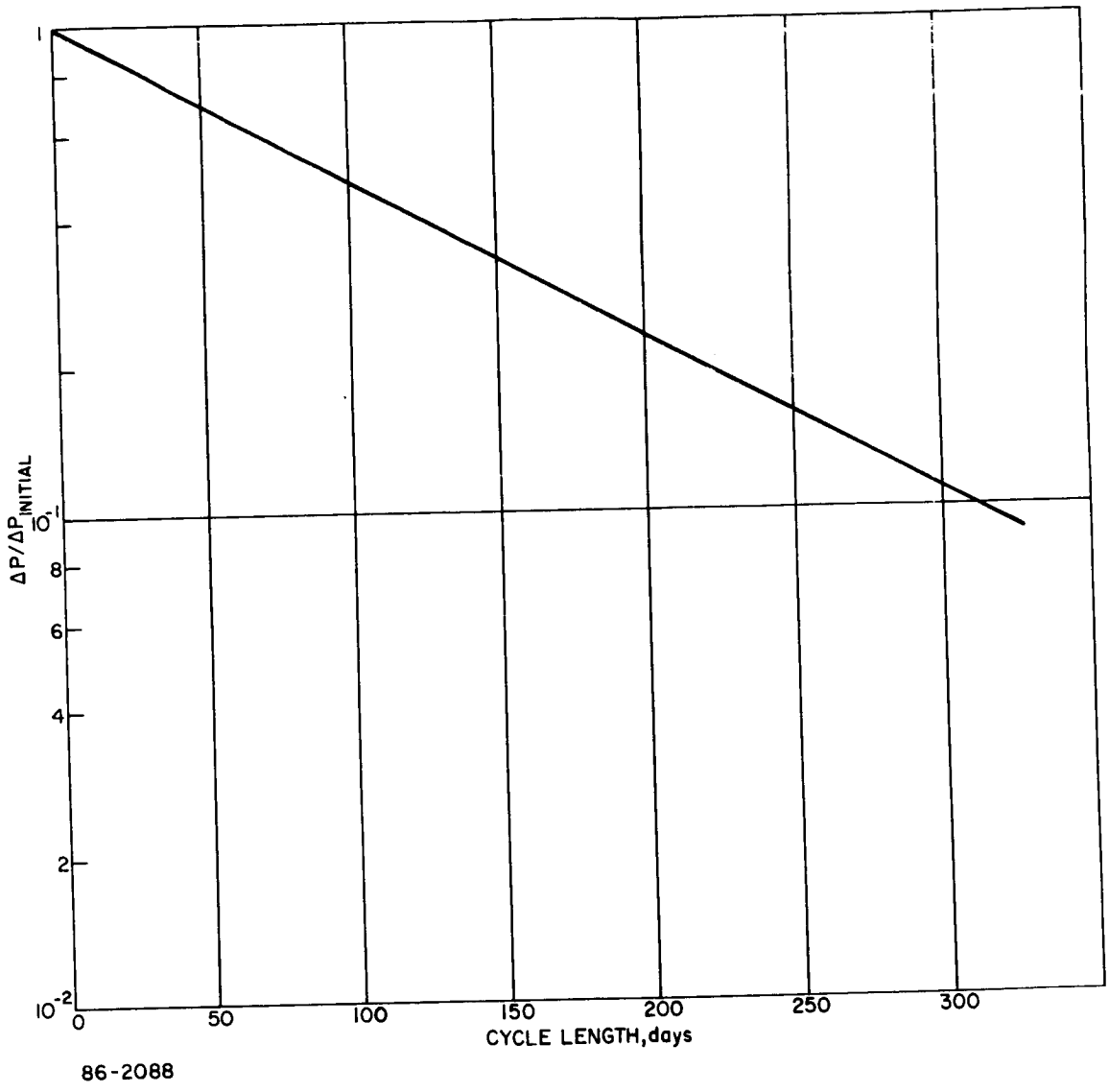

Figure 117 CYCLE LENGTH EFFECT ON STERILIZATION CANISTER PRESSURE DIFFERENTIAL

environments, to which the canister is exposed, should be controlled within limits that prevent the necessity of the relief mechanism operating. This is advisable even though the relief valve ports will contain micro filters, and will avoid any possibility of recontamination or problems with re-sealing the valve.

Detail design of the relief valve has not been done, but it must contain a pressure relief mechanism to allow venting of the canister if the differential pressure exceeds 1.0 lb/in.^{2} The most difficult requirement, however, is the venting of the canister during the launch phase. Immediately after the launch vehicle lifts from the launch pad, the relief valve must open to allow the internal gas to escape at a rate sufficient to maintain the differential pressure under 1.0 lb/in.^{2} Exact pressure change rates during the ascent of the Saturn V launch vehicle are not available but preliminary curves from the Saturn V manual indicate a time versus altitude relationship. An approximation of this curve is shown in Figure 118. The time of interest on this curve is the first 120 seconds at the end of which time the ambient pressure is well below 1.0 lb/in.^{2} By using this portion of the curve the ambient pressure-time relationship was determined and is shown in Figure 119. The pressure relief valve port size in the canister is then determined to match the maximum rate of ambient pressure change*.

Two 6-inch diameter relief valve ports were assumed for the reference design. They were evaluated for gas flow by the method shown in Reference 52 for an orifice where the pressure ratio across the orifice is less than the critical pressure (maximum flow pressure). From the reference, the flow through the orifice in ft^3/sec is:

$$q = \frac{31.5\, C\, d_z^2\, Y^1}{60\, \rho_1} \sqrt{\rho_2\, \Delta P} \quad (N)$$

N = number of orifices (relief valves)

C = orifice coefficient of discharge

d_1 = canister diameter, inches

d_2 = orifice diameter, inches

ρ_1 = canister gas density lb/ft^3

ρ_2 = orifice discharge gas density lb/ft^3

* The calculation assumes that the Saturn V ascent shroud is vented to ambient conditions during launch.

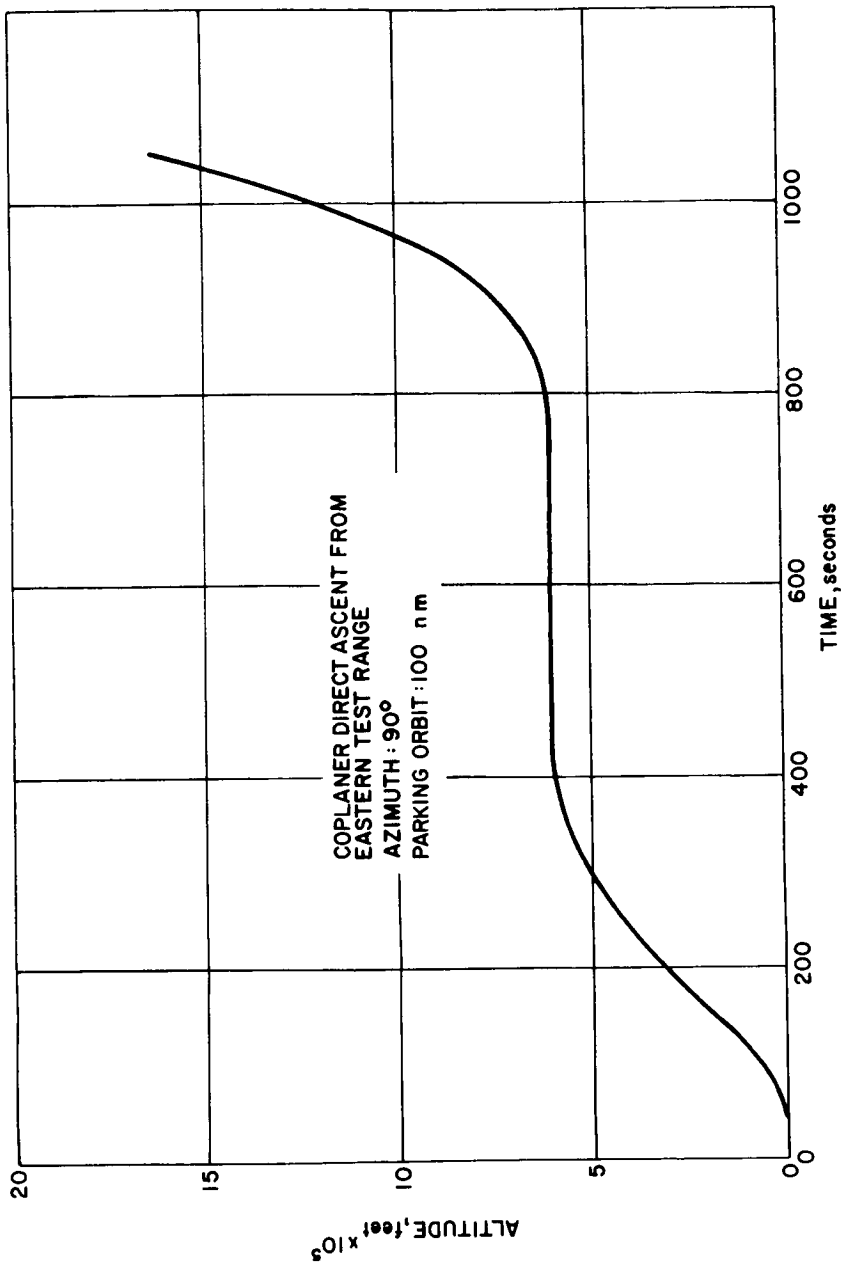

Figure 118 SATURN V LAUNCH/ALTITUDE HISTORY

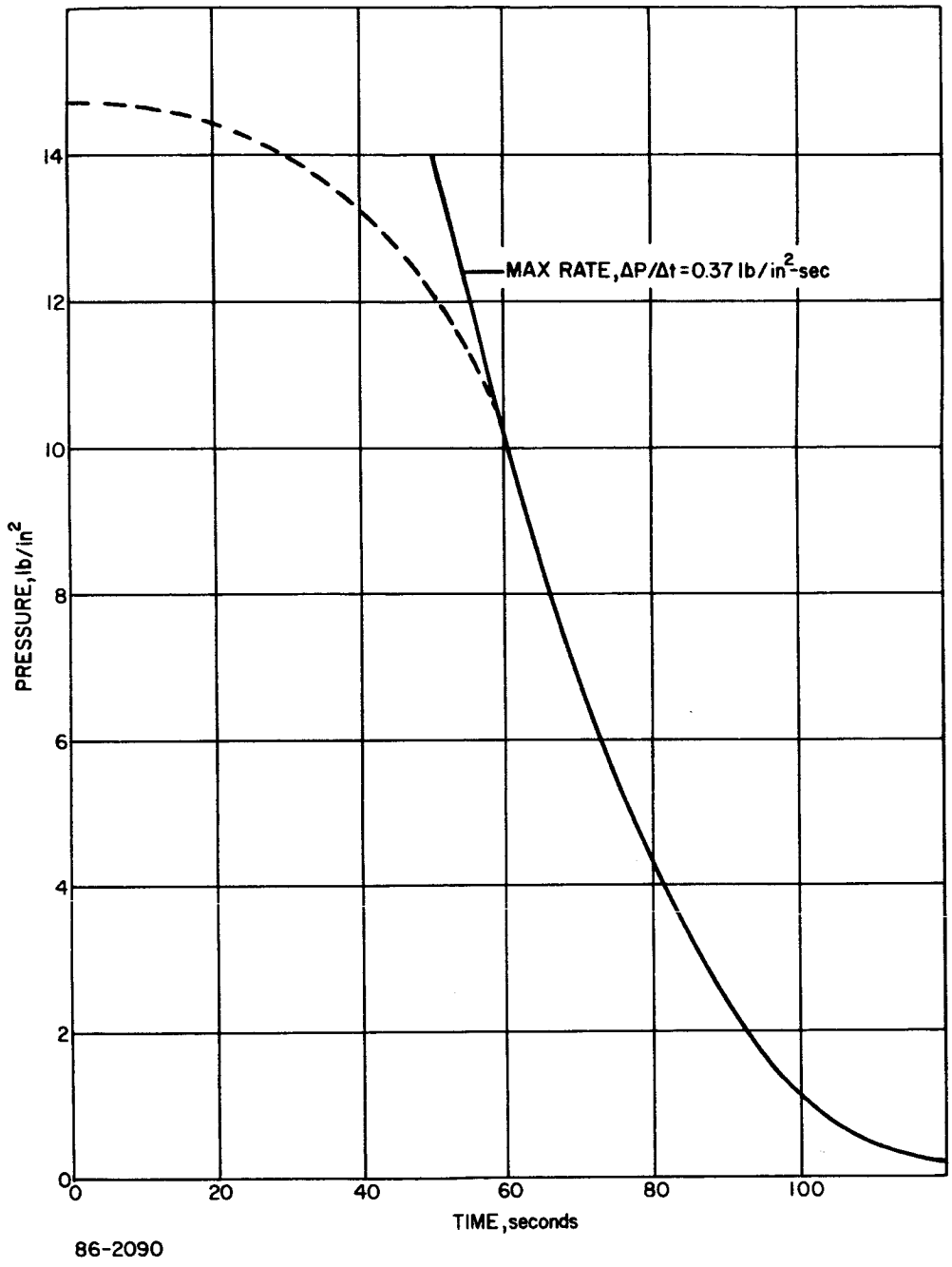

Figure 119 SATURN V LAUNCH AMBIENT PRESSURE HISTORY

P_1 = canister pressure, lb/in.^{2}

P_2 = orifice discharge pressure, lb/in.^{2}

$\Delta P = P_1 - P_2$

Y^1 - from the Table 38 Reference 52

assuming $\frac{d_2}{d_1} = 0$

$k = C_p/C_v = 1.40$ for nitrogen

Assuming that the ambient pressure has dropped to 14.2 lb/in.^{2} (less than 1000 foot altitude) upon opening of the relief valve, the gas flow will be 38.2 ft^3/sec. At 60 seconds after lift off the ambient pressure will be down to 10 lb/in.^{2} and the flow rate through the relief valve will have increased to 43.6 ft^3/sec. The maximum rate of change in the atmospheric ambient pressure will take place at approximately 60 seconds after lift-off and is 0.37 lb/in.^{2}/sec (see Figure 119). This rate of change in the atmospheric pressure requires a gas flow rate of 19 ft^3/sec from the sterilization canister, therefore, the vent area is approximately twice the required size and allows one orifice to be a redundant mechanism.

One vent will be in combination with a pressure relief valve for emergency actuation if required during the ground storage phase and for venting during the interplanetary cruise phase.

4.5 PROBLEM AREAS

There are three main categories in the pressurization subsystem and the problem areas can be divided according to these categories. They are: the sterilization maintenance, the pressure maintenance, and the pressure dumping. The sterilization problem areas are seal and joint leakage; not only of quantity of gas lost but methods to detect the leak and measure the leak rate. The detection and measurement problem, in the micro sizes of interest, in itself requires a development test program.

The problems of pressure maintenance are basically those of close tolerance pressure measuring equipment, leak free valve requirements and launch vehicle checkout times. In the pressure dumping realm, the relief valve port sizing requires more launch vehicle information and analysis of the pressure decay rate to be experienced by the canister. This decay rate may be influenced by the shroud or by the method of venting the shroud.

REFERENCES

1 Effect of Biological Sterilization and Vacuum on Certain Parachute Retardation System Components, Cook Technical Center CPT 4324, (August 1964)

2 Fabric Research Laboratories, Inc. Dedham, Mass. Fibrons Materials for Aerodynamic Decelerators, (July 1965)

3 The Effects of Design Parameters and Local Flow Fields on the Performance of Hyperflo Supersonic Parachutes and High Dynamic Pressure Parachute Concepts, L. W. Sims, Cook Electric Co., Tech. Rpt. AFFDL-TR-65-150, I, (October 1965).

4 NASA Engineering Models of the Mars Atmosphere for Entry Vehicle Design, Edited by George M. Levin, Dallas E. Evans, and Victor Stevens, NASA TN D-2525

5 Parachute Design Study for Mariner B Entry Capsule, Cook Technical Center Report FR-3807A, (March 1963)

6 Retrorocket-Parachute Landing System Study for Earth and Martian Entry Vehicles, Northrop Ventura RPT-NVR-3559 (June 1964)

7 Apollo Recovery System Dynamic Analysis, Northrop Ventura Report NVR-3528 (April 1964).

8 Performance of and Design Criteria for Deployable Aerodynamic Decelerators, Technical Report No. ASD-TR-61-579 (December 1963).

9 Daigle, D. L. and Lonborg, J. O., Evaluation of Certain Crushable Materials JPL Tech. Report No. 32-130 (13 January 1961).

10 Duke, W. Lunar Landing Problems, Advances in the Astronautical Sciences - 10, Manned Lunar Flight, pp. 102-155.

11 Landing Test Results on Surveyor Evaluation Program, American Cyanamid Co. Report.

12 Hexcel Products, Inc., Bulletin TSB-122.

13 Hexcel Products, Inc., Bulletin TB-702.

14 Hexcel Products, Inc., Bulletin TB-703.

REFERENCES (Cont'd)

15 Karnes et al, High-Velocity Impact Cushioning - Part V - Energy Absorption Characteristics of Paper Honeycomb, Univ. of Texas Structural Mech. Res. Lab. (May 1959).

16 Mechanical Properties of Hexcel Honeycomb Materials, Hexcel Products, Inc., Bulletin No. TSB-120, (February 1964).

17 RF Transparent, Energy Absorbing, Structural Elements - Phase II, Final Report, G. E. Doc. No. 64 SD 4329 (17 August 1964)

18 Smith, R. H., Final Report on Development of a Radio-Frequency Transparent, Energy-Absorbing, Structural Element, Northrup Ventura Report, in preparation (February 1965).

19 Energy Absorption Properties of Aluminum Honeycomb, Hexcel Products, Inc., Bulletin No. TSB-110 (10 January 1960).

20 Flex-core, Hexcel Products, Inc., Data Sheet 2700 (May 1964).

21 Lewallen, J. M., and Ripperger, E. A., Energy-Dissipating Characteristics of Trussgrid Aluminum Honeycomb, Univ. of Texas Structural Mech. Res. Lab., Report No. SMRL RM -5 (March 1962).

22 Avco/MSD internal memos.

23 Shield, R. and Covington, C, High-Velocity Impact Cushioning, Part VI-108C and 100C Foamed Plastics, Univ. of Texas Structural Mech. Res. Lab. (September 1960).

24 Cloutier, G. J., Dynamic Analysis of Crushable - Material Impact - Energy Absorbers, Avco/MSD document No. KHDR-15 (June 1965).

25 Final Report - Systems Study for Lunar Reconnaissance Probe, Space General Corp., Report SGC 4 0R-2, Part II, (21 February 1964).

26 Martin, E. D., and J. T. Howe, An Analysis of the Impact Motion of an Inflated Sphere Landing Vehicle, NASA TN D-314 (1960)

27 Howe, J. T. and E. D. Martin, Gas Dynamics of an Inflated Sphere Striking a Surface, NASA TN D-315 (1960).

28 Martin, E. D., A Design Study of the Inflated Sphere Landing Vehicle, Including the Landing Performance and the Effects of Deviations from Design Conditions, NASA TN D-692 (April 1961).

REFERENCE (Cont'd)

29 Martin, E.D., Skin Stresses in an Inflated Sphere During Impact, NASA TN D-1070 (1961).

30 Howe, J.T., Theory of High-Speed-Impact Attenuation by Gas Bags, NASA TN D-1298 (April 1962).

31 Esgar, J.B. and W.C. Morgan, Analytical Study of Soft Landings of Gas-Filled Bags, NASA TR R-75 (1960).

32 Turbow and Ogletree, The Energy-Dissipating Characteristics of Air-bags, Univ. of Texas Struct. Mech. Res. Lab. (August 1959).

33 Fisher, L.J., Landing Impact Dissipation Systems NASA TN D-975 (December 1961).

34 Schrader, C.D., Lunar and Planetary Soft Landings by means of Gas-Filled Ballons, ARS 2480-62 (Lunar Missions Meeting (17 - 19 July 1962).

35 Curchack, H.D., and Van Der Linden, R.E., Balloon for Soft Impact Landing, Diamond Ordnance Fuze Lab., Report No. TR-863, (AD-243 693) (October 1960).

36 Simonson, J.R., Study of Design Criteria for Landing Shock Absorption Devices for Recoverable Flight Vehicles, ASD-TR-61-583 (January 1962).

37 Bixby, H.W., Impact Attenuation Methods for Manned Spacecraft, Northrup Ventura Tech. Pub. No. 63.

38 Burns, A.B., Lunar Alightment Systems Investigation, ASD-TDR-63-454 (AMF) (June 1963).

39 Tomesak, S.L., Decelerator Bag Study, WADS TR 59-775 (Contract No. AF-33(600)30825) U.S.A.F. (June 1960).

40 Stubbs, S.M., and McGehee, J.R., Investigation of the Landing Characteristics of a Reentry Vehicle having a Canted Multiple-Air-Bag Load-Alevia-tion System, NASA TN D-1934 (August 1963).

41 McGehee, J.R., and V.L. Vaughan, Jr., Model Investigation of the Landing Characteristics of a Reentry Spacecraft with a Vertical-Cylinder Air Bag for Load Alleviation, NASA TN D-1027 (March 1962).

42 McGehee, J.R., and M.E. Hathaway, Landing Characteristics of a Reentry Capsule with a Torus-Shaped Air Bag for Load Alleviation, NASA TN D-628 (November 1960).

REFERENCES (Concl'd)

43 Spencer, Dwain F., Mars Engineering Atmosphere and Surface Models, JPL document (semi-final draft) (July 1965).

44 Leighton, Murray, Sharp, Allen, Sloan, Mariner IV Photography of Mars: Initial Results, Science, Vol. 149, pp. 627-630 (6 August 1965).

45 Allen, Mayfield, and Morrison, Dynamics of a Projectile Penetrating Sand, Journal of Applied Physics, Vol. 28, No. 3, pp. 370-376 (March 1957).

46 McMath, R.R., and Migotsky, E., Projectile Penetration Studies, Avco RAD document No. 64-1642, Rev. 1, Aug. 16, 1964 - Secret. (The material taken from this reference was taken from unclassified paragraphs).

47 Sowers and Sowers, Introduction Soil Mechanics and Foundations, Macmillan Co. (1961).

48 Voyager Design Studies - Volume Five: Lander Design - Part One, Avco RAD Doc. No. RAD-TR-63-34 (15 October 1963).

49 RAD-SR-65-264, Development of a Typical Mars Probe Sterilization Container - 1st quarterly report NASA Contract NAS 8-20502 (15 October 1965) p. 21.

50 Goetzal et al, Space Materials Handbook, Addison-Wesley (1965), pp 328-332.

51 Handbook of Geophysics and Space Environments, Air Force Cambridge Research Lab., McGraw-Hill (1965).

52 Marks' Mechanical Engineers Handbook, 6th Edition, Baumeister, McGraw-Hill, pages 4-60 to 4-62.

53 Development of a Typical Mars Landing Capsule Sterilization Container NASA Contract NAS 8-20502.

54 AFSC, Wright-Patterson AFB, Proceedings of the First Space Vehicle Thermal and Atmospheric Control Symposium, pp. 735-759, Choice of an Atmosphere for an Extended Space Mission by Robert S. Thomas, ASD-TDR-63-260, Project No. 6146 (April 1963).

55 Loeb, L.B., Kinetic Theory of Gases, Mc-Graw-Hill, New York (1934), pp. 301-310.

APPENDIXES

A. IMPACT DYNAMICS ANALYSIS - PROLATE AND OBLATE SPHEROID LANDERS

B. STERILIZATION CANISTER LEAKAGE RATE

APPENDIX A

IMPACT DYNAMICS ANALYSIS - PROLATE AND OBLATE SPHEROID LANDERS

1.0 INTRODUCTION

The impact dynamics analysis which have been performed in the past have been concerned with spherical and lenticular (i.e., made up of spherical segments) lander geometries (see Reference 24). However, during the initial stages of the Langley effort, interest was aroused in landers in the shape of a football. This shape, idealized as a prolate spheroid, is analyzed in this report. The oblate spheroid, which is quite similar to the lenticular shape, is also analyzed.

The analyses presented assume that the crushable material properties are isotropic. The results of anisotropic analyses of the spherical and lenticular shapes can be used to estimate the probable effects of anisotropy on the prolate spheroid parameters. By specifying the material to be isotropic, the results obtained below indicate that the existing impact attenuation system computer program (program 1960B) can be used to obtain parametric results with no modifications required.

2.0 ANALYSIS

Nomenclature

A	area
S	crushing stress of crushable material
V	volume
a	semi-major axis of generating ellipse
b	semi-minor axis of generating ellipse
m	mass
t	thickness of crushable material
V_o	impact velocity
$\ddot{y}_m$	maximum deceleration
ϵ	usable strain of crushable material
ρ	mass density

Subscripts

$( )_c$ crushable material

$( )_i$ internal payload

$( )_{1,2}$ regions defined on Figure A-1

The general configuration of the prolate spheroid is shown in Figure A-1. The areas and volumes of principle interest are tabulated below:

$$A_1 = \pi a b \left[2 \frac{t_1}{b} - \left(\frac{t_1}{b} \right)^2 \right] \tag{1}$$

$$A_2 = \pi b^2 \left[2 \frac{t_2}{a} - \left(\frac{t_2}{a} \right)^2 \right] \tag{2}$$

$$V_1 = \pi a b t_1 \left[\frac{t_1}{b} - \frac{1}{3} \left(\frac{t_1}{b} \right)^2 \right] \tag{3}$$

$$V_2 = \pi b^2 t_2 \left[\frac{t_2}{a} - \frac{1}{3} \left(\frac{t_2}{b} \right)^2 \right] \tag{4}$$

$$V_i = \frac{4}{3} \pi a b^2 \left[\left(1 - \frac{t_2}{a} \right) \left(1 - \frac{t_1}{b} \right)^2 \right] \tag{5}$$

$$V_c = \frac{4}{3} \pi a b^2 - V_i \tag{6}$$

The first step in the solution is to assume that $V_2 = V_1$. This assures that the impact energy can be absorbed during an impact in either of these orientations. It is further assumed that this procedure will take care of intermediate orientations. Thus, if Equation (3) is set equal to Equation (4), the result is

$$t_2 = \frac{a}{b} t_1 \tag{7}$$

Using this relation to compare Equation (1) and (2) shows that A_1 will be the maximum cross-sectional area. This area will then be used below in the calculation of maximum impact decelerations.

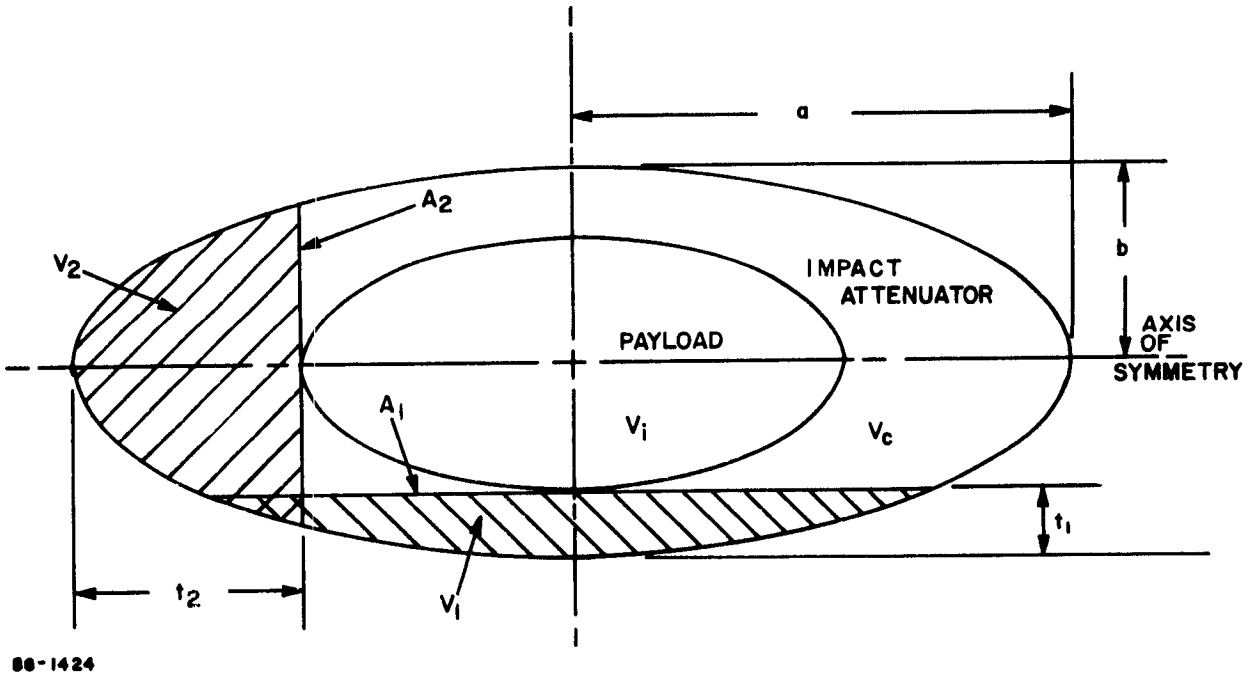

Figure A-1 PROLATE SPHEROID GEOMETRY

Now, the relevant equations of impact dynamics are (see Reference 24, pp. 7, 16).

$$\frac{1}{2}\,(m_i + m_c)\,V_o^2 = \epsilon S V_1 \tag{8}$$

$$(m_i + m_c)\,\ddot{y}_m = S \cdot A_1 \tag{9}$$

$$m_i = \rho_i V_i \tag{10}$$

$$m_c = \rho_c V_c \tag{11}$$

Equation (8) states that the amount of energy absorbed per unit volume of material crushed (ϵS) times the total volume crushed (V_1) should equal the total kinetic energy of the lander at impact. Equation (9) is simply Newton's Law.

Using equations (1) through (7) yields

$$\frac{(m_i + m_c)\,V_o^2}{2\epsilon S} = \pi b^3\,\frac{a}{b}\left[\left(\frac{t_1}{b}\right)^2 - \frac{1}{3}\left(\frac{t_1}{b}\right)^3\right] \tag{12}$$

$$\frac{(m_i + m_c)\,\ddot{y}_m}{S} = \pi b^2\,\frac{a}{b}\left[2\,\frac{t_1}{b} - \left(\frac{t_1}{b}\right)^2\right] \tag{13}$$

$$m_i = \frac{4}{3}\,\pi\,\rho_i\,b^3\,\frac{a}{b}\left(1 - \frac{t_1}{b}\right)^3 \tag{14}$$

$$m_c = \frac{4}{3}\,\pi\,\rho_c\,b^3\,\frac{a}{b}\left[1 - \left(1 - \frac{t_1}{b}\right)^3\right] \tag{15}$$

Now, the equations for an isotropic, spherical lander are simply the above equations with $a = b$. These sphere equations are programmed in digital computer program No. 1960B, where b is associated with R_2, the radius of the sphere. In fact, if the definition

$$m' = \frac{b}{a}\,m \tag{16}$$

is introduced into equations (12) to (15), the equations will be identical to those for a sphere. This means that program 1960B can be used, without modification, to generate parametric data for the prolate spheroid. All one has to do is to use equation (16) after running the program, i.e., multiply all the masses used in the program, both as inputs and outputs, by the $\frac{a}{b}$ ratio of interest to obtain the equivalent masses pertaining to the prolate spheroid.

Similarly, it can be shown that in the case of the oblate spheroid (a shape similar to the lenticular), the equations can be made identical with those pertaining to the sphere if the substitution

$$m'' = \left(\frac{b}{a}\right)^2 m \tag{17}$$

is made. In this case also, the semi-minor axis of the generating ellipse, b, is associated with R_2 in the program.

3.0 SUMMARY

In order to obtain parametric results for prolate spheroid lander, the procedure consists of running program 1960B, setting the value of R_2 in the program equal to b, the semi-minor axis of the spheroid, and by multiplying all masses involved in the program by the a/b ratio of interest. This procedure yields the prolate spheroid parameters.

The same type of procedure can be used to determine oblate spheroid parameters, except that all masses involved in the 1960B program are multiplied by $(a/b)^2$ to obtain the corrected masses.

APPENDIX B

STERILIZATION CANISTER LEAKAGE RATE

1.0 INTRODUCTION

Avco is developing a typical Mars probe sterilization container under contract to NASA (see Reference 53). From this program and other studies it was determined that post assembly leakage holes through the canister (container) must be smaller than the microorganism to which the canister would probably be exposed. Results of these studies established the maximum non-repairable hole size at 0.2 microns and the leakage rate to be a function of molecular effusion.

Using analytical methods for determining molecular flow and probable equivalent leak areas from the experimental work of others (see Reference 54), a conservative estimate of the initial leak rate of the canister was found. Reworking the initial leak rate formulas to account for the exponential decay of the internal pressure in relation to ambient, the final pressure was determined as a function of the leakage time.

2.0 ANALYSIS

The surface area of the sterilization canister has been calculated to be 6.56×10^4 in^2 for a 188 inch Flight Capsule design (see Volume III, Book 1, paragraph 3.5). Using a conservative leakage area estimate, for sealed vehicles, of 2.5×10^{-10} square inches of leakage area for each square inch of surface area, (see Reference 54) the equivalent leakage area is 1.64×10^{-5} in^2. If the leakage flow is considered molecular, rather than continuum (i.e., the dimension of the leakage hole is smaller than the gas molecules mean fee path), the gas leakage rate, G, may be expressed as (see Reference 55):

$$G = K_1 (P_{int} - P_{out}) A_{leak} \sqrt{\rho_1} \text{ (lbs/sec)}$$

where:

K_1 = .1885 (for G in lb/sec)

P_i = psi (internal pressure)

P_o = psi (external pressure)

A_{leak} = in^2

$\sqrt{\rho_1}$ { gas property, $(lb/ft^3/lb/in^2)^{1/2}$ $(W/VP)^{1/2}$; 0.07157 for air ; 0.07033 for N_2 ; 0.02660 for H_e

W gas weight, pounds

P gas pressure, lb/in^2

V gas volume, ft^3

Using nitrogen as the pressurization gas and a 1.0 lb/in^2 differential pressure, the initial leak rate, G, is 2.17×10^{-7} lb/sec or 18.75×10^{-3} lb/day. For other pressure differentials, the initial leak rate will vary in a direct linear manner.

Let us now consider the problem of Earth storage after assembly and prior to launch. Assume that after sterilization an initial internal pressure above ambient is established. If there is no gas resupply, and if 300 days elapse prior to launch, some residual internal pressure will be present at launch, and the canister internal pressure will have decayed exponentially. Considering this time dependent leakage problem, for molecular flow, using previous definitions:

$$G = dW/dt = -k_1 A_{leak} \Delta P \sqrt{\rho_1} = -k_1 A_{leak} (P_{int} - P_{out}) \sqrt{\rho_1} \quad (1)$$

For a constant internal canister gas temperature and assuming perfect gas relationships:

$$(1/P_{int_o})\, dP_{int}/dt = (1/W_o)\, dW/dt \quad \text{or} \quad dW/dt = (W_o/P_{int_o})\, dP_{int}/dt$$

(Note: subscript "o" denotes T = 0 sec)

Combining (1) and (2):

$$(dP_{int}/dt)\, W_o/P_{int_o} = -k_1 A_{leak} (P_{int} - P_{out}) \sqrt{\rho_1} \quad (3)$$

or

$$dP_{int} = (-k_1 A_{leak} \sqrt{\rho_1}\ P_{int_o}/W_o)(P_{int} - P_{out})\, dt \quad (4)$$

or

$$dP_{int}/(P_{int} - P_{out}) = (-k_1 A_{leak} \sqrt{\rho_1}\ P_{int_o}/W_o)\, dt \quad (5)$$

For P_{out} = constant this takes the form:

$$dx/ax + b = K\,dt \tag{6}$$

where

$$a = 1 \qquad b = P_{out}$$

$$K = -k_1 A_{leak} \sqrt{\rho_1} \quad \frac{P_{int_o}}{W_o}$$

Integrating both sides of (6) between appropriate limits:

$$(1/a) \log_e (ax + b) \Big|_{x_o}^{x} = Kt \Big|_{t_o}^{t} \tag{7}$$

or

$$\log_e (P_{int} - P_{out}) \frac{P_{int}}{P_{int_o}} = -k_1 A_{leak} \sqrt{\rho_1} \frac{P_{int_o}\, t}{W_o} \Bigg|_{t=0}^{t} \tag{8}$$

then

$$\log_e (P_{int} - P_{out}/P_{int_o} - P_{out}) = \frac{-k_1 A_{leak} \sqrt{\rho_1}\ P_{int_o}\ t}{W_o} \tag{9}$$

Noting that $\log_e (J) = L$ or $e^L = J$

we obtain:

$$P_{int} - P_{out}/P_{int_o} - P_{out} = e^{-(k_1 A_{leak} \sqrt{\rho_1}\ P_{int_o}/W_o)\, t} \tag{10}$$

(Note that at $t = 0$, $e^0 = 1$ and $P_{int} - P_{out} = P_{int_o} - P_{out}$)

We may substitute ΔP for $P_{int} - P_{out}$, then

$$(\Delta P/\Delta P_{initial}) = e^{-(k_1 A_{leak} \sqrt{\rho_1}\ P_{int_o}/W_o)\, t} \tag{11}$$

But, from previous molecular leak definitions:

$$G_o = -k_1 A_{leak}\ \Delta P_{init} \sqrt{\rho_1} \tag{12}$$

Therefore:

$$\Delta P/\Delta P_{initial} = e^{-[G_o P_{int_o}/(W_o \Delta P_{init})]t} \quad (13)$$

From previous definitions

$$\rho_1 = W_o/V_o P_{int_o} \quad (14)$$

or

$$W_o/P_{int_o} = \rho_1 V_o \quad (15)$$

Substituting into (13), and for a constant ambient pressure, P_{out} :

$$\Delta P/\Delta P_{initial} = e^{-[G_o/(\Delta P_{initial} \rho_1 V_o)]t} \quad (16)$$

The ratio $\Delta P/\Delta P$ initial is the relationship of the final pressure to the initial pressure in the canister. The final pressure can be determined for a span of time, t , in days if the following factors are known:

1. G_o , initial leak rate in lb/day
2. ΔP , initial differential pressure in psi
3. V_o , canister volume in cubic feet
4. ρ_1 , or $(\sqrt{\rho_1})^2$ as identified previously, is 0.00495.
5. P_{out}, ambient pressure, is a constant

Assuming a ΔP of 0.5 lb/in^2 the leak rate, G , becomes $\frac{18.75 \times 10^{-3}}{2}$ or 9.38×10^{-3}. Using ρ_1 as $(0.07033)^2$ and the initial volume, V_o , as 517 ft^3, then for 300 days:

$$\Delta P/\Delta P_{initial} = 0.11$$

The timewise relationship between $\Delta P/\Delta P$ initial is shown in Figure B-1 assuming no replenishment of the pressurant gas and no change in the ambient temperature and ambient pressure. Having assumed a ΔP initial of 0.5 lb/in^2 the final pressure will be 0.5 x 0.11 or 0.055 lb/in^2. Almost any increase in Earth storage environmental embient pressure or decrease in the internal pressurizing gas temperature would allow the canister-pressure differential to become negative and below the minimum limit which is established by the sterilization criteria. (see Section 4.0).

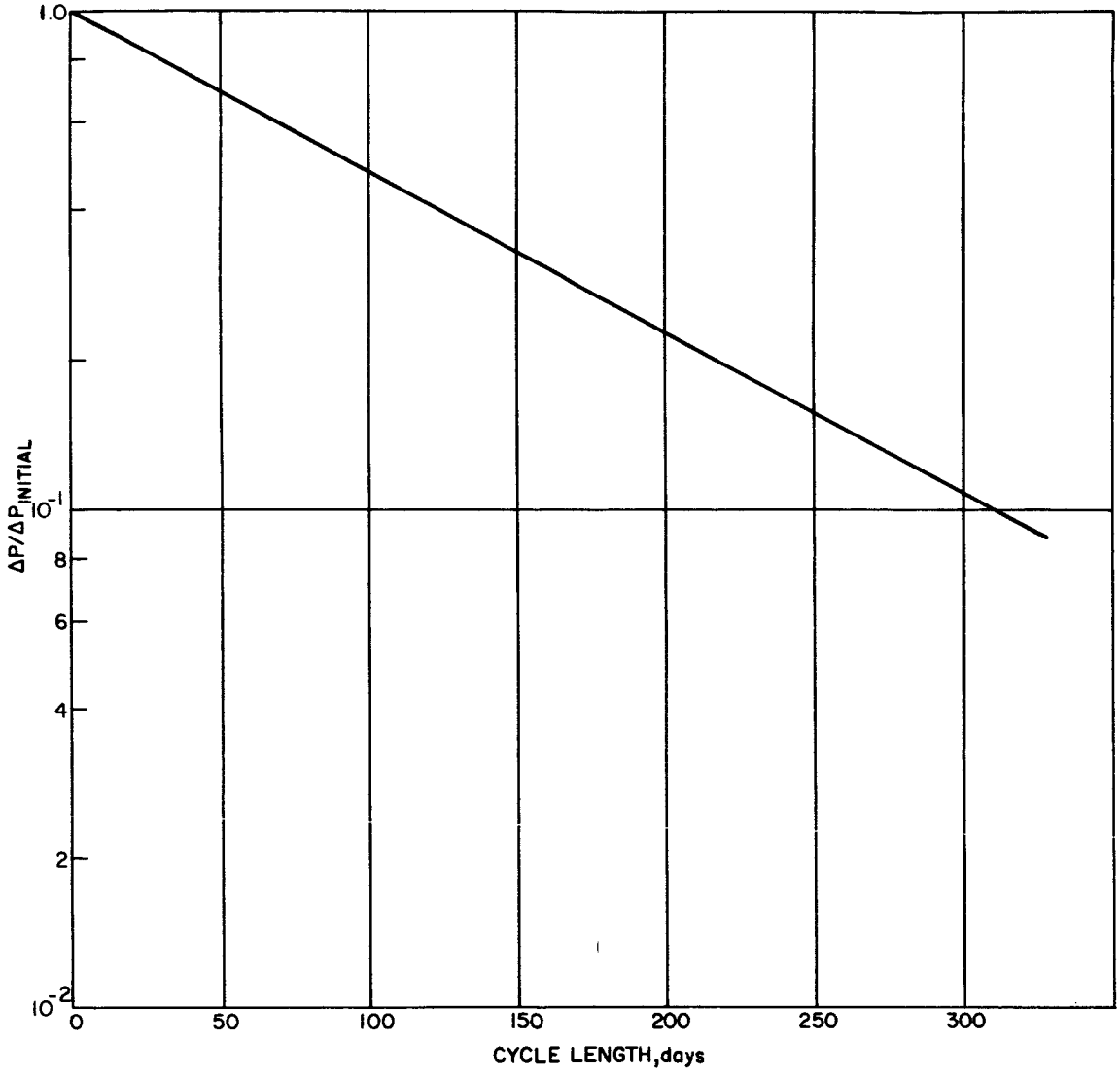

Figure B-1 CYCLE LENGTH EFFECT ON STERILIZATION CANISTER PRESSURE DIFFERENTIAL

3.0 CONCLUSION

From the previous calculations, it has been shown that it is advisable to have an auxiliary supply of gas to prevent the sterilization canister internal pressure from falling below ambient conditions due to small environmental changes.